

The
University
Of
Sheffield.

False Brinelling and Fretting Wear in Wind Turbine Pitch Bearings

Eladio Enrique Hurtado Molina

A thesis submitted in partial fulfilment of the requirements for the degree of
Doctor of Philosophy

The University of Sheffield
Faculty of Engineering
Department of Mechanical Engineering

March 2023

I would like to dedicate this thesis to my son Dante ...

Abstract

Pitch bearings connect the blades to the rotor hub of a wind turbine and allow the blades to rotate and optimise their position under different wind speeds. The rotation of the blades is necessary to change the angle of attack to control power production and loads acting on wind turbine components. Accurate positioning of pitch bearings is essential to maximise the productivity of wind turbines and ensure their operational safety. Double-rowed eight-point contact ball bearing is the most widespread bearing solution used in pitch systems. Wear in wind turbine pitch bearings is a tribological issue that has attracted more research interest in recent years, motivated by the challenge of improving the reliability of components and systems of modern large-scale wind turbines, which are rapidly increasing their size with demanding lightweight design requirements. False Brinelling and fretting corrosion are two wear modes affecting pitch bearings produced by oscillatory movements of small-amplitude. The characteristics and differences of False Brinelling and fretting corrosion in pitch bearings are not clearly defined and variations exist among different research publications. Moreover, the effect of operating conditions on these wear modes is not fully understood. This research project aims to characterise the damage modes in wind turbine pitch bearings produced by small-amplitude oscillations and investigate the effect of the most relevant variables involved in these failure modes.

To achieve the research aims, a series of simulations and experimental studies were conducted. Firstly, a finite element analysis of the load distribution in a pitch bearing assembly and the damage investigation of a failed pitch bearing section were conducted. The finite element simulation and damage observation results provided information about the damage characteristics of the bearing under actual operating conditions and allowed the estimation of the conditions that produced the damage found on the raceway surface. Secondly, two experimental studies were carried out to reproduce fretting wear under simplified pitch bearing conditions and analyse the effect of different testing parameters, such as the oscillation amplitude, contact force, oscillation frequency, presence of lubricant, contact geometry and number of cycles. The first experimental study consisted of a small-scale configuration using a standard tribometer consisting in ball-in-flat rolling/sliding contact with a 9 mm diameter ball. The results showed limitations of the experimental setup due to the scale and the kinematics of the ball. These

limitations were overcome by designing a bespoke medium-scale fretting test rig where the balls are in contact with two grooved samples, allowing a more realistic movement of the balls. Finally, a finite element analysis of the ball contact considering the geometry of both experimental configurations was developed implementing two different approaches to predict the occurrence of wear and to gain a better understanding of contact variables to complement the experimental results.

Based on the main results and conclusions obtained in this research project, it was possible to define the main characteristics of fretting wear produced under pitch bearing testing conditions. These characteristics correspond to adhesive and abrasive wear combined with oxidation, whose shape and profile depend on the operating conditions and the sliding regime. However, it was not possible to provide a better differentiation between false Brinelling and fretting corrosion. The experimental studies and finite element analyses allowed different effects of the key testing parameters to be understood which made it possible to outline a proposal to mitigate fretting wear under pitch bearing conditions. The main recommendations consisted of decreasing the oscillation amplitude when actively pitching, reducing the contact force by improving the load distribution, and optimising the contact geometry. Lubrication was not the main focus of this PhD work, therefore, conducting an in-depth analysis of greases and their properties was suggested as possible future work. It is also recommended to conduct an investigation of the effect of variable oscillation amplitude and force, because in this research, all the tests were performed considering these parameters constant.

The novelty of the work presented in this thesis lies in the experimental methods where the testing conditions were defined to be representative of wind turbine pitch bearing conditions and the test rigs were designed to account for the complex kinematics taking place in these kinds of bearings, which are not the same normally assumed in standard fretting tests.

Acknowledgements

The completion of this thesis is the result of four years of hard work, but I have not been alone. This achievement would have not been possible without the help and support of many people. I would like especially to thank some of them.

I would like to express my sincere gratitude to my supervisor, Prof Hui Long, for providing invaluable guidance, support and feedback throughout this project.

Thank you to my industrial advisors, Rob Rowntree and Mike Lewis, for your help to understand the industrial relevance of this research project and for your willingness to share your knowledge and experience with me.

Thank you to Jamie Booth, Dave Webster, Luke Callaghan, Richard Kay and Tes Monaghan for your technical advice on the design and analysis of experimental tests.

Thank you to my research colleague, Rui Dai, for your valuable support in sample preparation.

Thank you to my friends in Sheffield for all the experiences we had together in the past four years and for making this place my home.

Thank you to my family in Chile for always being there for me despite the long distance. Especially to my mom, sister and niece.

Above all, I would like to express my deepest gratitude to Roxana for your huge support throughout these four years and for being my biggest motivation along with our little son Dante.

The author acknowledges the support received from the Chilean National Agency for Research and Development (ANID)/Scholarship Program / Doctorado Becas Chile/2018 - 72190145.

Table of contents

List of figures	xiii
List of tables	xix
Nomenclature	xxi
1 Background and Literature Review	1
1.1 Introduction	1
1.1.1 Pitch Bearings and Pitch System	1
1.1.2 Pitch Systems	2
1.2 Research Problem	3
1.3 Literature Review	4
1.3.1 Pitch Bearing Life	5
1.3.2 Damage Modes of Pitch Bearings	6
1.3.3 Fretting	10
1.3.4 Factors Affecting False Brinelling and Fretting Wear	15
1.3.5 Friction in Fretting Contacts	21
1.3.6 Experimental Analysis of Fretting Test Rigs	24
1.3.7 Prediction of False Brinelling and Fretting Corrosion	27
1.3.8 Summary	29
1.4 Research Aim and Objectives	30
1.5 Research Novelty and New Contribution	30
1.6 Thesis Outline and Structure	31
2 Analysis of Load Distribution in Pitch Bearing Balls	33
2.1 Introduction	33
2.2 Methods	34
2.3 Description of the FE Model	35
2.3.1 Geometry and Materials	35

2.3.2	Finite Element Mesh	40
2.3.3	Interactions and Boundary Conditions	42
2.3.4	Loading Conditions	45
2.4	Results and Analysis	47
2.4.1	Bearing Rings Displacements	48
2.4.2	Load Distribution Analysis	50
2.4.3	Contact Angle Analysis	54
2.4.4	Hoop Stresses	57
2.4.5	Effect of Balls Losing Contact	60
2.5	Conclusions	60
3	Damage Characterisation of a Failed Pitch Bearing Section	63
3.1	Introduction and Aims	63
3.2	Materials and Methods	64
3.2.1	Pitch Bearing Section	64
3.2.2	Surface Damage Observation by Optical Microscopy	65
3.2.3	Wear Scars Measurements	66
3.2.4	Identification of Oxidation Products	67
3.2.5	Analysis of Tribologically Transformed Structure	67
3.3	Results	69
3.3.1	Surface Observation of the Damaged Bearing Raceway	69
3.3.2	Surface Mapping of Wear Scars	72
3.3.3	Hardness Profile and Microstructure Analysis	74
3.3.4	Chemical composition of oxidation products	76
3.4	Discussion	77
3.4.1	Location and Shape of Wear Scars	77
3.4.2	Operating Conditions	79
3.5	Conclusions	82
4	Experimental Fretting Study in a Small-Scale Configuration	85
4.1	Introduction and Aims	85
4.2	Materials and Methods	86
4.2.1	Tribometer	86
4.2.2	Samples and Lubrication	86
4.2.3	Testing Conditions	88
4.2.4	Measurement of Friction and Analysis of Fretting Loops	89
4.2.5	Measurement of Wear Scars	91

4.2.6	Derivation of Wear Rates	92
4.3	Results	93
4.3.1	Preliminary Tests	93
4.3.2	Fretting Loops	94
4.3.3	Coefficient of Friction	96
4.3.4	Sliding Distance	98
4.3.5	Frictional Energy	100
4.3.6	Wear Damage	101
4.3.7	Wear Rate Coefficients	103
4.4	Discussion	104
4.5	Conclusions	106
5	Design and Experimental Study of a Medium-Scale Fretting Test Rig	107
5.1	Introduction and Aims	107
5.2	Fretting Test Rig Design	108
5.2.1	Aims of Fretting Test Rig	108
5.2.2	Test Rig Requirements and Constraints	108
5.2.3	Contact Configuration	109
5.2.4	Design of Fretting Test Rig	110
5.2.5	Data Acquisition	111
5.3	Materials and Methods	112
5.3.1	Equipment	112
5.3.2	Samples and Lubrication	112
5.3.3	Testing Conditions	114
5.3.4	Measurement of Wear Damage	115
5.3.5	Measurement of Friction Indicator	116
5.4	Results	116
5.4.1	Observation and Measurement of Wear Scars	116
5.4.2	Effect of Testing Conditions on Wear Damage	119
5.4.3	Effect of Testing Conditions on Friction Indicator	125
5.5	Discussion	126
5.5.1	Analysis of Wear Scars	127
5.5.2	Comparison of Experimental Setups	128
5.5.3	Mitigation of Wear Damage in Pitch Bearings	129
5.6	Conclusions	130

6	Finite Element Analysis of a Rolling Ball Contact	133
6.1	Introduction and Aims	133
6.2	Methods	134
6.3	Description of the FE models	134
6.3.1	Small-Scale Contact FE Model	134
6.3.2	Medium-Scale Contact FE Model	138
6.4	Results	141
6.4.1	Small-Scale Contact FE Model	141
6.4.2	Medium-Scale Contact FE Model	146
6.4.3	Sensitivity Study on the Coefficient of Friction	150
6.5	Discussion	151
6.6	Conclusions	154
7	Conclusions and Future Work	155
7.1	Conclusions	155
7.2	Future Work	157
	References	159
	Appendix A Python Functions for the Analysis of Fretting Loops	167
	Appendix B Medium-Scale Fretting Test-Rig Drawings	171
	Appendix C Medium-Scale Fretting Test-Rig FEA	183
C.1	Description of the FE Model	183
C.2	Stress Analysis Results	184
	Appendix D Implementation of UMESHMOTION	187
D.1	Description of UMESHMOTION User Subroutine	187
D.2	UMESHMOTION Code for Fretting Wear	187

List of figures

1.1	Pitch bearing cross section view	2
1.2	Steady pitch curve [2]	3
1.3	Damage modes of rolling bearings [16].	7
1.4	Illustration to differentiate the two Brinelling mechanisms.	8
1.5	Simplified fretting loop.	11
1.6	Mindlin’s definition of contact condition [33].	11
1.7	Fretting map proposed by Vingsbo and Söderberg [32].	12
1.8	Schematic representations of RCFM and MRFM [34].	13
1.9	Fretting modes.	14
1.10	Illustration of different definitions of the oscillating amplitude.	16
1.11	Cycle counting results reproduced from the simulation of the IWT 7.5-164 reference wind turbine.	17
1.12	Examples of different $x/2b$ ratios.	18
1.13	Examples of Coulomb and non-Coulomb fretting loops indicating the location of the maximum coefficient of friction and geometric independent coefficient of friction.	23
1.14	Schematic test rig configuration for tangential fretting reproduced from [54].	24
1.15	Schematic test rig configuration for rotational fretting reproduced from [55].	25
1.16	Test rig for torsional fretting reproduced from [55].	26
1.17	Test rig for radial fretting of bearing sections reproduced from [57].	27
2.1	Blades, pitch bearings and hub assembly.	35
2.2	Blade and Hub geometries	36
2.3	Blade model dynamic results - Normalised displacement magnitude [mm].	38
2.4	Blade model static results - Displacement magnitude [mm].	39
2.5	Pitch bearing geometry	40
2.6	Assembly FE mesh.	41
2.7	Interaction definitions for bolted connections of the pitch bearing.	43

2.8	Spring force-displacement curve.	44
2.9	Balls contact modelling.	45
2.10	Model fixation and loads.	46
2.11	Nomenclature used in results.	47
2.12	Radial displacements of the bearing rings [mm].	49
2.13	Axial displacements of the bearing rings[mm].	49
2.14	Summary of radial displacements for all assembly configurations.	50
2.15	Summary of axial displacements for all assembly configurations.	50
2.16	Comparison of radial displacements [mm].	51
2.17	Load distribution row 1 - Base configuration.	51
2.18	Load distribution row 2 - Base configuration.	52
2.19	Load distribution due to bending moment.	53
2.20	Load distribution indexes for all assembly configurations.	54
2.21	Comparison of load distribution between the base configuration and the configuration with the 50mm thickness plate in the hub.	54
2.22	Schematic representation of free contact angle.	55
2.23	Change of contact angle for base configuration - Row 1.	56
2.24	Change of contact angle for base configuration - Row 2.	56
2.25	Schematic representation of the allowable change of the contact angle.	57
2.26	Maximum change of contact angle for all configurations.	58
2.27	Comparison of change of contact angle between the base configuration and the configuration with the 50mm thickness plate in the hub.	58
2.28	Hoop stresses of bearing rings [MPa].	59
2.29	Summary of hoop stresses.	60
2.30	Comparison of load distribution between the base configuration and the model with five balls suppressed.	61
3.1	Pitch bearing sections.	64
3.2	Zeiss AX10 optical microscope used for detailed surface damage observation.	65
3.3	Alicona InfiniteFocus-SL and raceway surface inspected.	66
3.4	Equipment for EDX analysis and illustrative scheme of the technique.	67
3.5	Prepared samples for sub-surface investigation	68
3.6	Damage modes on pitch bearing raceway surface.	69
3.7	Detailed surface damage observed by optical microscopy and surface mapping of the surface damage.	70
3.8	Location of measured wear scars on raceways 1 and 2.	71
3.9	Wear scars surface maps of raceway 1.	72

3.10	Wear scars surface maps of raceway 2.	72
3.11	Wear scar profiles of raceway 1.	73
3.12	Wear scar profiles of raceway 2.	73
3.13	Hardness profile measurements of unworn and worn raceway sections.	75
3.14	Optical microscope images - 20x magnification.	76
3.15	Orientation map and phase map obtained from EBSD analysis of the worn section.	76
3.16	SEM image and oxygen map from EDX analysis.	77
3.17	Possible contact load distribution of the raceway sections.	78
3.18	Schematic representation of wear scar profiles overlapping.	78
3.19	Damage ratio and wear scar depth from measured data.	79
3.20	Estimation of loading conditions based on Hertzian calculation and wear scar measurement.	80
3.21	Schematic representation of the method for the estimation of the sliding distance.	81
3.22	Plots for estimation of sliding conditions.	81
4.1	UMT-3 used for fretting tests.	87
4.2	Example of asymmetric behaviour of tangential force.	91
4.3	Analysis of a fretting loop to derive sliding distance and dissipated frictional energy.	92
4.4	Scheme of wear volume calculation with the Soap Film method.	92
4.5	Schematic of wear rates calculation.	93
4.6	Comparison of measured COF versus oscillation amplitudes under pure tangential fretting and rolling+tangential fretting.	94
4.7	COF measured for test C02 repeated three times (1 mm - 100 N - 1 Hz).	94
4.8	Measured fretting loops for tests C01, C02, C05 and C08.	95
4.9	Fretting loops under different oscillation amplitudes (100 N - 1 Hz.	96
4.10	Fretting loops under different contact forces (1 mm - 1 Hz.	96
4.11	Fretting loops under different oscillation frequencies (1 mm - 100 N.	97
4.12	10 s sample of tangential force signal measured in test (1 mm - 100 N - 1 Hz).	97
4.13	Comparison of four calculation methods for the COF.	98
4.14	COF under different testing conditions.	99
4.15	Sliding distance under different testing conditions.	99
4.16	Dissipated energy under different testing conditions.	100
4.17	Optical surface measurements and SEM images for tests C06 and C15.	101
4.18	Greased lubricated samples after completed tests showing debris trapped in the grease.	102

4.19	Wear profiles from tests C02 and C11.	102
4.20	Accumulated wear depth under different testing conditions.	103
4.21	Wear volume rate by energy analysis.	104
4.22	Local wear rate by accumulated energy density analysis.	104
5.1	Mayes 3 bi-axial hydraulic machine used to applied the load and cyclic motion.	108
5.2	Comparison of contact geometries.	110
5.3	CAD model of the fretting test rig design.	111
5.4	CAD assembly of samples and balls.	111
5.5	Fretting test rig for medium-scale fretting experimental study.	112
5.6	An example of manufactured samples and balls.	114
5.7	Surface measurements of tests D01 and L01 (texture and height colour maps).	117
5.8	Locked and microslip regions.	118
5.9	Wear profiles of tests D01 and L01 (5 mm - 20 kN - 1 Hz).	118
5.10	Microstructure analysis of AISI O1 steel samples under optical microscope.	119
5.11	Maximum wear depth under different oscillation amplitudes.	120
5.12	Comparison of wear maps of dry tests under different oscillation amplitudes.	121
5.13	Maximum wear depth under different contact forces.	121
5.14	Comparison of wear maps of dry tests under different contact forces.	122
5.15	Maximum wear depth under different oscillation frequencies.	122
5.16	Maximum wear depth under different contact geometries.	123
5.17	Comparison of wear maps of dry tests with different contact geometries.	123
5.18	Maximum wear depth under different number of cycles.	124
5.19	Comparison of wear maps of dry and lubricated tests at 3000 cycles.	124
5.20	Plots of frictional indicator of four tests.	125
5.21	Average frictional indicator under different testing parameters.	126
6.1	FE model of the small-scale contact configuration.	135
6.2	Mesh convergence results of small-scale contact configuration FE model.	136
6.3	Boundary conditions, interactions and loads applied on the small-scale contact FE model.	137
6.4	Loading and oscillations sequence in small-scale contact FE model.	137
6.5	Medium-scale contact configuration FE model.	139
6.6	Mesh convergence results of medium-scale contact configuration FE model.	140
6.7	Boundary conditions, interactions and loads applied on the medium-scale contact FE mode.	141
6.8	Loading and oscillation sequence in medium-scale contact FE model.	142

6.9	FE model verification by comparison of fretting loops and accumulated frictional energy.	142
6.10	Comparison of worn surfaces under equivalent conditions.	143
6.11	Comparison of wear profiles.	144
6.12	Accumulated slip during the first cycle.	144
6.13	Traction lines during the first cycle.	145
6.14	Ball rotation over the modelled cycles.	145
6.15	Contact pressure variation over cycles and wear damage accumulation.	146
6.16	Frictional energy density (E_d) from FE model compared to measured worn surface (height) under different oscillation amplitudes.	147
6.17	Frictional energy density (E_d) from FE model compared to measured worn surface (height) under different contact forces.	147
6.18	Frictional energy density (E_d) from FE model compared to measured worn surface (height) under different contact geometries.	148
6.19	Summary of the maximum frictional energy density of all models and comparison with the maximum wear depth from experimental tests.	149
6.20	Frictional energy density (E_d) from FE model compared to measured worn surface (height) under an oscillation amplitude of 5 mm.	149
6.21	Incremental slip and traction lines at three points of the oscillation cycle.	150
6.22	Maximum frictional energy density under different COFs.	151
C.1	Geometry and mesh for FEA of medium-scale test rig.	184
C.2	Loads and positions considered for the FEA of the medium-scale test rig.	185
C.3	Maximum principal stress distribution results [MPa].	185

List of tables

2.1	Blade main dimensions and properties [2].	37
2.2	Blade stiffness indicators.	38
2.3	Main dimensions and properties of the pitch bearing.	39
2.4	Hub properties and dimensions.	40
2.5	Mesh statics.	41
2.6	Load applied to the blades and resulting loads at the blade root.	46
2.7	Plate thickness in the six assembly configurations.	48
3.1	Pitch bearing geometry and material properties.	65
3.2	Alicona parameters for wear scar surface mapping.	66
3.3	Parameters for sample preparation.	69
3.4	Summary of wear scars dimensions.	74
3.5	Surface roughness measured on the wear scars and calculated damage ratio.	74
3.6	Relative element concentration Wt%.	77
4.1	UMT-3 specifications.	86
4.2	Specifications of flat samples.	87
4.3	Selected grease properties and comparison with reference greases [40, 85].	88
4.4	Testing conditions to study coefficient of friction.	90
4.5	Testing conditions to study wear rates.	91
4.6	Wear volume rate and local wear rate by energy analysis.	103
5.1	Mayes 3 testing specifications.	109
5.2	Testing requirements.	109
5.3	Chemical composition comparison between 42CrMo ₄ and O1 steels.	113
5.4	Main properties of samples.	114
5.5	Testing conditions for unlubricated and grease lubricated conditions.	115
5.6	Maximum contact pressure, contact area width, and normalised oscillation amplitude for the considered testing parameters.	116

6.1	Material properties for rolling ball contact FE model.	135
6.2	Different conditions evaluated in the medium-scale FE model.	141
C.1	Yield failure analysis results.	186
C.2	Fatigue analysis results.	186

Nomenclature

Roman Symbols

a	Major semi-axis of a elliptical contact area or radius of a circular contact area in point contact
b	Minor semi-axis of elliptical contact area in a point contact
D	Diameter of rolling element
Δh_i	Incremental wear depth at the end of the i-th increment
ΔN	Jump cycle factor
d_m	Pitch diameter of the bearing
e	Sliding ratio
Ed	Frictional energy
Ed_h	Frictional energy density
Ed_{th}	Wear energy threshold
F_a	Bearing radial force
$F(\kappa)$	Elliptic integral of the first kind
F_r	Bearing axial force
h	Wear depth
K	Contact stiffness
$LD_{bearing}$	Load distribution index bearing
$LD_{row,i}$	Load distribution index row i

M	Bearing bending moment
N	Total number of cycles
P	Normal contact force
P_{ea}	Bearing equivalent load
Q	Tangential force
Q^*	Tangential force amplitude
q_0	Maximum shear stress at the contact area
Q_{max}	Maximum ball contact load
R	Raceway diameter
R_a	Arithmetical mean roughness
r_m	Bearing pitch radius
R_z	Mean peak to valley roughness
S	System stiffness
$S_{z,exp}$	Surface roughness after a fretting test
SG	Maruyama's damage ratio
$S(\kappa)$	Elliptic integral of the second kind
$S_{z,new}$	Surface roughness before a fretting test
V	Wear volume
x	Linear oscillation amplitude
Z	Number of rolling element in a row

Greek Symbols

α_{allow}	Allowable change of contact angle
α_h	Local energy wear coefficient
α	Nominal contact angle

α_V	Volume energy wear coefficient
α_0	Half of the bearing raceway arc
δ	Contact deformation
δ^*	Slip amplitude
Δ	Far-field displacement
Δ^*	Far-field displacement amplitude
δ_n	Relative deformation of the two bearing rings along the normal of the contact
γ	$D \cos \alpha / d_m$
κ	Ellipse elongation
ϕ	Oscillating amplitude (a quarter of the total arc)
θ	Harris' oscillating amplitude
θ_{crit}	Harris' critical oscillating amplitude
θ_{dith}	Harris' dither oscillating amplitude

Subscripts

<i>ball</i>	ball
<i>i</i>	inner ring
<i>o</i>	outer ring

Acronyms / Abbreviations

BCC	Body centred cubic
BSE	Back scattered electron imaging
COF	Coefficient of friction
EBS	Electron back scatter diffraction
EMD	Electrical Discharge Machining
EDS	Energy dispersive X-ray spectroscopy

<i>EDX</i>	Energy dispersive X-ray spectroscopy
<i>IPC</i>	Elasto-hydrodynamic lubrication
<i>FCC</i>	Face centre cubic
<i>FE</i>	Finite element
<i>FEA</i>	Finite Element Analysis
<i>FEM</i>	Finite Element Method
<i>IPC</i>	Individual pitch controller
<i>MRFM</i>	Material response fretting map
<i>NLGI</i>	National Lubricating Grease Institute
<i>RCFM</i>	Running condition fretting map
<i>SEM</i>	Scanning electron microscope
<i>TTS</i>	Tribologically transformed structure
<i>UMT</i>	Universal Mechanical Tester
<i>WT</i>	Wind turbine

Chapter 1

Background and Literature Review

1.1 Introduction

This section briefly introduces the pitch bearing and the pitch system, the wind turbine component that this PhD thesis investigates. This section covers the type of bearing normally used in this application, the main characteristics of pitch bearings and their relevance to the operation of wind turbines. Moreover, the basics of the pitch system is explained to understand the pitch bearing operation.

1.1.1 Pitch Bearings and Pitch System

Wind energy faces unique challenges related to the reliability of wind turbine components despite its significant improvement over the last decade. These challenges are associated with critical and large-scale components of a large number of wind turbines and their remote locations, especially in offshore wind farms, making their maintenance a difficult and expensive task.

Electrical components usually exhibit the highest failure rates [1]; however, they are small and easy to replace. In contrast, mechanical components affected by tribological issues present lower failure rates but their failures are difficult to predict and pose higher replacement or repair costs; thus, they are getting more attention from wind turbine manufacturers and wind farm operators. One of the systems affected by these tribological issues is the pitch system. This system consists of a large slewing bearing, known as pitch or blade bearing rotated by an electric or hydraulic pitch actuation system. Pitch bearings connect the blades to the hub allowing the blades to oscillate to change the angle of attack that faces the wind to control the power and loads of wind turbines.

Pitch bearings of modern large-scale wind turbines operate under unfavourable conditions. When standing still or oscillating at low speeds they are subjected to high combined axial, radial and moment loads. The lightweight design of their supporting structures, namely hub and blade, provide little support to the bearing, thus they may be subjected to large deformation under loading. Double-row eight-point contact ball bearing shown in Figure 1.1 is the most widespread bearing solution used in pitch systems, whereas three-row roller bearings are gaining popularity in recent years. The research presented in this thesis focuses only in double-row ball bearings.

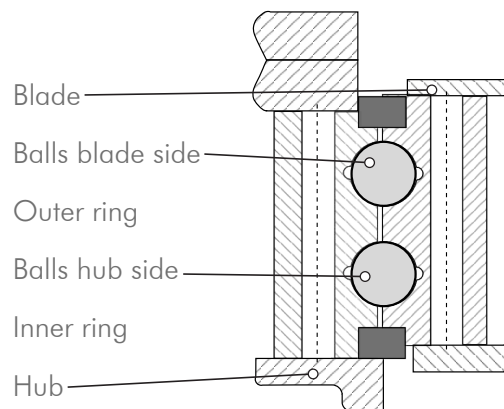


Figure 1.1: Pitch bearing cross section view

1.1.2 Pitch Systems

Modern large-scale wind turbines are equipped with pitch systems which have individual drives for each blade and individual pitch controller (IPC). This enables each blade to pitch independently from the other blades. The two most commonly used pitch drive systems are hydraulic and electric. The connection of the blades with the hub through pitch bearings has the advantage of pitching the blades in both directions, clockwise and counterclockwise, without any structural limitation.

Figure 1.2 shows the steady pitch curve of the IWT-7.5-164 reference wind turbine to illustrate how the pitch system works. No pitching activity occurs for wind speeds between the

cut-in and the rated wind speed, and the blades remain at a zero-degree position to maximise the power generated. The blades begin to pitch once the rated wind speed is reached to control drive train loads and maintain the power output constant.

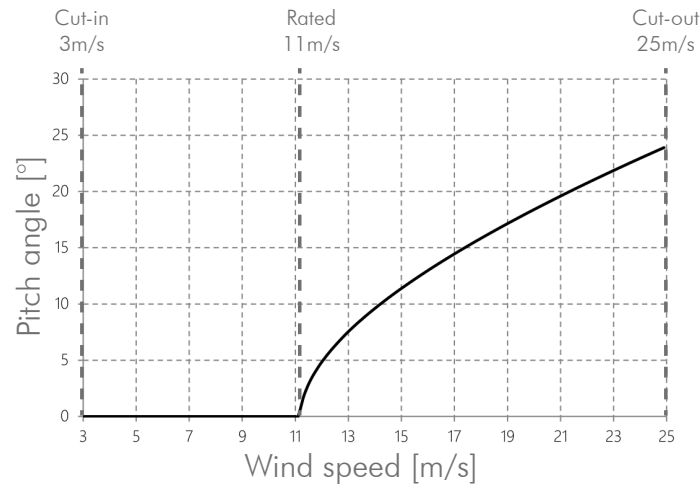


Figure 1.2: Steady pitch curve [2]

1.2 Research Problem

For oscillating bearings, such as pitch bearings, which experience intentional oscillations due to pitching movements, and unintentional oscillations due to vibrations, no established international design standard exists to calculate their service life accurately. This inaccuracy is mainly because some damage modes in pitch bearings are not fully understood. Moreover, the fact that these bearings are highly damage-tolerant and the absence of reliable field data of actual pitch bearings' service life in the public domain makes it difficult to determine their service life accurately.

Design adaptations based on rotational bearings, such as [3] and [4], are currently the usual approach to calculating pitch bearing life. These adaptations are based on rolling contact fatigue and are not valid for bearings operating under small amplitude oscillations that develop different damage modes. These methods has been proved not to be reliable as they produced different results under the same conditions [5]. Moreover, these methods have not been validated with field service data of wind turbines. This problem has led pitch bearings to be designed with different, and non-standardised approaches.

Harris et al. [3] suggested that keeping oscillation amplitudes above a certain critical value was an effective way to prevent bearing damage and failures. However, the implementation of IPC for pitch bearing in modern large-scale wind turbines has multiplied the pitching activity

of blades, particularly the number of small-amplitude oscillating movements [6, 7]. The amplitude, frequency and number of oscillatory cycles have a significant effect on the damage mechanisms of these bearings. Small amplitude oscillations can lead to false Brinelling and fretting corrosion in pitch bearings [8]. These wear modes result in indentations in the raceway preventing the smooth operation of the positioning system [9] which is critical to wind energy generation and the safety of wind turbines.

False Brinelling and fretting corrosion occur between loaded contacting surfaces under cyclic relative motion of small amplitude. Godfrey [8] describes False Brinelling as mild adhesive wear that occurs under lubricated contact conditions and fretting corrosion occurs under dry conditions. False Brinelling and fretting corrosion can occur simultaneously in real oscillating bearing applications depending on the operating conditions. Moreover, no clear distinction exists in the literature between these two wear mechanisms, and it is still debated whether false Brinelling and fretting corrosion are different damage modes or if false Brinelling is the incubation process of fretting corrosion. Next section presents an in-depth literature review to understand the existing research, debates on the topic and identify the research gaps that this thesis aims to fill.

1.3 Literature Review

False Brinelling and fretting corrosion are two wear modes produced by small-amplitude oscillations in pitch bearings. Although these wear modes have been researched at a fundamental level for many years, they are not fully understood for a complex application such as wind turbine pitch bearings. The literature review presented in this chapter surveys a wide range of published research papers to study and understand different aspects regarding pitch bearings and their failure modes, with a particular emphasis on false Brinelling and fretting corrosion. The reviewed articles are selected according to their relevance to the following topics.

- Pitch bearing life
- Pitch bearing failure mechanisms
- False Brinelling and fretting corrosion in pitch bearing life
- Factors affecting pitch bearing life due to wear damage caused by small-amplitude oscillations
- Experimental fretting analysis and test rigs
- Prediction of wear damage

1.3.1 Pitch Bearing Life

Life calculation of rotating bearings has been extensively researched and well standardised. In contrast, oscillatory bearings have not been investigated to a similar depth, and no international design standard exists. The lack of a standard calculation method has resulted in pitch bearings calculated with different non-standardised approaches. The main limitation regarding standards for rotating bearings is that rolling contact fatigue is considered the main damage mode and it may not be applicable to fretting damage.

Harris and Kotzalas et al. [10] proposed a method to estimate rolling bearing's life in oscillating bearings based on the equations and procedures provided in international standards [11–14], and Harris et al. [3] applied this method in a design guideline for wind turbine pitch and yaw bearings. This guideline suggests that the minimum pitch angle should be higher than a critical value θ_{crit} , as shown in Equation 1.1. This critical amplitude is defined as the angle of rotation for which one rolling element touches the raceway surface without overlapping the section stressed by the adjacent rolling element. This critical oscillating amplitude defines two regions: (i) when $\theta > \theta_{crit}$ the contact area of rolling elements overlap, and (ii) when $\theta \leq \theta_{crit}$, the individual contact regions do not overlap, and each rolling element has its discrete stressed volume. Harris et al. defined a third region in this design guideline [3] for small oscillations based on a second critical oscillation amplitude θ_{dith} , as shown in Equation 1.2. This dither angle is defined as the width of the contact footprint divided by the radius of the rolling path of the ball over the raceway surface .

$$\theta_{crit} = \frac{720^\circ}{Z(1 \mp \gamma)} \quad (1.1)$$

$$\theta_{dith} = \frac{720^\circ b}{\pi d_m (1 \mp \gamma)} \quad (1.2)$$

To prevent the occurrence of fretting corrosion in pitch bearings, Harris et al. [3] argued that the amplitude of oscillations should be higher than half of the critical amplitude ($\theta > \theta_{crit}/2$) and emphasised that when the amplitude is lower than the dither angle ($\theta \leq \theta_{dith}$) fretting corrosion is more likely to occur. Reducing small-amplitude oscillations seems to be the first approach to prevent fretting corrosion in pitch bearings, yet current operating conditions makes this strategy impossible to achieve, especially after the implementation of IPC in large scale wind turbines that has increased the number of small oscillations of pitch bearings.

Schwack et al. [5] applied four different methods for calculating bearing life [3, 4, 10, 11] for an IPC-controlled pitch bearing from the reference wind turbine IWT 7.5 MW [2]. None of the four methods led to service life longer than two years, far too shorter than the 20 year life required by wind turbines. These results considered standard conditions for rotating

bearings that were not suitable for oscillating bearings in wind turbine applications. For example, the lubrication condition in a pitch bearing does not always correspond to an EHL regime. The comparison of pitch bearing life calculations between the four methods showed differences up to 300%. The results and conclusions presented by Schwack et al. [5] showed that these approaches were not reliable for calculating pitch bearing life. The limitations of these methods come from the fact that the damage modes in oscillating bearings are different from rotating ones where rolling contact fatigue is assumed the main damage mode, especially when oscillating bearings operate under small-amplitude oscillations. This demonstrates the need for developing a deeper understanding of false Brinelling and fretting corrosion before progressing to propose standardised pitch bearing life calculation methods.

To illustrate the relevance of small-amplitude oscillations in the damage modes affecting pitch bearings, it is worth mentioning the study conducted by Stammler et al. [6], who developed a time series-based method to characterise the oscillating movements. In this work, it was pointed out that IPC produces different movement patterns in pitch bearings with a significant number of small amplitude oscillations within the range between 0.2° and 1.5° . This method was applied to the IWT 7.5MW reference wind turbine [2] for which the Harris' critical angle was calculated to be 2.5° . Most research information regarding oscillation amplitude comes from fundamental knowledge of fretting which not necessarily correspond to the contact conditions in pitch bearings, as the contact conditions and oscillating patterns are more complex in these bearing. Therefore it is necessary to develop experimental test methods to obtain relevant data under those specific conditions.

1.3.2 Damage Modes of Pitch Bearings

Oscillating bearings may experience different damage modes when compared with rotating bearings [6, 15]. Figure 1.3 presents all the possible damage modes that a rolling element bearing used in general applications can experience [16].

Stammler et al. [15] analysed the possible damage modes in pitch bearings and these include fatigue, core crushing, ring fractures, edge loading, fretting and false Brinelling.

Fatigue in through-hardened bearings initiates at the position of the maximum equivalent stress under Hertzian conditions, below the raceway contact surface. In pitch bearings, raceways are commonly surface-hardened, fatigue may also start at the location of the maximum stress or the allowable limit between the surface hardened layer and the bulk material. In this case, the damage mode is core crushing. Bearing rings may also experience fatigue due to high dynamic bending moments resulting in ring fractures.

Large deformation of the bearing rings because of the flexibility of surrounding parts causes a translation of the contact area towards the raceway edge. When the contact path crosses the

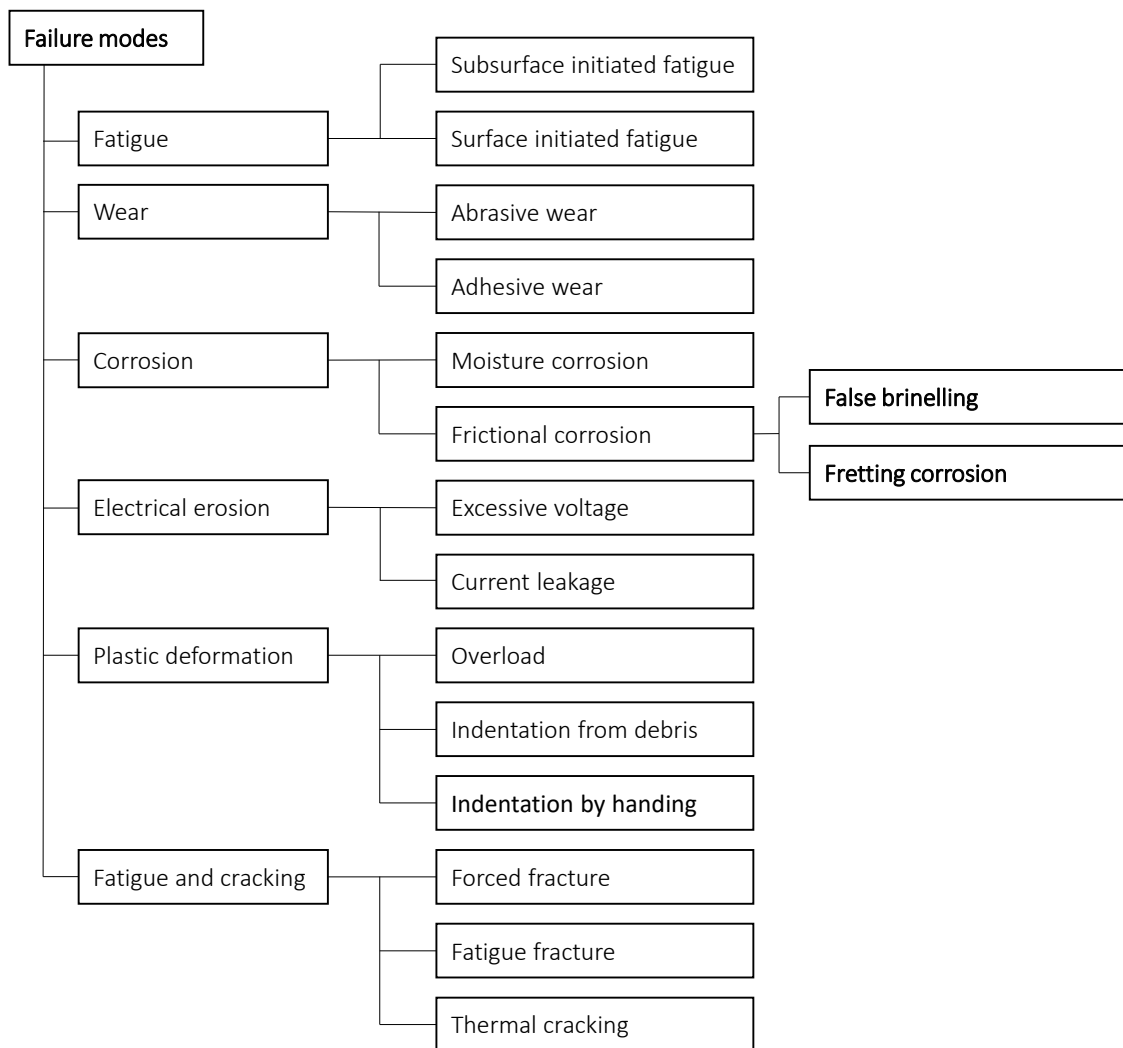


Figure 1.3: Damage modes of rolling bearings [16].

raceway edge, the contact area becomes smaller, therefore the remaining area withstands higher stresses. If the contact stresses exceed the allowable levels, the raceway will be damaged by edge loading.

Stammler et al. [15] pointed out that fatigue, core crushing, ring fractures and edge loading were damage modes that could be assessed during the design phase of pitch bearings. However, this is not true for surface-initiated wear damage under small-amplitude oscillations such as fretting corrosion and false Brinelling.

False Brinelling and fretting corrosion have been identified as common tribological issues in wind turbine pitch bearings [3, 9]. These two wear modes have been extensively discussed in the

literature. However, their similarities and differences are not clearly defined, and controversy exists around this matter.

Godfrey [8] provided one of the clearest descriptions of their differences; fretting corrosion is defined as the fretting damage in unlubricated contact surfaces under relative, reciprocating sliding motion of small amplitude. This fretting damage occurs with corrosion, usually, oxidation when exposed to air, and is characterised by red films or reddish debris as a result of the formation of Hematite Fe_2O_3 , the oxidation product of iron exposed to air in the absence of lubricant.

False Brinelling is defined as a worn depression on raceways of lubricated rolling element bearings due to the slight movement of the rolling elements. This condition prevents the formation of an elastohydrodynamic oil film leading to boundary lubrication. The worn depressions replicate the shape and position of rolling elements without any shoulder around the depression as it occurs in true Brinelling as illustrated in Figure 1.4 [8]. The oxidation product of false Brinelling is Magnetite Fe_3O_4 .

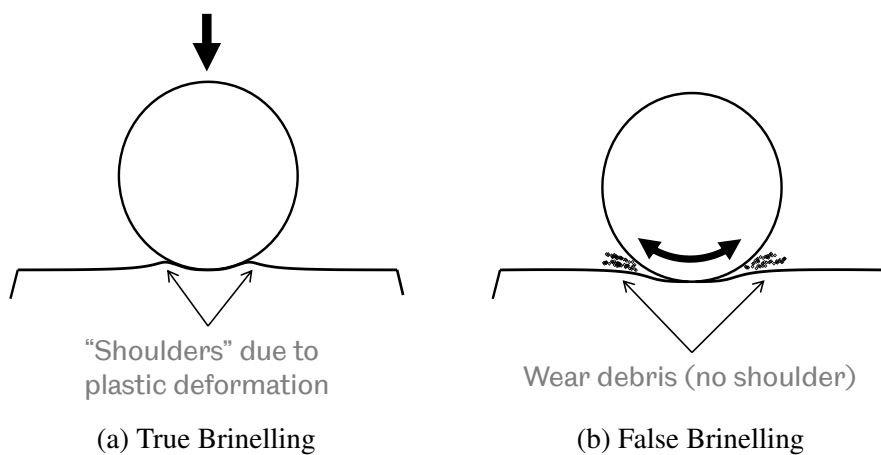


Figure 1.4: Illustration to differentiate the two Brinelling mechanisms.

Harris et al. [3] defined fretting corrosion as a wear mechanism between surfaces in contact subjected to pressure and cyclic motion of small amplitude. Under these conditions, lubricant is squeezed out from the contact area and removes the oxide films which protect the surfaces; consequently, metal-to-metal contact occurs, causing adhesive wear. The main difference between the definition provided by Harris and Godfrey relates to the difference between false Brinelling and fretting corrosion. Harris claimed that false Brinelling was the incubation process of fretting, whereas Godfrey differentiated two different wear modes based on the lubrication condition, making it unclear the relationship between these damage mechanisms.

Recent studies on false Brinelling in pitch bearings have defined false Brinelling as a form of fretting wear [17, 18].

False Brinelling is a damage mode that has been always associated with rolling element bearings, in most cases produced by vibrations during transportation [19, 20]. Unlike false Brinelling, fretting corrosion has been related to a wide variety of applications where small-amplitude oscillations occur in contacts; for example, landing gears [21], hip replacements [22], riveted joints [23] and bearing shafts [24]. So far, it is possible to agree on two key elements common to these wear modes: small-amplitude oscillations and oxidative wear.

In pitch bearings, false Brinelling has been normally associated with vibrations produced by the wind when the blades at idle [9], resulting in unintentional minute movements of the rolling elements. This may suggest that this condition occurs at low loads. In contrast, fretting corrosion is related to intentional small-amplitude oscillations generated intentionally by the pitch systems when active; therefore, the loading conditions are supposed to be higher. It is also true that the amplitude of the oscillations generated by the pitch system is higher than the movements induced by vibrations. Therefore, it is possible to agree with the statement that false Brinelling is a form of fretting wear [17, 18]. Understanding the role of the oscillation amplitude is then essential to establish the difference between these two wear modes and establish which condition generates more severe damage.

Regarding the oxidative wear, it was previously mentioned that Magnetite Fe_3O_4 was the oxidation product for false Brinelling and Hematite Fe_2O_3 for fretting corrosion [8]. This difference has been attributed to the lubrication condition: lubricated for false Brinelling and unlubricated for fretting corrosion. However, this is not true in pitch bearings as they are grease lubricated, and fretting has been observed as a relevant damage mode, suggesting that the lubrication is not the only factor involved in the formation of oxidation products. Certainly, lubrication contributes to preventing the access of oxygen [25], but there is no evidence on how oscillation amplitude or load may affect this phenomenon. Magnetite and Hematite are iron oxides with different oxidation states. Magnetite contains both 2+ and 3+ Fe, and Hematite only the 3+ Fe [26]. This difference means that the formation of Hematite needs more oxygen than Magnetite. Thus, it would be possible to suggest that fretting corrosion occurs in an oxygen-rich environment, which could be changed to false Brinelling depending on the lubrication and contact conditions which may decrease the oxygen access. Moreover, operating conditions affect the impact of oxidative wear on fretting; Fouvry et al. [27] studied the fretting wear process in a Ti-6Al-4V cylinder on flat dry contact and found that the oxygenation of the contact area was affected by contact force and oscillation frequency. A low contact force and oscillation frequency eased the access of oxygen, and the predominant wear mechanism was

abrasion. A higher contact force and frequency reduced the oxygenation, and adhesion became the relevant wear mechanism.

Godet [28] and Berthier et al. [29] described wear produced by reciprocating motion as a process of debris formation and ejection. Depending on the contact geometry, the wear process may be controlled by the rate of debris formation or the rate of debris ejection. For example, in non-conforming geometries, such as ball-on-flat configuration, debris can be more easily ejected from the interface and the wear rate is controlled by the rate of debris formation.

1.3.3 Fretting

In the previous section, fretting corrosion has been identified as one of the most relevant wear modes in wind turbine pitch bearings. Understanding the different approaches used to study this wear mode, not only in pitch bearings but also in different applications, is essential to identify any possible research gap and define the methods for this research project.

Fretting Loops

Fretting loops depict graphically the relationship between tangential force and displacement amplitude in fretting contacts, usually along a third temporal axis [30]. Fretting loops have been used to characterise fretting behaviour, specifically for the development of fretting maps and the identification of fretting regimes. Both topics will be discussed in the following sections.

Pearson and Shipway [31] summarised the terminology used to describe fretting loops, as shown in Figure 1.5. The displacement (Δ) is usually measured at a remote location and not in the contact itself. The far-field displacement amplitude (Δ^*) usually includes not only the slip distance but also the elastic deformation between the contact and the location of the displacement sensor. Sources of this elastic deformation can be a combination of the contact, bulk specimen, fixture and rig elastic displacement. The elastic deformation is commonly described as a system stiffness (S). The actual slip amplitude (δ^*) is normally obtained by post-processing the fretting loops calculating the displacement at the vertical axis origin when the tangential force is equal to zero. Finally, the vertical axis of a fretting loop plot corresponds to the tangential force (Q), whose amplitude (Q^*) depends on the normal contact force and the coefficient of friction.

Fretting Maps

Fretting maps are probably one of the most relevant advances in the study of fretting. Fretting maps were firstly introduced by Vingsbo and Söderberg [32] in 1988. The development of these maps was based on the comprehension of the contact mechanics theory proposed by

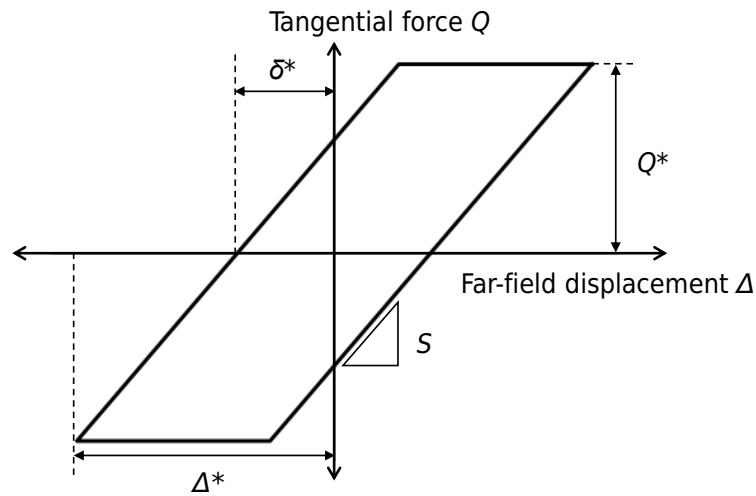


Figure 1.5: Simplified fretting loop.

Mindlin [33]. This theory explains that the contact area in a ball-on-flat configuration under normal load and experiencing a tangential load is divided into two regions: an inner central region that is under sticking condition and an outer zone that exhibits slip condition, as shown in Figure 1.6). Fretting can be referred to fatigue or wear, which behave as two competitive mechanisms. Vingsbo and Söderberg [32] identified three fretting regimens in their fretting maps and related them to the fatigue and wear damage: (i) stick regime characterised by low slip amplitude and associated with low surface and fatigue damage; (ii) partial slip that takes place under intermediate slip amplitude and results in accelerated crack growth and reduces fatigue life, but exhibits a low wear rate; (iii) gross slip occurs for larger slip amplitude and results in severe wear damage, and limited crack formation.

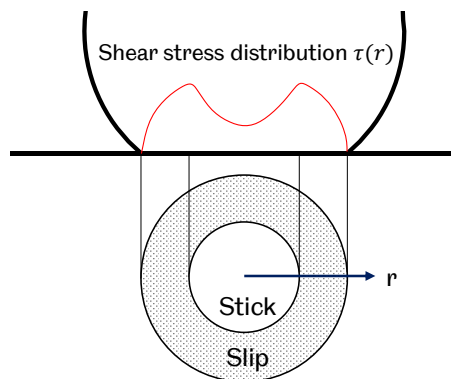


Figure 1.6: Mindlin's definition of contact condition [33].

Pearson and Shipway [31] reviewed the fretting maps of Vingsbo and Söderberg [32] in 2015. They argued that there were two primary limitations in early work by Vingsbo and Söderberg [32]. Firstly, measuring the far-field displacement and not the actual slip. Secondly, not recognising the existence of a threshold in terms of the dissipated energy, below which wear does not occur. These limitations resulted in fretting maps presented by Vingsbo and Söderberg in Figure 1.7 showing a strong dependency of the wear coefficient on displacement amplitude. This conclusion disagrees with more recent research on fretting, where a more limited dependence of the wear coefficient on the displacement amplitude has been observed [31].

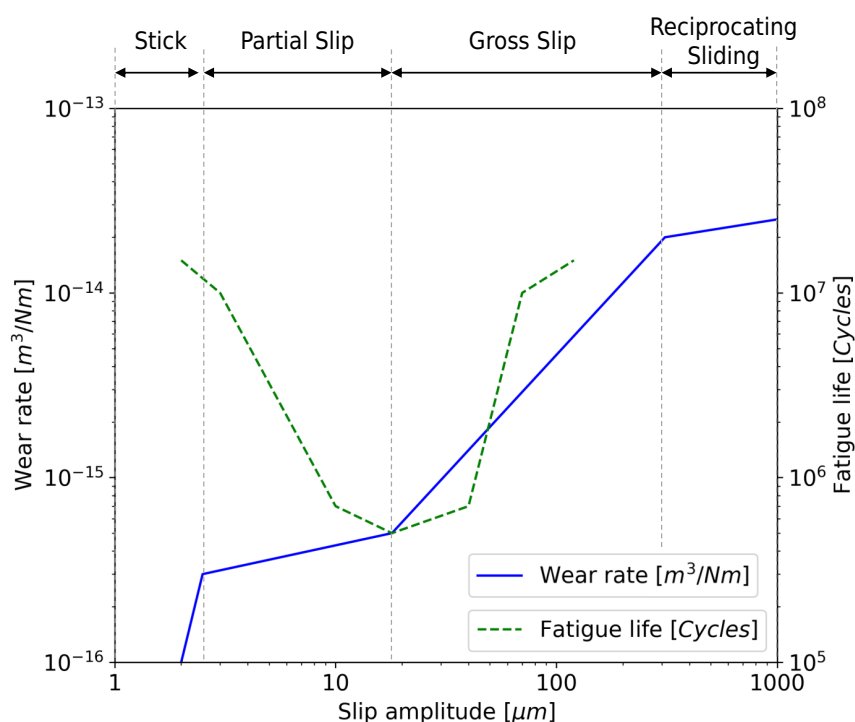
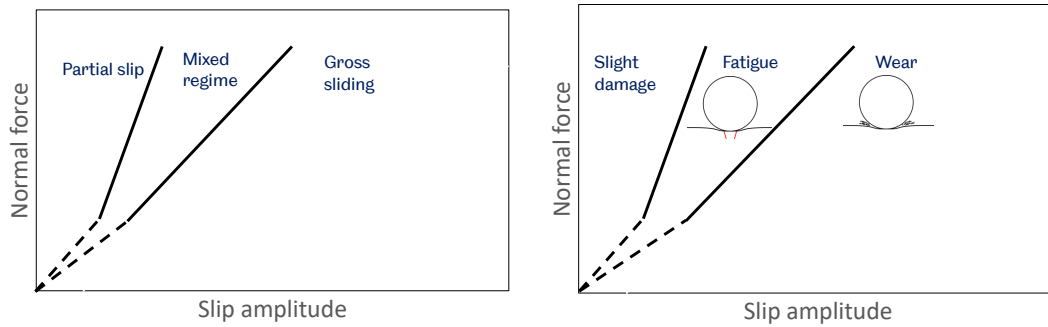


Figure 1.7: Fretting map proposed by Vingsbo and Söderberg [32].

Zhou and Vincent [34] proposed two different fretting maps: Running condition fretting map (RCFM) and material response fretting map (MRFM). Figure 1.8 shows schematic representations of these fretting maps.

RCFM distinguishes different regimes: partial slip regime, mixed fretting regime, and slip regime, which are defined as follow:



(a) Running condition fretting map (RCFM) (b) Material response fretting map (MRFM)

Figure 1.8: Schematic representations of RCFM and MRFM [34].

1. In partial slip, the contact behaviour is as described by Mindlin [33], i.e., sticking in the central region and micro slip in the outer region. This fretting regime is associated with closed fretting loops.
2. In mixed fretting regime, the initial gross-sliding due to lubrication effect is created by surface oxides and contaminant film. The oxide particles are quickly removed, resulting in an increment of the tangential force and regions of metal-to-metal adhesive contact. This regime has been identified as the most critical condition in both fretting fatigue and fretting wear. This fretting regime is characterised by unstable fretting loops, changing between closed, elliptically-shaped, and fully open loops.
3. In gross slip regime there is no stick region in the contact area. This regime is related to fully open fretting loops.

The main difference between these regimes and the fretting regimes firstly introduced by Vingsbo and Söderberg [32] is that Zhou and Vincent [34] ignored the stick regime, arguing that there was always some region of the contact experiencing slip. In other words, Zhou and Vincent [34] believed that the regime with a contact area completely stuck did not exist.

MRFM is related to the damage of the material. Compared with RCFM, these fretting maps differentiates three regions: slight damage, fatigue damage and wear damage.

Fretting Modes

Zhu and Zhou [35] identified four fretting wear modes for a contact of ball-on-flat according to the relative motion direction between the two contacting bodies: tangential, radial, rotational and torsional fretting. Figure 1.9 depicts these four modes. Several experimental studies have investigated tangential fretting. In contrast, radial, rotational, and torsional fretting have not

been studied in detail because of the difficulties to create these conditions experimentally. Zhu and Zhou [35] investigated the four wear modes individually. A combination of multiple fretting modes can occur simultaneously in complex applications. For instance, the contact between balls and raceways in wind turbine pitch bearings may potentially experience the four modes at the same time; radial fretting due to the dynamic nature of the loads, tangential and rotational fretting because of the rotation of the ball, and torsional fretting due to the spinning of the ball caused by the variation of the contact angle.

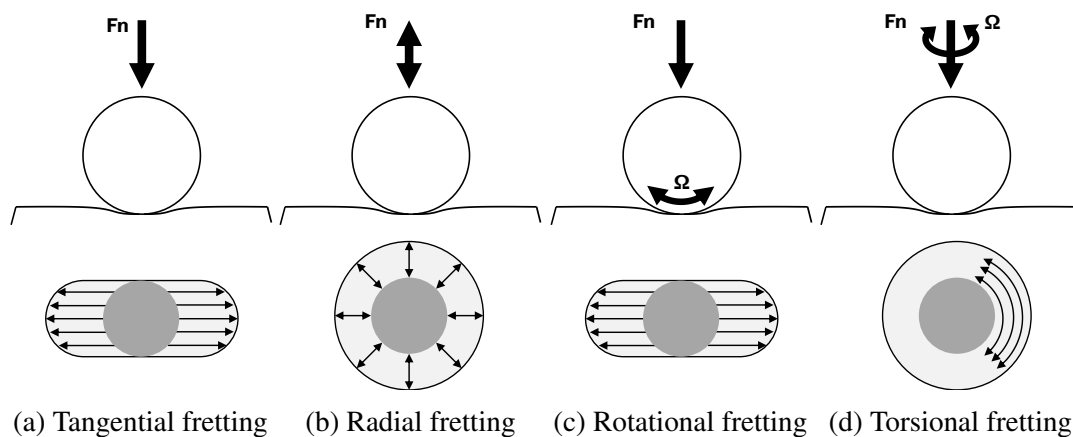


Figure 1.9: Fretting modes.

Energy Description of Fretting

Fouvry et al. [36] proposed an energy approach to describe the wear mechanisms of oscillating sliding contacts. This approach was proposed due to the need of considering the effect of variable coefficient of friction behaviour on the wear coefficient. This energy approach consists of comparing the wear volume (V) with the accumulated frictional energy dissipated at the contact area (Ed). This energy corresponds to the energy enclosed in every fretting loop cycle. Fouvry et al. [36] observed a linear relationship between the wear volume and the accumulated dissipated energy. Then, an energy wear coefficient (α_V) could be obtained by calculating the slope of the linear curve. For some metallic materials, the linear curve did not cross the origin of the diagram relating the wear volume and the accumulated frictional energy dissipated. The offset in the energy axis was associated with an energy threshold (Ed_{th}) required to modify the microstructure of the contact surface to a harder phase known as tribologically transformed structure (TTS). The fracture of the TTS was found to lead the debris formation. The energy wear approach to determine the wear volume is then expressed by Equation 1.3.

$$V = \begin{cases} 0, & \text{if } \sum Ed \leq Ed_{th}, \\ \alpha_V(\sum Ed - Ed_{th}), & \text{if } \sum Ed > Ed_{th} \end{cases} \quad (1.3)$$

The approach proposed by Fouvry et al. [36] relies on an important hypothesis, the energy dissipated by friction on the contact surface must be higher than any of the other processes taking place during the wear process. The other processes include plastic deformation and the formation of TTS. It was estimated that the plastic deformation can take up to 10% of the total energy, which validates the hypothesis of this approach.

Fouvry et al. [36] highlighted the wear volume analysis as a powerful tool to quantify fretting wear but pointed out that the wear damage was frequently assessed in one dimension, the depth. For this reason, a local wear analysis was needed. The local wear approach consisted of comparing the wear depth (h) with the dissipated energy density (Ed_h). Similarly to the wear volume approach, a linear relationship was observed between these two variables and a local wear coefficient (α_h) could be derived from the slope. The energy density dissipated at a specific point of the contact surface is given by the expression of Equation 1.4 for an oscillation amplitude of $2x$.

$$Ed_h(x, y) = \int_{-x}^{+x} q(x, y) ds \quad (1.4)$$

where $q(x, y)$ is the shear stress of the contact surface.

The wear depth is then express by Equation 1.5.

$$h = \alpha_h \sum Ed_h \quad (1.5)$$

1.3.4 Factors Affecting False Brinelling and Fretting Wear

More than 50 parameters have been reported to be related to fretting [37]. These parameters are difficult to study and test because of their strong interconnections. Collins [37] suggested that these parameters could be grouped into eight categories: relative slip amplitude, contact pressure, local state of stress, number of cycles, material and surface conditions, cyclic frequency, temperature, and environmental surrounding of the surfaces.

The parameters studied in this research are grouped into the following four categories: motion profile, load profile, bearing geometry and lubrication. These categories are discussed in detail in the following subsections.

Motion Profile

Motion profile is the characterisation of the movement in an oscillatory system. In pitch bearings, the motion profile refers to the oscillating amplitude, frequency, and the number of cycles. Figure 1.10 illustrates the oscillating amplitude of a rolling ball. The oscillation amplitude definition is not entirely unified, resulting in two different ways to measure this amplitude: one half of the total arc traced during one cycle of oscillation (θ), and one-quarter of the total arc traced during one oscillation cycle (ϕ). For this reason, it is necessary to be consistent with the notation used, particularly when comparing different studies.

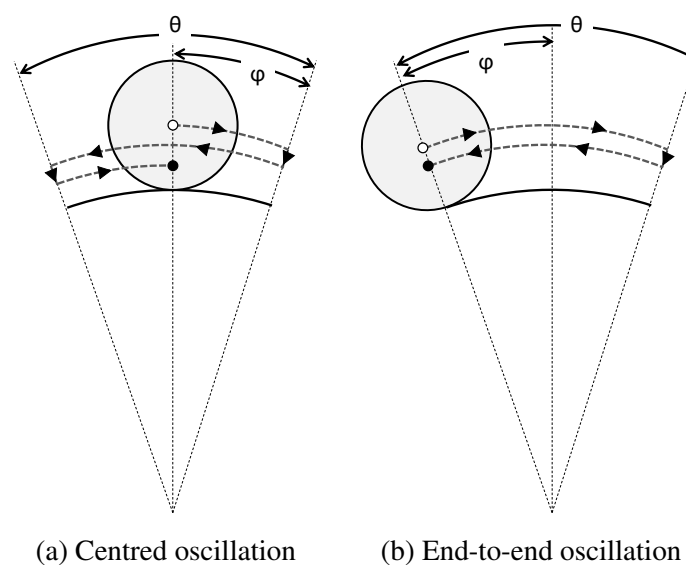


Figure 1.10: Illustration of different definitions of the oscillating amplitude.

As discussed in Section 1.3.1, the implementation of IPC in wind turbines has largely increased the number of small-amplitude oscillations cycles. Stammer [6] proposed a method for cycle counting and analysed time-series data obtained from simulations of the IWT 7.5-164 reference wind turbine [2]. The results of this analysis showed that most oscillating cycles have an amplitude in the range between 0.03° and 5° and the frequency is lower than 0.5 Hz, as shown in Figure 1.11.

The motion profile has been recognised as one of the most important factors to understand the occurrence of false Brinelling and fretting corrosion in pitch bearings. Small-amplitude oscillations have been identified as the main cause of these damage mechanisms and are the reason why different existing approaches fail to predict pitch bearing life accurately. The common approach to prevent false Brinelling and fretting corrosion is to avoid the small-amplitude movements. Avoiding small-amplitude oscillation is possible in other applications where the oscillations due to vibrations are unintentional, but this is not possible in pitch

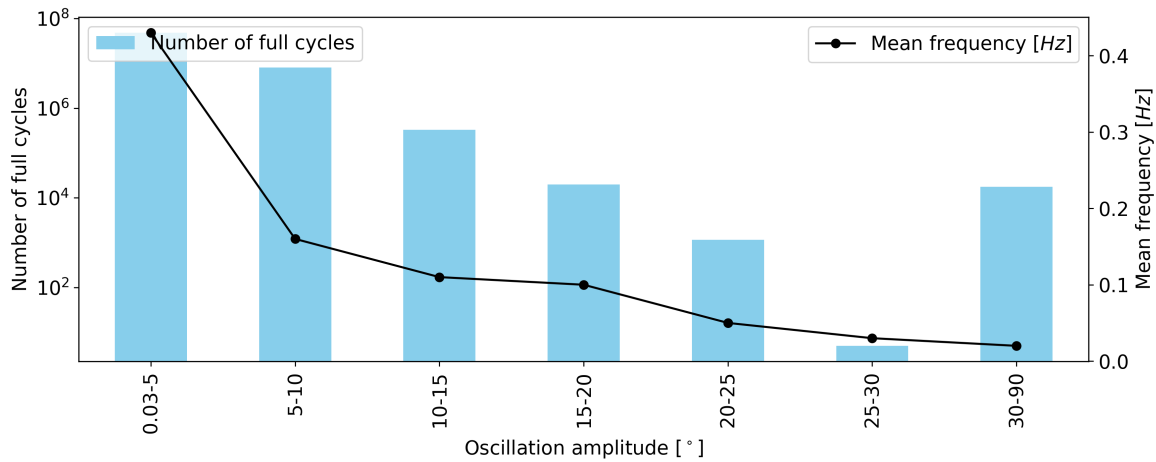


Figure 1.11: Cycle counting results reproduced from the simulation of the IWT 7.5-164 reference wind turbine.

bearings, where small-amplitude oscillations are intentional and required as the main function of the pitch system, especially after the implementation of IPC in modern wind turbines.

Bearing Geometry

Bearing geometry is closely related to the motion profile. The arc traced by a oscillation of 1° is not the same in a 1-metre diameter bearing as it is in a 6-metre diameter bearing. The sliding ratio $x/2b$, defined by the oscillation amplitude (x) over the width of the Hertzian contact area ($2b$) is usually used to characterise the slip regimes. For a sliding ratio lower than 1, there is an unexposed surface. Fouvry et al. [36] defined a transition between fretting and reciprocating sliding when the sliding ratio was equal to 1. Figure 1.12 illustrates different sliding ratios. This definition applies to fundamental fretting in dry contacts, but for more complex applications, reported threshold values of the sliding ratio are inconsistent in recent studies.

Maruyama [38] studied the oil film behaviour under minute vibrating conditions in EHL point contacts and used the sliding ratio to analyse the results. Maruyama's results show that a sliding ratio of 1.6 is required to establish the lubrication film. Schwack [39] claimed that under sliding ratios of over 1.6 fatigue is the dominating damage mechanism based on Maruyama's results and smaller $x/2b$ values could lead to greater wear damage. However, in a more recent study, Schwack [40] found that the damage produced by larger sliding ratios generated more fretting wear damage.

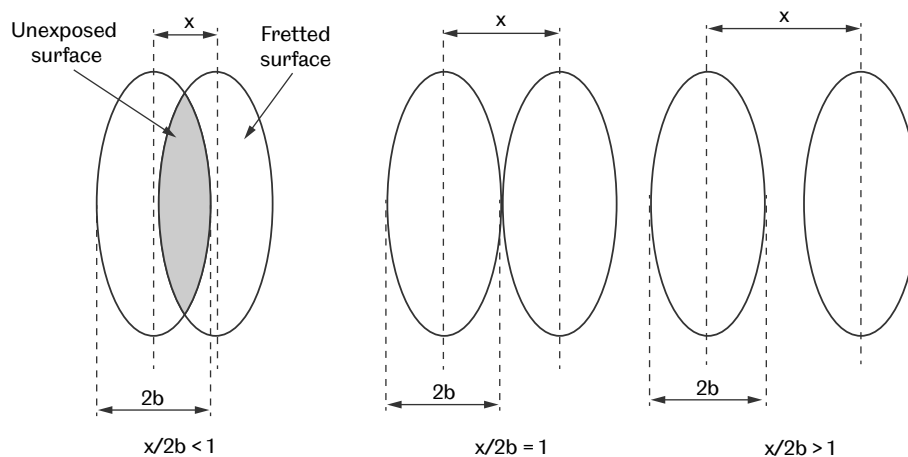


Figure 1.12: Examples of different $x/2b$ ratios.

The analysis of the film behaviour based on the sliding ratio shows that not only the macro dimensions of the bearing geometry play an important role in understanding what small oscillations mean. The contact area, particularly the ellipse semi-axis b is a relevant factor. This dimension is determined by different geometrical dimensions, such as the groove radius, ball diameter, and raceway diameter. This explained why the conformity, defined as the ratio between the groove radius and the ball radius, has been found to be a relevant parameter in investigating the occurrence of fretting wear. Schwack et al. [39] found that low conformity values produced a more favourable slip behaviour resulting in more wear damage.

Load Distribution on Bearing Rolling Elements

Load distribution is the individualization of the contact forces on each rolling element. Pitch angle, load angle (contact angle), and load magnitude have been found to be the most relevant parameters affecting the load distribution [6, 5]. The effect of these parameters on the load distribution was studied by Stammer [6] in a three-row roller bearing. The influence of the pitch angle was analysed for a range of 15° that corresponds to most production states of wind turbines, and it was found that resulting load and load sharing only changed in a small percentage. This suggests that it is reasonable to neglect the influence of pitch angle on load variation for fatigue life calculations. On the contrary, the load angle has been found to have a more dominant influence on both, resulting in load and load sharing of the individual rollers. The load angle was evaluated for a range of 60° ($\pm 30^\circ$). The results showed that any deviations from 0° lead to a higher resulting load. Regarding the load magnitude, it has a significant contribution as expected. This influence is significant in any bearing application.

Previous studies have investigated the effect of surrounding structures on the load distribution [6, 5, 41, 42]. Schwack et al. [5] investigated the free contact angle and how this angle was affected by the low stiffness of supporting structures, namely blades and hub. The free contact angle is the actual contact angle in operation that differs from the nominal contact angle of a bearing. This difference is because of the huge axial forces and bending moments acting on the pitch bearing, and the low stiffness provided by the surrounding parts that produce considerable deformation in the bearing rings. Free contact angle is not considered in most design guidelines and standards [3]. Schwack et al. [5] concluded that normal operating conditions of wind turbines produce an average increment of the contact angle of 5° which does not lead to truncation effects (edge loading). On the other hand, special operating conditions produce an increment of contact angle above the allowable angle resulting in raceway edge loading and high stresses in a concentrated reduced contact area. Chen et al. [41] used a finite element model to evaluate the influence of the rotor hub and the stiffener plate interface on the load distribution in a wind turbine pitch bearing. Results showed that stiffness variation of the supporting structure greatly affected the load distribution, and a detailed model of the surrounding components was necessary for an accurate assessment of the actual load distribution of large wind turbine pitch bearings. Stammli et al. [6] studied the effect of the blades and the hub, and concluded that the structural behaviour of the blades was the reason for the majority of the changes in load distribution and resultant loads. However, the hub should not be neglected as it had been shown in previous studies that also had a certain influence on the load distribution. The effect of the pitch gear was also assessed, but it was found insignificant. Olave et al. [42] proposed an elastic calculation procedure to calculate the load distribution of a four-point contact bearing considering the flexibility of the bearings and supporting structures. This procedure was validated with the results of a finite element model.

After discussing the general implications of effects of various factors on the load distribution of rolling elements of a pitch bearing, it is worth looking at the effect of the contact force on the studied wear modes. Most studies on fretting pay more attention to the sliding amplitude rather than the contact force which is assumed to be constant in most experimental tests. The effect of the contact force is implicit in many of the factors already analysed in this review. A higher normal force produces a larger contact area which indirectly affects the sliding ratio, therefore the transition between the different slip regimes. The contact force is also directly related to the contact pressure and stresses, and thus, it influences the frictional energy. Harris et al. [3] suggested a maximum contact Hertz stress of 2.4 GPa as a limit value to prevent wear damage, based on information from a wind turbine pitch and yaw bearings manufacturer. This recommendation is not consistent with current research studies that have shown the occurrence of fretting at lower contact pressures [43, 27, 44]. As discussed previously, it was also observed

that the contact area size and the contact pressure influence the oxygen access and impact on the wear mechanisms and the wear profile shape [27]. No data has been found about the effect of the contact force on false Brinelling and fretting corrosion under pitch bearing operating conditions.

Lubrication

Lubrication has been claimed to be one of the major procedures to prevent or reduce fretting wear [25]. Lubricants can lower COF and limit oxygen access to the contact area. Pitch bearings are usually grease lubricated. Grease is a two-phase lubricant composed of a thickener dispersed in a base oil. Guidelines for the selection of bearing grease exist based on laboratory analysis and field observations [45]. Nevertheless, the role of individual grease components in frictional behaviour is not clear. De Laurentis et al. [45] studied the influence of different grease components on the frictional behaviour of non-conformal contacts. Results showed that under high speeds, the frictional behaviour of the grease lubricated contact surfaces depend mainly on its base oils, whereas, under low speeds, the frictional behaviour relies more on the grease thickener and the properties of the lubricating film.

Zhou and Vincent [25] conducted a review on lubrication in fretting in 1999. They suggested that the analysis should be based on fretting regimes, as it was found that different lubricants performed differently depending on the fretting regime. For example, solid lubricants were found more efficient in the partial slip regime and grease and oil in the gross slip regime. Zhou and Vicent [25] also pointed out that the lubrication mechanisms in fretting were not well understood. More recently, Haviez et al. [46] studied the effect of fretting on grease-lubricated contacts using a cylinder-on-flat test set-up and a commercial grease G1, a lubricant commonly used in pitch and yaw bearings. This study identified three lubrication regimes based on the experimental analysis.

1. Partial slip domain: The contact under stick regime, and the lubricant cannot penetrate into the contact area.
2. Gross slip domain: Grease penetrates into the fretted interface. Wear volume is mainly affected by metal interactions and does not depend on the viscosity of the lubricant.
3. Fully lubricated domain: Characterised by a low and stable coefficient of friction and no occurrence of wear.

Selecting a suitable grease for pitch bearings that helps reduce wear can be a challenging task due to the complex pitch controller strategy. The oscillating amplitude may vary from small oscillations to large rotations of over 45 degrees. Schwack et al. [47] investigated the

effect of different greases on fretting wear; and found that a grease with low viscosity exhibits the lowest wear rate under small oscillations. However, as argued by De Laurentis et al. [45], a more extensive analysis of all components of grease was required.

Later in 2020, Schwack et al. [40] conducted a study to investigate six different greases under WT pitch bearing conditions. These greases have significant differences regarding the base oil type and viscosity, thickener type and NLGI class. The experiments showed that none of the tested lubricants reduced wear under all the tested conditions; a grease with good performance under certain conditions may perform worse under different conditions. Schwack et al. [40] also concluded using an 80 mm diameter bearing that false Brinelling occurred under small amplitude oscillations of $x/2b = 0.9$, resulting in mild wear damage. However, fretting corrosion took place under larger amplitudes of $x/2b = 13.3$, causing more severe fretting wear, and no wear damage occurred under the largest amplitude of oscillations of $x/2b = 29.1$. These oscillation amplitudes are different to the threshold of $x/2b = 1.6$ identified by Maruyama [38], where it was claimed that the lubricant film was fully established and no wear was expected. In the analysis of experimental results, the damage ratio (SG) defined by Maruyama et al. [48] was used to quantify the change in the worn surface, as defined in Equation 1.6. This ratio compares the surface roughness of the samples before and after the experiment. It was mentioned that polished surface produced by asperity contacts might result in this parameter not being the best damage indicator and suggested using this ratio only in the damaged region. Schwack et al. [40] carried out a simple test in addition to the down-scaled bearing experiments. In that test, a 10 mm diameter ball was tested on a flat surface, and it was claimed as an alternative to evaluate grease performance in this application. However, as discussed previously, the kinematics of the ball and the size of the contact are relevant factors to determine the resulting wear mode.

$$SG = \frac{S_{z,exp}}{S_{z,new}} \quad (1.6)$$

1.3.5 Friction in Fretting Contacts

Friction is probably one of the most complex phenomena in a tribological system. Several friction models exist: from simple static models such as Coulomb friction to complex dynamic friction models such as Dahl, LuGre, or Leuven models which include hysteresis functions.

In some applications, friction is a positive phenomenon that makes simple tasks possible, like walking or braking a bike. However, friction can also cause unwanted effects such as wear. In the case of pitch bearings, friction plays both roles: it is the driven mechanism of the ball rolling but also causes the wear damage.

Schwack [43] conducted finite element simulations and experimental analysis of false Brinelling and fretting corrosion in oscillating bearings and used the frictional work density as an indicator of the occurrence of wear. A constant COF equal to 0.3 was assumed for the FEA because this value showed the best agreement with the experimental results. Assuming a constant coefficient of friction only allowed predicting the total wear damage produced by a constant load under a constant amplitude oscillation. However, this validation was made by comparing the damage region without looking at the wear scar profile in more detail. Moreover, this assumption does not explain how the wear rate behaves; in other words, at which stage of the oscillation cycles the damage occurs. For this reason, understanding the frictional behaviour over time is essential to analyse the damage generated by false Brinelling and fretting corrosion.

Coefficient of friction can be calculated from fretting loops. However, more than one calculation method exists, and the selection of an appropriate method depends on the fretting regime and the shape of the fretting loops. Llavori et al. [49] analysed different derivation methods to obtain the coefficient of friction, pointed out there was no agreed definition of the coefficient of friction in fretting tests and discussed the impact of using different approaches. The following derivation methods for the coefficient of friction were analysed in their study.

1. Maximum coefficient of friction: Defined as the ratio between the maximum tangential force and the contact load in a cycle. This method is effective when tangential force does not change across the oscillation according to Coulomb's friction law, and the fretting loop is parallelogram-shaped. However, this approach is not appropriate when the fretting loops exhibit a non-Coulomb friction behaviour due to the hook-like feature, as shown in Figure 1.13.
2. Mean coefficient of friction: Defined as the mean absolute value. Llavori et al. [49] argues that this method might overestimate the coefficient of friction in cases exhibiting non-Coulomb behaviour because there is more data points near the maximum COF location since the increment of the tangential force occurs at the minimum speed.
3. Energy coefficient of friction: Fouvry et al. [50] developed a method to derive the coefficient of friction from the energy dissipated over the fretting loop. This method dealt effectively with the issue encountered in the maximum and mean coefficient of friction methods when it had a non-Coulomb behaviour. Fouvry et al. [50] also explained this behaviour as a result of the interaction between the edges of the ball or cylinder and the wear scar on the flat surface.
4. Geometric independent coefficient of friction (GICOFF): This method, firstly developed by Mulvihill et al. [51] and later improved by Jin et al. [52], proposed that computing the

GICOF is needed to find the point where the loop intersects a linear curve with a slope equal to the system stiffness that crosses the origin, as shown in Figure 1.13, assuming that coefficient of friction does not vary along the stroke and the only variation is due to geometrical effects in the measurement.

Llavori et al. [49] used a synthetic data analysis to compare these four derivation methods to obtain the coefficient of friction. Geometric independent coefficient of friction method was recommended for gross slip because of its robustness, followed by the energy method.

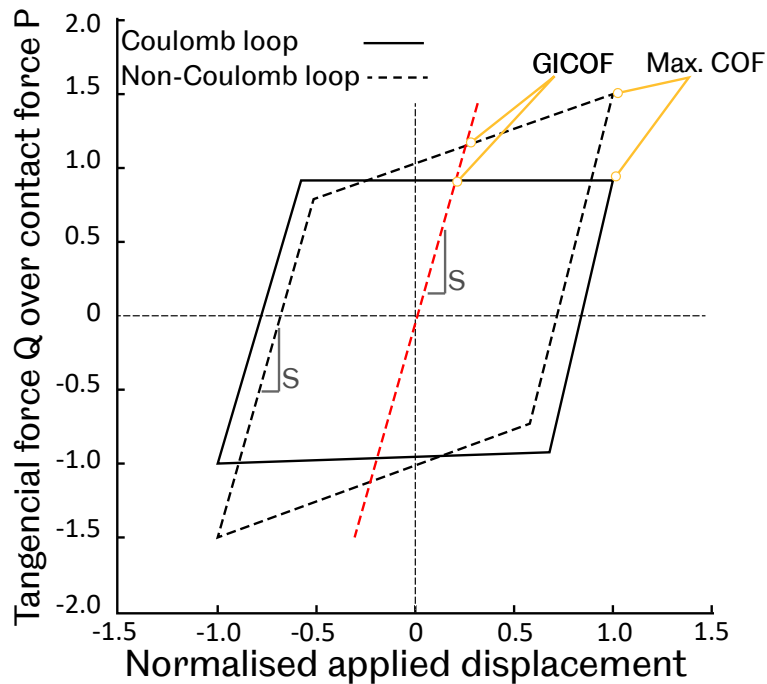


Figure 1.13: Examples of Coulomb and non-Coulomb fretting loops indicating the location of the maximum coefficient of friction and geometric independent coefficient of friction.

Hintikka et al. [53] introduced the concepts of stable and unstable friction based on experiments consisting of annular flat-on-flat tests related to frictional behaviour. Under ideal Coulomb behaviour, the friction is argued to remain constant [51, 53]. On the contrary, the coefficient of friction was expected to be higher at early cycles during gross sliding under non-Coulomb friction. The analysis of the annular flat-on-flat test showed that friction instability existed in gross sliding, and no fretting was expected if the friction condition remained under the threshold before reaching the unstable friction.

Fouvry et al. [50] also studied the frictional behaviour in a cylinder-plane contact configuration. It was identified that the sliding transition from partial slip to gross sliding was based on an energy discontinuity. This transition was related to the maximum coefficient of friction,

which exhibited a pressure dependence. The frictional behaviour under gross sliding conditions was defined based on an energy approach and showed no dependence on the pressure.

Different contact configurations, materials, and operating conditions can lead to different conclusions regarding the frictional behaviour. These differences suggest that a bespoke testing approach is required to test the frictional behaviour under pitch bearing operating conditions.

1.3.6 Experimental Analysis of Fretting Test Rigs

The test rigs reviewed in this section were classified into two different groups: general fretting rigs and bearings rigs. The first group corresponds to rigs conceived to study fretting wear in standard tribological configurations or applications; the second group corresponds to test rigs used specially to study fretting wear or false Brinelling in bearing applications.

Fretting Test Rigs for General Purposes

One of the most common set-up for fretting analysis is the pin-on-flat configuration. This set-up consists of a flat specimen clamped at its both ends in contact with a cylindrical pin where a normal force and cyclic tangential displacements are applied. Additionally, a cyclic load or elongation can be applied on one end of the flat specimen when experiments aim to investigate fretting fatigue. Pannemaecker et al. [54] employed a mixed approach involving modelling with experimental methods to predict fretting fatigue crack growth. The experimental set-up of their work consisted of pin-on-flat configuration as schematically presented in Figure 1.14.

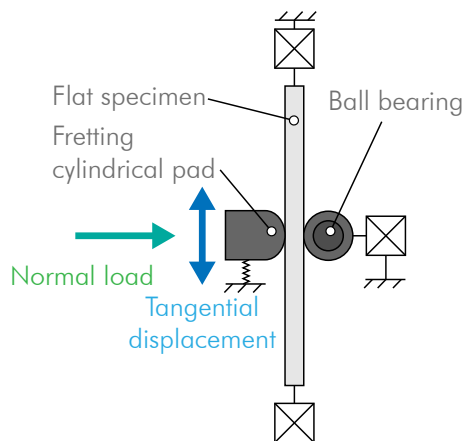


Figure 1.14: Schematic test rig configuration for tangential fretting reproduced from [54].

The second test rig of this revision is the equipment used by Mo et al. [55] to study rotational fretting wear in a ball-on-flat configuration. This set-up consists of a ball specimen fixed in

a lower holder mounted in a rotational driver and a fixed flat specimen in an upper holder mounted in a force/torque sensor. The centreline of the ball must strictly match the rotational driver axis, and the specimen rotates according to the driver motion in the range of $0.01^\circ/\text{s}$ to $5^\circ/\text{s}$. The set-up also has a vertical and horizontal positioning system. The experimental set-up is shown in Figure 1.15. The angular displacement and the forces were measured and used to characterise the rotational fretting running behaviour through $F_t - \theta$ and F_t/F_n curves.

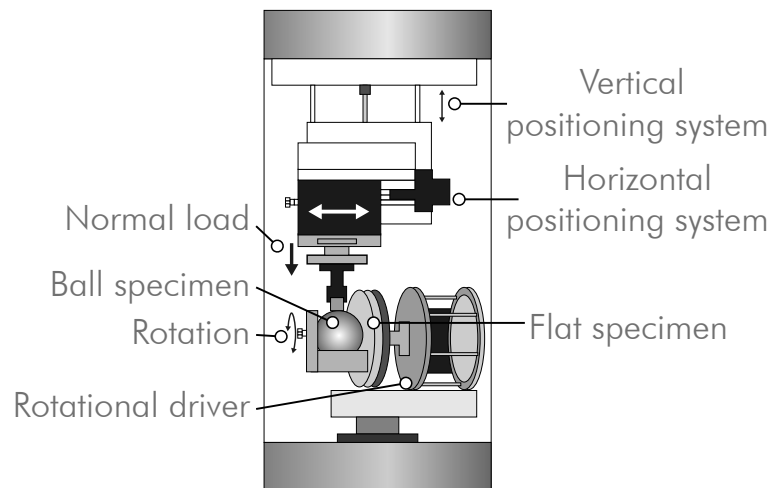


Figure 1.15: Schematic test rig configuration for rotational fretting reproduced from [55].

Hintikka et al. [53] carried out torsional fretting tests using an annular flat-on-flat test rig. In this set-up, fretting contact occurs between two identical axisymmetric specimens with annular contact surfaces as illustrated in Figure 1.16. The specimens are attached to one fixed holder and one detachable holder. The normal load is provided by hydraulic cylinders acting on the fixed holder; the angular oscillations are applied by an electric shaker through a lever arm rotating the detachable specimen holder. The rotation is measured by using an eddy current probe, the frictional torque by strain gauges and the normal load by a commercial s-beam load cell. One-second samples are extracted from the full signal with exponentially increasing time steps. This provided much data at the early stages of the experiment when COF changes the most.

These three different set-ups represent the majority of standard fretting test rigs. They are usually capable of reproducing just one type of fretting mode at a time, either tangential, radial, rotational or torsional. Therefore, their main limitation when it comes to testing fretting in pitch bearings is that these test rigs are unable to reproduce the complex kinematics of the ball-raceway contact, which usually exhibits a combination of the four fretting modes.

Different standard tests exist to study wear in contacts. Particularly, Fafnir test[56] is used to evaluate the property of lubricating greases to protect oscillating bearings from fretting

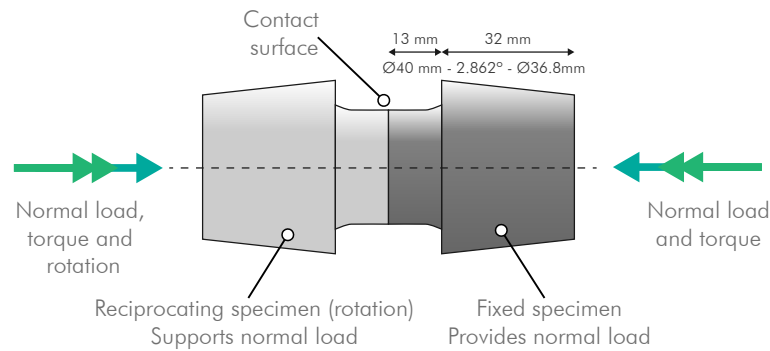


Figure 1.16: Test rig for torsional fretting reproduced from [55].

wear. This test consists of two ball thrust bearings (16 mm internal diameter) with fixed testing conditions: 12° oscillation amplitude, 30 Hz oscillation frequency and 2450 N contact load. Fretting wear is reported as average mass loss of bearing raceways.

Fretting Test Rigs for WT pitch bearings

When it comes to test rigs to study false Brinelling or fretting corrosion in wind turbine pitch bearings, the number of rigs reported in the literature is limited. This limitation can be attributed to the large scale of these bearings. In this section, two test rigs, examples of the two most commonly employed approaches to analyse these wear mechanisms in pitch bearings, are reviewed. The first approach consists of using smaller bearings; in other words, a downscaled specimen testing. The two main advantages of this strategy are that it is possible to test realistic oscillatory patterns and consider the complex kinematics of the ball movement. The downside, on the other hand, is that it overlooks the size effect. The contact area, defined partly by the bearing dimensions, is an important parameter to establish what a small oscillation is relevant. The second approach consists of using a small section of an actual pitch bearing. The section must be large enough to cover the oscillation arc of one ball. This strategy copes with the size effect but struggles with considering the complex actual operating conditions, which results in simplified testing conditions. This might seem a downside, but it can also be seen as a positive feature, as this allows the isolation of operational parameters to be studied independently.

Schwack et al. [43] developed a test rig to reproduce false Brinelling and fretting corrosion in bearings. Test results were used to validate a FE model and predict these wear mechanisms using the frictional work density as an indicator. In this experimental set-up, two bearings are mounted on a shaft, the oscillating motion is applied through a stepper motor connected to the shaft, and the load by disc springs. The testing bearing is an angular contact bearing of the size 7208 (80 mm outer diameter). This test rig can reproduce wear damage in a small-scale

bearing. However, it has been discussed that the size effects are relevant to these damage mechanisms. Furthermore, this test rig is not able to control precisely the contact loads and local displacements.

He et al. [57] also developed a test rig to validate a FE model to analyse the influence of contact angle on fretting wear. The shape and depth of the indentation of the contact surface and the load-deformation curves were investigated. This experimental set-up consists of one section of a 1200 mm raceway diameter single-row four-point contact pitch bearing and one 32 mm diameter ball as shown in Figure 1.17. The normal load is applied by a hydraulic actuator, and the radial displacement is measured with a displacement sensor. Neither tangential displacement nor rolling of the ball on the raceway was considered in this experiment. The main advantage of this test rig is that it allows using an actual pitch bearing section considering the size effects.

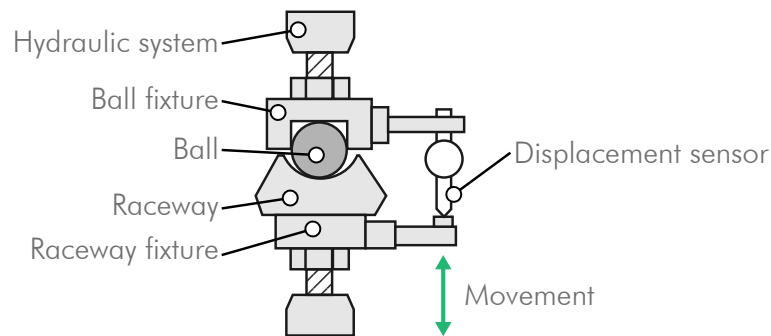


Figure 1.17: Test rig for radial fretting of bearing sections reproduced from [57].

1.3.7 Prediction of False Brinelling and Fretting Corrosion

Modelling of wear has been extensively researched [58] and the different models found in literature [59–62] can be grouped into two categories: mechanistic models based on failure mechanisms such as ratchetting [63] and phenomenological models that involve contact mechanics principle, such as Archard’s wear model.

These two categories of wear models have been used in numerical simulations [64]. Particularly, phenomenological models have been integrated into FE models. For example, the classical Archard’s wear model was firstly integrated into a FE model of fretting wear by McColl et al. [65] in 2004. The energy model described in Section 1.3.3 was developed for the first time in a FE model by Mary and Fouvry [66] in 2007. Some recent works used to predict fretting wear are discussed in the following paragraphs.

Schwack et al. [43] conducted finite element simulations and experimental analysis of an 80 mm diameter ball bearing. Frictional work density was used as an indicator of the occurrence of wear and validated by comparing the frictional energy density distribution with the damaged area of the experimentally tested bearings. A numerical study of the coefficient of friction was performed, finding that a value of 0.3 matched the experimental results in dry conditions. The results also showed that the coefficient of friction did not affect the total dissipated energy, but it did affect the maximum value of the frictional work density, related to the location of the most damaged area. The most worn area was located at both ends of the elliptical contact area, which suggests that the sliding condition corresponds to Mindlin's definition [33], i.e. a stick area in the centre of the ellipse with no damage surrounded by an external slip zone. The location of the maximum frictional work density, which coincided with the location of the most damaged area, was explained by the superposition of the Heathcote-slip and spin-slip. This work proposes a method to predict the occurrence of wear in bearings. However, it fails to include time variations of coefficient of friction.

Similar approaches have been adopted in different applications. Zhang et al. [21] developed a numerical simulation to study the friction and predict the wear in a finger lock chuck of a landing gear. In this work, a finite element model using the software ABAQUS complemented with the user sub-routines UMESHMOTION and VFRIC allowed simulating the dynamic operating conditions of the finger lock and the wear of the parts in contact. Similarly to the analysis conducted by Schwack et al. [43], the wear formulation considered the frictional energy density. The maximum values of the frictional energy density coincided with the most worn areas observed in experimental tests. Furthermore, the wear rate obtained from the simulations agreed with the wear tests. This approach has been also successfully applied to wear prediction using adaptive mesh at the modular taper interface of hip implants [22].

Brinji et al. [44] developed an analytical model to predict false Brinelling in bearings based on the energy dissipation theory proposed by Fouvry [27, 36]. This model simulated the wear process of a cylindrical roller bearing under lateral and axial displacements and predicted the wear produced by false Brinelling at the location of each roller. This method was validated through comparison with FE simulations and experimental tests showing differences of less than 10% but the analytical model overestimates the wear volume, and it was claimed to be 10,000 times more time-efficient than FE simulations. However, this model has many limitations. For instance, the load distribution of the rollers does not consider the flexibility of the supporting structures, it is not possible to apply more complex and realistic operating conditions, and it neglects that wear can occur under different fretting regimes.

1.3.8 Summary

False Brinelling and fretting corrosion are two concerning tribological issues in wind turbine pitch bearings. The distinction between these wear modes is unclear, and these damage modes are not properly considered in the existing international standards, resulting in pitch bearings being designed based on non-standardised methods and, in some cases, failing prematurely. The main difficulty to incorporate these damage modes into the standardised methods arises from the effect of small-amplitude oscillations that are not fully understood and makes it difficult to predict pitch bearing service life accurately. This main research gap suggests that understanding false Brinelling and fretting corrosion under wind turbine pitch bearing operating conditions is an essential requirement. For this reason, the first research question/aim is to characterise these wear modes in pitch bearing applications.

The review of the main factors affecting false Brinelling and fretting corrosion shows a complex relationship among them. For example, both the bearing geometry and loads affect the sliding ratio. The sliding ratio has been used to define the limit of the oscillations amplitude that cause wear. Some degree of controversy has been observed in the definition of the limit sliding ratio that produces these wear modes, which is also associated with the complicated interaction among the different factors. Moreover, all the factors have been found highly dependent on the operating conditions resulting in fretting; while many fundamental research may not be representative of the wear modes under pitch bearing conditions. The main reason for these differences comes from the fact that different wear mechanisms can take place depending on the contact area size, load, frequency, oscillation amplitude and lubrication. Fretting wear can occur as adhesive or abrasive wear combined with oxidation. Thus, the second research question/aim of this research project is to investigate the effect of these parameters on the wear modes produced by small-amplitude oscillations under pitch bearing operating conditions.

Fretting loops have been identified as a powerful and simple tool to analyse frictional and wear behaviour during fretting tests. By analysing the relationship between the tangential force and the oscillating distance it is possible to obtain the coefficient of friction, the actual sliding distance in the contact area, and the frictional energy dissipated in every fretting cycle. The frictional energy and measurements of the wear volume allow the wear rate to be calculated. This energy approach has been well developed and appears to be a good method to incorporate in FE simulations of wear to complement experimental results.

Regarding the development of experimental testing methods in fretting, it has been argued that standard tribometer configurations are limited for pitch bearing conditions, as the scale of the test is important due to the oxidation process taking place, and because of the complex kinematics of the balls' movement over raceways' surfaces. Moreover, as previously mentioned, the testing conditions must be equivalent to actual pitch bearing operating conditions.

1.4 Research Aim and Objectives

This research project aims to characterise the damage modes in wind turbine pitch bearings produced by small-amplitude oscillations and investigate the effect of the most relevant variables involved. The findings will enable an in-depth understanding of wear mechanisms of false Brinelling and fretting corrosion and propose insightful recommendations to improve pitching control strategies and design to reduce unpredicted failure and unscheduled maintenance of pitch bearings. The following specific objectives are defined to achieve this aim:

- To conduct a literature review to identify research gaps regarding pitch bearing damage modes and define the most relevant parameters.
- To analyse the load distribution and deformation of the pitch bearing under wind turbine design loads.
- To examine a damaged pitch bearing section from field and understand the damage features corresponding to false Brinelling and fretting corrosion.
- To develop an experimental methodology to investigate the influence of the most relevant variables of false Brinelling and fretting corrosion.
- To validate a modelling method developed to predict wear produced by small-amplitude oscillations in pitch bearing with the tested experimental data.
- To propose recommendations to reduce wear in pitch bearings.

1.5 Research Novelty and New Contribution

The novelty of this research comes from two main aspects. Firstly, the experimental approach considers different testing scales, a small-scale by employing desktop testing machines and a medium-scale comparable to actual pitch bearings size by developing a bespoke tribometer. Testing conditions were carefully defined to represent equivalent pitch bearing operating conditions. Mechanical components of wind turbines are usually tested on actual size scale test rigs resulting in costly and limited tests; therefore, the proposed experimental strategy has a significant advantage to conduct detailed tests and study a complex phenomenon in cost and resource efficient configuration. The damage characterisation of a damaged pitch bearing section from the field contributes to new understanding of pitch bearing failure that is not usually available in the public domain.

A clearer understanding of false Brinelling and fretting corrosion in pitch bearings and a validated method to predict these wear modes will contribute towards improving the design methods currently employed to define and predict pitch bearing's service life. An in-depth comprehension of relevant factors affecting false Brinelling and fretting corrosion in pitch bearings will provide answers on how to improve bearing's design and pitch controller strategies. This is particularly relevant as the trend in the growth of wind turbines maintains over time, including pitch bearings, and the need to develop cost-effective wind turbine maintenance strategies.

1.6 Thesis Outline and Structure

This section outlines the thesis structure and provides a summary of each chapter to provide the reader with an overview of the main research activities and show their alignment to the objectives defined in Section 1.4.

Chapter 1 presents a literature review in which a wide range of relevant topics related to damage modes in wind turbine pitch bearings are presented and discussed. These topics include a general discussion on current methodologies for calculating pitch bearing life, damage mechanisms and a review of the state-of-the-art of investigation methods and modelling tools in fretting corrosion and false Brinelling. This literature review aims to identify the research gaps in this topic and set the framework in which this research will be conducted.

Chapter 2 presents a study of the load distribution in a double-row ball pitch bearing. The analysis is conducted by developing a Finite Element model of the bearings and their supporting structures. Modelling the assembly allows the effect of the supporting structure's flexibility to be studied and offers the opportunity to understand the overall deformation behaviour of the bearings under normal loading conditions. This work is essential for studying the contact behaviour between the balls and the raceways in the following chapters.

Chapter 3 presents an investigation of a damaged pitch bearing section that was previously in service. Although the information of the operating conditions of this bearing is limited, it is possible to characterise some fundamental features of the wear damage produced by small-amplitude oscillations. Reverse engineering analysis is conducted to estimate the operating conditions that generated the damage. The information extracted from this pitch bearing section from field service is key to compare with the damage generated under laboratory testing conditions.

Chapter 4 presents the first experimental approach using a standard desktop tribometer to study wear on a ball-on-flat configuration in a small-scale configuration. Testing conditions defined for these tests are equivalent to pitch bearing's operating conditions. These tests aim to

understand the effect of parameters such as the oscillation amplitude and frequency, load, and lubrication on the coefficient of friction and the wear damage. Limitations of this experimental setup are also discussed in this chapter.

Chapter 5 presents the development of a bespoke medium-scale test rig that aims to overcome the limitations encountered in the tests from the small-scale tests. This second experimental approach involves an increase of the testing scale to allow a larger contact area and a modification of the tribosystem to ensure the ball movement is as similar as possible to actual pitch bearings. This chapter includes the design of the test rig, the definition of experimental conditions and the analysis of the tests. The parameters investigated on these tests are oscillation amplitude and frequency, load, geometry, and lubrication.

Chapter 6 presents the development of a FE model of the contact between a ball and the raceways to predict the wear damage produced by small-amplitude oscillations. This model provides an in-depth understanding of some variables which experimental tests cannot accurately quantify. For example, the sliding that takes place in the contact area. Having a numerical model to predict wear also allows expanding the extent of the experimental analysis by including the effect of some variables that cannot be investigated experimentally due to limitations of the machines utilised.

Chapter 7 presents a summary of key findings based on all the activities conducted in this research. All the results are combined together to deliver the project aim and find answers to the research problem previously defined. These aims are to characterise the wear mechanisms due to small amplitude oscillations, determine the influence of operational and geometrical parameters, and provide recommendations to improve pitch bearing's design and operation.

Chapter 2

Analysis of Load Distribution in Pitch Bearing Balls

2.1 Introduction

Contact force has been considered as an important factor for false Brinelling and fretting corrosion in the literature review chapter. In pitch bearings, contact forces acting on bearing rolling elements result from the loads transmitted from the blades: flapwise due to the wind thrust and edgewise due to gravity [67]. Contact forces on bearing rolling elements determine the contact area and pressure, and they are associated with the worn area and the damage severity of the raceways of a pitch bearing.

A commonly used method to study the load distribution in pitch bearing rolling elements is conducting a finite element analysis (FEA). The main advantages offered by a numerical approach like the finite element method (FEM) are being more time-cost efficient compared to large-scale tests and the capability of including the effect of supporting structures. The investigation of the load distribution is also difficult to achieve by using the analytical methods provided in technical standards and scientific books [3].

Load distribution in pitch bearings has been largely investigated in previous studies, which are outlined and discussed in Section 1.3.4. In those studies, the relevance of the supporting structures, namely hub and blades, on the load distribution has been investigated and argued to be a key factor contributing to the poor load distribution among rolling elements usually exhibited by these bearings. The quality of the load distribution is associated with its uniformity. An uneven load distribution results in some rolling elements carrying significantly higher load. Many previous studies considered the actual wind turbine geometry in the analysis and compared the results to the case of a bearing on a rigid support. No evidence exists on

how different supporting structures with different stiffness can modify, either improving or worsening, the load distribution of a wind turbine pitch bearing.

The analysis presented in this chapter aims to develop a FE model to study the load distribution in pitch bearing balls by considering the stiffness provided by the hub and the blades as supporting structures. Parameters to quantify the uniformity of the load distribution and the effect of the stiffness of the supporting structures are proposed to understand how the load distribution could be improved. The variation in the contact angle between the raceway and rolling element surfaces and stresses of the bearing raceway ring are investigated to ensure the modifications of the supporting structures do not cause other failure modes, such as edge loading or ring fractures. Moreover, the impact on the load distribution when some balls are not in contact with the raceways due to the large deformation of the bearing rings is also included in the analysis.

2.2 Methods

The analysis of the load distribution was carried out by developing a FE model considered as a static analysis using the solver ABAQUS/STANDARD in the commercial package ABAQUS 2018. This type of analysis allows the contact forces acting on each bearing ball due to the equivalent static loads acting on the blades to be obtained, neglecting any variation due to dynamic effects. This is a reasonable assumption, bearing in mind that this FE model aims to compare the load distribution for different stiffness of the supporting structures. Therefore, the magnitude of the contact forces between the balls and the raceway is given mainly by the static loads. Moreover, this analysis considers the bearing design load and not the actual load from the blade in wind turbine operation.

A 2-metre diameter pitch bearing, the hub and the blades were modelled. Since a 2-metre bearing consists of more than two hundred balls, a simplified approach was required to model these rolling elements in order to avoid an excessively large FE model. This approach consisted in modelling the balls with traction-only springs and rigid elements. The detail of this modelling strategy is explained in Section 2.3.3. The stiffness of the supporting structures was modified by adding stiffener plates into the hub and blades and the effect of these plates and their thickness on the load distribution was investigated. The results obtained from this model included the contact forces on each contact pair of each ball, variation of the contact angle, and hoop (circumferential) stresses.

In addition to the effect of the flexibility of the supporting structures on the load distribution, the case when some balls are not in contact with the raceway and its impact on the load

distribution was also investigated. This situation might be the consequence of the large deformations of the bearing raceway rings under certain operating conditions.

2.3 Description of the FE Model

2.3.1 Geometry and Materials

Three components of the wind turbine rotor were included in the model: blades, pitch bearings and hub. The assembly is presented in Figure 2.1.

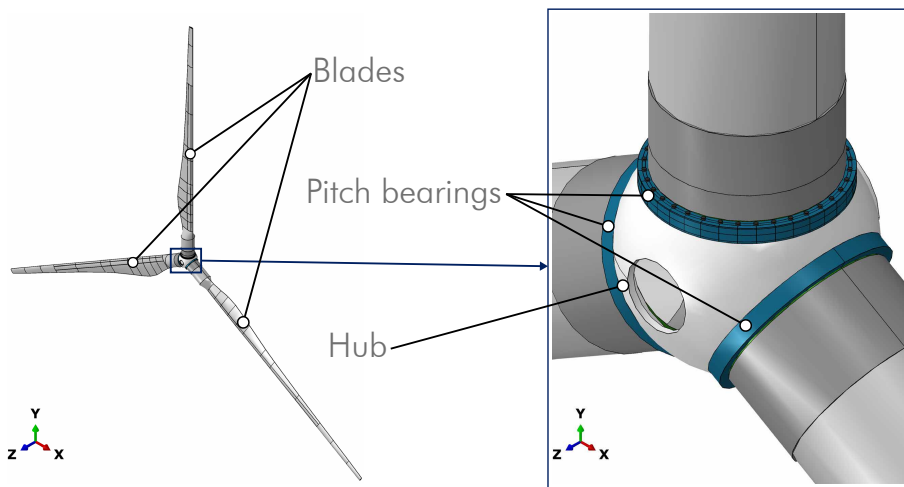


Figure 2.1: Blades, pitch bearings and hub assembly.

Three 40-metre length blades with simplified geometry were modelled. Wind turbine blades fulfil two main functions. The aerodynamic function, as they must transform the wind energy into mechanical torque to rotate the rotor; and the structural function, because they must also withstand the wind loads whilst achieving an optimal lightweight design. From the modelling point of view and considering the aim of the model being to simulate the load distribution of rolling elements of a pitch bearing, the stiffness provided by the blades is the main aspect to be captured by the model. In fact, only the stiffness at the interface with the bearing matters for the purpose of this analysis. For this reason, some simplifications were introduced to the complex geometrical features of the blades in order to model these large components efficiently. The main simplification consisted of neglecting the twisting angle between the different airfoil sections of each blade. Table 2.1 summarises the main dimensions and properties of the blades, and Figure 2.2a shows the blade geometry and stiffness plates between the blades and hub. The properties were obtained from the IWES 6.5 MW reference wind turbine [2] and scaled down a

wind turbine using pitch bearings of 2-meters diameter accordingly, based on the length and the root diameter of the blades.

The geometry of the blades was modelled as surfaces, except for the blade root. Modelling the blade root as a solid was required to model the bolted connections to the bearing rings in detail. A circular stiffener plate was included at the blade root, also modelled as a surface. Modelling the stiffener plate as a surface enabled its thickness to be parameterised without modifying the geometry for every simulation, as the thickness is a property of shell elements used to mesh surfaces.

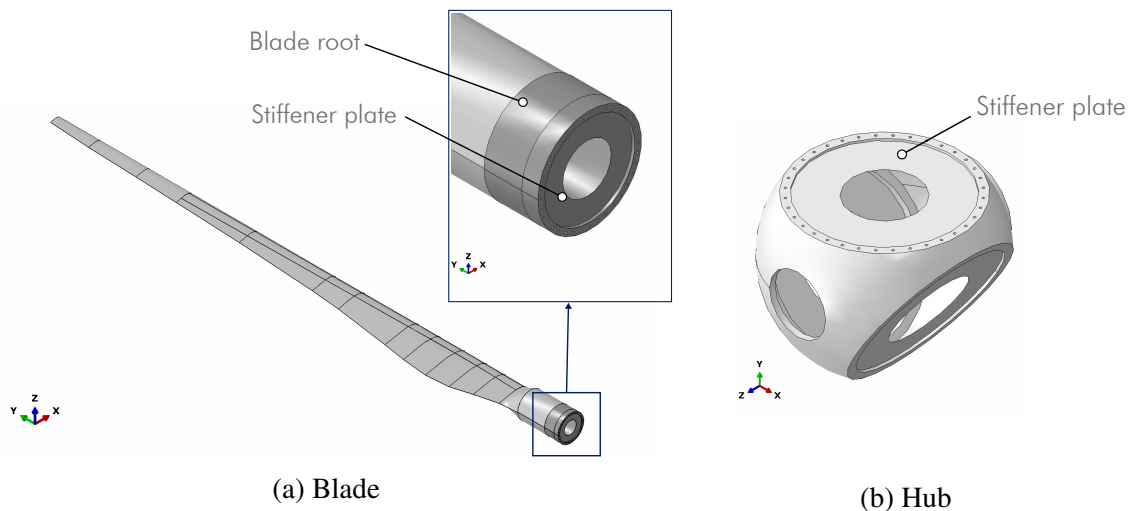


Figure 2.2: Blade and Hub geometries

Three stiffness indicators were considered under different loading conditions in order to obtain a representative stiffness of the blade. These indicators are described below.

1. First flapwise and edgewise modes: These indicators represent the compromise between the blade mass and flexibility, as the natural frequencies depends mainly on these two parameters. Natural frequencies of these vibration modes were obtained from a modal analysis of the blade.
2. Static flexibility along the flapwise and edgewise directions: The deflection of the blade due to a 1 kN load applied at the end of the blade along flapwise and edgewise directions were obtained from a static model of the blade.
3. Deflection due the blade's own weight: This last indicator can be considered to be redundant since the static flexibility along the two non-axial axes were already considered. However, this value is still useful, as it can be compared to the IWES 6.5 MW reference wind turbine [2].

Table 2.1: Blade main dimensions and properties [2].

Airfoil	Length [mm]	Chord length [mm]	Mass per unit of length [kg/m]	Thickness [mm]	Young Modulus [MPa]
Circle	0	1900	2489.51	100.00	25300
Circle	4000	1900	1714.60	100.00	24500
FFA-W3-211	5266	2034	694.24	60.00	9300
FFA-W3-211	6796	2421	594.08	52.78	8430
FFA-W3-211	8193	2831	528.05	51.28	8520
FFA-W3-211	9820	2961	467.01	49.54	10100
FFA-W3-211	11633	2780	426.80	47.60	10900
FFA-W3-211	13274	2514	369.72	45.85	12500
DU91-W2-250	17285	1957	293.01	41.55	19000
DU91-W2-250	19441	1751	261.19	39.24	20500
DU91-W2-250	25251	1374	178.64	33.02	22700
DU91-W2-250	30176	1148	111.06	27.75	19800
DU91-W2-250	33304	1007	89.80	24.40	19300
DU91-W2-250	36968	868	56.32	20.48	16500
DU91-W2-250	40000	675	31.76	17.24	15900

The results corresponding to the dynamic model of the blade are presented in Figure 2.3 and the results corresponding to the static model in Figure 2.4. Table 2.2 summarises all the blade stiffness indicators. The differences observed between the simplified blade model of this study and the reference blade [2] are because of the differences in length, mass, as well as the simplification of neglecting the twisting angle. Despite these differences, the simplified blade provides a representative flexibility within the same order of magnitude as the reference blade thus the model is adequate to perform the comparative analysis proposed in this chapter.

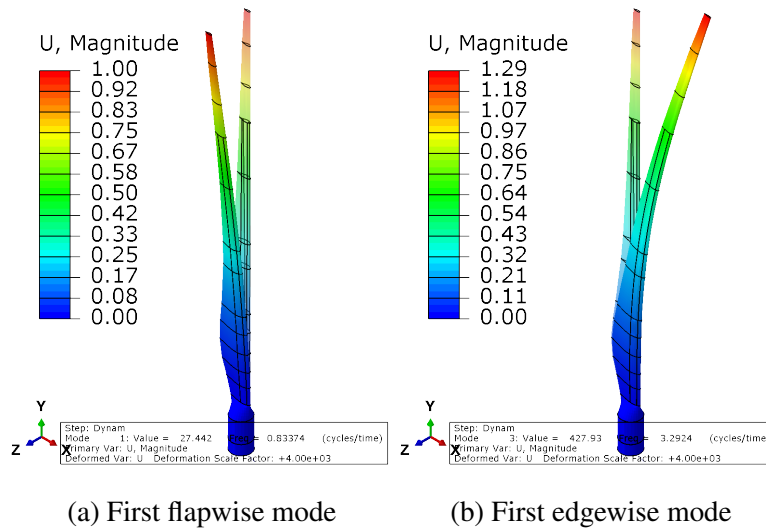


Figure 2.3: Blade model dynamic results - Normalised displacement magnitude [mm].

Table 2.2: Blade stiffness indicators.

Indicator	Simplified blade model	Reference blade	Difference [2] [%]
Length [m]	40	80	-50%
Mass [kg]	15431	30862	-50%
First flapwise mode [hz]	0.83	0.66	26%
First edgewise mode [hz]	3.29	1.02	223%
Blade pre-bending [m]	0.975	4.5	-78%
Flapwise flexibility [mm/kN]	253.72	-	-
Edgewise flexibility [mm/kN]	17.09	-	-

Three 2-metre diameter double-rowed eight-point contact ball pitch bearings were included in the assembly model. The main dimensions and material properties are presented in Table 2.3. Figure 2.5a shows the main dimensions of the bearing cross section and Figure 2.5b illustrates the geometry of the modelled bearing. The bearing balls were not directly modelled. They

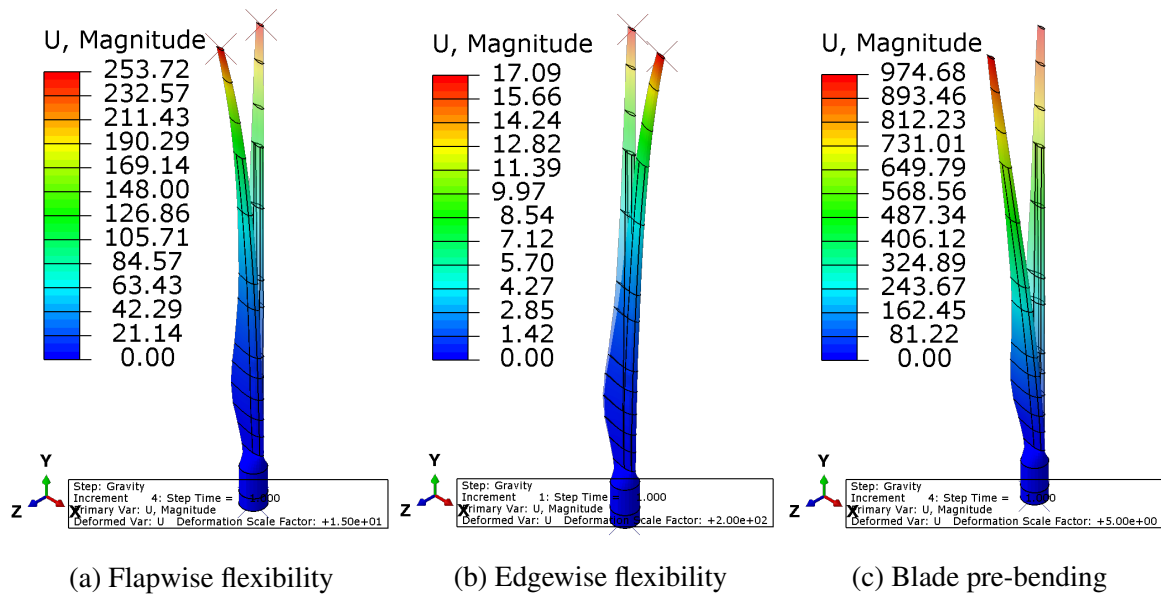


Figure 2.4: Blade model static results - Displacement magnitude [mm].

were modelled as springs instead and the details of this modelling strategy is described in section 2.3.3.

Table 2.3: Main dimensions and properties of the pitch bearing.

Parameter	Value
Ball diameter [mm]	45
Number of rows	2
Number of balls per row	120
Conformity	0.52
Contact angle [°]	45
Bearing ring material	42CrMo4 EN10083-3 Steel
Young Modulus [GPa]	210
Poisson's ratio	0.3
Balls material	100Cr6 Steel
Young Modulus [GPa]	210
Poisson's ratio	0.3

Finally, a simplified hub was also included in the model. The properties and dimensions of the hub are summarised in Table 2.4. Stiffener plates modelled as surfaces were added to each bearing interface. The rest of the hub was modelled as a solid body. Figure 2.2b shows the geometry of the hub and its stiffener plates.

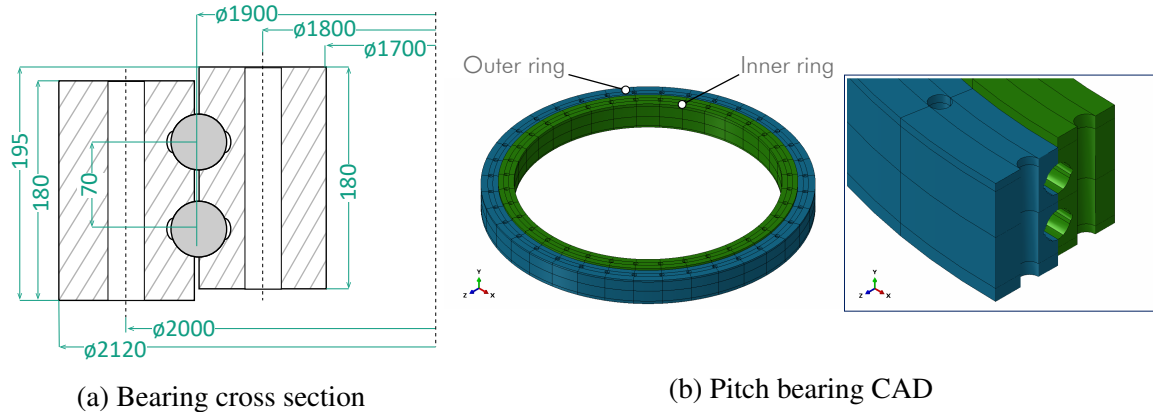


Figure 2.5: Pitch bearing geometry

Table 2.4: Hub properties and dimensions.

Parameter	Value
Shell thickness [mm]	75
Stiffener plates thickness [mm]	30
Mass [kg]	6636.7
Young Modulus [GPa]	169
Poisson's ratio	0.275

2.3.2 Finite Element Mesh

Different aspects were considered when meshing the model in order to find a good balance between results accuracy and model size, such as the complexity of the geometry or the results to be obtained in a certain part. Blades roots were meshed with solid elements and the parts modelled as surfaces were meshed with shell elements. The thickness of the shell elements was defined accordingly to the values listed in Table 2.1. Pitch bearings rings require a finer mesh in order to obtain accurate results and to properly define the interaction with the balls. The bearing rings were divided into partitions to ensure that nodes were placed on each ball contact area and the mesh size was set fine enough to ensure that the element size is approximately the size of the contact area. Bearing rings were meshed with hexahedral elements. The hub does not require any special meshing consideration, apart from a good element quality at the contact region between the hub and the bearings to avoid any convergence issues. The hub was meshed using tetrahedral elements. The whole model was meshed with second order (quadratic) elements. The meshing details are summarised in Table 2.5. Figure 2.6 illustrates different zones of the mesh of the assembly model. The development of this model did not consider a mesh independence study because the main result are nodal forces. Nodal results

are not highly sensitive to the element size compared to elemental results such as stresses or strains. Moreover, the model is large with more than 2 million nodes and takes time to run all the necessary iterations to build the mesh independence curve. To ensure the quality of the results, it is just necessary to ensure a fine mesh in the region of interest, which in this model is the blade bearing.

Table 2.5: Mesh statics.

Element type	Element shape	Geometric order	Elements
C3D10	Tetrahedral	Quadratic	93890
C3D20R	Hexahedral	Quadratic	425094
S8R	Quadrilateral	Quadratic	21276
STRI65	Triangular	Quadratic	111
Total number of elements			540371
Total number of nodes			2296605

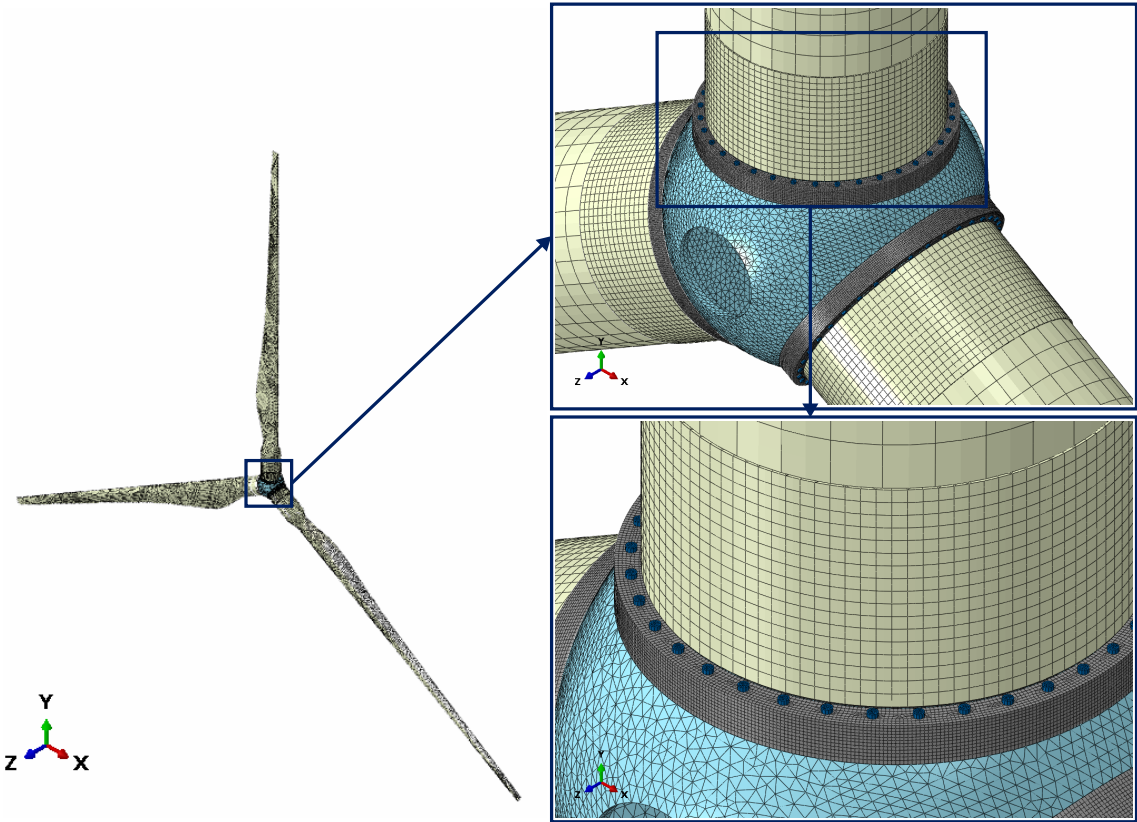


Figure 2.6: Assembly FE mesh.

2.3.3 Interactions and Boundary Conditions

Assembly Interactions

Bolted connections between the outer ring and the hub, and between the inner ring and the blade were modelled in detail. The following interactions were applied to these interfaces, as shown in Figure 2.7.

- a Frictional contacts with a coefficient of friction of 0.3 were defined between the hub bolt heads and the outer ring.
- b Frictionless contacts were defined between the hub bolt shanks and the outer ring bolt holes.
- c A frictional contact with a coefficient of friction of 0.3 was defined between the hub and the outer ring.
- d *Tie* interactions were defined between the hub and the hub bolts.
- e Frictional contacts with a coefficient of friction of 0.3 were defined between the blade bolt heads and the inner ring.
- f Frictionless contacts were defined between the blade bolt shanks and the inner ring bolt holes.
- g A frictional contact with a coefficient of friction of 0.3 was defined between the blade root and the inner ring.
- h *Tie* interactions were defined between the blade root and the blade bolts.

Note: The coefficient of friction of the bolted union was defined as 0.3 based on international standards for wind turbine design [68, 69].

Pitch Bearing Balls

In order to model the bearing balls with traction-only springs as previously mentioned, it was required to estimate the ball stiffness. The ball stiffness was calculated by using an analytical method proposed by Guay [70].

The contact stiffness (K) was defined by Equation 2.1.

$$P = K_i \delta_i^{3/2} = K_o \delta_o^{3/2} \quad (2.1)$$

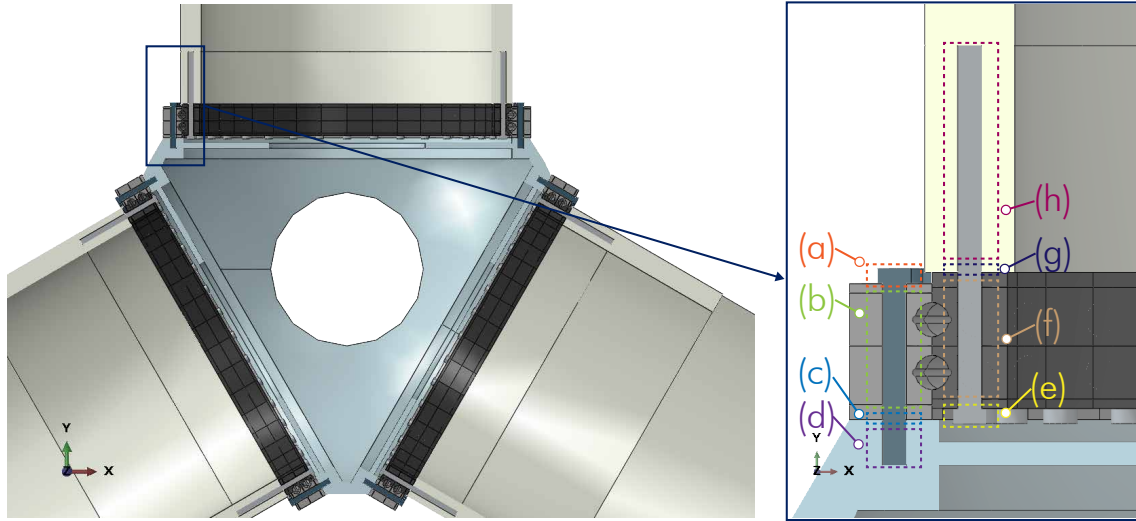


Figure 2.7: Interaction definitions for bolted connections of the pitch bearing.

Where P is the contact force, δ is the contact deformation and the indexes i and o refer to the inner and outer raceway, respectively. The contact deformation δ is given by the Hertz theory presented in Equation 2.2.

$$\delta = \frac{F(\kappa)}{(2S(\kappa)R)^{1/3}} \left(\frac{3P}{\pi\kappa E} \right)^{2/3} \quad (2.2)$$

Where F is the elliptic integral of the first kind, given by Equation 2.3, S the elliptic integral of the second kind, given by Equation 2.4, R the raceway diameter, and κ is the ellipse elongation, given by Equation 2.5.

$$F(\kappa) = \frac{\pi}{2} + q(1 + \ln \rho) \quad (2.3)$$

$$S(\kappa) = 1 + \frac{q}{\rho} \quad (2.4)$$

$$\kappa = \rho^{2/\pi} \quad (2.5)$$

Where:

$$\rho = \frac{R_x}{R_y} \quad (2.6)$$

$$q = \frac{\pi}{2} - 1 \quad (2.7)$$

Then, the contact stiffness K is defined by equation 2.8.

$$K = \frac{\pi}{3} \kappa E \sqrt{\frac{2S(\kappa)R}{F(\kappa)^3}} \quad (2.8)$$

The ball stiffness K_{ball} is defined by equation 2.9

$$P = K_{ball} \delta_{ball}^{3/2} \quad (2.9)$$

Where δ_{ball} is the relative deformation of the two rings along the normal direction of the contact. This relative deformation can be expressed in terms of the deformation at the inner and outer raceways as given by Equation 2.10

$$\delta_{ball} = \delta_i + \delta_o \quad (2.10)$$

Combining with Equation 2.1, the ball stiffness K_{ball} is given by Equation 2.11

$$K_{ball} = \left(\frac{1}{K_i^{2/3}} + \frac{1}{K_o^{2/3}} \right)^{-3/2} \quad (2.11)$$

Figure 2.8 presents the relationship of the contact force and ball deformation derived from Equation 2.11 and used to model the contact stiffness of the bearing balls. This curve is nonlinear, meaning neither the contact force nor the ball stiffness K_{ball} is linear with the change of the ball deformation but it is independent of the contact area.

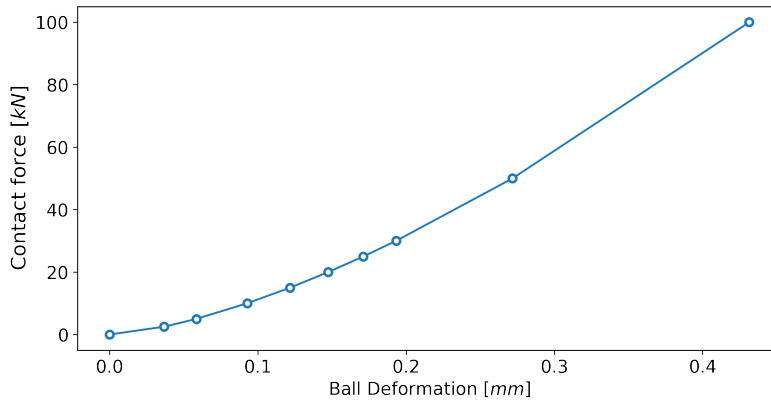


Figure 2.8: Spring force-displacement curve.

The contact between the balls and the bearing raceways was modelled using traction-only springs linked to the contact area through rigid beams [71]. This method assumes that when

a four-point contact bearing is in static equilibrium, the contact forces between the ball and the arcs of regions 1 and 4 are through the centre of the arcs of regions 1 and 4, C1 and C4 respectively. The contact forces between the ball and the arcs of regions 2 and 3 are through the centre of the arcs of regions 2 and 3, C2 and C3 respectively, as shown in Figure 2.9a. Thus, the contact forces can be simulated using two traction springs with the same stiffness. The spring C1C4 simulates the contact between the ball and the arcs of regions 1 and 4, and the spring C2C3 simulates the contact between the ball and the arcs of regions 2 and 3, as shown in Figure 2.9b. To keep the contact forces normal to the arc surfaces, each arc centre must move with its arc. This can be achieved with two rigid beams joining the arc to its centre, as shown in Figure 2.9c. The force-displacement curve presented in Figure 2.8 was defined as the behaviour for each spring. It is worth mentioning that this approach neglects the effect of the grease-lubrication on the ball stiffness.

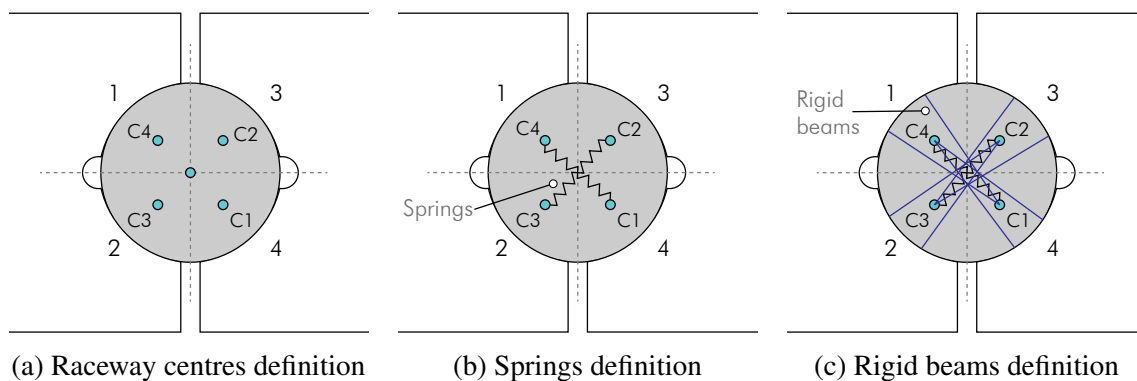


Figure 2.9: Balls contact modelling.

Fixations Boundary Conditions

The rear flange that connects the hub to the main shaft of the drivetrain was fixed in all degrees of freedom. The fixed surface was highlighted in Figure 2.10a.

2.3.4 Loading Conditions

Concentrated loads were applied to each blade in their local coordinate system. The loads were applied at a point such that the resulting forces and moments at the blade root were equal to those listed in Table 2.6. Load application points were linked to the blade nodes by means of "couple" interactions. Figure 2.10b shows the location and direction of the loads applied to the blades. The loads applied on the blades did not necessarily represent how wind loads act on these components. These loads correspond to the bearing design load under normal operating conditions, in order to take into consideration of the stiffness of the blades.

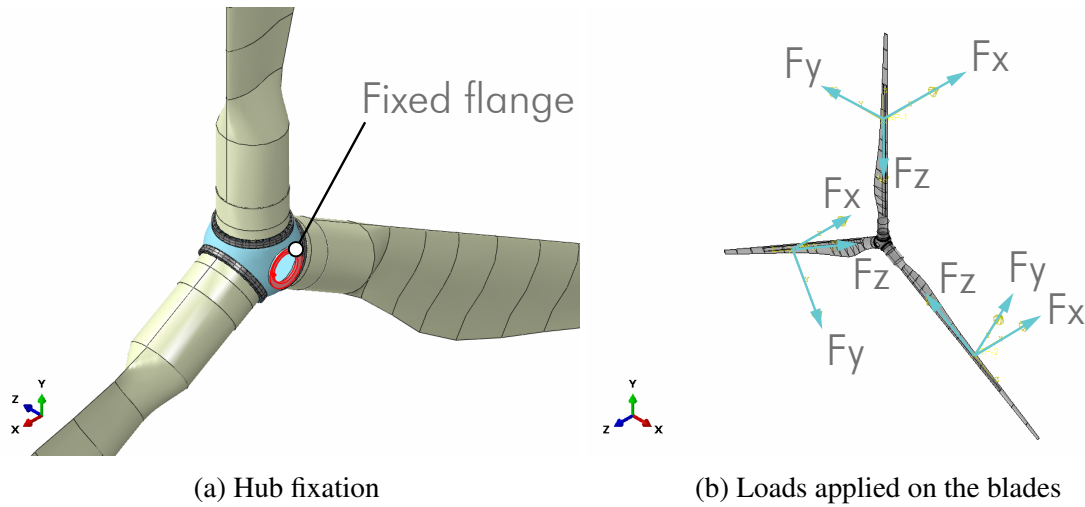


Figure 2.10: Model fixation and loads.

Menck et al. [72] conducted fatigue life calculations of pitch bearings by considering blade-dependent loads and highlighted that three of the most influential factors on the pitch bearings loads are the resulting moment, the angle of the resulting moment, also known as load angle, and the pitch angle of the blade. Although these factors were not considered in this analysis, as they do not contribute significantly to understand the effect of the stiffness on the load distribution, it is deemed to be appropriate to comment on these three variables. The resulting moment and the load angle determine which bearing rolling element takes the maximum load and its relative angular position. The pitch angle rotates the load distribution without changing its magnitude and direction, except due to small variations in the hub stiffness which is not symmetric. The loads considered for this analysis result in a moment of 1600 kNm at the blade root, a load angle of 225° , and the blade is positioned at a pitch angle of 0° .

Table 2.6: Load applied to the blades and resulting loads at the blade root.

Load component	Value
Force along blade x axis [kN]	60
Force along blade y axis [kN]	40
Force along blade z axis [kN]	-220
Resultant axial force at blade root [kN]	220
Resulting radial force at blade root [kN]	72
Resulting moment at blade root [kNm]	1600

2.4 Results and Analysis

The results and analysis conducted from the post-processing of the pitch bearing assembly FE model are presented in this section. The analysis aims to understand the role of the stiffness provided by the supporting structures on the load distribution among the bearing rolling elements. The bearing ring displacements, stresses and variation of contact angle were also post-processed and investigated to complement the analysis of the contact forces and gain a deeper understanding on how these two variables are related. Figure 2.11 presents the bearing rows numbering, contact pair definition, balls numbering, and angular position. These definitions are used in all the results presented in this section.

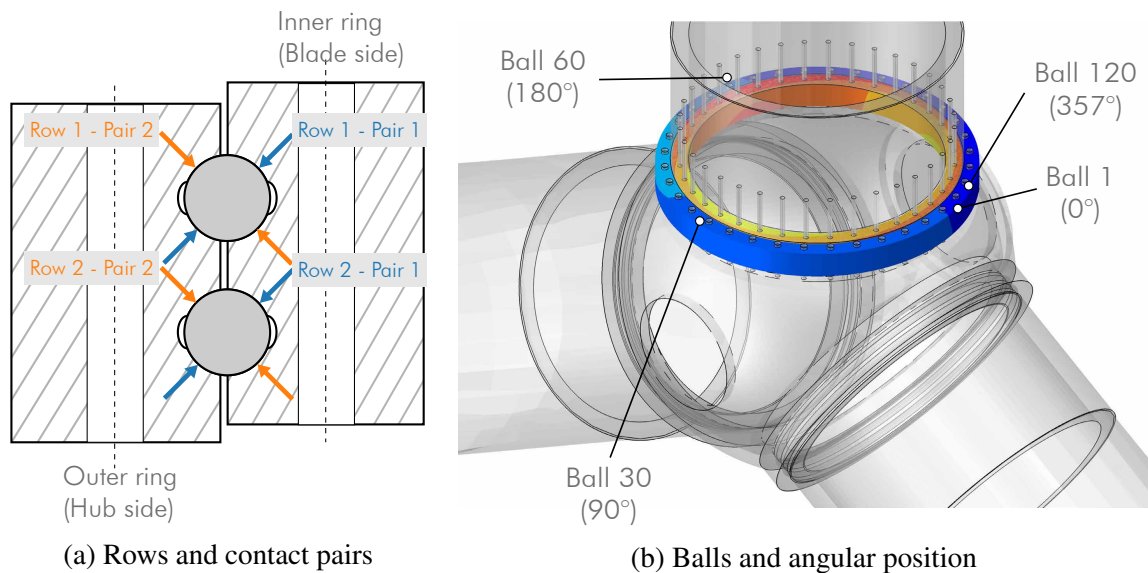


Figure 2.11: Nomenclature used in results.

Six different assembly configurations are post-processed. The difference among these configurations consists of whether there are stiffer plates in the hub and blades and the thickness of those plates. The following configurations were defined: a base configuration with no stiffer plates; two configurations with stiffer plates of two different thickness only in the blades; two configurations with stiffer plates of two different thickness only in the hub; and one configuration with stiffer plates in both hub and blades. The different thicknesses considered for the plates in each configuration are summarised in Table 2.7. The location of the stiffer plates is shown in Figure 2.2. These six assembly configurations allow the assessment of the effect of modifying the flexibility of the bearing support structures on the load distribution.

Table 2.7: Plate thickness in the six assembly configurations.

Configuration	Blade stiffener plate thickness [mm]	Hub stiffener plate thickness [mm]
Base	-	-
Blade stiffener plate 25mm	25	-
Blade stiffener plate 50mm	50	-
Hub stiffener plate 25mm	-	25
Hub stiffener plate 50mm	-	50
Blade and hub stiffener plate 50mm	50	50

2.4.1 Bearing Rings Displacements

The displacements of the bearing rings are analysed by defining a local cylindrical coordinate system located at the centre of the bearing to ease the analysis and make it more intuitive considering the circular geometry of the bearing rings. Results for the base configuration are presented in detail, followed by summary plots for all the six assembly configurations.

Base Configuration

Radial and axial displacements of the bearing rings are presented in Figure 2.12 and Figure 2.13, respectively. Radial deformation results show an oval shape of the rings, where two diametrically opposed points at 45° and 225° are deformed inwards and the opposite points at 135° and 315° are deformed outwards. Axial deformation results show that the greatest difference between the inner and outer race happens at 225° , where the inner ring is more downwards deformed than the outer ring. The position of the maximum radial deformation coincides with the load angle.

All Configurations

The maximum and minimum radial and axial displacements of the six assembly configurations are summarised in Figure 2.14 and Figure 2.15, respectively. These plots also include a radial and axial flexibility defined in Equation 2.12 and Equation 2.13. The magnitudes of the flexibility allow a direct comparison between different load cases and bearing sizes. However, for the comparative analysis only one load case and size were considered.

$$\delta_{radial} = \frac{d_{radial,max}}{P_{ea}} \quad (2.12)$$

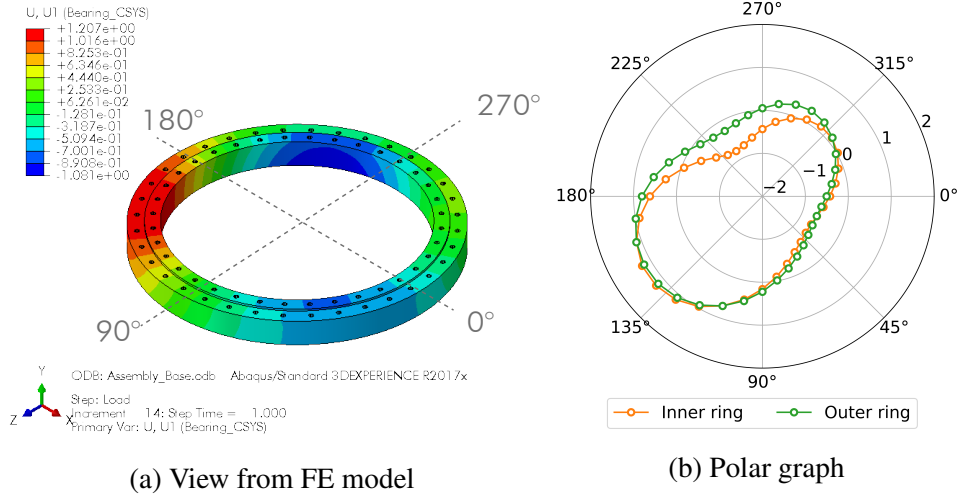


Figure 2.12: Radial displacements of the bearing rings [mm].

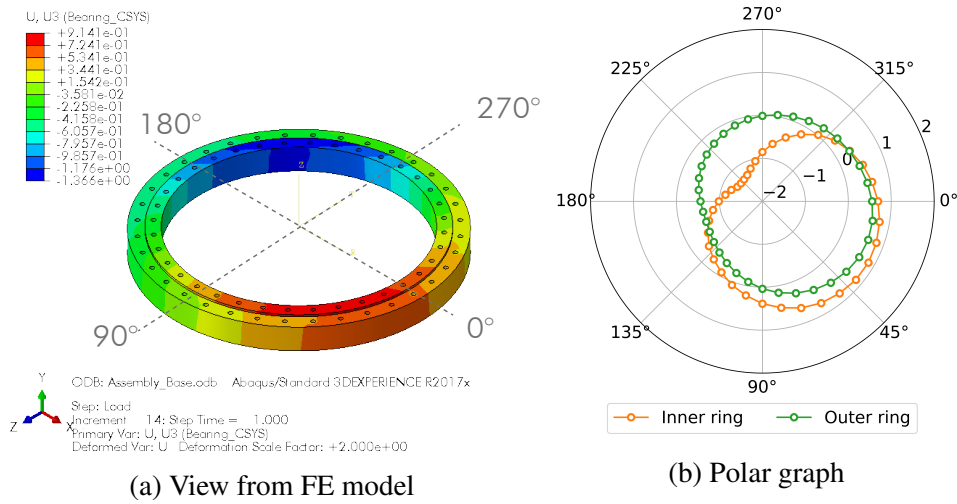


Figure 2.13: Axial displacements of the bearing rings [mm].

$$\delta_{axial} = \frac{d_{axial,max}}{P_{ea}} \tag{2.13}$$

Where, $d_{radial,max}$ and $d_{axial,max}$ are the maximum radial and axial displacement of the bearing ring, respectively, and P_{ea} the bearing equivalent load defined in equation 2.14 [3].

$$P_{ea} = 0.75F_r + F_a + \frac{2M}{d_m} \tag{2.14}$$

Where, F_r is the bearing radial force, F_a the bearing axial force, M the bearing bending moment, and d_m the bearing pitch diameter.

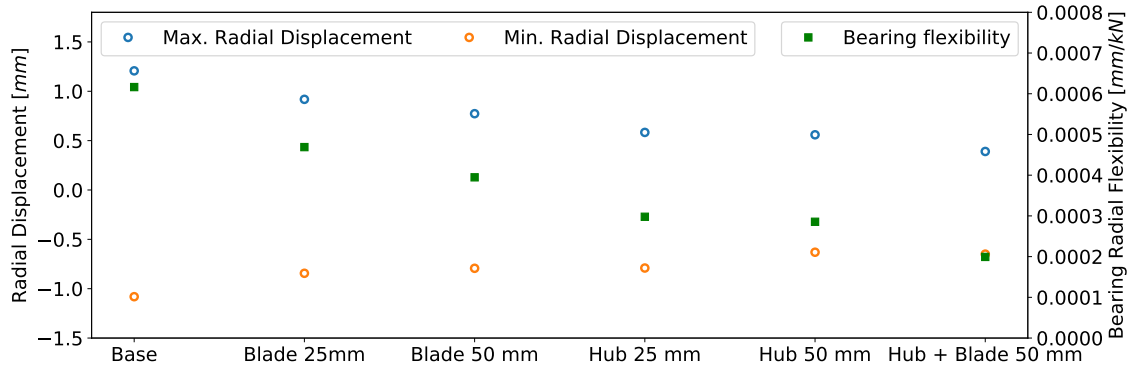


Figure 2.14: Summary of radial displacements for all assembly configurations.

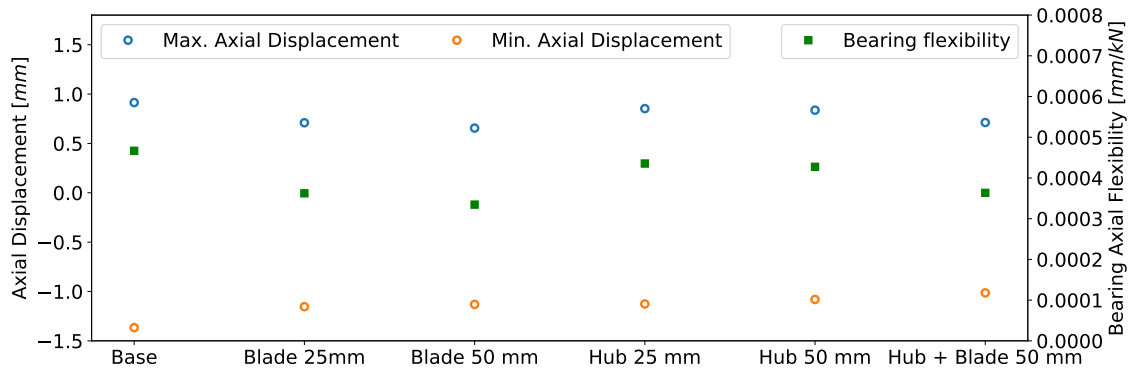


Figure 2.15: Summary of axial displacements for all assembly configurations.

When comparing the results of all the assembly configurations, it can be observed that adding plates in the hub has a greater impact on reducing the radial displacements of the bearing rings. On the contrary, adding plates in the blades has a greater impact on reducing the axial displacement. The same is observed in terms of the flexibility. In order to illustrate how the flexibility is improved by adding the stiffener plates, Figure 2.16 shows a comparison of the radial deformation between the base configuration and the configuration with a stiffener plate of 50 mm in the hub.

2.4.2 Load Distribution Analysis

Load distribution is the individualization of the contact forces on every ball due to the loads applied to the blades. Similar to the presentation of the displacement results, load distribution results are presented in detail for the base configuration and summarised for all the assembly configurations.

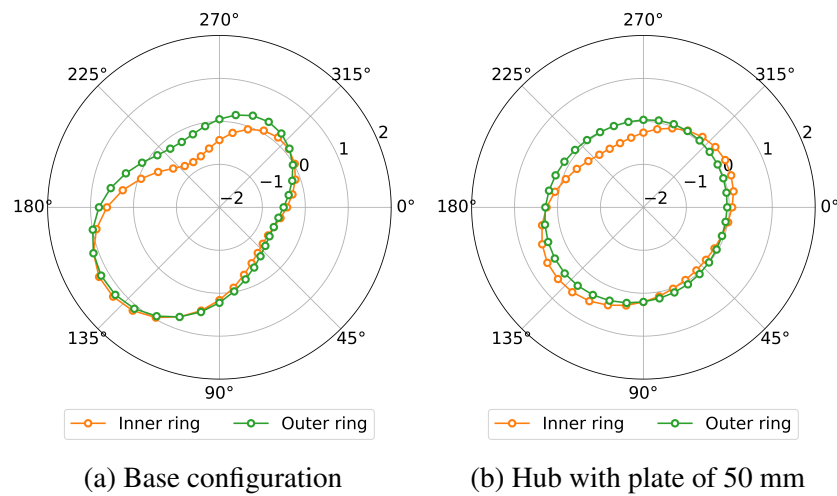


Figure 2.16: Comparison of radial displacements [mm].

These results were also analysed to validate the model. The validation was done by comparing to similar simulations found in literature. For example, results presented by Dadie et. al [71] and Schwack et. al [73] show the same distribution as the results presented in this chapter. A more detailed explanation and understanding is presented below.

Base Configuration

Load distributions for row 1 and 2 are shown in the Figures 2.17 and 2.18 according to the nomenclature and numbering presented in Figure 2.11.

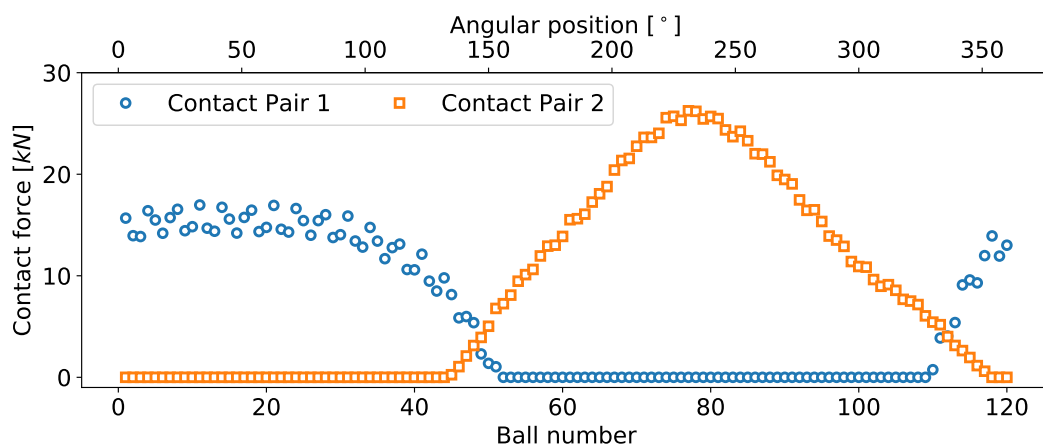


Figure 2.17: Load distribution row 1 - Base configuration.

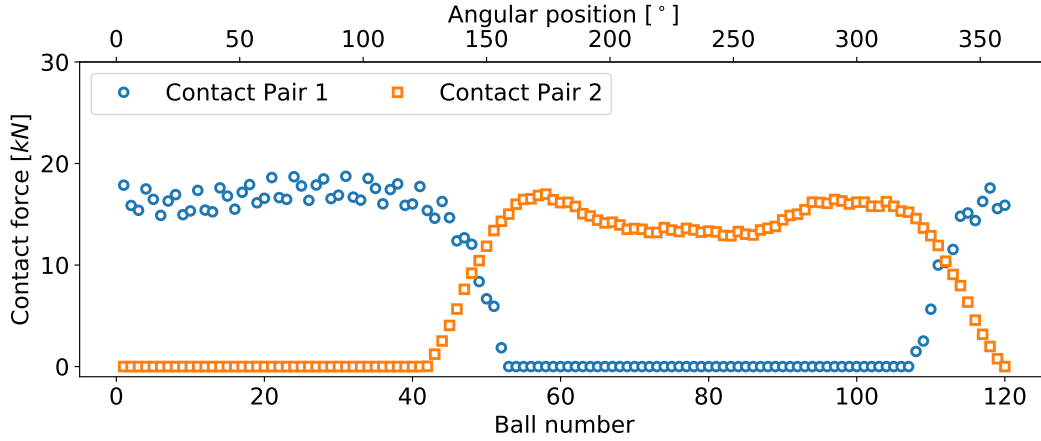


Figure 2.18: Load distribution row 2 - Base configuration.

The maximum load is 26.2 kN in row 1, which is the row next to the blade. This value is 8.3% higher than the maximum contact load obtained using Equation 2.15 [3].

$$Q_{max} = 0.55 \left(\frac{2Fr}{Z \cos \alpha} + \frac{F_a}{Z \sin \alpha} + \frac{4M}{d_m Z \sin \alpha} \right) \quad (2.15)$$

Where, Z is the number of balls per row, and α the initial contact angle.

The maximum load in row 2 located next to the hub is 18.7 kN. The maximum load in row 1 is 55% higher than the maximum load in row 2. This difference is due to the fact that row 1 is closer to the load application point in the blade. Maximum loads are located at the same angular position where the maximum and minimum displacements occur.

Both load distribution plots show that most balls are loaded at only one contact pair which means a two-point contact. The only balls where the nominal four-point contact is maintained is where the axial force due the bending moment is zero at the angular position of 146° and 326° , as shown schematically in Figure 2.19. This particular angular position is explained by the fact that at this position the combination of the contact forces due to the bending moment and the axial force cancel each other.

Load Distribution Indexes

Defining a parameter to quantify the uniformity of the load distribution is essential to compare the different assembly configurations. Two indexes are defined for this purpose. The first index compares the maximum load of contact pair 1 and 2 within a given row (LD_{row}). The second index compares the maximum load of row 1 and 2, at the contact pair where the maximum value occurs ($LD_{bearing}$). In other words, this index compares the load distribution within the

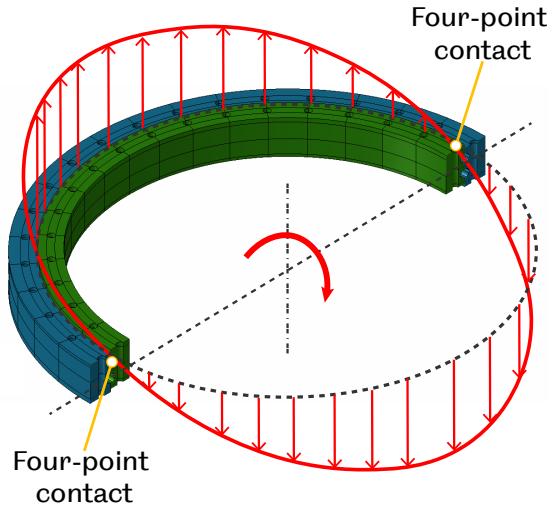


Figure 2.19: Load distribution due to bending moment.

whole bearing. The expressions for these indexes are given in Equations 2.16 and 2.17. The closer the indexes are to 1, the better the load distribution will be. A load distribution perfectly uniform will result in indexes equal to 1.

$$LD_{row,i} = \frac{MaxContact\ Force(Row\ i - Pair\ 1)}{MaxContact\ Force(Row\ i - Pair\ 2)} \quad (2.16)$$

$$LD_{bearing} = \frac{MaxContact\ Force(Row\ 1)}{MaxContact\ Force(Row\ 2)} \quad (2.17)$$

All Configurations

The proposed load distribution indexes are presented in Figure 2.20 for all the assembly configurations. These results show that adding a stiffener plate in the hub better improves the load distribution as all the indexes are the closest to 1.

Figure 2.21 presents a comparison of the load distribution of the base configuration and the configuration with the stiffener plates of 50 mm in the hub. These plots illustrate what the improvement in the load distribution is like, which basically consists of a decrease of the maximum load of row 1, resulting in a more evenly distributed load around the location where the maximum load occurs.

From the bearing deformation analysis, it can be concluded that adding plates in the blades reduces the axial deformation, and adding plates to the hub reduces the radial deformation of the bearing rings. Considering those results, it can be also concluded that radial displacement, and therefore the ovalisation of the rings has the greatest impact on the load distribution.

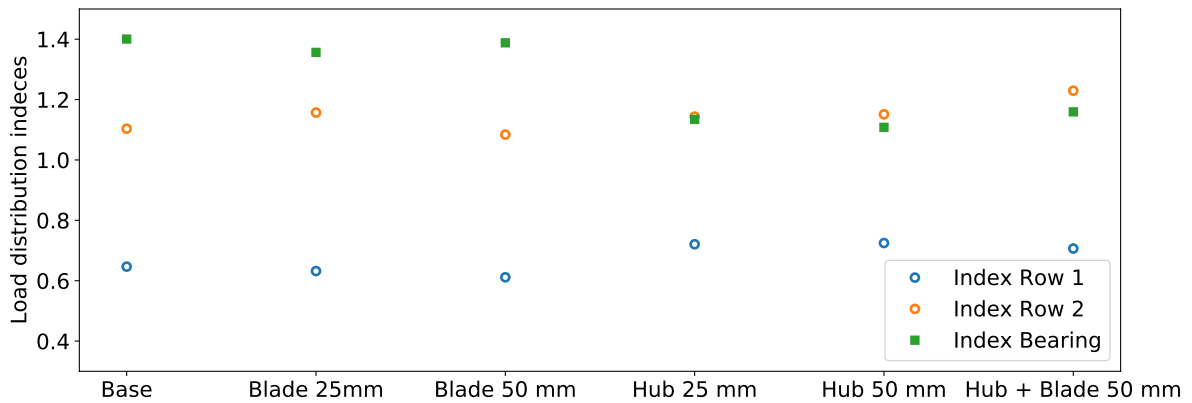


Figure 2.20: Load distribution indexes for all assembly configurations.

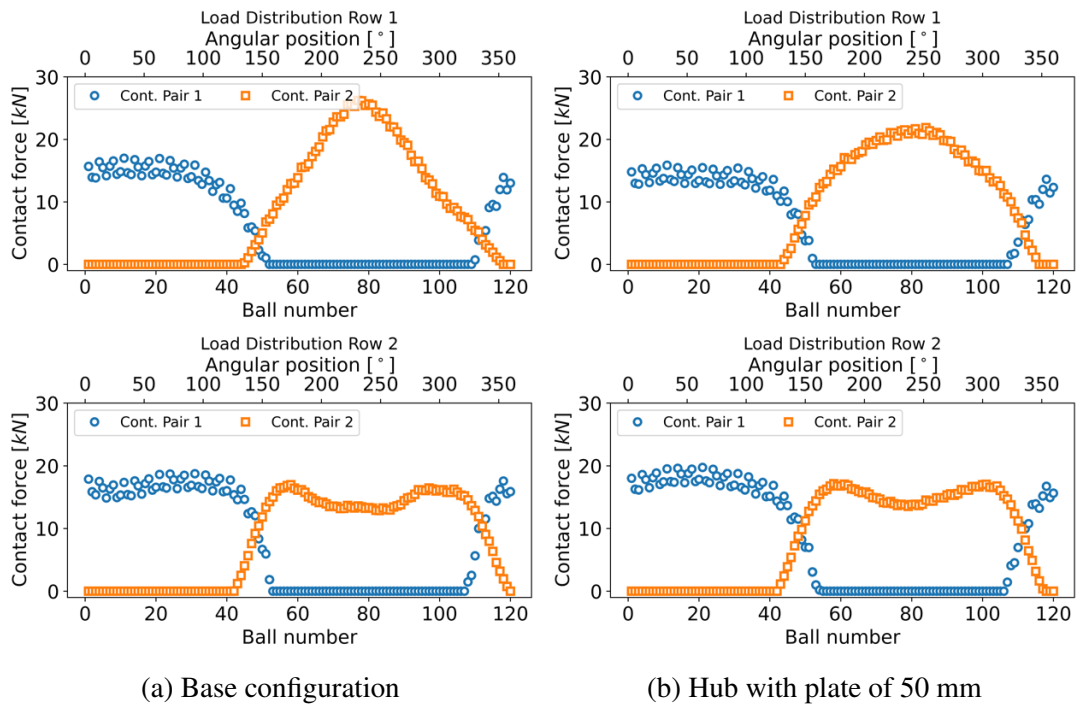


Figure 2.21: Comparison of load distribution between the base configuration and the configuration with the 50mm thickness plate in the hub.

2.4.3 Contact Angle Analysis

Definition of Contact Angle

Double rowed ball pitch bearings are designed to have four-point contacts for every ball. The nominal contact angle for the pitch bearing studied is 45° . The design contact angle changes during wind turbine operation, and the load is transmitted through the ball only at two contact

points [5]; the shifted contact angle is also known as free contact angle. The change of the contact angle leads to different contact conditions, which can result in a modification of the bearing capacity. The contact angle is neglected in the life prediction calculation in international standards [3] because it is required to take into account the flexibility of the bearing supporting structures. The scheme presented in Figure 2.22 illustrates the change of the contact angle from the nominal contact angle α to the loaded free contact angle α' .

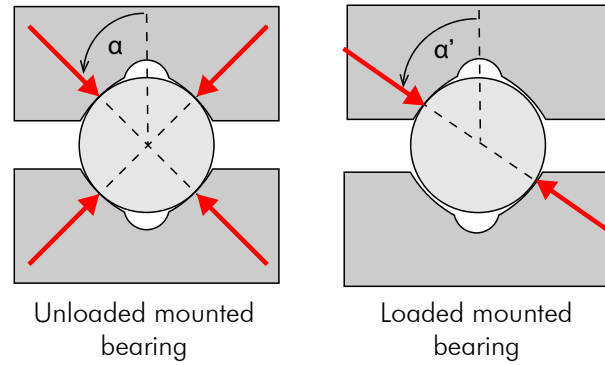


Figure 2.22: Schematic representation of free contact angle.

In the FE model of the pitch bearing assembly developed in the chapter, where the balls are modelled with traction-only springs and rigid elements linked to the contact area, post-processing the change of the contact angle directly is not possible. Instead, the free contact angle is calculated as the change of the contact angle, based on the relative displacements of the spring elements.

Base Configuration

The changes of the contact angle in row 1 and 2 for the base configuration are presented in Figures 2.23 and 2.24. The allowable change of the contact angle is also included in these plots. When this value is exceeded, edge loading occurs. The allowable change of the contact angle is a function of the major semi-axis a of the contact ellipse, and therefore it also depends on the contact force. When the load is zero, the contact area is nonexistent, and the allowable change of the contact angle corresponds to half of the raceway arc. As the load increases, so does the contact area, and the fraction available from the bearing raceway arc becomes smaller, resulting in a smaller allowable change of contact angle. The allowable contact angle is given by Equation 2.18.

$$\alpha_{allow} = \alpha_0 - \frac{a}{r_m} \quad (2.18)$$

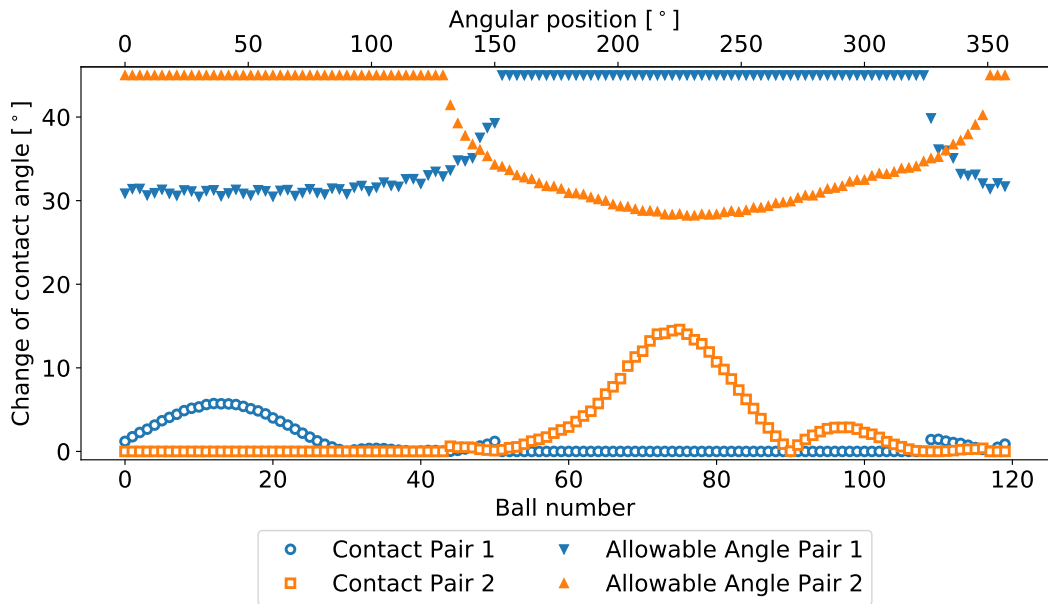


Figure 2.23: Change of contact angle for base configuration - Row 1.

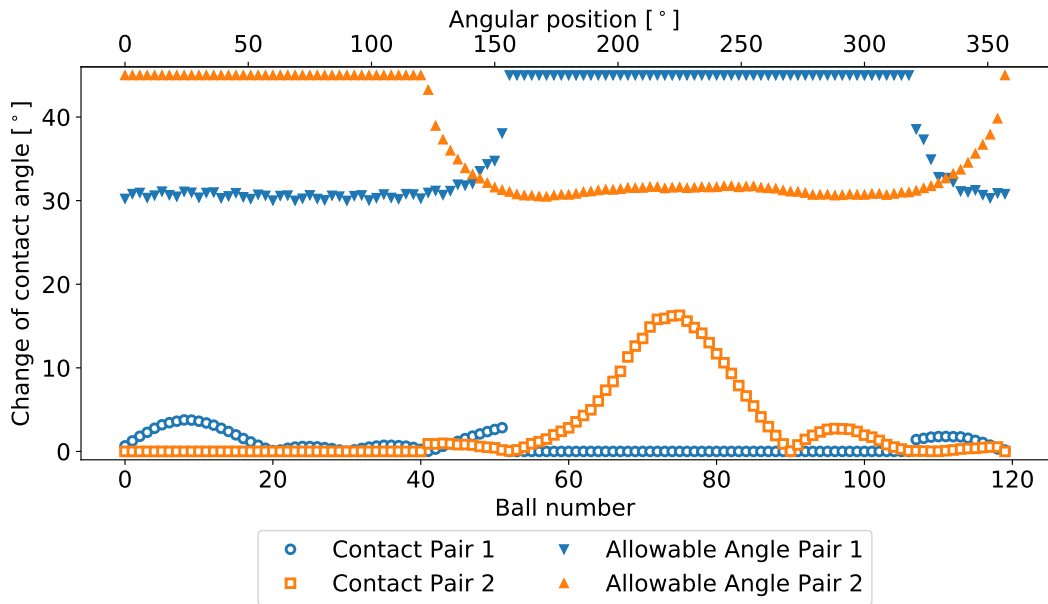


Figure 2.24: Change of contact angle for base configuration - Row 2.

Where, α_{allow} is the allowable change of the contact angle, α_0 half of the bearing raceway arc, a major ellipse semi-axis, and r_m the pitch radius. A scheme of the contact angle is shown

in Figure 2.25. For this analysis, α_0 is considered equal to 45° , although in most bearing designs is slightly smaller.

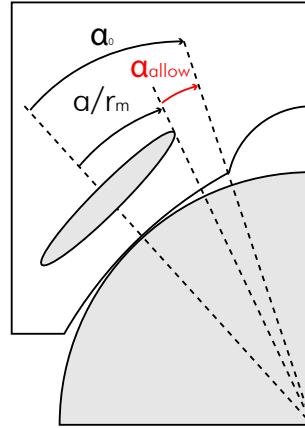


Figure 2.25: Schematic representation of the allowable change of the contact angle.

The results show that the allowable change of the contact angle is not exceeded for the loads considered in the model. These loading conditions correspond to values of normal operating conditions. Edge loading, the damage mechanism occurring when the allowable is exceeded, usually occurs for limit and special loading conditions [5] and not under normal loading conditions. These results also show a clear correlation between the contact force and the contact angle; with the maximum values occurring at the same angular position.

All Configurations

The maximum change of the contact angles obtained for all the assembly configurations are summarised in the graph presented in Figure 2.26.

These results also show that adding a plate in the hub best reduces the change of the contact angle. This can be also related to the radial flexibility. Figure 2.27 shows a comparison between the contact angle distribution of the base configuration and the configuration with the 50mm thickness plates in the hub. Something that draws the attention from the graph presented in Figure 2.26 is that the configurations with plates in the blade exhibit a higher change of the contact angle when compared to other configurations. This may be explained by the fact that for those configurations, the load distribution in row 1 is worse than the base configuration.

2.4.4 Hoop Stresses

The hoop (or circumferential) stresses are post-processed from the model. The analysis of these results aims to ensure that making the bearing support stiffer will not increase the stresses in the

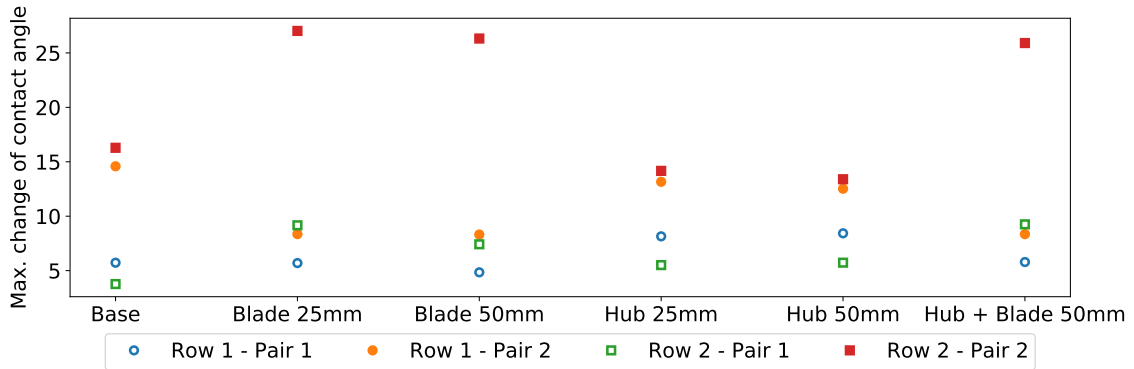


Figure 2.26: Maximum change of contact angle for all configurations.

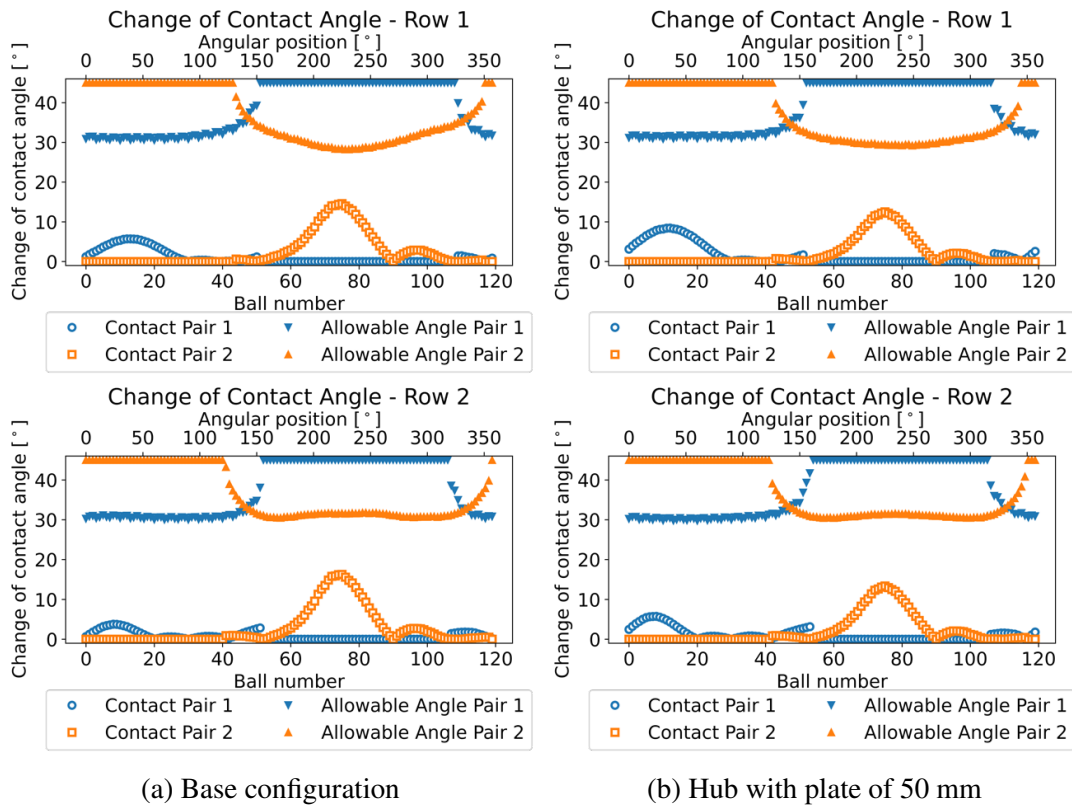


Figure 2.27: Comparison of change of contact angle between the base configuration and the configuration with the 50mm thickness plate in the hub.

bearing. The variation of the hoop stresses can produce fracture due to fatigue in the bearing rings.

Base Configuration

The location where the hoop stresses are post-processed is presented in Figure 2.28. This location is not exactly where the maximum stresses occur since the maximum circumferential stresses are located next to the stress concentration produced by the bolt holes. The results around the hole are highly influenced by the boundary conditions, and in order to obtain accurate stress values in that area, a finer mesh would be required. A larger model would have been inefficient considering that the stresses are not essential for the load distribution analysis. Moreover, this section does not aim to accurately obtain the stresses to perform a fatigue life calculation but compare the effect of modifying the stiffness of the assembly on these results. For that reason, post-processing the non-concentrated values is appropriate for this purpose.

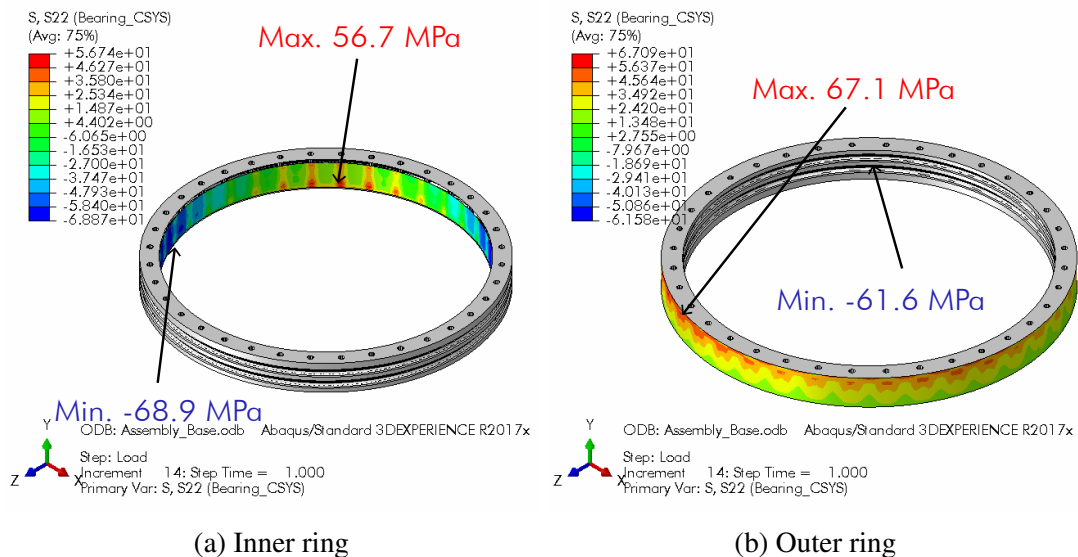


Figure 2.28: Hoop stresses of bearing rings [MPa].

All Configurations

The maximum and minimum hoop stresses in the inner and outer ring for all the assembly configurations are summarised in the plot presented in Figure 2.29. Once again, adding the plates in the hub exhibits slightly better results in reducing the maximum stress; however, it also increases the minimum stress, resulting in a higher amplitude of load variation. A higher load amplitude could result in ring fracture due to fatigue and care must be taken to find a balance between the stiffness of the bearing and the hoop stresses to prevent a different failure mode when trying to improve the load distribution.

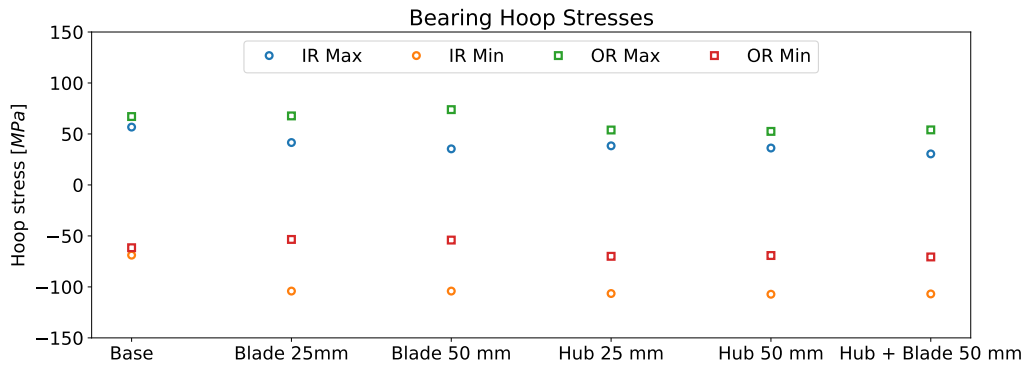


Figure 2.29: Summary of hoop stresses.

2.4.5 Effect of Balls Losing Contact

The large deformation experienced by bearing rings may result in some balls losing contact with the raceways. This model is not able to capture this, as balls are simulated as traction-only springs and rigid beams and no actual contact is defined. Moreover, no method has been found in literature to establish the maximum allowable deformation to prevent this issue. With the purpose of assessing the effect of balls losing contact with the raceways on the load distribution, it has been proposed arbitrarily that five balls around the location of the maximum deformation are suppressed from the model. The maximum deformation takes place at 225° . The results of the load distribution suppressing the contact of five balls are presented in Figure 2.30 and compared to the base configuration. Suppressing the contact of five balls at the location of maximum deformation produces an increase of the maximum load of 15.8 kN equivalent to 60% on the adjacent balls.

The maximum variation of load between two consecutive balls is also assessed. In the base configuration, the maximum variation between two adjacent balls is 4.3 kN and in the model with five balls suppressed is 5.7 kN; equivalent to an increase of 32%. The average load change produced by suppressing five balls increased by 20% compared to the base configuration.

The purpose of this analysis is to illustrate additional issues, generated by the high flexibility of the bearing supporting structures, that may worsen the load distribution.

2.5 Conclusions

The model strategy presented in this chapter allows effectively analysing the load distribution in pitch bearings and investigating the effect of the flexibility of the bearing supporting structures.

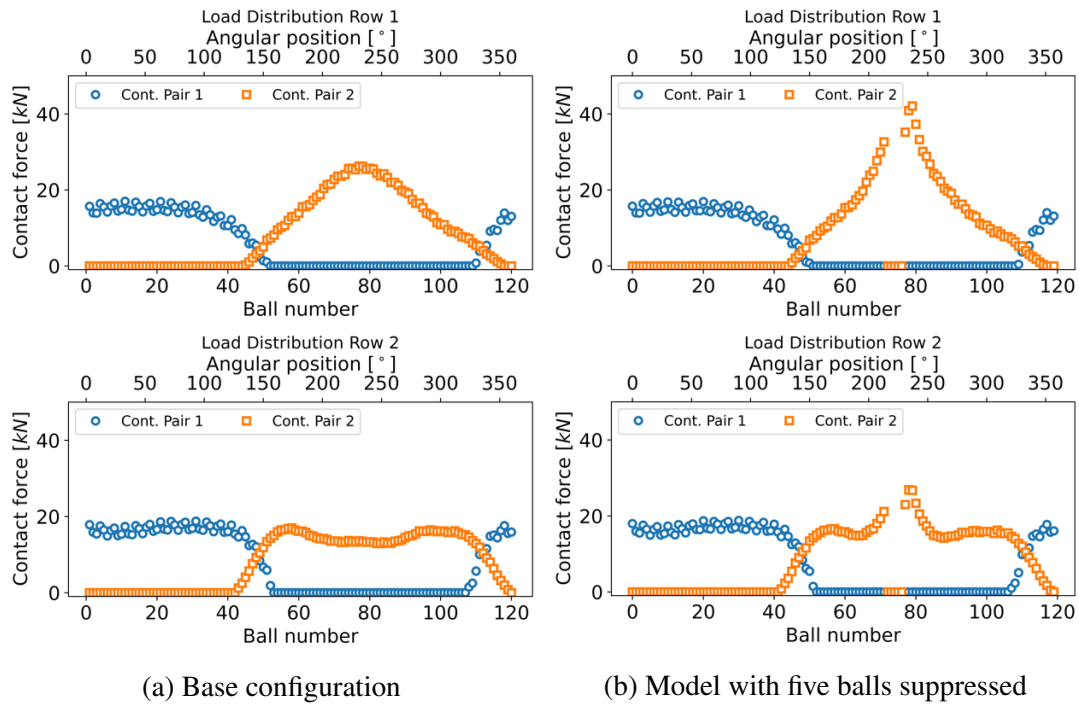


Figure 2.30: Comparison of load distribution between the base configuration and the model with five balls suppressed.

However, some improvements could be made to the model to improve its efficiency. The bearing load distribution is not affected by the load applied on the adjacent bearings and cyclic symmetry could be considered to model one bearing and one third of the hub. The bearing support flexibility is mainly defined by the blade root and the rest of the blade could be suppressed from the model.

Regarding the general results of the load distribution, it was observed that the row next to the blade carries 55% more load than the row next to the hub, which is explained by the fact that the row next to the blade is closer to the load application point. The maximum load obtained from the FE model is 8% higher than the maximum analytical load obtained which does not take into account the effect of the flexibility of the adjacent structures.

The flexibility of the bearing supporting structures were modified by adding stiffener plates to the blade and the hub of different thickness. Six different assembly configurations were analysed. Adding plates in the hub results in the best load distribution, decreasing the maximum load in 20%. In terms of the bearing displacements analysis, adding plates to the hub decreases the radial displacements and the bearing support flexibility. Therefore it is possible to conclude that the radial flexibility has a significant impact on the load distribution.

The change of the contact angle was also analysed. The allowable change of the contact angle was not exceeded in any configuration under the normal loading condition considered in

this study. Adding the plates in the hub exhibits the lowest change of the contact angle and adding the plates in the blades results in the largest ones.

The hoop stresses in the bearing rings were assessed. Adding the stiffener plates in the hub exhibits the best load distribution, however it increases the stress amplitude, which might result in ring fatigue fracture depending on the load conditions. Care must be taken in the design phase to find a balanced solution between increasing the bearing support stiffness and reducing the bearing stresses.

To illustrate a case that may worsen the load distribution, a model with five balls suppressed at the location of the maximum loads was analysed to simulate the situation where the balls are not in contact at any point with the raceway, which may be caused by the large deformations of the rings. The results of this analysis show that in this case the maximum load increases by 60% compared to the base configuration. The maximum load change between two consecutive balls increased by 20%.

Having a more evenly distributed load is essential to reduce the occurrence of different damage modes existing in pitch bearings and therefore improve their reliability. This is particularly important as modern large-scale wind turbines are rapidly increasing their size, resulting in more flexible bearings and supporting structures.

The results presented in this chapter fit within the main aims of this research project, as the contact load is one of the main parameters investigated in the occurrence of fretting wear in pitch bearings. Understanding the overall loading behaviour in pitch bearings contributes to improving the analysis of the contact force in line with the actual application that motivates this research. For example, if the experimental tests show that the wear damage produced by fretting increases with the load, the load distribution results will contribute to understanding the damage distribution in the whole bearing. Moreover, it will be possible to correlate the improvement of the load distribution in terms of reducing the wear damage.

Chapter 3

Damage Characterisation of a Failed Pitch Bearing Section

3.1 Introduction and Aims

This chapter presents the damage characterisation of a failed pitch bearing section that was in service in a wind turbine. Very limited published studies exist in public domain investigating the damage characteristics of false Brinelling and fretting corrosion, and the operating conditions leading to these wear modes in pitch bearings.

The investigation presented in this chapter aims to identify the main characteristics of the damage produced by small-amplitude oscillations in a pitch bearing under actual operating conditions. The analysis of these characteristics was used to determine the likely operating and loading conditions that produced the damage observed on the bearing raceway.

The findings of the damage characterisation and the estimation of the likely operating and loading conditions can be used to validate the results from experimental tests usually employed to investigate the wear modes of wind turbine pitch bearings.

It is worth mentioning that operating and loading conditions during the bearing's service life were not available. This lack of information certainly limited the extent of the conclusions that can be drawn regarding the effects of the operating conditions on damage development. However, valuable information can still be obtained from the damage characteristics of the pitch bearing section.

3.2 Materials and Methods

The damage characterisation was performed by analysing the bearing raceway surface of the failed bearing section. The analysis consisted of an overall damage identification on the surface, followed by a surface mapping at the regions where wear scars were observed. A chemical analysis of the oxidation products at the worn surface was also performed. Finally, hardness measurements of the worn subsurface were carried out to determine the existence of a tribologically transformed structure (TTS).

3.2.1 Pitch Bearing Section

The failed bearing section comes from the outer ring of a 1900 mm diameter double row four-point contact ball bearing with similar dimensions as the bearing considered for the load distribution analysis in Chapter 2. Information about the operating conditions is not available and the reason why this bearing was removed cannot be shared due to a confidential agreement. The bearing section has an arc length of 120 mm, equivalent to an angular section of 7.2° , which covers the distance of the raceway circumference between approximately two balls out of 120 balls in total. The damaged bearing section was initially cut into four sections, namely raceway 1, 2, 3 and 4, as shown in Figure 3.1, to position each raceway surface at the most suitable orientation during the surface measurement. Raceways 1 and 2 belong to the row next to the blade and raceways 3 and 4 to the row next to the hub. The main specifications of the pitch bearing are presented in Table 3.1. The balls belonging to this bearing are not available.

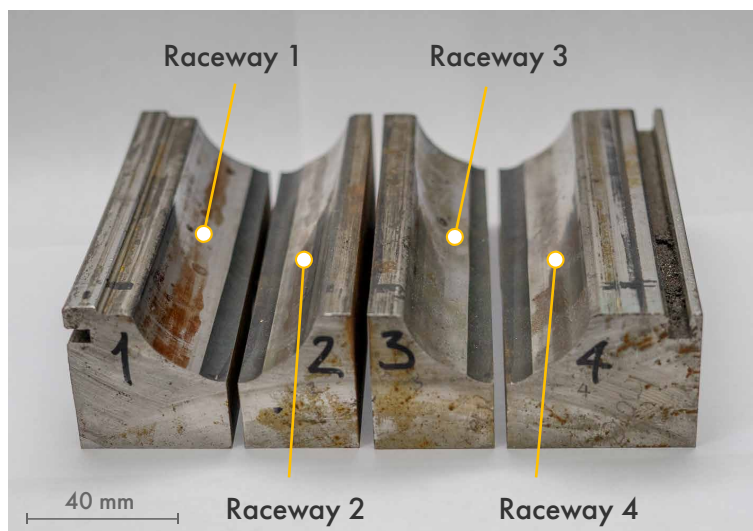


Figure 3.1: Pitch bearing sections.

Table 3.1: Pitch bearing geometry and material properties.

Geometrical Parameters	
Pitch Diameter	1900 mm
Ball Diameter	45 mm
Number of balls	120
Conformity	0.52
Contact Geometry	2 rows with 4-point contact
Initial contact angle	45°
Material Properties	
Ring Material	42CrMo ₄ quenched and tempered
Ring Type	Forged seamless
Bulk Material Hardness Range	260-290 HB
Surface Hardness	59±4 HRC
Hardened Layer Thickness	4.5 mm
Minimum Yield Strength	700 MPa
Minimum Tensile Strength	870 MPa

3.2.2 Surface Damage Observation by Optical Microscopy

The different damage modes on the bearing raceway were firstly identified by visual inspection. A Zeiss AX10 optical microscope, presented in Figure 3.2, was then used to capture more detailed images of the bearing raceway surface.



Figure 3.2: Zeiss AX10 optical microscope used for detailed surface damage observation.

3.2.3 Wear Scars Measurements

The Alicona InfiniteFocus-SL was used to carry out the surface mapping of the bearing raceways. The Alicona SL InfiniteFocus-SL is a high-resolution non-contact optical measurement tool capable of measuring 3D surfaces to a resolution of up to 10 nm [74]. The Alicona SL InfiniteFocus-SL and its main components are presented in Figure 3.3.

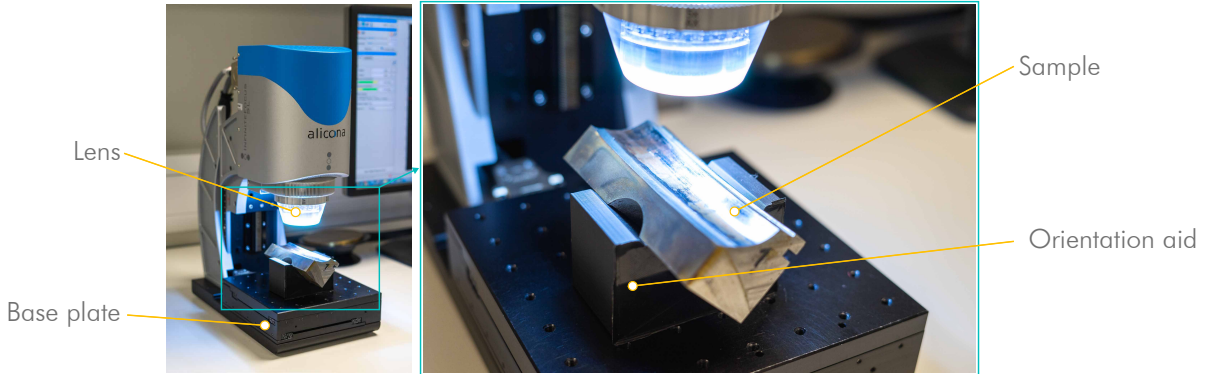


Figure 3.3: Alicona InfiniteFocus-SL and raceway surface inspected.

Measuring the whole raceway surface would have taken excessively long time and generated a large amount of unnecessary data. For this reason, only the regions of the raceway surface with visible wear scars were scanned. To measure each wear scar, the corresponding raceway was placed on the equipment base-plate. However, to minimise the change of curvature of the raceway surface during the measurement and avoid any exposure problems, the different raceways needed to be oriented by means of an positioning aid, as shown in Figure 3.3. Alicona MeasureSuit 5.3 was used to conduct the surface mapping of the wear scars. The main parameters used in the surface mapping are summarised in Table 3.2.

Table 3.2: Alicona parameters for wear scar surface mapping.

Parameter	Value
Lens magnification	5x
Polarizer	Off
Contrast	0.5
Brightness	Auto
Vertical resolution	500 nm
Lateral resolution	5 μm

Two main steps were considered for the post-processing of the surface measurements. The first step consisted of straighten the measured surface by applying a *Form Removal* utility

included in the software Alicona MeasureSuit 5.3. This utility straightens the overall shape of the measured object keeping the roughness profile of the surface unaffected. For the measured raceways, their cylindrical shape was removed using this tool. This made it possible to measure the wear scar dimensions using an appropriate coordinate system. Every measurement was then saved as *al3D* files in order to carry out the second step, which consisted in using a Matlab conversion program [75] to process and measure the dimensions of the wear scars.

3.2.4 Identification of Oxidation Products

The chemical composition of the oxide particles adhered to the raceway surface was determined by employing energy dispersive X-ray spectroscopy (EDX or EDS) and back scattered electron imaging (BSE) using the FEI Inspect F50 scanning electron microscope (SEM). EDX is a method to identify and quantify elemental composition of small samples by exciting the different atoms on the surface with a electron beam. The excited atoms emit X-rays that are analysed by an energy dispersive detector and associated with the corresponding elements. Figure 3.4 presents the equipment used for the EDX analysis and a illustrative scheme of the technique.

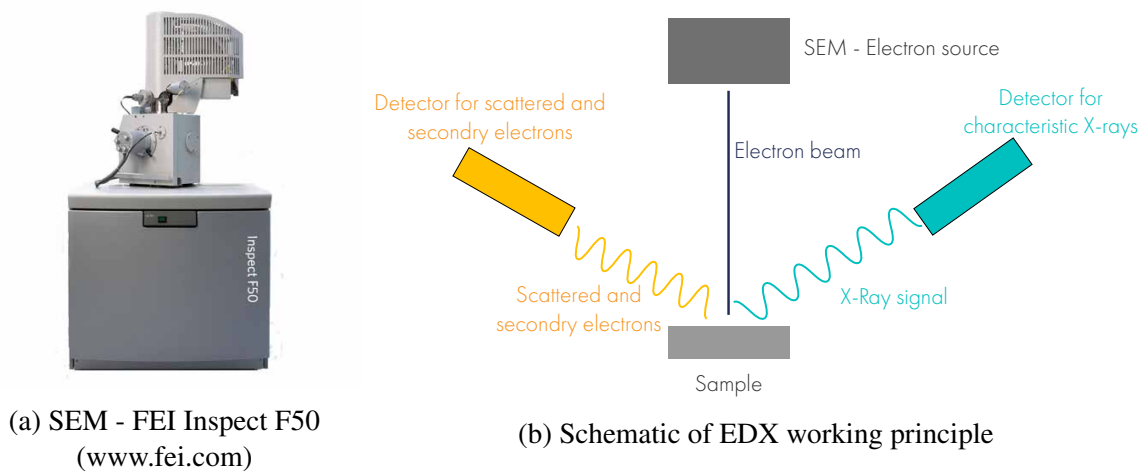


Figure 3.4: Equipment for EDX analysis and illustrative scheme of the technique.

3.2.5 Analysis of Tribologically Transformed Structure

The tribologically transformed structure can result in an altered sub-surface microstructure [76]. In order to determine its existence under the wear scars, the raceway 1 was sectioned into smaller samples to investigate the sub-surface microstructure under wear scar 1. A second sample was extracted from an apparently unworn area of the raceway section. The examination

of the second sample allows the effect of wear to be compared with a base condition. The sample preparation process for the metallographic investigation consisted of different stages that are described below based on [77]. Figure 3.5 shows the prepared samples after completing the described procedure.

1. Sectioning: Two samples, one from a wear scar and another from an unworn area on raceway 1 were sectioned by the IsoMet, a high precision cutter, using a 1 mm diamond blade.
2. Mounting: The extracted samples were mounted on a cylindrical support of Bakelite using the SimpliMet, a hot mounting machine. This stage was required for the grinding and polishing steps.
3. Grinding and polishing: Three stages of grinding and three of polishing were carried out on the samples using the AutoMet 250. The parameters used for the grinding stages are summarised in Table 3.3.
4. Etching: Samples were etched in a Nital mixture of 2% nitric acid and 98% methanol. The etching time was defined to reveal the grain size of the hardened layer, resulting in the rest of the sample over-etched.

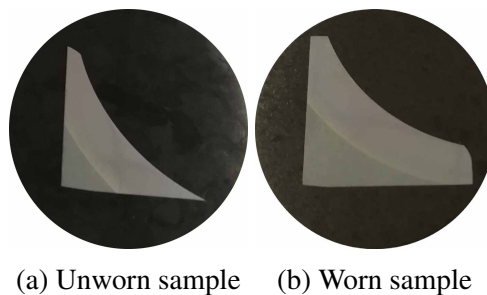


Figure 3.5: Prepared samples for sub-surface investigation

The prepared samples were investigated by employing different techniques. Firstly, the hardness profile was measured using a hardness-testing machine Mitutoyo HM-101. Secondly, the microstructure of the sample from the worn area was analysed by optical microscopy and compared to an unworn sample. Finally, a small section of the sample was analysed by Electron Back Scatter Diffraction (EBSD). EBSD allows crystallographic information to be obtained, such as orientation and crystal type.

Table 3.3: Parameters for sample preparation.

Step	Abrasive	Time [min]	Force [N]	Head/platen speed [RPM]	Relative direction head/platen
1	P240	1	27	60/305	Same
2	P600	1	27	60/305	Same
3	P1200	1	27	60/305	Same
4	9 μm diamond	5	27	60/150	Opposite
5	3 μm diamond	3	27	60/150	Same
6	1 μm diamond	2	27	60/150	Opposite

3.3 Results

3.3.1 Surface Observation of the Damaged Bearing Raceway

Different damage modes were identified on the bearing raceway surfaces after the initial inspection: wear scars, fatigue spalls, micropitting and microcracks. Oxidation products were also observed on the surface. Figure 3.6 presents pictures of the four raceways indicating the location of the different damage observed. Figure 3.7 shows detailed views of some of these damage captured by optical microscopy and surface mapping using the optical profilometer (Alicona).

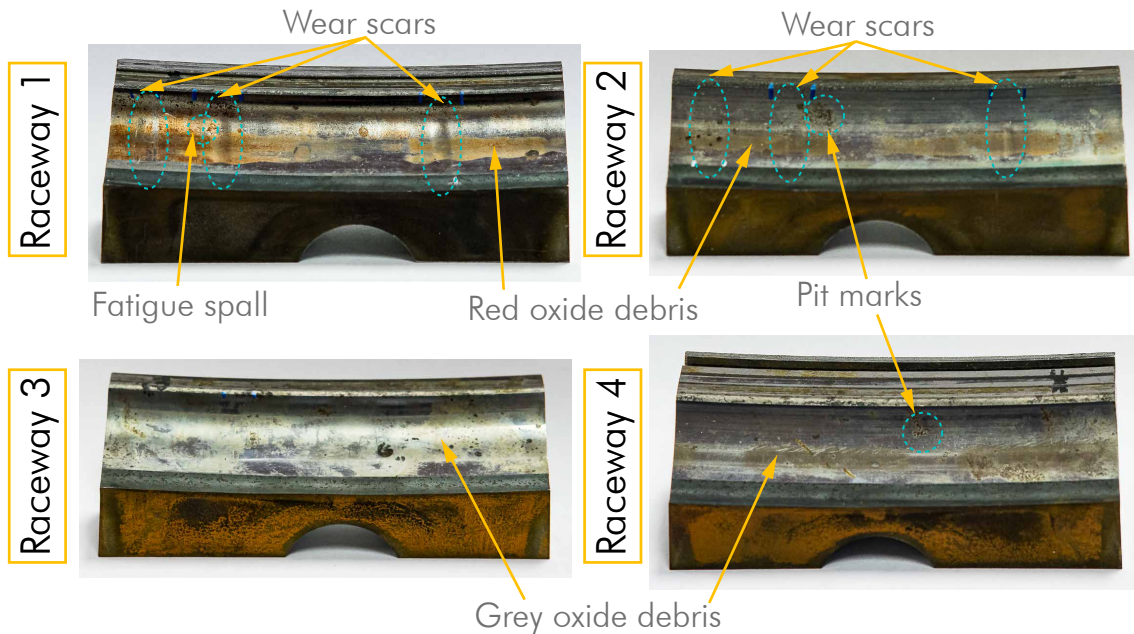


Figure 3.6: Damage modes on pitch bearing raceway surface.

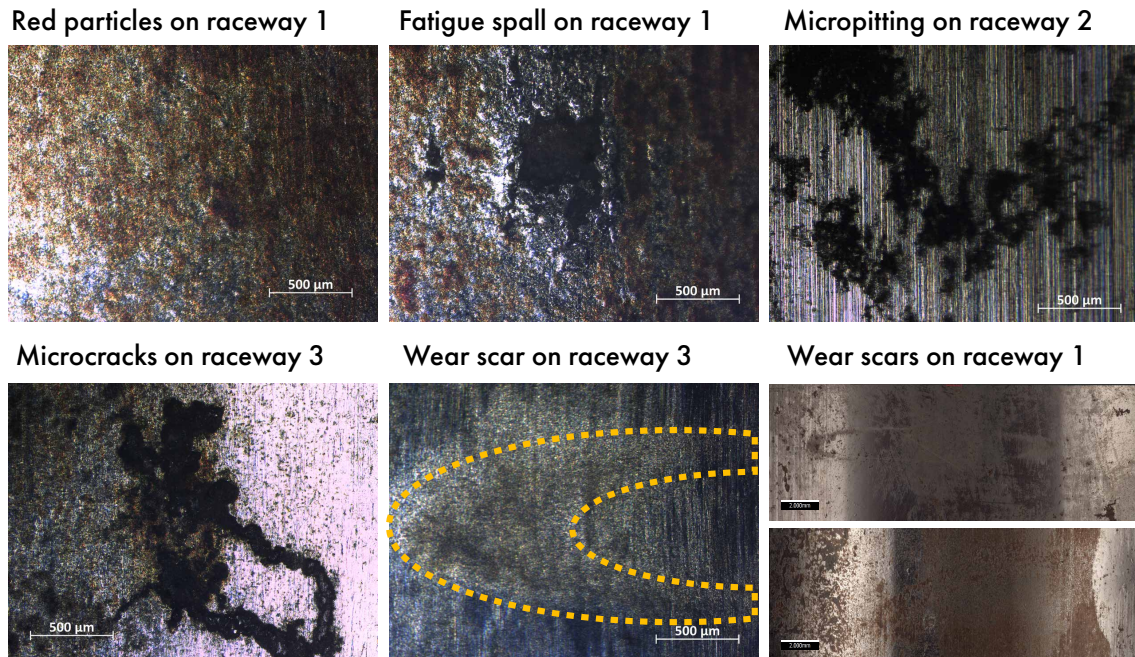


Figure 3.7: Detailed surface damage observed by optical microscopy and surface mapping of the surface damage.

The main damage mode observed on the surface was wear scars. Wear scars exhibit an elliptical shape, which can be related to the contact area between the bearing balls and the raceways. These wear scars correspond to false Brinelling and/or fretting corrosion according to the damage definitions and features given by Godfrey [8]. One of the characteristics easily recognisable to the damage modes, in addition to the elliptical shape, is the reddish and grey oxide particles on the worn surface [78]. These particles might correspond to Hematite and Magnetite. A more detailed analysis of the oxide particles is presented in Section 3.3.4.

The damage found in the bearing section was mild when compared with the damage produced by fretting corrosion and false Brinelling in pitch bearings published by bearing companies available in public domain [79]. This is coherent considering that the wind turbine from where this pitch bearing was taken out, operated with a collective pitch controller. This means that the number of small amplitude oscillations during its service life was not as large as in more modern wind turbines fitted with individual pitch controller [7].

Three wear scars were identified on raceway 1 and 2, which belong to the row next to the blade. The location of these wear scars is presented in Figure 3.8. The position of the scars on raceway 1 is approximately the same as the scars on raceway 2. This suggests that the conditions that produced the damage of scar 1 in raceway 1, also produced the damage of scar 1 in raceway 2. The observations are similar for scars 2 and 3. It could be also observed that

the separation between scars 1 and 2 was measured as 53 ± 5 mm, meaning that these wear scars were produced by two consecutive balls, as the separation between balls in a 1900 mm diameter bearing with 120 balls per row is 50 mm. Wear scars 3 are located at a distance of 20 ± 5 mm away from scars 2, which suggests that they both were produced by the same ball but at a different pitch angle. All wear scars are located slightly outward of the raceway groove and not exactly at the centre of the raceway. This is the result of the change of the contact angle due to the flexibility of the bearing's supporting structures [73]. It is likely that this damage occurred during normal loading conditions, as extreme load conditions would have resulted in edge loading and truncation of the contact area [15].

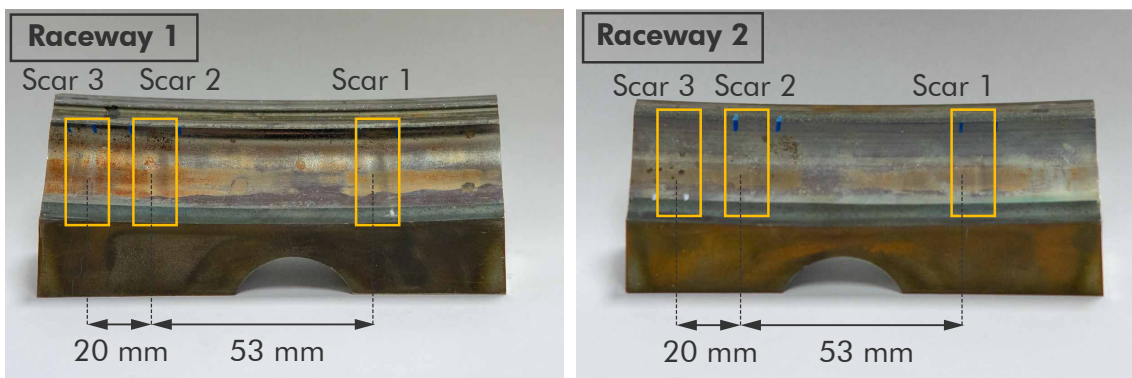


Figure 3.8: Location of measured wear scars on raceways 1 and 2.

Corrosion pits and fatigue spalls were also identified on the raceway surfaces of the bearing section. Kotzalas and Doll [1] reviewed the major tribological issues in wind turbine components and argued that micropitting in main shaft bearings is caused by an important amount of sliding, resulting in high shear stresses, and translating the maximum contact stresses to the surface. The sliding between the rolling elements and the raceway increases when the lubricant film is not sufficiently thick to separate surface asperities. Pit marks are produced at the contact by hardened debris particles, which results in even higher contact stresses at the surface. These conditions are also likely to occur in pitch bearings, where the small amplitude oscillations and the slow rotational speed result in an inadequate film thickness and sliding between the balls and the raceways [43], which might explain the presence of pit marks on the raceway of the bearing section. The fatigue spall could be the result of micropitting or fretting fatigue. In this case, the most possible cause seems to be fretting fatigue, as the spall is located at the edge of a wear scar. Fretting fatigue usually initiates at this location where the shear stress is maximum [15], [80], [54]. Another possibility is that the spall was subsequent to the wear scar which acted as stress concentration.

3.3.2 Surface Mapping of Wear Scars

The six wear scars on the raceways of the bearing sections presented in Figure 3.8 were further studied by conducting surface measurements. The datasets from these measurements, saved as al3d files from Alicona Measure Suit software, were read in MATLAB using the program Alicona Data Handling [37]. For each wear scar, the data was post-processed to produce a surface map plot and two cross-section profiles of the wear scar height, one along its length and another along its width. Figures 3.9 and 3.10 present the surface map plots of wear scars on raceway 1 and 2, respectively. Figures 3.11 and 3.12 show the wear scar profiles along the wear scar length and width on raceways 1 and 2, respectively. The dimensions of the measured wear scars are summarised in Table 3.4.

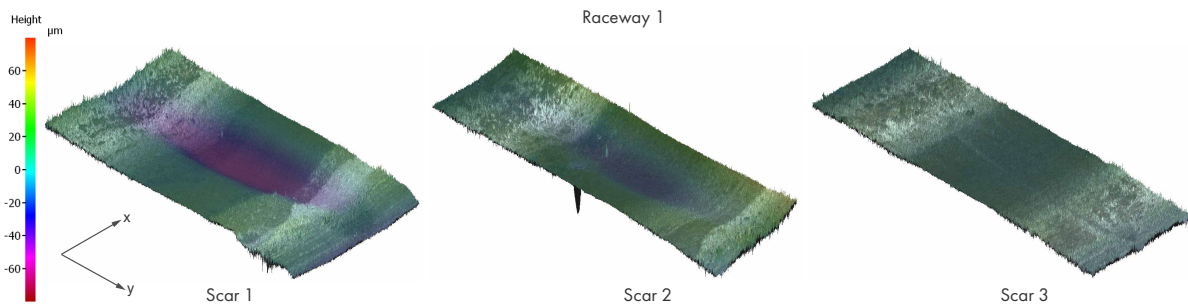


Figure 3.9: Wear scars surface maps of raceway 1.

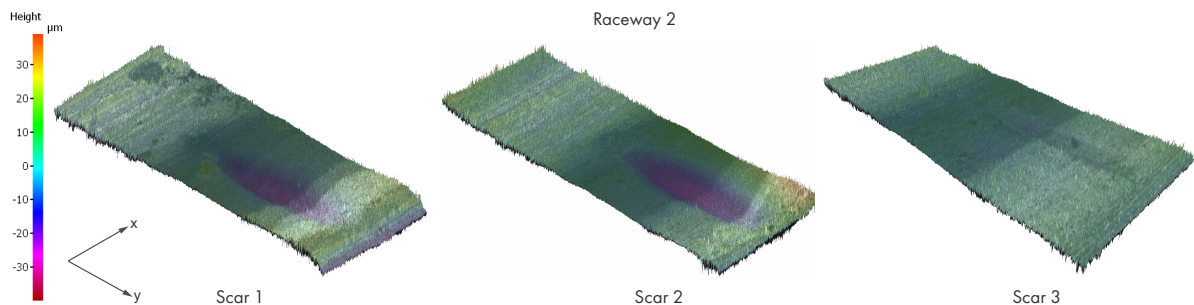


Figure 3.10: Wear scars surface maps of raceway 2.

The surface roughness of the worn surfaces was also measured from the surface mapping datasets. These measurements were used to calculate the damage ratio proposed by Maruyama et al. [48] defined as the ratio between the surface roughness after and before wear. It was originally proposed that this ratio would be calculated using the maximum peak to valley height R_z . However, this is only suitable for lab-based experimental conditions. In the pitch bearing sections analysed for this work, which worked under unknown operating conditions, the R_z

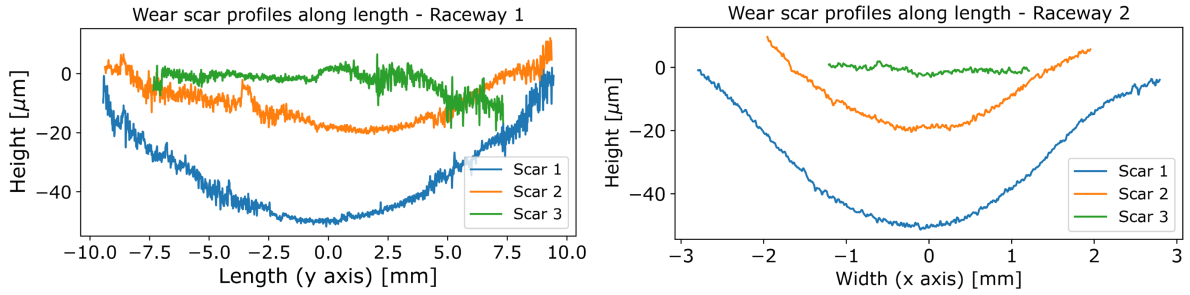


Figure 3.11: Wear scar profiles of raceway 1.

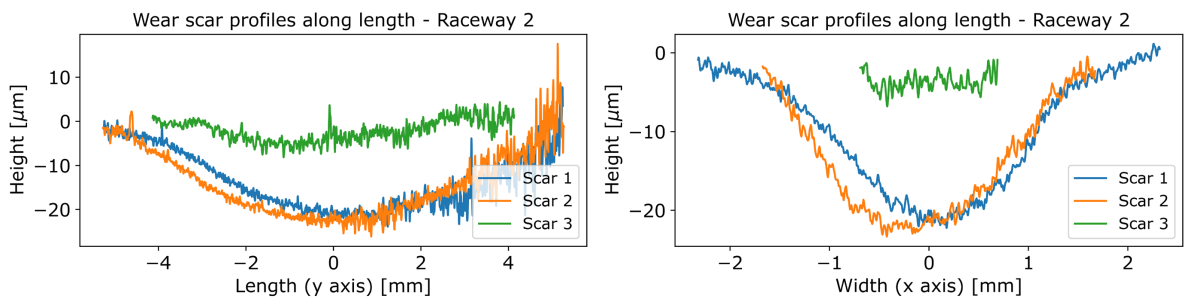


Figure 3.12: Wear scar profiles of raceway 2.

value varies significantly with the position of the wear scar profile. For this reason, the damage ratio is modified in this analysis and the arithmetical mean deviation R_a is used, as shown in Equation 3.1. The surface roughness was measured according the standards ISO-4287 [81] and ISO-4288 [82].

$$\text{Damage ratio} = \frac{R_a \text{ after wear}}{R_a \text{ before wear}} \quad (3.1)$$

The surface roughness before the wear was unknown and there was not information available about its nominal value. To overcome this issue, the surface roughness before wear was measured on a region of the specimen close to the wear scar with no damage or a very low damage. Table 3.5 presents the roughness measured and the damage ratio calculated for each wear scar. Schwack et al. [40] used this damage ratio to study the effect of grease lubricants under wind turbine pitch bearing conditions. It was pointed out that this ratio should not be analysed independently as in some cases wear may reduce the surface roughness. However, it was not the case in this work, as all calculated ratios were greater than 1.0.

Table 3.4: Summary of wear scars dimensions.

Raceway 1			
Scar	Length [mm]	Width [mm]	Depth [μm]
Scar 1	18.3 \pm 0.10	5.7 \pm 0.04	50.8 \pm 0.55
Scar 2	17.4 \pm 0.85	3.5 \pm 0.13	20.2 \pm 0.46
Scar 3	14.1 \pm 0.12	2.1 \pm 0.09	2.7 \pm 0.47
Raceway 2			
Scar	Length [mm]	Width [mm]	Depth [μm]
Scar 1	10.0 \pm 0.12	4.1 \pm 0.06	21.6 \pm 0.58
Scar 2	10.4 \pm 0.18	3.2 \pm 0.14	24.2 \pm 0.52
Scar 3	6.8 \pm 0.15	1.3 \pm 0.14	5.9 \pm 0.80

Table 3.5: Surface roughness measured on the wear scars and calculated damage ratio.

Raceway 1			
Scar	R_a after wear [μm]	R_a before wear [μm]	Damage ratio
Scar 1	1.13 \pm 0.03	0.91 \pm 0.04	1.25
Scar 2	1.10 \pm 0.09	0.71 \pm 0.07	1.55
Scar 3	1.22 \pm 0.10	0.65 \pm 0.02	1.87
Raceway 2			
Scar	R_a after wear [μm]	R_a before wear [μm]	Damage ratio
Scar 1	1.13 \pm 0.03	0.75 \pm 0.06	1.71
Scar 2	1.10 \pm 0.09	0.73 \pm 0.06	1.41
Scar 3	1.22 \pm 0.10	0.89 \pm 0.11	1.29

3.3.3 Hardness Profile and Microstructure Analysis

The hardness profile was measured in two different samples. The first sample was obtained from a region apparently undamaged, and the second sample was extracted from the raceway cross-section at the centre of a wear scar. Figure 3.13 presents the results of the hardness profile measurements for both samples. Figure 3.13a shows the hardness profile for the unworn section, where it can be observed that the thickness hardened layer is 4.75 \pm 0.25 mm. The mean hardness of this layer is 690 \pm 42 HV, equivalent to 58 HRC and agrees with the bearing specification hardness presented in Table 3.1. Figure 3.13b shows a comparison between the worn and unworn sections over the hardened thickness layer. The hardness profiles of the hardened layer of both samples are similar and no significant changes can be observed between

them. Figure 3.13b also shows the samples after the preparation including grinding, polishing and etching. The etching reveals the hardened layer that exhibits a uniform thickness.

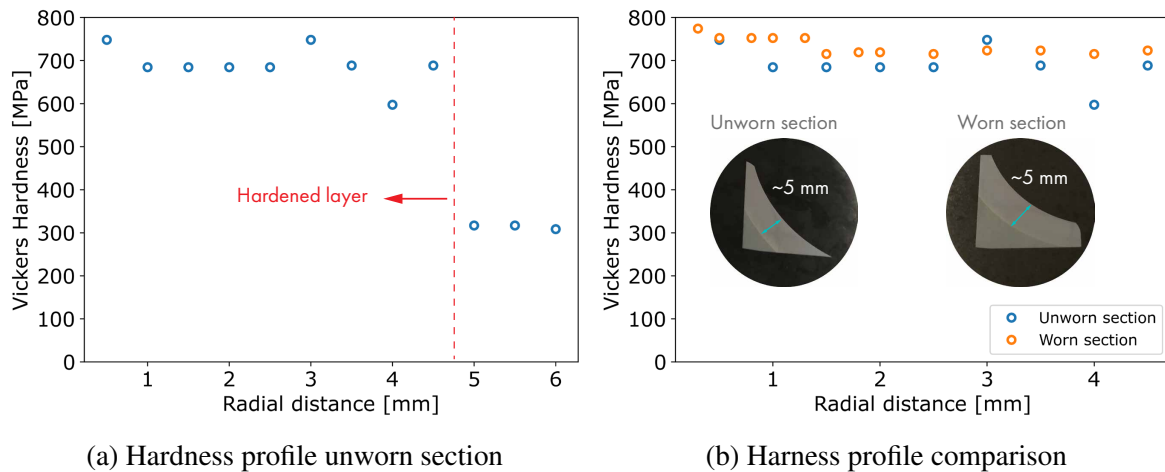


Figure 3.13: Hardness profile measurements of unworn and worn raceway sections.

These sections were also analysed under the optical microscope to compare the microstructure of both samples, as shown in Figure 3.14. These images show a microstructure formed by pearlite inside austenite grains for both samples. The prior austenite grain boundaries are more visible for the worn section, which can be attributable to differences in the etching process.

An EBSD characterisation was performed on the worn section at the Sorby Centre for Electron Microscopy of the University of Sheffield to observe the microstructure more clearly. Figure 3.15a presents an orientation map that reveals, despite the low indexing ratio of about 50%, the microstructure of pearlite inside an austenite grain boundary of approximate $50 \mu\text{m}$. Figure 3.15b also shows a phase map, where mainly a body centred cubic (BCC) structure is observed. This structure is made of tempered martensite with finer carbides inside the austenite grains. This structure is usually related to the heat treatment and not to contact stresses [83]. The unchanged hardness profile and microstructure between the worn and unworn sections suggest that the TTS is not present in the contact, possibly due to two reasons. The first reason might be that the TTS was never formed; this can occur in certain brittle materials [76] and could be possible as the raceway surface is induction hardened. The second reason is that the TTS was possibly removed after a certain number of cycles; it is common not to find evidence of a TTS layer in damaged bearings that were in service for long periods of time [36].

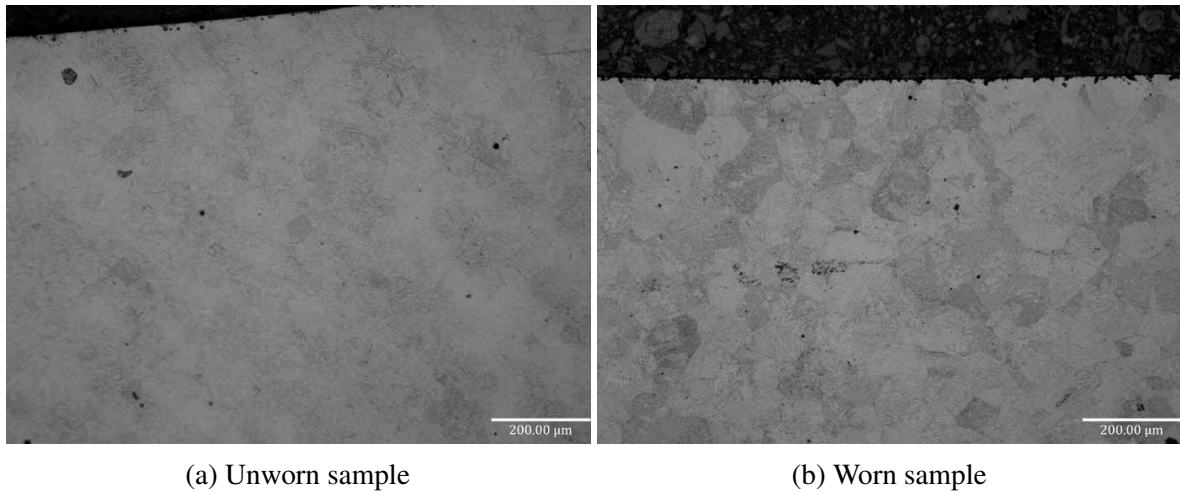


Figure 3.14: Optical microscope images - 20x magnification.

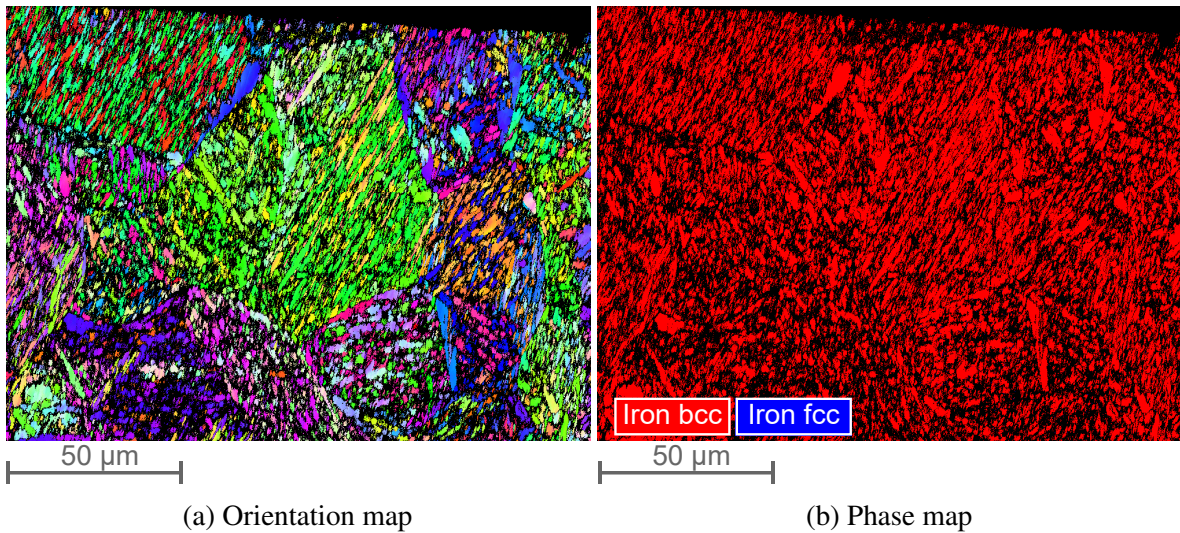


Figure 3.15: Orientation map and phase map obtained from EBSD analysis of the worn section.

3.3.4 Chemical composition of oxidation products

A small worn surface section (10 mm x 10 mm) was analysed by EDX to investigate the composition of the surface material. Figure 3.16a presents an SEM image of the analysed region. Fretting corrosion involves oxidation, therefore this analysis aims to confirm the presence of oxygen on the worn surface. Figure 3.16b shows an oxygen map of the surface. As shown in Figure 3.16a, the regions that exhibit evidence of adhesive wear (dark regions) correspond to the zones with the largest amount of oxygen. The chemical composition was measured at two points as shown in Figure 3.16a. The results are summarised in Table 3.6 and

they show the difference in oxygen amount between the two regions, produced by the presence of oxidation products.

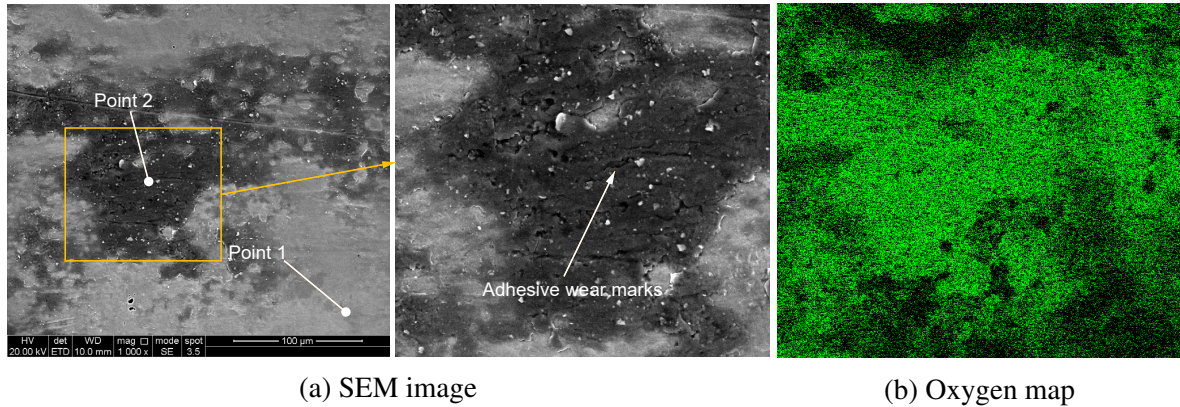


Figure 3.16: SEM image and oxygen map from EDX analysis.

Table 3.6: Relative element concentration Wt%.

Element	Point 1	Point 2
Fe	88.4%	64.9%
C	5.8%	8.9%
O	2.9%	20.8%
Cr	1.1%	0.8%
Mn	0.8%	0.6%
Co	0.4%	0.3%
Si	0.3%	0.3%
Al	0.1%	0.2%
Zn	0.1%	2.3%

3.4 Discussion

3.4.1 Location and Shape of Wear Scars

Wear scars were only present on raceways 1 and 2. This could be difficult to understand at first because most of the balls in a four-point contact ball bearing work under a two-point contact configuration where two non-successive raceways are loaded at the same time in the same ring; either raceways 1 and 3 or raceways 2 and 4, as shown in Figure 3.17. Therefore, the fact that two successive rows are loaded suggests either that the wear on raceways 1 and 2 did not occur at the same time under the same operating conditions, or it was produced at the same

time under fluctuating overturning moments which flipped the contact points. Regarding the unnoticeable amount of wear present on raceways 3 and 4, a possible explanation might be that the loading and sliding conditions were not high enough to produce wear damage.

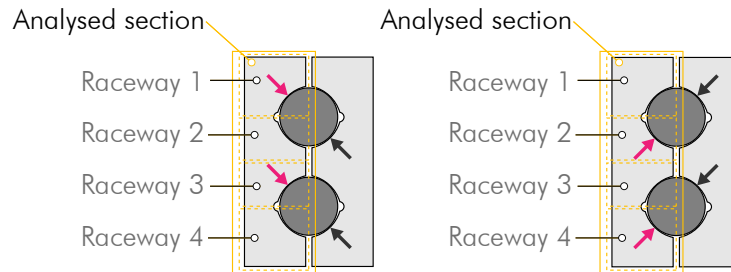


Figure 3.17: Possible contact load distribution of the raceway sections.

The profiles presented in Figures 3.11 and 3.12 show a clear u-shape for the most developed wear scars, scars 1 and 2, which are likely to have been produced by two consecutive balls under similar conditions. This shape suggests that there was no stick region within the contact area and the damage was generated under gross slip regime [35], in agreement with the first fretting maps proposed by Vingsbo and Söderberg [32], and the running condition and material response shown by fretting maps defined later by [34]. For a contact geometry of a ball on a grooved and curved surface, Heathcote and spin slips play an important role [43], [84]. Under constant amplitude oscillations and loads, it would be expected that a greater wear depth occurs at the outer contact region. The fact that this was not observed in the wear scar profiles presented in Figures 3.11 and 3.12 may be because of the variable load that the bearing experienced. Variable contact load results in different sizes of the contact area that overlap the wear damage profile. The scheme presented in Figure 3.18 shows how the superposition of wear profiles from different-sized contact areas could result in a different wear shape.

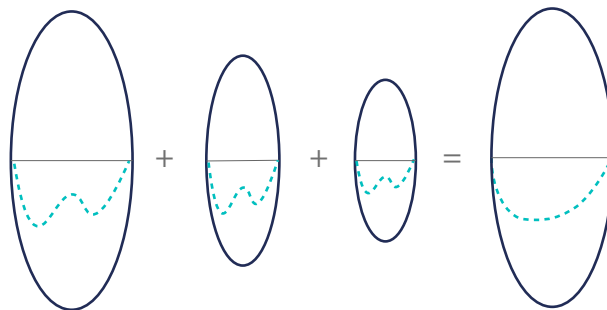


Figure 3.18: Schematic representation of wear scar profiles overlapping.

Scars 3 on both raceways are different to the other two. Their separation from scars 2 suggests that they were generated by the same ball, but at a different pitch angle under different operating conditions. Unlike scars 1 and 2, wear damage in scars 3 is significantly lower regarding the wear depth, and the fretted region is only observed in the outer region of the contact area as shown in Figure 3.6. This wear pattern corresponds to a running regime of partial slip, described by Mindlin's solution [33], which implies that there is a stick region at the centre of the contact area and microslip at the outer region. The wear mechanism under the partial slip regime is slightly abrasive wear, whereas, in the gross slip regime, it can be a combination of abrasive wear, oxidative wear and delamination, depending on the material [35].

The damage ratio based on the change of the surface roughness was previously discussed in Section 3.3.2. It was pointed out in [48] that based on this parameter alone could lead to wrong conclusions. To validate this damage ratio in this work, it is plotted against the wear depth for each scar as shown in Figure 3.19. It can be observed that the damage is greater than 1.0 for all the wear scars, meaning that in any case, the wear damage resulted in a rougher surface. However, the variation of the damage ratio is not the same as the wear scar depth. This implies that this parameter is valid to determine whether there is damage, but not to quantify the amount of wear.

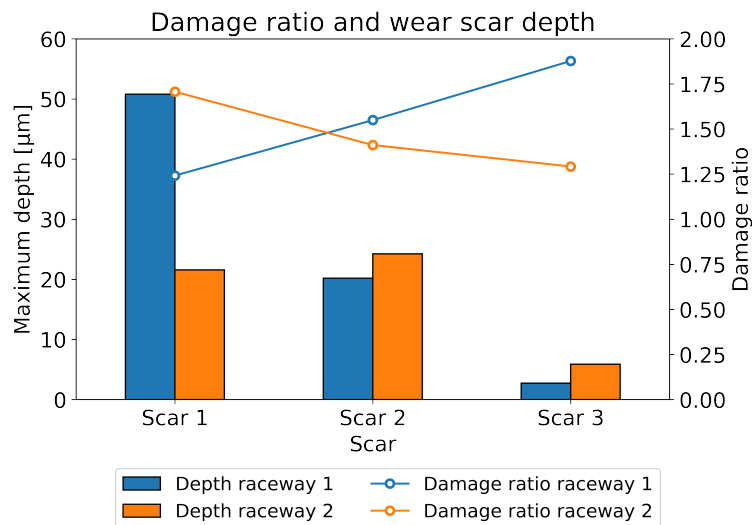


Figure 3.19: Damage ratio and wear scar depth from measured data.

3.4.2 Operating Conditions

Contact force and sliding distance conditions which generated the wear on the bearing section could be estimated from the wear scar dimensions using Hertzian equations for contact me-

chanics. Considering the assumptions of the Hertzian equations, and that the contact force is constant, meaning that the contact area does not change, it was possible to estimate a maximum value for the contact force by assuming that the length of the contact area is equal to the length of the wear scar. Figure 3.20a and 3.20b show the contact force as a function of the length of the contact area and the contact force estimated by using the measured dimensions of each wear scar of the analysed pitch bearing raceways, respectively.

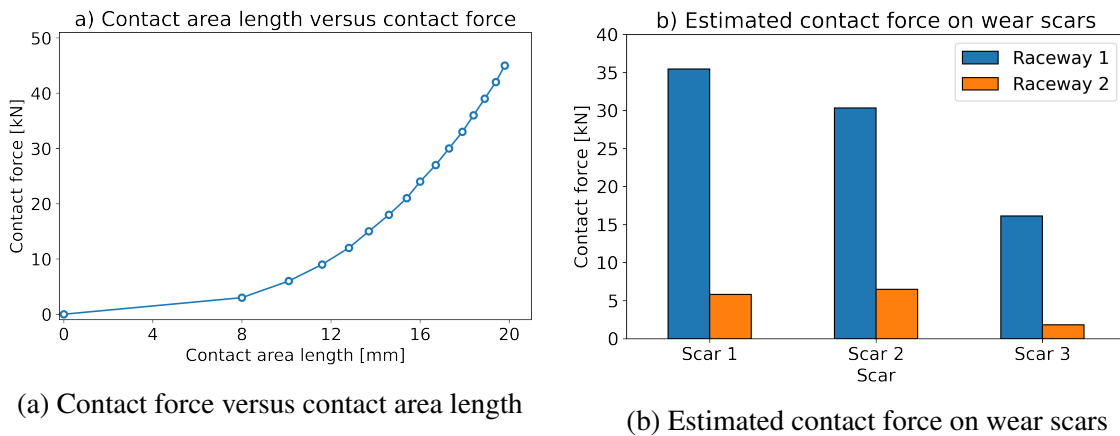


Figure 3.20: Estimation of loading conditions based on Hertzian calculation and wear scar measurement.

By comparing the estimated loading conditions to the results of the load distribution presented in Chapter 2, it can be observed that the maximum estimated contact force is within the load range obtained from the FE model for the case when all the bearing balls were in contact and when the contact of five balls was suppressed simulating a possible loss of contact due to large deformation of the bearing rings. This proves that the estimated forces that produced the wear are within the normal design range of the pitch bearing, and it is possible to assume that some balls could be not in contact with the raceway due to the large deformation experienced by the bearing rings. The variation between the estimated contact force in scars 1 and 2 is 5.1 kN for raceway 1 and 0.7 kN for raceway 2. This agrees with the load variation obtained from the FE simulations and also supports the assumption that some balls may lose contact, or another kind of imperfection not considered in the idealised model, which can make the load distribution more uneven than that only considering the flexibility of the supporting structures.

The method to estimate the sliding distance considered the same assumptions for analysing the contact force. Firstly, the contact area was calculated using Hertzian equations, which should be less than or equal to the measured wear scar width. Secondly, the sliding distance was estimated by calculating the difference between the Hertzian contact area width and the

measured wear scar width, as illustrated in Figure 3.21. Figure 3.22a shows the estimated sliding distance and the sliding ratio $x/2b$ of the wear scars.

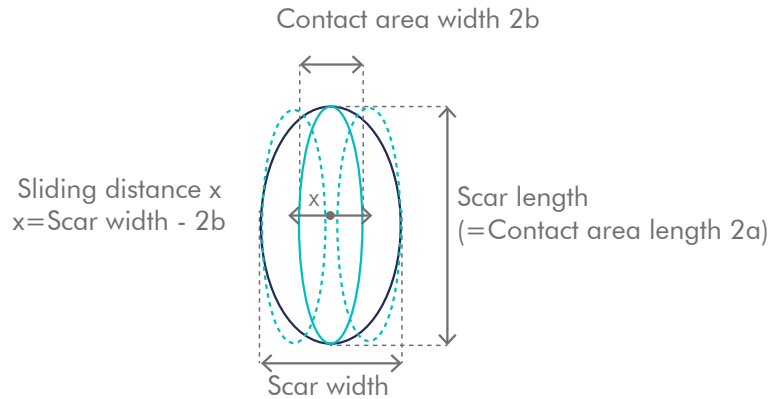


Figure 3.21: Schematic representation of the method for the estimation of the sliding distance.

From the estimated sliding distance results, it can be observed that the magnitude is different at each wear scar. Considering that pitch bearing oscillation angles and frequency must have been the same for all balls at a given time, the different sliding distances could be explained by variations of the contact force, which affects the coefficient of friction, lubrication, and sliding regime. The relationship between the estimated sliding distance and contact force is plotted in Figure 3.22b, where it can be seen that the sliding distance increases with the contact force. This might be considered a result of increased friction due to the increase of the bearing load.

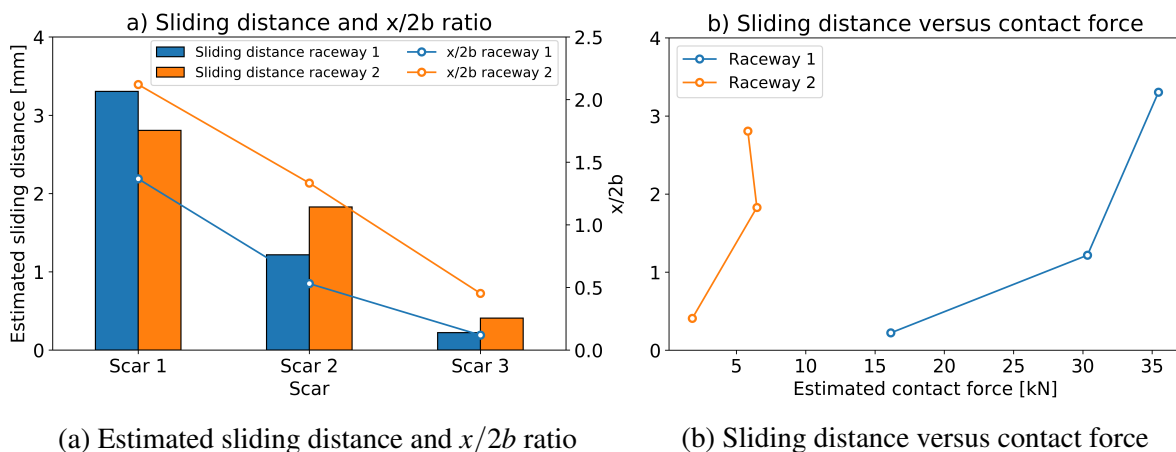


Figure 3.22: Plots for estimation of sliding conditions.

Regarding the estimated sliding ratios $x/2b$, in pure tangential fretting, wear occurs in the range of $x/2b$ corresponding to the transition between partial slip and gross slip ($x/2b < 1.0$), and $x/2b$ corresponding to the transition between gross slip and reciprocating sliding

($x/2b = 1.0$) [36]; in other words, for $0 < x/2b < 1$. However, the estimated sliding ratios for the pitch bearing section were in many cases greater than 1.0, suggesting that in a more complex application, where up to three fretting modes can take place simultaneously (tangential, rotational, and radial fretting), fretting wear can occur under larger sliding distances. This is in agreement with the findings of Maruyama and Saitoh [38] who argued that for $x/2b$ less than 1.6 the lubricant film is not fully established and fretting wear damage is prone to occur. Schwack et al. [40] found that severe fretting wear damage was produced for $x/2b$ greater than 10.

3.5 Conclusions

This chapter set out to investigate the damage of a failed pitch bearing section by measuring the wear scars on the raceway surface and analysing its sub-surface microstructure. Moreover, the possible sliding and loading conditions were estimated by employing a reverse engineering method based on the Hertzian theory of contact mechanics and the FEA conducted for the load distribution of the pitch bearing.

The main damage mode found on the raceways of the analysed pitch bearing section corresponds to wear scars produced by small-amplitude oscillations. Two of the raceways, where these wear scars were found, had large amounts of oxidation, usually related to fretting corrosion and false Brinelling.

Two different patterns of wear scar profiles were observed: u-shaped profiles and w-shaped profiles. U-shaped profiles can be explained as the result of tangential and rotational fretting under gross slip regime and variable load. W-shaped profiles exhibit slight damage, the fretted area is located only at the edge of the worn surface and this behaviour occurs under partial slip regime.

Gross slip regime takes place under larger oscillation amplitude and higher loads compared to partial slip. The estimated oscillation amplitudes and contact forces at the wear scars associated with gross slip (wear scars 1 and 2) are larger than the values estimated at the wear scars associated with partial slip (wear scars 3). The wear depth is also greater at the wear scars where the damage was produced under gross sliding regime.

Other damage modes were found on the bearing section such as micropitting, microcracks and fatigue spalls. All these damage modes can be also attributed to damage generated by small amplitude oscillations.

The estimated contact forces are in the range of the load distribution resulting from normal operating conditions loads. It is concluded that issues produced by the large deformation of the

bearing rings are possible, for instance, some balls not being in contact with the raceway, and they can make the load distribution more uneven.

The results presented in this chapter contribute to the understanding of complex wear modes existing in wind turbine pitch bearings. Their behaviour can be different to the one observed in standard tests as in an actual pitch bearing many damage modes can occur simultaneously. Care should be taken when extending the results to other bearings because the damage mechanisms are highly dependent on many factors such as operating conditions, loading, lubrication and bearing size.

Chapter 4

Experimental Fretting Study in a Small-Scale Configuration

4.1 Introduction and Aims

The complexity of fretting wear on raceway surfaces of pitch bearings suggests that an experimental approach is required to study the effect of various parameters involved in this phenomenon. However, the large size of pitch bearings makes it difficult and extremely expensive to perform tests under actual scale. A common strategy to overcome complex tribosystems when investigating tribological issues is to simplify the system and use either standard commercial tribometers or bespoke down-scaled tribometers. Using this strategy has clear advantages, it allows smaller samples to be used, reducing the testing time and costs. However, many studies have shown that this simplification can lead to testing conditions that are not representative of the actual application. For this reason, particular attention needs to be paid when defining the testing conditions and critically assessing the effects and limitations of reducing the scale of the testing set-up.

This chapter presents an experimental study of fretting wear using a ball-on-flat contact configuration considering a small-scale contact geometry. The study aims to investigate the effect of relevant factors of fretting wear and evaluate the limitations of using a standard tribometer for a larger and more complex application.

The results and conclusions of this experimental study provide not only a first understanding of fretting wear under equivalent pitch bearing operating and loading conditions, but it also offers insights into design a bespoke medium-scale test rig that overcomes most of the limitations found when employing a small-scale test configuration using a standard tribometer.

4.2 Materials and Methods

4.2.1 Tribometer

Fretting tests were conducted on the Bruker's Universal Mechanical Tester (UMT); the version UMT-3 was used. The UMT-3 is designed for comprehensive macro- mechanical tests of lubricants and materials in a load range of 0.1 N to 1000 N. This modular equipment can be fitted with different drives, load cells and sample holders. For this experimental setup, the linear drive with a ball holder were employed. It allowed both rotation and sliding of the ball, and a load cell capable of measuring a load range of 10 N to 1000 N were used. The specifications of the UMT-3 are tabulated in Table 4.1. Figure 4.1 shows the UMT with its main components and a schematic of the experimental setup.

Table 4.1: UMT-3 specifications.

Property/Feature	Value/Description
Vertical travel	Distance: 150 mm Encoder resolution: 0.5 μm Speed: 0.002 - 10 mm/s
Lateral travel	Distance: 120 mm Encoder resolution: 0.25 μm Speed: 0.002 - 10 mm/s
Load range (with load cell DFH-100)	10 - 1000 N
Linear stage	Distance: 120 mm Position resolution: 1.0 μm Max. travel: 120 mm
Reciprocating stage	Frequency: 0.1 to 60 Hz

4.2.2 Samples and Lubrication

The samples with a flat surface were manufactured from a pitch bearing section made of 42CrMo4 steel. The samples were extracted from a section away from the raceway surface. Therefore, the hardness of the samples corresponds to the hardness of the bulk material. The flat surface was ground to achieve the required surface finish of 1.6 μm , which corresponds to the minimum surface roughness normally required for pitch bearings. Table 4.2 summarises the main properties of the flat sample. The balls used in the experiment had a diameter of 9.5 mm and were made of AISI 52100 with a hardness of 60 HRC, equivalent to 730-740 HV.

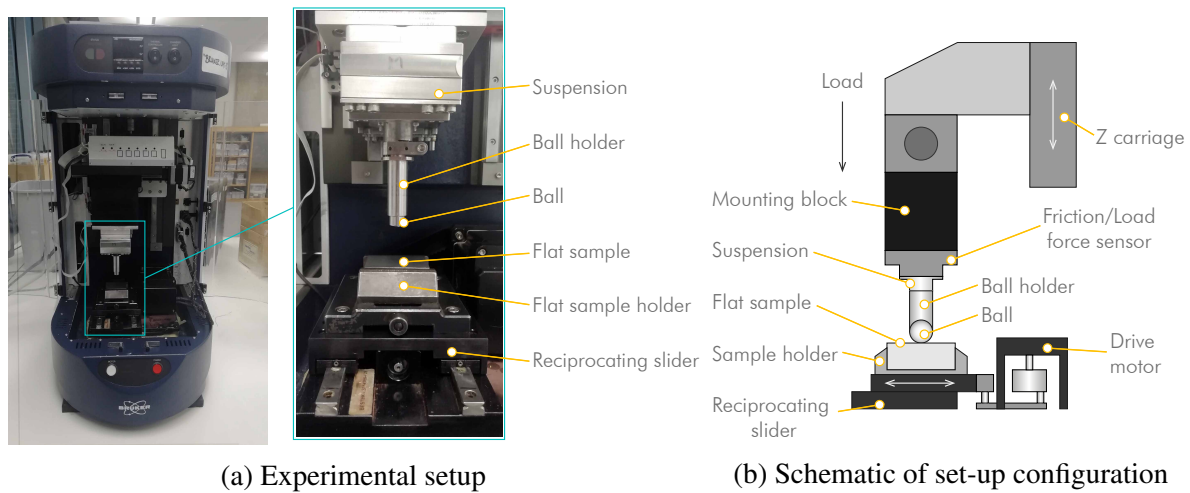


Figure 4.1: UMT-3 used for fretting tests.

The hardness difference between the flat sample and the ball is larger compared to the actual ball/raceway contact pair in pitch bearings which has a possible positive effect of accelerating the wear rate in the flat sample. However, this hardness difference might impact the wear mechanisms. This is analysed and discussed in Section 4.3.6.

Table 4.2: Specifications of flat samples.

Dimensions	Surfaceroughness	Hardness
50mmx40mmx20mm	$R_a=1.6\mu\text{m}$	320 HV

Dry and grease lubricated contacts were tested with the UMT-3. The selection of the grease was made by considering the information available in literature. A Lithium complex grease, Castrol LMX, was selected for the lubricated tests. The main properties of this grease are presented in Table 4.3 [85]. Table 4.3 shows the properties of the selected grease comparing to other greases commonly used in pitch bearing applications [40]. The properties of the selected grease are within the range of the greases used in pitch bearing applications. However, this does not ensure that the selected grease is the most effective lubricant in reducing wear under the tested conditions. This uncertainty is due to some unknown relevant properties, such as additives of the lubricant. Moreover, the significant variation observed in the base oil viscosity suggests that more than one criteria is considered for the grease selection. This study does not aim to study the effect of different greases and their properties on fretting wear under pitch bearing conditions, but to compare the damage generated under dry and lubricated conditions. This is driven by the fact that normally the difference between false Brinelling and fretting corrosion is associated with the lubrication condition. False Brinelling is associated

with lubricated condition and fretting corrosion with unlubricated condition [8]. Despite an extensive investigation is not in the scope of this thesis, it is possible to discuss on the effect of the base oil viscosity. For large oscillation amplitude (larger than contact width), high viscosity base oil may reduce damage (thicker film). On the contrary, for oscillation amplitudes lower than contact area width, high viscosity oil will make things worse (cannot penetrate contact so lubrication is poor). For this experimental activity, a grease with base oil viscosity in the mid range of the reference greases presented in Table 4.3 was chosen.

Table 4.3: Selected grease properties and comparison with reference greases [40, 85].

Grease	Base oil	NLGI	Thickener	Base oil viscosity @40°C
Tested grease	Mineral	2	Lithium complex	180
Grease 1	Synthetic	2	Lithium	50
Grease 2	Ester	2	Lithium	295
Grease 3	Synthetic	1-2	Lithium complex	420
Grease 4	Mineral/Synthetic	1-2	Calcium	13
Grease 5	Mineral/Synthetic	2	Calcium complex	134
Grease 6	Mineral/Synthetic	1	Lithium complex	130

4.2.3 Testing Conditions

Testing conditions were defined to represent equivalent pitch bearing conditions. The parameters investigated in this experimental study were the oscillation amplitude, contact force, oscillation frequency, number of oscillation cycles and lubrication. The criteria to define each of these parameters are described below.

1. **Oscillation amplitude:** Despite that classic fretting wear is argued to occur for sliding ratios lower than 1.0 [36], no clear limit has been defined for complex contact interfaces such as in pitch bearings balls in contact with raceways. For this specific application, fretting wear has been reported for sliding ratios greater than 1.0 [53], [40]. In fact, it has been found that intermediate oscillation amplitudes, where the sliding ratio was about 10, produced more severe wear damage compared to actual small oscillations, where the sliding ratio was lower than 1.6 [40]. For this experimental study, the tested oscillation amplitudes were defined as 0.5 mm, 1.0 mm, 1.5 mm and 2.0 mm. This could be equivalent to sliding ratios in the range of 1.7 to 6.8 if the far-field displacement were equal to the actual contact sliding [31]. However, the actual sliding is expected to be smaller and therefore also is the actual sliding ratios, as the far-field also includes elastic

effects. The sliding distance was post-processed from the test data and presented later in this chapter.

2. **Contact force:** Fretting wear is argued to take place under high contact pressure [3]. Wind Turbine Design Guideline DG03: Yaw and Pitch Rolling Bearing Life [3] recommends a maximum contact pressure of 2.4 GPa to avoid the occurrence of fretting wear under mean operating conditions. It was found that the mean loading condition that caused the wear damage on the failed bearing section investigated in Chapter 3 was 20 kN. This load is equivalent to a contact pressure of 1.3 GPa under Hertzian conditions, showing that lower contact pressure could also generate fretting wear. For this experimental study, the tested contact forces were defined in the range of 50 N to 150 N. This load range is equivalent to maximum contact pressures between 1.8 GPa and 2.5 GPa.
3. **Oscillation frequency:** Small oscillations in pitch bearings take place in the range of 0.5 Hz to 2 Hz [2]. In order to keep similar oscillation speeds, frequencies between 0.5 Hz and 5 Hz were defined for the tests.
4. **Number of cycles:** The number of cycles was defined considering two criteria. Firstly, the measurement of friction had to exhibit stable and steady behaviour. Secondly, the wear scar must be well-developed to be measured. By conducting preliminary tests, it was found that these two requirements were met for tests lasted for 1500 cycles.

Considering the range of testing parameters defined above, a total of 18 tests were conducted to study the coefficient of friction. Moreover, 10 tests were carried out to obtain the wear rate coefficients. These 10 tests were performed considering different amounts of cycles to observe the wear evolution under the same testing conditions. Every test condition to study the wear rates was run for 500, 1000, 2500 and 5000 cycles. Table 4.4 and 4.5 summarise the testing parameters considered to study the coefficient of friction and the wear rate, respectively.

4.2.4 Measurement of Friction and Analysis of Fretting Loops

The main data measured from the fretting tests is the frictional force and the oscillatory distance. These two variables define the fretting loops and it is possible to derive the coefficient of friction from them by using the different methods described in Section 1.3.5. These methods are the maximum COF, mean COF, energy COF, and Geometric independent COF [49]. They were assessed to establish the most suitable method to analyse the COF from the tests presented in this chapter.

Table 4.4: Testing conditions to study coefficient of friction.

Test ID	Oscillation amplitude [mm]	Contact force [N]	Oscillation frequency [Hz]	Lubrication
Test C01	0.5	100	1.0	Dry
Test C02	1.0	100	1.0	Dry
Test C03	1.5	100	1.0	Dry
Test C04	2.0	100	1.0	Dry
Test C05	1.0	50	1.0	Dry
Test C06	1.0	150	1.0	Dry
Test C07	1.0	100	0.5	Dry
Test C08	1.0	100	2.0	Dry
Test C09	1.0	100	5.0	Dry
Test C10	0.5	100	1.0	Grease
Test C11	1.0	100	1.0	Grease
Test C12	1.5	100	1.0	Grease
Test C13	2.0	100	1.0	Grease
Test C14	1.0	50	1.0	Grease
Test C15	1.0	150	1.0	Grease
Test C16	1.0	100	0.5	Grease
Test C17	1.0	100	2.0	Grease
Test C18	1.0	100	5.0	Grease

In addition to assessing the method to obtain the coefficient of friction, it was important to take into account a common issue related to the measurement of frictional force in oscillating tests. This is the issue involving the tangential force exhibiting asymmetric behaviour. The causes of this asymmetry are not evident. They can be produced by equipment characteristics, issues with the calibration of the force sensor, or the tribosystem itself [86]. Figure 4.2a shows an idealised behaviour with symmetric tangential force in both directions of the oscillation, where a static friction force peak is observed at the change of direction and then it reduces to a steady-state kinetic friction force [86]. Figure 4.2b shows an illustration of the asymmetry in the tangential force. This behaviour was addressed when defining the most suitable method to derive the coefficient of friction.

Fretting loops provide not only the information to calculate the COF but they also enable the post-processing of other results, such as the sliding distance and the dissipated frictional energy [36]. The sliding distance corresponds to the fretting loop width measured when the tangential force is equal to zero. The dissipated frictional energy is the area enclosed in every fretting loop. Figure 4.3 shows a scheme of these results that can be extracted from the analysis of the fretting loops.

Table 4.5: Testing conditions to study wear rates.

Test ID	Oscillation amplitude [mm]	Contact force [N]	Oscillation frequency [Hz]	Lubrication
Test W01	1.0	100	1.0	Dry
Test W02	2.0	100	1.0	Dry
Test W03	1.0	150	1.0	Dry
Test W04	1.0	100	2.0	Dry
Test W05	1.0	100	5.0	Dry
Test W06	1.0	100	1.0	Grease
Test W07	2.0	100	1.0	Grease
Test W08	1.0	150	1.0	Grease
Test W09	1.0	100	2.0	Grease
Test W10	1.0	100	5.0	Grease

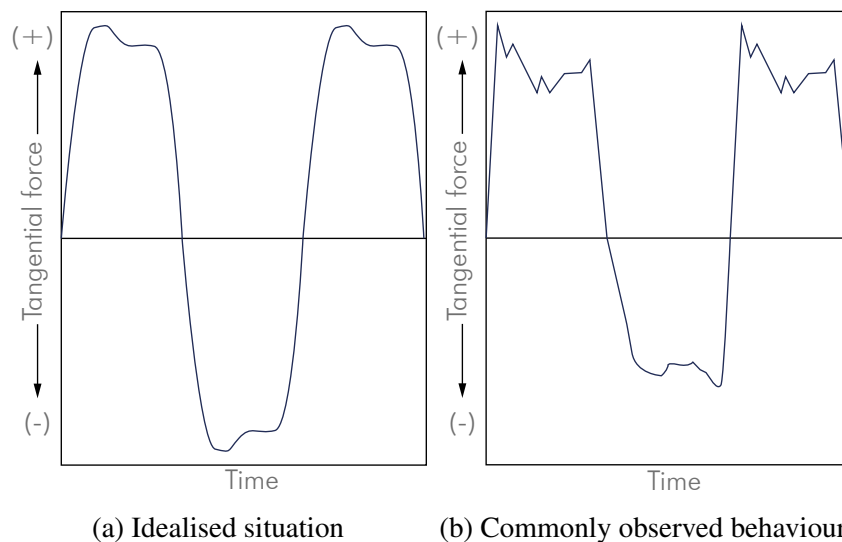


Figure 4.2: Example of asymmetric behaviour of tangential force.

4.2.5 Measurement of Wear Scars

The wear scars generated during every test were measured using the Alicona following the same procedure presented in Section 3.2.3. Wear profiles along both principal axes of a wear scar were post-processed to obtain the maximum wear depth. The wear volume was also measured using the *Soap Film* calculation method included in the software Alicona MeasureSuit 5.3. The principle of the Soap Film calculation method consists in covering the object with a slight bulge without including the areas that surmount the selected area [74]. This method considers that any material above the reference plane used for the measurement of the wear volume is

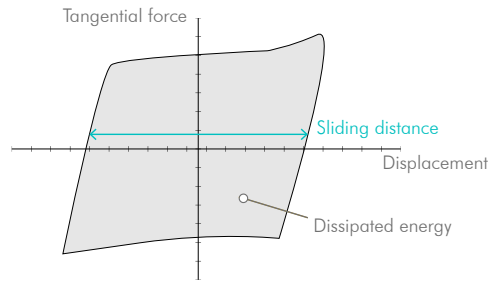


Figure 4.3: Analysis of a fretting loop to derive sliding distance and dissipated frictional energy.

transferred material from the ball or debris [31]. Figure 4.4 shows schematically how the wear volume is measured with the Soap Film method.

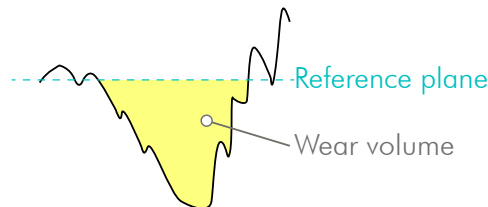


Figure 4.4: Scheme of wear volume calculation with the Soap Film method.

To understand the wear mechanisms the wear scars were also analysed under the optical microscope and SEM using a similar procedure as previously described in Section 3.2.2.

4.2.6 Derivation of Wear Rates

The wear rates were estimated by employing the energy description proposed by Fouvry et al. [36] and explained in Section 1.3.3.

The volume wear rates α_v were estimated by calculating the slope of the linear trend in a plot of the wear volume versus accumulated frictional energy, as shown in Figure 4.5a. The wear volume was measured with the Alicona for all the tests presented in Table 4.5 and the accumulated frictional energy was calculated from the measured fretting loops.

Similarly, the local wear rates α_h were estimated by calculating the slope of the linear trend in a plot of the wear depth at the centre of the wear scar versus the accumulated frictional energy density at the same location Ed_{h0} , as shown in Figure 4.5b. The wear depth was measured from the wear profiles, and the accumulated frictional energy density was calculated using the analytical expression of Equation 4.1 [36].

$$Eh_{h0} = \begin{cases} 2q_0a(e(1-e^2)^{1/2} + \arcsin(e)), & \text{if } e < 1, \\ q_0a\pi, & \text{if } e \geq 1 \end{cases} \quad (4.1)$$

Where q_0 is the maximum shear stress at the contact centre, a is the contact radius and e the sliding ratio. Equation 4.1 assumes unidirectional sliding and Hertzian conditions [36]. It is worth mentioning that the maximum energy density is a function of the sliding ratio when $e < 1$, but when $e \geq 1$ it is independent of the sliding amplitude and remains constant.

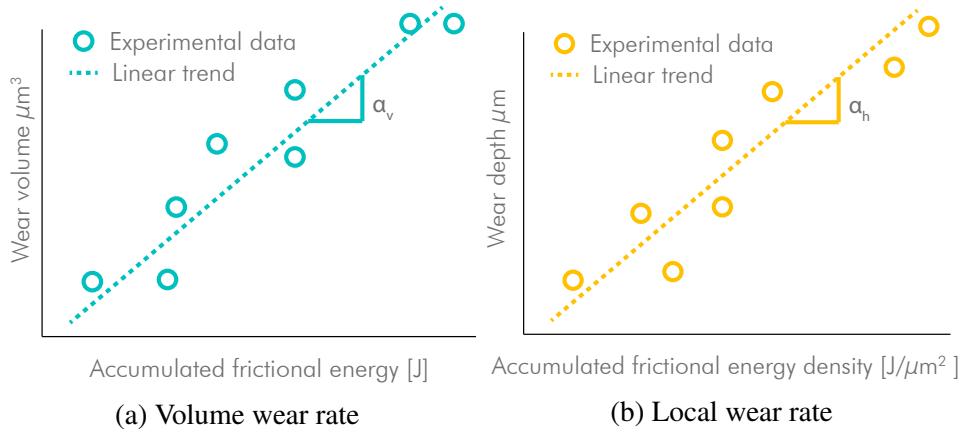


Figure 4.5: Schematic of wear rates calculation.

4.3 Results

4.3.1 Preliminary Tests

A series of preliminary tests were conducted to validate the proposed testing methods. The first tests were related to the ball holder. The ball holder allows the ball to rotate and slide. However, the ball movement was not a controlled variable during the tests. For example, it was possible that the ball got stuck within the holder and worked under pure sliding. Therefore, it was necessary to check that this holder produced different results than that using a holder for pure sliding with the ball fully fixed inside of it. For this purpose, tests C01 to C04, which considered four oscillation amplitudes, were conducted with both holders for a reduced number of cycles of 900. The results of these preliminary tests are presented in Figure 4.6. It can be seen that under pure tangential fretting, the COF was highly influenced by the oscillation amplitude, whereas under rolling-sliding, its variation was comparatively lower. These results validate the effect of using a holder that allows rotation and sliding.

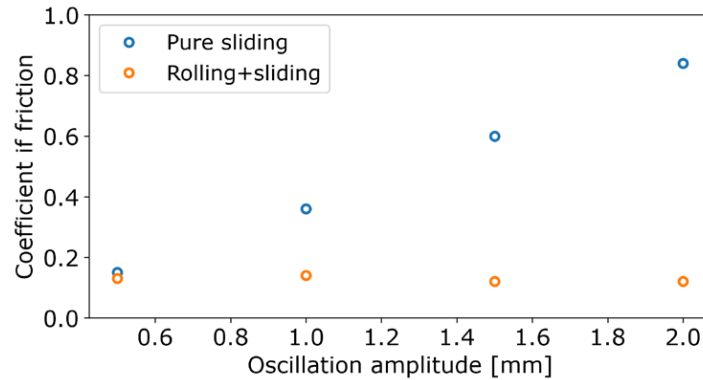


Figure 4.6: Comparison of measured COF versus oscillation amplitudes under pure tangential fretting and rolling+tangential fretting.

The second series of tests was carried out to assess the repeatability of the tests. Repeatability is relevant considering the number of variables not controlled during the tests, such as temperature, humidity or friction between the ball and the ball holder. Figure 4.7 shows the measured coefficient friction for test C02 repeated three times. High variability in the first 400 cycles can be observed from the results. However, the variability was reduced after that initial amount of cycles.

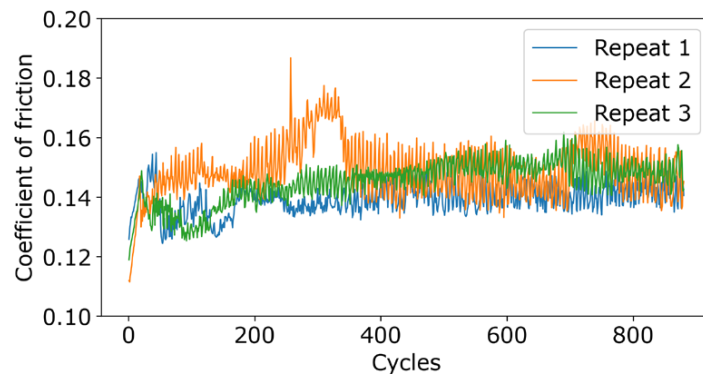


Figure 4.7: COF measured for test C02 repeated three times (1 mm - 100 N - 1 Hz).

4.3.2 Fretting Loops

Fretting loops were plotted and analysed for all the performed tests. A first analysis of the fretting loops reveals information related to the frictional behaviour, the slip regime and the sliding distance. Figure 4.8 shows four examples of measured fretting loops. Most fretting

loops showed open stable shape corresponding to the gross sliding regime [34]. The only test with a different behaviour was the test with an oscillation amplitude of 0.5 mm. The fretting loops for this test began with a partially open shape and then became completely closed before reaching the first hundred cycles. This behaviour corresponds to partial slip regime.

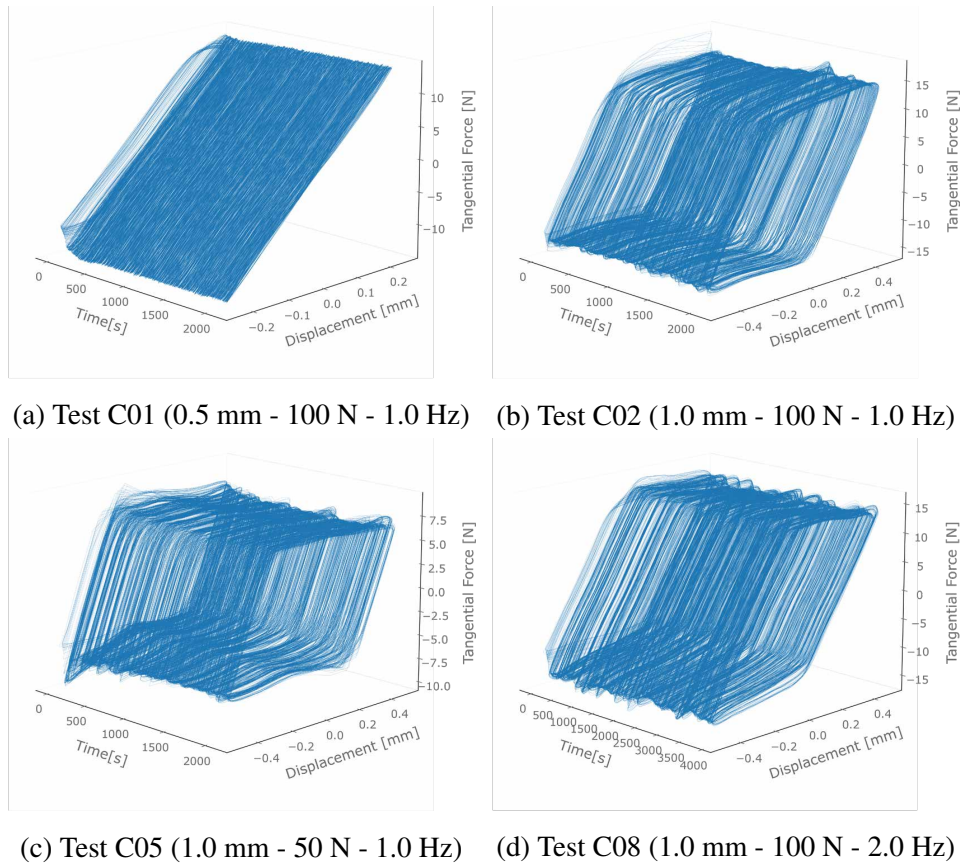


Figure 4.8: Measured fretting loops for tests C01, C02, C05 and C08.

To analyse the effect of the different operating parameters on the fretting loops, they were plotted at different cycle numbers, the 10th, 100th, 500th and 1000th cycles. Figure 4.9, 4.10, and 4.11 show the fretting loops obtained for different oscillation amplitudes, contact forces and oscillation frequency, respectively. These fretting loops correspond to the dry condition, tests C01 to C09 presented in Table 4.4. Grease lubricated tests exhibited similar behaviour.

The analysis based on the observation of the fretting loops provides an initial understanding of the effect of the tested parameters on the sliding distance and frictional behaviour. For instance, the sliding distance, corresponding to the loop width, increases with the oscillation amplitude, which is an intuitive result. The behaviour of the sliding distance under different contact forces is not as intuitive, as the fretting loop width decreases when the contact force increases. This behaviour suggests that a certain higher contact force could change the slip

regime from gross sliding to partial slip. This observation is in agreement with the study conducted by Fouvry et al. [36] where different transition criteria between partial slip and gross slip regimes were investigated. It was argued that not only the oscillation amplitude was a relevant variable when defining the sliding transition criteria [87], but also the contact force. The frictional behaviour could be also studied from the shape of the fretting loops. However, only small variations were observed. An in-depth analysis of the coefficient of friction and the effect of the different testing parameters is presented in the next section.

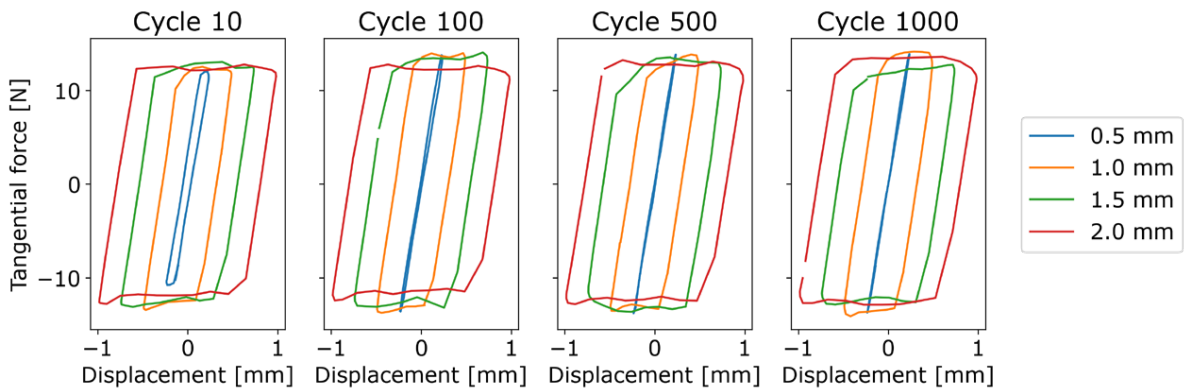


Figure 4.9: Fretting loops under different oscillation amplitudes (100 N - 1 Hz).

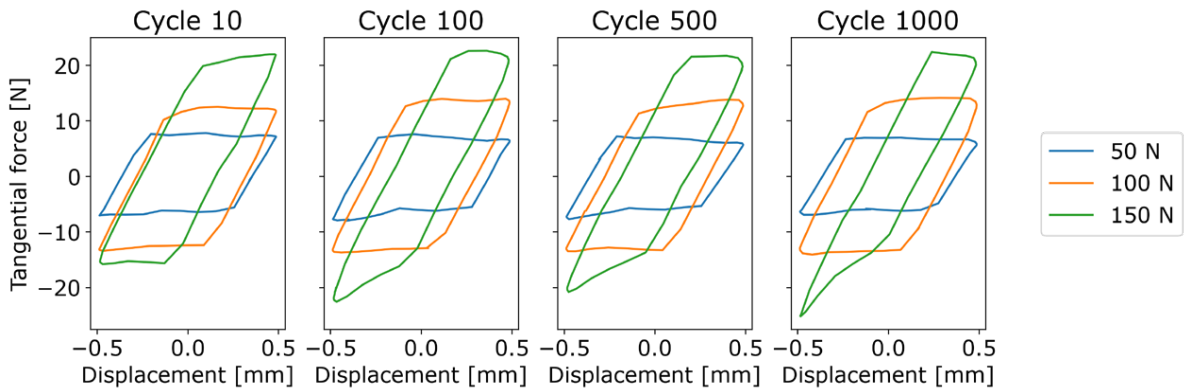


Figure 4.10: Fretting loops under different contact forces (1 mm - 1 Hz).

4.3.3 Coefficient of Friction

Before starting to analyse the effect that the different operating parameters have on the coefficient of friction, the method to calculate the COF needed to be defined. Firstly, the raw data of

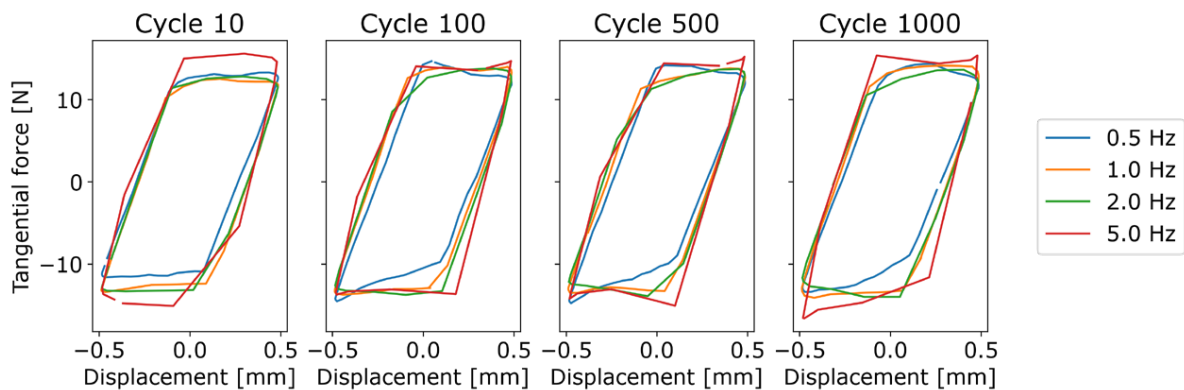


Figure 4.11: Fretting loops under different oscillation frequencies (1 mm - 100 N).

the measured tangential force was studied. Figure 4.12 shows a sample of the tangential force and it can be observed that the maximum and minimum values are symmetric, but the data shows some minor differences in the peak shapes. This indicates that the possible asymmetry discussed in Section 4.2.4 in the frictional force measurement is not an issue in these tests. A Python code function was developed to calculate the COFs as well as to analyse the fretting loops. The code is included in Appendix A.

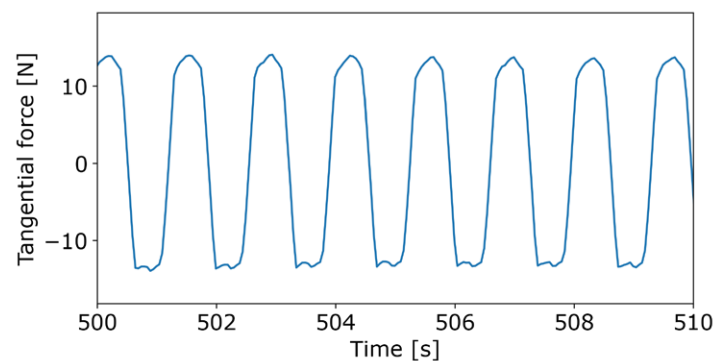


Figure 4.12: 10 s sample of tangential force signal measured in test (1 mm - 100 N - 1 Hz).

The four methods for the calculation of the coefficient of friction, presented in Section 1.3.5, were compared for tests C02, C03 and C04. Test C01 was excluded because the partial slip regime exhibited by this test made it numerically impossible to calculate the Geometry Independent COF (GICOF). Figure 4.13 shows the results of the comparison for the four different methods. The COFs calculated by the four methods show a small variation of 5% on average. The mean COF and the energy COF are almost identical. These small differences can be explained due to the symmetric behaviour of the tangential force and the stable behaviour

of the COF over time, as shown in Figure 4.7. This stable behaviour allows the mean value of the measured COF over time to be considered for the study of the effect of the different operating parameters presented in Figure 4.14. Note that the mean COF was used for the rest of the analysis presented in this work.

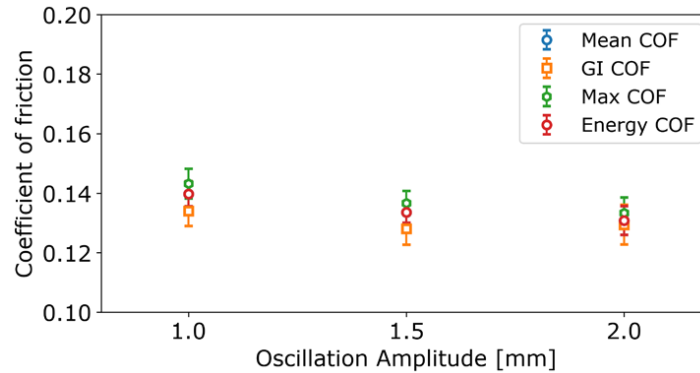


Figure 4.13: Comparison of four calculation methods for the COF.

After assessing the repeatability of the tests and defining the method to calculate the COF, the effect of the oscillation amplitude, contact force, oscillation frequency and lubrication on the COF was investigated. Figure 4.14 presents the plots of the COF versus these parameters. The oscillation amplitude, contact force and oscillation frequency only produced small variations on the COF comparable to the variations observed when the repeatability of the tests was assessed. These results suggest that none of the three variables within the analysed range produced a significant effect on the COF. The lubrication showed a more noticeable effect; the tested greased reduced the COF by 10% on average.

4.3.4 Sliding Distance

The sliding distance, corresponding to the distance at the zero tangential force crossing in the fretting loops as shown in Figure 4.3, was post-processed for all the tests presented in Table 4.4. As the shape of the fretting loops remained stable during most of the testing time, it was possible to use the average sliding distance to compare the effect of the different investigated parameters. Figure 4.15 presents the calculated sliding distance under the different testing conditions. The Python code function developed to calculate the sliding distance is included in Appendix A.

The sliding distance increased linearly with the oscillation amplitude. If the load and the system stiffness do not change, increasing the oscillation amplitude makes the fretting loop wider and therefore the sliding distance increases, which was clearly observed in Figure 4.9.

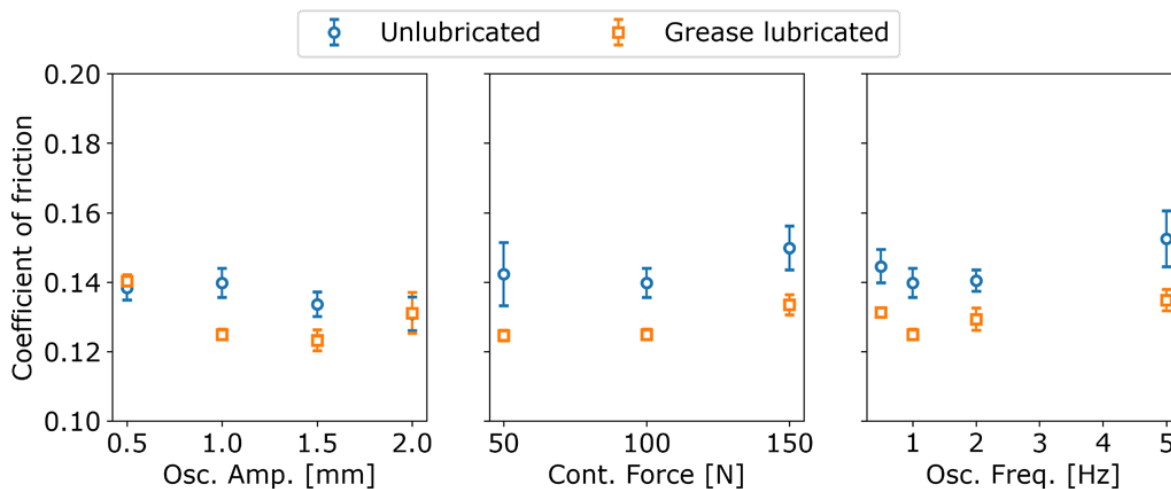


Figure 4.14: COF under different testing conditions.

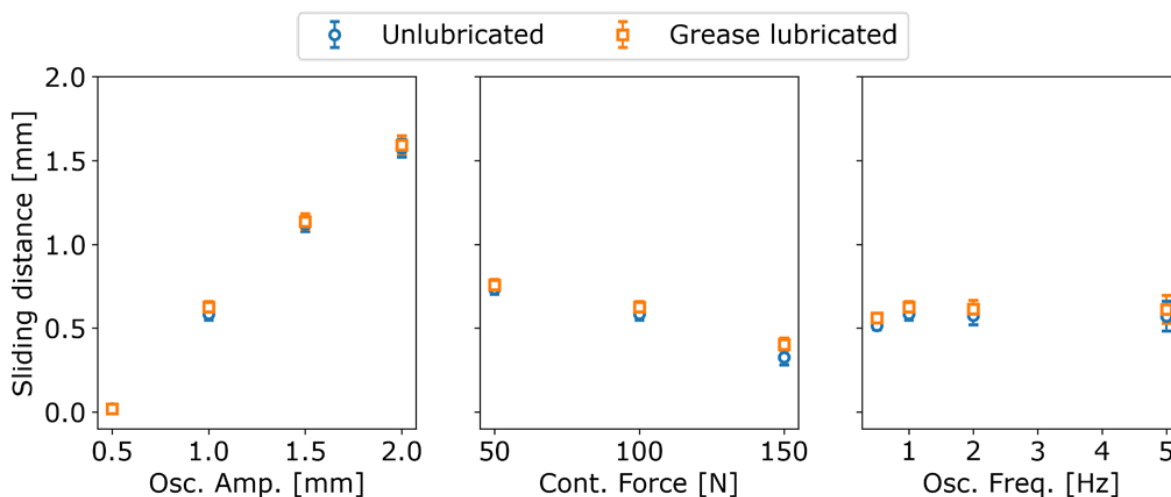


Figure 4.15: Sliding distance under different testing conditions.

The increase of the contact force produced a decrease of the sliding distance. This results was already analysed from the observation of the fretting loops, as show in Figure 4.10. The variations produced by different oscillation frequencies are small and its effect is not relevant in the range of tested frequencies. Regarding the effect of the lubrication, as it was found that the grease reduced the COF, it would be expected also an effect on the sliding distance. However, the reduction of 10% in the COF did not produced a significant variation of the sliding distance.

4.3.5 Frictional Energy

The dissipated frictional energy corresponds to area inside the fretting loops, as shown in Figure 4.3. The area inside the fretting loop was calculated by applying a numerical integration method called trapezoidal rule [88]. The code was developed in Python is included in Appendix A. The results of the average dissipated frictional energy per cycle under different testing conditions are summarised in the plots presented in Figure 4.16.

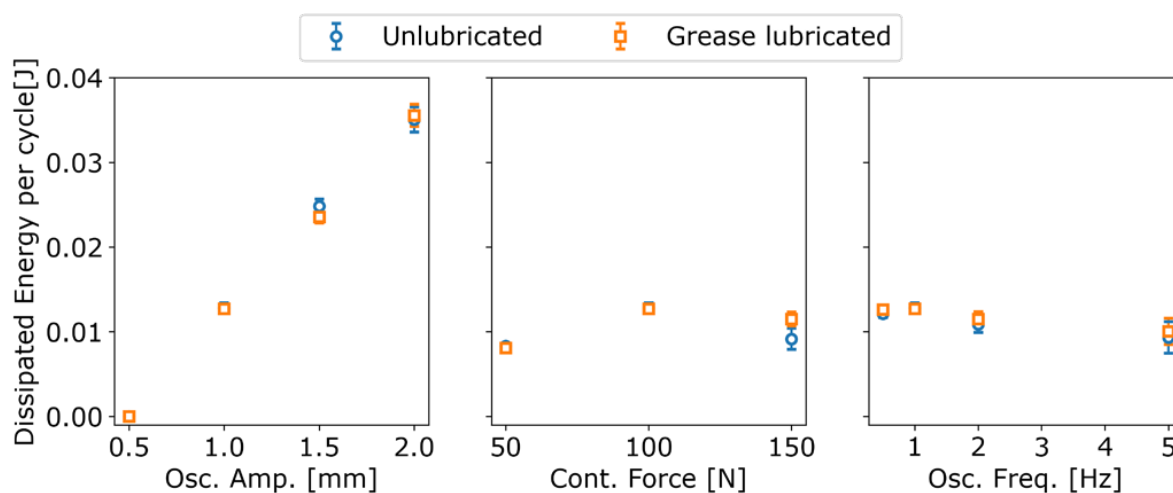


Figure 4.16: Dissipated energy under different testing conditions.

The dissipated frictional energy increased linearly with the increasing oscillation amplitude. The reason of this behaviour is the same as previously explained for the analysis of the sliding distance. Increasing the oscillation amplitude and keeping the contact force and system stiffness constant makes the fretting loops wider. Therefore, the area inside also increase. When analysing the behaviour of the frictional energy under an increasing contact forces, it can be observed an increase of the energy, followed by a decrease. This behaviour is produced by two opposite effects. Firstly, the increase of the contact force decreases the sliding distance, making the fretting loop thinner; and secondly, the increase of the contact force increases the tangential force, making the fretting loop larger in the vertical axis. At low contact forces, the effect on the tangential force is larger, but it reaches a turning point where the effect of the contact force on the sliding distance becomes more relevant. The influence of the oscillation frequency on the dissipated frictional energy is again not significant in the range of the tested frequencies.

4.3.6 Wear Damage

The wear damage was observed by SEM and measured with the Alicona. Figure 4.17 shows the wear scars for two representative tests, C06 and C15. The wear mechanism observed in the wear scar produced by test C06 is mostly adhesion, as shown in Figure 4.17a. Figure 4.17b shows the wear scar of test C15 and it exhibits a combination of adhesion of abrasion. Test C15 was carried out under grease lubricated condition, and after the completion of the test, debris was found trapped in the grease, as shown in Figure 4.18, which may act as third-body in the abrasion mechanism. Another interesting observation from the analysis of the wear scars was the absence of oxidation products in most of the tests. This can be explained due to the small contact area size [27] with a radius of approximately $150\ \mu\text{m}$.

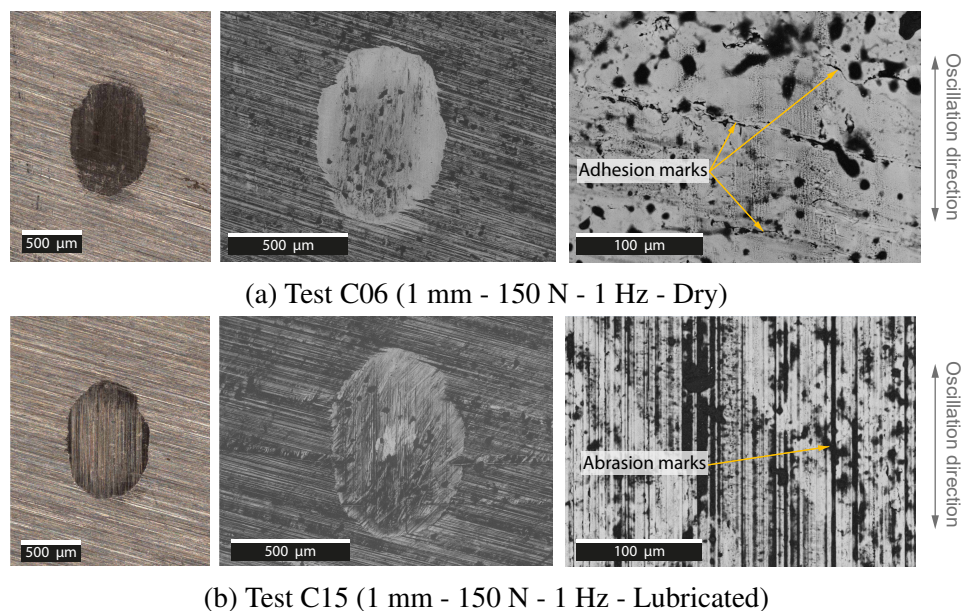


Figure 4.17: Optical surface measurements and SEM images for tests C06 and C15.

The surface measurements also allow the analysis of the shape of the wear scar profiles. Figure 4.19 presents the measured 3D surfaces and wear profiles along both main axes in tests C02 and C11. Along the width and length, u-shaped profiles can be observed. These tests were identified under gross slip regime and this regime is associated with a u-shaped wear scar profiles [35].

Figure 4.20 presents the maximum wear depth under different testing conditions. When looking at the effect of the oscillation amplitude, it can be observed that for amplitudes greater than 1 mm, the wear depth remained constant. These results suggest that the maximum wear depth increases with the oscillation amplitude in the partial slip regime and reaches an upper limit when the transition criterion between partial slip and gross sliding is reached. The wear

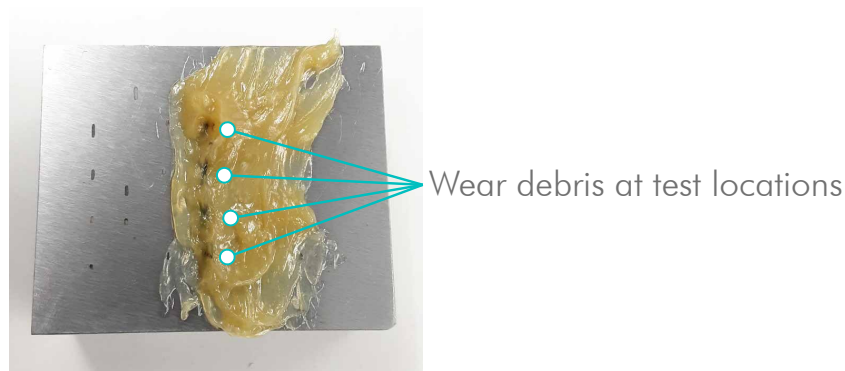


Figure 4.18: Greased lubricated samples after completed tests showing debris trapped in the grease.

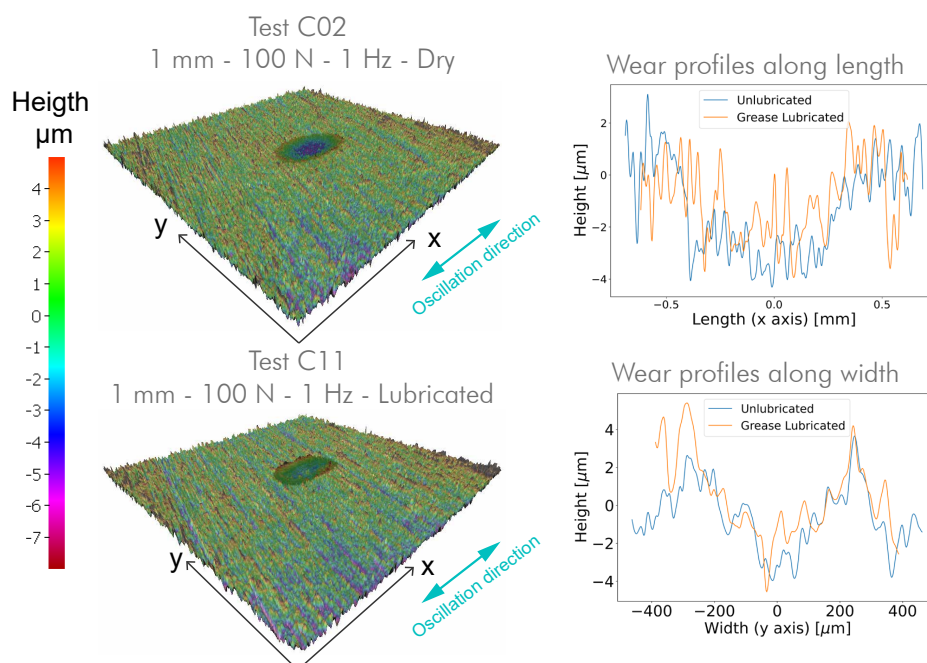


Figure 4.19: Wear profiles from tests C02 and C11.

does not continue increasing under gross slip because a given point on the worn surface becomes unexposed during an oscillation and does not accumulate more frictional energy density when the sliding distance is greater than the contact area width. Different transition criteria have been defined [89–91]. These different methods establish the threshold oscillation amplitude between 0.5 mm and 1.0 mm for the tested conditions, which agrees with the observed behaviour in this study. The wear depth showed a linear increasing relationship with the contact force. However, no clear correlation is observed between the wear depth and the frequency, and the tested grease

did not have a significant effect on the wear depth. Moreover, in some tests the grease generated a larger amount of wear, explained by the occurrence of abrasive wear under grease lubricated condition.

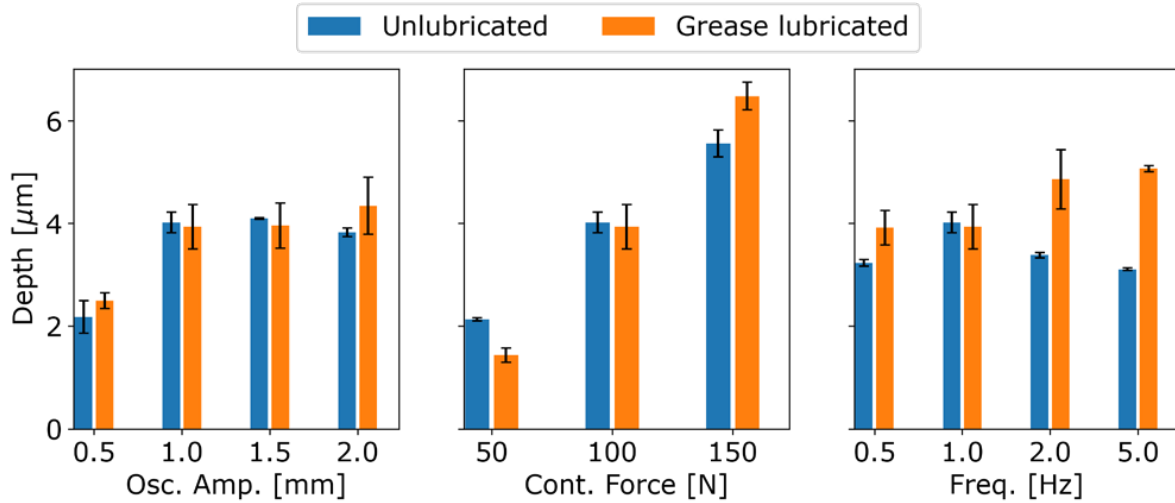


Figure 4.20: Accumulated wear depth under different testing conditions.

4.3.7 Wear Rate Coefficients

The energy description proposed by Fouvry et al. [36] was used to derive the volume and the local wear energy wear rates, α_v and α_h , respectively. The method was explained in Section 4.2.6. Figure 4.21 and 4.22 present the plots for the calculation of the volume and local wear rates, respectively. The results are also summarised in Table 4.6. The data of these plots was obtained from the results of the tests presented in Table 4.5.

Table 4.6: Wear volume rate and local wear rate by energy analysis.

	Dry	Lubricated	Difference [%]
Volume wear rate α_v [$\mu\text{m}^3/\text{J}$]	57025.1	33354.0	-41.5%
R^2 for α_v	0.91	0.81	-
Local wear rate α_h [$\mu\text{m}^3/\text{J}$]	1118.0	1067.0	-4.4%
R^2 for α_h	0.91	0.86	-

The volume wear rate for grease lubricated tests is 42% lower than the volume wear rate obtained for unlubricated tests. The linear trend of the wear volume versus the accumulated frictional energy presented in Figure 4.21 intersects the energy axis at zero, which means there is no energy threshold associated with the formation of a tribologically transformed structure.

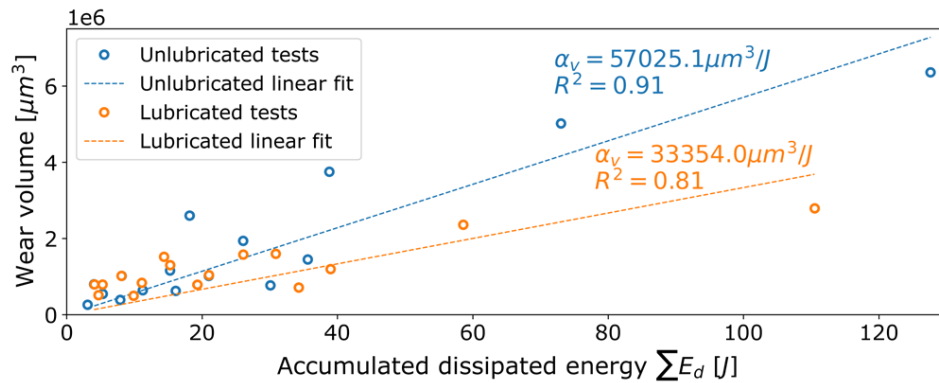


Figure 4.21: Wear volume rate by energy analysis.

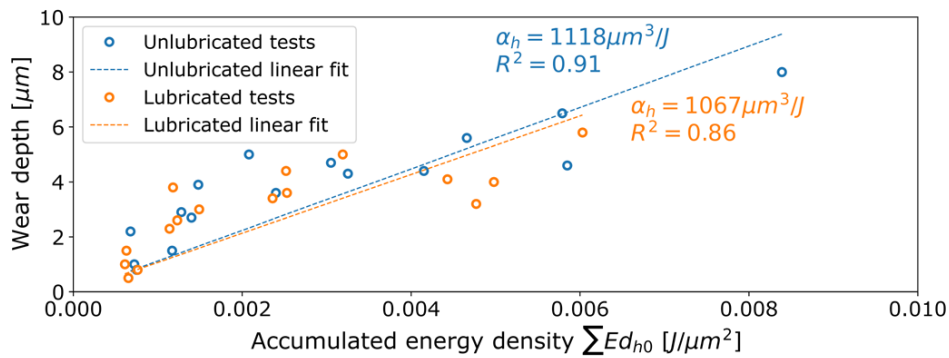


Figure 4.22: Local wear rate by accumulated energy density analysis.

For the local wear rate, the difference between grease-lubricated and unlubricated tests is only 4%, which is consistent with the results presented in Figure 4.20, where it has been found that grease has almost no effect on the wear depth.

4.4 Discussion

The discussion of the results presented in this chapter focuses on answering the question to what extent the results obtained with this downscaled experimental setup can be representative and applicable for the actual application which is fretting wear in pitch bearing under small-amplitude oscillations.

To answer that question, it is necessary to understand the differences and limitations of the proposed experimental setup. The first aspect is related to the kinematics of the ball. In a pitch bearing, each ball is in contact with two grooved circular raceways and the contact points are at an angle different than zero, making the ball movement composed of multi-axial

rotation, rotation and spinning. In this rolling ball-on-flat configuration, the movement is only composed of uni-axial sliding and rolling. This difference results in a different slip distribution and generates different wear profiles to that observed in the raceway surfaces of pitch bearings [43, 27, 84].

The second difference that limits the results presented in this chapter is associated with the size of the contact area. The circular contact area with the ball of 9.5 mm is approximately 0.07 mm^2 for a load resulting in a contact pressure 2.1 GPa, while for a ball of 45 mm diameter in a 2-metre diameter pitch bearing, the elliptical contact area is 250 mm^2 for an equivalent load. The difference in the contact area size affects the tribological behaviour of the contact surfaces, as there are different wear mechanisms involved. Particularly, the contact area size affects the oxidation taking place during the fretting wear [27].

The last difference limiting the results relates to the testing conditions. All the tests were conducted under constant amplitude and constant contact force. A variable oscillation amplitude, as it occurs in pitch bearings can have a positive effect on lubrication, due to redistribution of the grease by a larger oscillation [92, 93]. The variable loads, produced by the dynamic nature of variable wind speeds and operation controls in wind turbines can result in radial fretting. However, radial fretting is associated with elastic slip that takes place when the contact bodies have different elastic properties [94]. This is not the case, since the flat sample and the ball are made of very similar steels.

Considering the limitations of the experimental setup, it is possible to evaluate the main results of this chapter. The coefficient of friction should not change under different contact geometry or slip distribution if the operating conditions are under gross sliding since this regime is characterised by a stable frictional behaviour [35]. The results of wear damage would change if the geometry were modified. However, the effect concerning the different tested parameters should not vary significantly. For example, the fact that the wear depth remained constant under larger oscillation amplitudes should be still valid if the operating condition is under gross sliding. However, it is not clear whether the calculated wear rates would be valid for a different contact geometry, as previously discussed the contact geometry may affect the wear mechanisms involved in fretting. Finally, the effect of lubrication is difficult to extrapolate to different testing conditions and contact geometries, because all the tests were performed under constant amplitude, which is probably the less favourable condition for test lubrication.

4.5 Conclusions

This chapter proposed a downscaled experimental approach to study fretting wear under pitch bearing conditions using a standard commercial tribometer. The key conclusions drawn from the experimental results are:

- Test parameters representing pitch bearing operating conditions were investigated, including oscillation amplitude, contact force, oscillation frequency, number of oscillation cycles and lubrication.
- The COF exhibited a stable behaviour without significant dependence on the testing parameters. The tested grease reduced the COF by 10%.
- Wear damage remains constant for amplitudes greater than 1 mm and the relationship between the load and the wear depth is linear.
- Application of grease reduces the volume wear rate by 42%, but has almost no effect on the local wear rate and wear depth.

These results provide a good understanding of fretting under pitch bearing operating conditions, but not all the results are valid to actual pitch bearings as different wear mechanisms are involved and scale of the contact area is also a relevant factor.

The limitations identified will be considered to design a medium-scale fretting test rig that is presented in the next chapter.

Chapter 5

Design and Experimental Study of a Medium-Scale Fretting Test Rig

5.1 Introduction and Aims

The small-scale experimental study presented in the previous chapter provided valuable results to understand fretting wear under pitch bearing operating conditions. However, its limitations were also identified; being the kinematics of the ball and the contact area size two of the main reasons why those results and conclusions cannot be directly applied to the actual application. The review of different experimental setups presented in Chapter 1.3 showed that the same limitations have been found in other studies using small-scale test rigs.

This chapter presents the design and manufacturing of a medium-scale test rig that overcomes the limitations found using a standard small-scale tribometer. An experimental study was carried out to investigate the same parameters studied in the previous chapter using this bespoke medium-scale test rig by defining equivalent testing conditions.

The analysis of the results of this second experimental study on fretting under pitch bearing operating conditions makes it possible to determine which results of the small-scale experimental setup are valid and not affected by the scale of the tests and the limitations of the ball holder. These results also provide a more in-depth understanding of the effect of the different operating and loading conditions in pitch bearings. This information can be useful to define actual scale tests, normally carried out by wind turbine manufacturers or large research institutions in the wind energy sector.

5.2 Fretting Test Rig Design

5.2.1 Aims of Fretting Test Rig

The first step to design this medium-scale fretting test rig was to define the aims as follows:

- To reproduce fretting wear under pitch bearing operating conditions in a raceway/ball contact configuration by developing accelerated tests.
- To allow the analysis of the key testing parameters affecting fretting wear: oscillation amplitude, contact force, oscillation frequency, lubrication, contact geometry and number of cycles.

5.2.2 Test Rig Requirements and Constraints

The design of the motion and load drive systems was not part of the test rig design in this study. One of the hydraulic machines available in the LEA lab at The University of Sheffield was used to develop the medium-scale fretting test rig. After assessing the equipment options available and discussing the purpose of the test rig with the technicians in charge of the lab, it was decided to use a hydraulic bi-axial machine, the Mayes 3, shown in Figure 5.1. This bi-axial machine consists of four actuators that can work under force or displacement control and static and dynamic conditions. The specifications of the Mayes 3, presented in Table 5.1, impose the main constraints for the fretting test rig design.

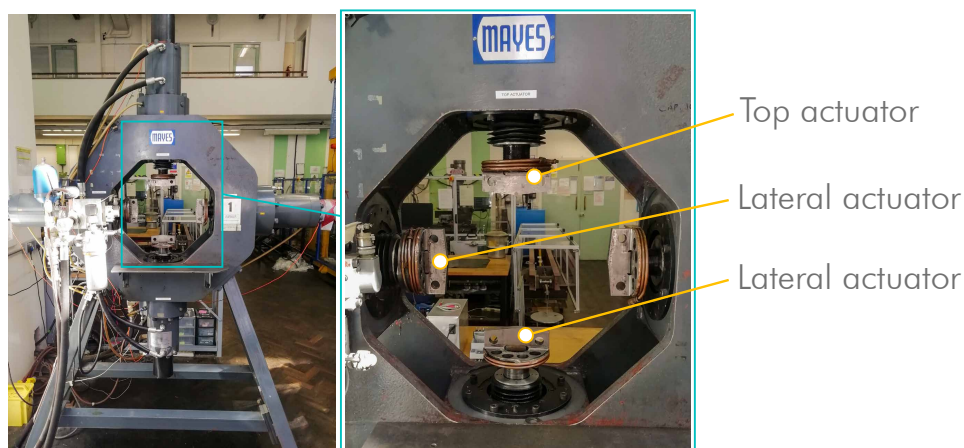


Figure 5.1: Mayes 3 bi-axial hydraulic machine used to applied the load and cyclic motion.

Table 5.2 presents the requirements for the range of testing parameters. These ranges were defined considering the same criteria as in Chapter 4 based on equivalent sliding ratios, contact

Table 5.1: Mayes 3 testing specifications.

Parameter	Value
Maximum distance between actuators [mm]	475
Minimum distance between actuators [mm]	425
Load range [kN]	0 - 100
Oscillation amplitude range [mm]	0 - 50
Oscillation frequency range [Hz]	0 - 10

pressures and oscillation speeds for pitch bearing applications. Increasing the ball diameter from 9.5 mm to 25 mm or larger resulted in a contact area being increased at least 100 times. Additionally, in this experimental study, the geometrical contact parameters were considered including the ball size and conformity. Two different ball diameters were tested under the same conformity, which required an increase of the groove radius of the test specimen. Furthermore, two different conformity values were considered by increasing the groove radius of the test specimen but with the same ball size.

Table 5.2: Testing requirements.

Parameter	Value
Oscillation amplitude [mm]	2 - 8
Contact force [kN]	10 - 30
Frequency [Hz]	1 - 2
Conformity	0.52 & 0.56
Ball diameter [mm]	25 & 28
Number of cycles	3000 - 10000

5.2.3 Contact Configuration

The kinematics of the ball was previously mentioned as one of the issues limiting the application of the results of the small-scale tests. This limitation was produced by the holder of the UMT, as the contact interface was different to that at one of the two contact points of pitch bearings. Therefore, one possible solution to this problem was to suppress the holder and make the ball oscillate between two grooved samples, similarly to an actual pitch bearing and also allowing the ball to slide and roll. However, the proposed contact geometry still has some simplifications in comparison the pitch bearing. The first simplification was suppressing the curvature of the ring; in other words, the raceway groove was straight and the oscillatory movement linear. This simplification prevented the ball from spinning. Nevertheless, the spinning effect becomes

less relevant as the diameter of the pitch bearing increases in large-scale wind turbines, a general trend in the wind industry. The second simplification was related to the contact angle. For pitch bearings, the nominal contact angle is usually 45° , and it changes during wind turbine operation [73]. The contact angle was considered equal to zero in the proposed contact configuration of the fretting test rig design. These two simplifications were motivated by the limitations of the bi-axial machine. The actuators can only move linearly and take in-plane loads. Figure 5.2 shows a scheme comparing the contact configuration in a pitch bearing and the proposed contact geometry in the fretting test rig.

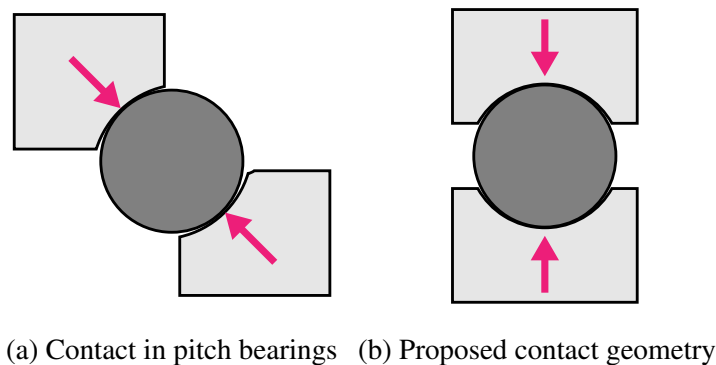


Figure 5.2: Comparison of contact geometries.

5.2.4 Design of Fretting Test Rig

Figure 5.3 presents the CAD model of the designed fretting test rig mounted in the actuator of the bi-axial machine presented in Figure 5.1 that fulfils requirements by considering the constraints described in the previous sections. The test rig was designed with three attachment parts that connect the rig to the actuators and two sample holders. The top holder is assembled to the top attachment and the bottom holder to the lateral actuator by means of bolts. The bottom holder lies and slides on the bottom attachment, where a 3 mm PTFE plate acts as a slider at the interface of these two components. The contact load is applied through the top actuator, and the oscillatory movement by the lateral actuator. The drawings of all the components of the fretting test rig with detailed dimensions are presented in Appendix B. The mechanical strength of the proposed rig design was assessed by FEA. The FEA results are presented in Appendix C.

The proposed design consisted of two 25 mm diameter balls. Two balls improve the stability of the experimental setup, which prevents any ball moving away of the force line and also increases the repeatability of the tests, as two wear scars are generated on each sample. The distance between each ball and the force line needed to be the same to ensure that each

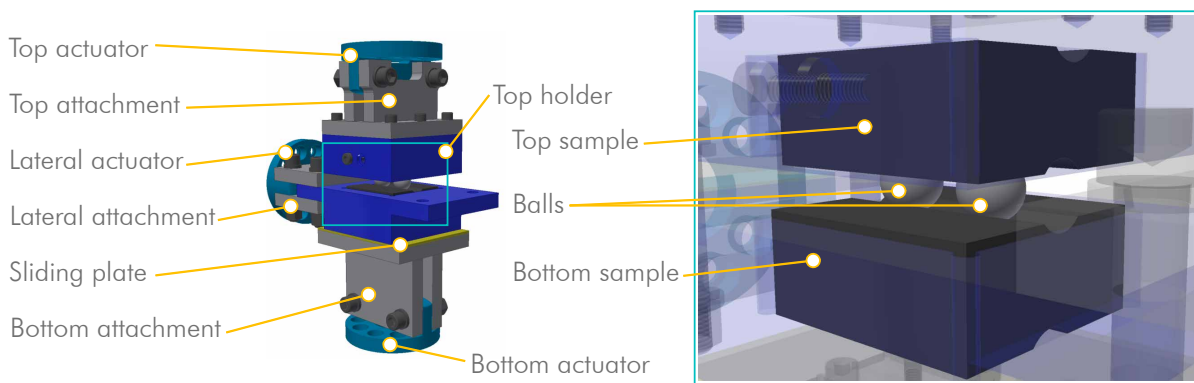


Figure 5.3: CAD model of the fretting test rig design.

ball took half of the load applied by the top actuator. This was achieved by using a 3D-printed ball positioning aid.

Suppressing the ball holder and having two samples instead of one also offered some advantages for the efficiency of the tests. Dry and lubricated contact under the same testing conditions could be tested in one single test. As a drawback, it was not possible to assess the effect of lubrication on the coefficient of friction. However, direct measurement of the friction force was not possible as explained in the next section.

Each sample had a grooved surface on the top face and another on the bottom face, which allowed each sample to be tested twice and minimised the number of samples required. Figure 5.4 shows the CAD assembly of the grooved samples and balls.

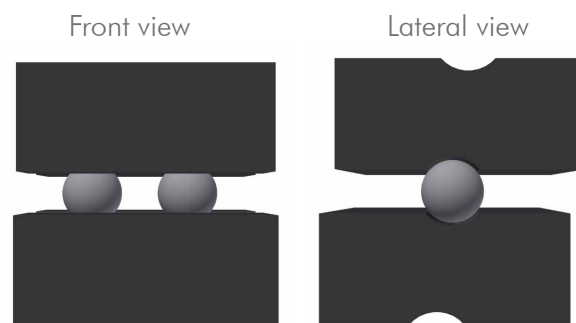


Figure 5.4: CAD assembly of samples and balls.

5.2.5 Data Acquisition

Each actuator of the bi-axial machine has a channel with a Moog digital controller [95] with an in-built function generator capable of internally logging feedback and control signals of forces

and position. Position and forces can be only measured in the axial direction. This means that the frictional force cannot be measured on the top actuator where the load is applied, as it was done on the UMT. Spatial constraints did not allow the use of an external tri-axial load cell with the required load capacity. Alternatively, the force feedback at the lateral actuator was used to measure the frictional force. However, the force measured at this actuator does not correspond only to the frictional force at the balls/raceways contacts but it also includes the inertial forces; small compared to the frictional force given the low accelerations, and the frictional force between the bottom holder and the PTFE plate. Nevertheless, the force measured at the lateral actuator could be used as a frictional indicator to compare the effect of the different testing parameters, except the lubrication as dry and lubricated tests for each set of parameters were performed simultaneously.

5.3 Materials and Methods

5.3.1 Equipment

The developed bespoke fretting test rig using the bi-axial machine was used to study fretting wear in a medium-scale configuration. Figure 5.5 shows the designed test rig mounted on the bi-axial machine.

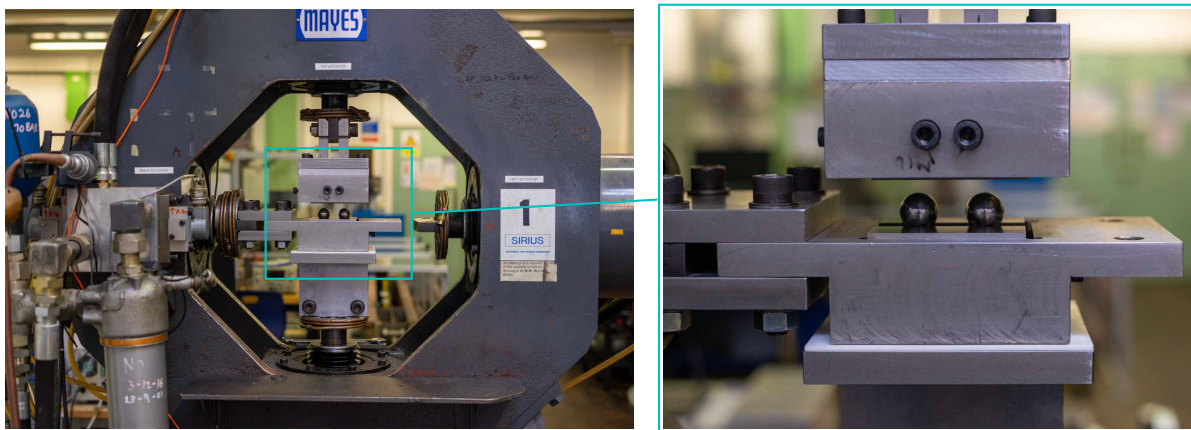


Figure 5.5: Fretting test rig for medium-scale fretting experimental study.

5.3.2 Samples and Lubrication

Unlike the samples used in the small-scale tests, the samples used in the medium-scale tests did not come from a pitch bearing section; they were manufactured from a commercial steel

bar. The previously analysed pitch bearing section was made of 42CrMo₄ steel (EN31) and the surface hardness was achieved by induction hardening. Induction hardening is a suitable heat treatment for pitch bearing raceways considering their large size, but it is not cost-efficient for the sample size used in this study. For this reason, through hardening was selected to achieve the required surface hardness because it allowed all the samples to be heat treated in the same batch. A hardness of 60 HRC cannot be achieved in 42CrMo₄ steel by through-hardening given its microstructure; thus, an alternative material had to be used for manufacturing the samples. After considering the feedback from the heat treatment provider, a tool steel O1 was chosen to manufacture the samples. Table 5.3 shows a comparison of the chemical composition of 42CrMo₄ and O1 steels [96, 97].

Table 5.3: Chemical composition comparison between 42CrMo₄ and O1 steels.

Element	42CrMo ₄	O1
Carbon	0.35-0.45%	0.95%
Manganese	0.50-0.80%	1.25%
Vanadium	-	0.20%
Chromium	0.90-1.50%	0.50%
Tungsten	-	0.50%
Molybdenum	0.20-0.40%	-
Silicon	0.10-0.35%	-

The manufacturing process of the samples consisted of four main steps. Firstly, the steel bar was sectioned to the required dimensions. Secondly, the samples were sent for heat treatment. Then, the samples were processed for facing and grooving by Electrical Discharge Machining (EDM). Finally, the grooved surfaces were manually polished with P1200 grit paper to remove the rusty appearance produced by the EDM cutting. Balls used in the tests were AISI 52100 grade 100 with a diameter of 25 mm and 28 mm. The grease applied was the same used in the small-scale tests on the UMT, whose properties were presented in Table 4.3. Figure 5.6 shows a manufactured sample with the balls. Table 5.4 summarises the relevant properties of the samples. Regarding the surface roughness of the sample, a $R_a = 1.6\mu m$ corresponds roughly to the upper limit of the roughness range normally required for pitch bearings.

Using a different material for manufacturing the samples certainly had an impact on the results, even if the surfaces of the samples have the same hardness. Wear properties are not only a function of the surface hardness. Bourithis et al. [98] compared the wear properties of two tool steel when subjected to different wear modes, O1 and D1 with the same hardness (60 HRC), and found those steels to show different wear properties. For instance, O1 performed well under adhesive wear at low sliding speeds. This fact means that it is likely that the wear

rates obtained using the small-scale experimental set-up on the UMT are not valid for these samples using tool steel O1. However, the material and samples proposed for the tests presented in this chapter are useful to study the effect of different test parameters on the wear damage.

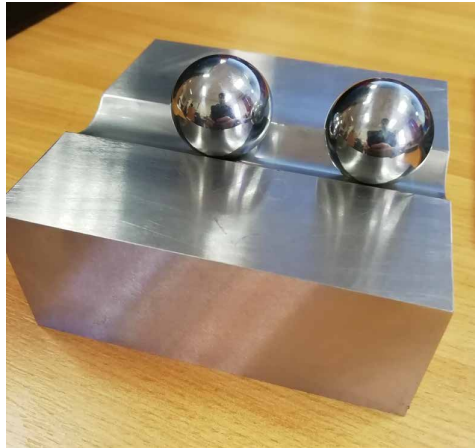


Figure 5.6: An example of manufactured samples and balls.

Table 5.4: Main properties of samples.

Property	Value
Material	AISI O1 tool steel
Surface hardness	60 ± 2 HRC
Surface finish R_a	$1.6 \mu\text{m}$

5.3.3 Testing Conditions

A total of 24 tests were conducted using the medium-scale fretting test rig. These tests consisted of 12 sets of testing parameters of oscillation amplitude, contact force, oscillation frequency, ball size, conformity and number of cycles under unlubricated and grease lubricated conditions. Table 5.5 summarises the testing conditions for the 24 tests. The maximum contact pressure and contact area width calculated based on Hertzian contact mechanics equations, and the normalised oscillation amplitude for the considered testing parameters are summarised in Table 5.6.

Table 5.5: Testing conditions for unlubricated and grease lubricated conditions.

Dry tests							
Test ID	Ball diam. [mm]	Groove rad. [mm]	Conformity	Osc. Amp. [mm]	Cont. For. [kN]	Osc. Freq. [Hz]	Cycles
D01	25	13	0.52	5.0	20	1.0	10000
D02	25	13	0.52	2.0	20	1.0	10000
D03	25	13	0.52	8.0	20	1.0	10000
D04	25	13	0.52	2.0	10	1.0	10000
D05	25	13	0.52	5.0	10	1.0	10000
D06	25	13	0.52	2.0	30	1.0	10000
D07	25	13	0.52	5.0	30	1.0	10000
D08	25	14	0.56	5.0	20	1.0	10000
D09	28	14.56	0.52	5.0	20	1.0	10000
D10	25	13	0.52	5.0	20	1.0	3000
D11	25	13	0.52	5.0	20	0.5	10000
D12	25	13	0.52	5.0	20	2.0	10000
Lubricated tests							
Test ID	Ball diam. [mm]	Groove rad. [mm]	Conformity	Osc. Amp. [mm]	Cont. For. [kN]	Osc. Freq. [Hz]	Cycles
L01	25	13	0.52	5.0	20	1.0	10000
L02	25	13	0.52	2.0	20	1.0	10000
L03	25	13	0.52	8.0	20	1.0	10000
L04	25	13	0.52	2.0	10	1.0	10000
L05	25	13	0.52	5.0	10	1.0	10000
L06	25	13	0.52	2.0	30	1.0	10000
L07	25	13	0.52	5.0	30	1.0	10000
L08	25	14	0.56	5.0	20	1.0	10000
L09	28	14.56	0.52	5.0	20	1.0	10000
L10	25	13	0.52	5.0	20	1.0	3000
L11	25	13	0.52	5.0	20	0.5	10000
L12	25	13	0.52	5.0	20	2.0	10000

5.3.4 Measurement of Wear Damage

The produced wear scars were measured with the Alicona by following the same procedure as described in Section 3.2.3 and analysed to identify their main characteristics. The wear profiles post-processed from the surface measurements were analysed to study the effect of the different testing conditions on the wear depth.

Table 5.6: Maximum contact pressure, contact area width, and normalised oscillation amplitude for the considered testing parameters.

Contact force [kN]	Max. Contact pressure [GPa]	Half contact area width b [mm]	Normalised oscillation amplitude ($x/2b$)		
			x=2 mm	x=5 mm	x=8 mm
10	2.2	0.51	1.95	4.88	7.81
20	2.8	0.65	1.55	3.88	6.20
30	3.2	0.74	1.36	3.39	5.42

Three metallographic samples were prepared following the same procedure of Section 3.2.5 to investigate the microstructural changes during the tests. The first sample was a section of annealed steel before the heat treatment, the second sample came from a heat treated section, and the last one corresponded to cross section cut from a tested sample underneath a wear scar.

5.3.5 Measurement of Friction Indicator

The displacements and forces were measured at the top and lateral actuators. This data allowed the comparison of the frictional behaviour under the different testing parameters. As previously discussed, this was not an accurate measure of the COF but an equivalent approach to the one used in actual bearings where the COF is not measured at each ball; instead, frictional torque is used as a friction indicator.

5.4 Results

5.4.1 Observation and Measurement of Wear Scars

Figure 5.7 presents the wear scars of two representative tests D01 and L01. These wear scars exhibit similar wear patterns consisting of three regions, 1, 2 and 3. Region 1 is located at both ends of the long axis of the worn area. In this region, high levels of oxidation can be observed, as well as the highest wear depth. Region 2 is located at the centre with lower levels of oxidation and less accumulated wear damage. Evidence of sliding of the ball that shifted the centre of oscillation is also observed, which explains the small amount of wear on the left of both wear scars, probably produced during the first cycles. Then, the oscillatory movements stabilised at region 3, where most the wear damage is concentrated.

The highest level of oxidation is observed at the outer region of the wear scars where the contact pressure is minimum. In addition to the oxidation, the maximum sliding takes place at region A. This sliding is mainly produced by a combination of Heathcote slip [84] and

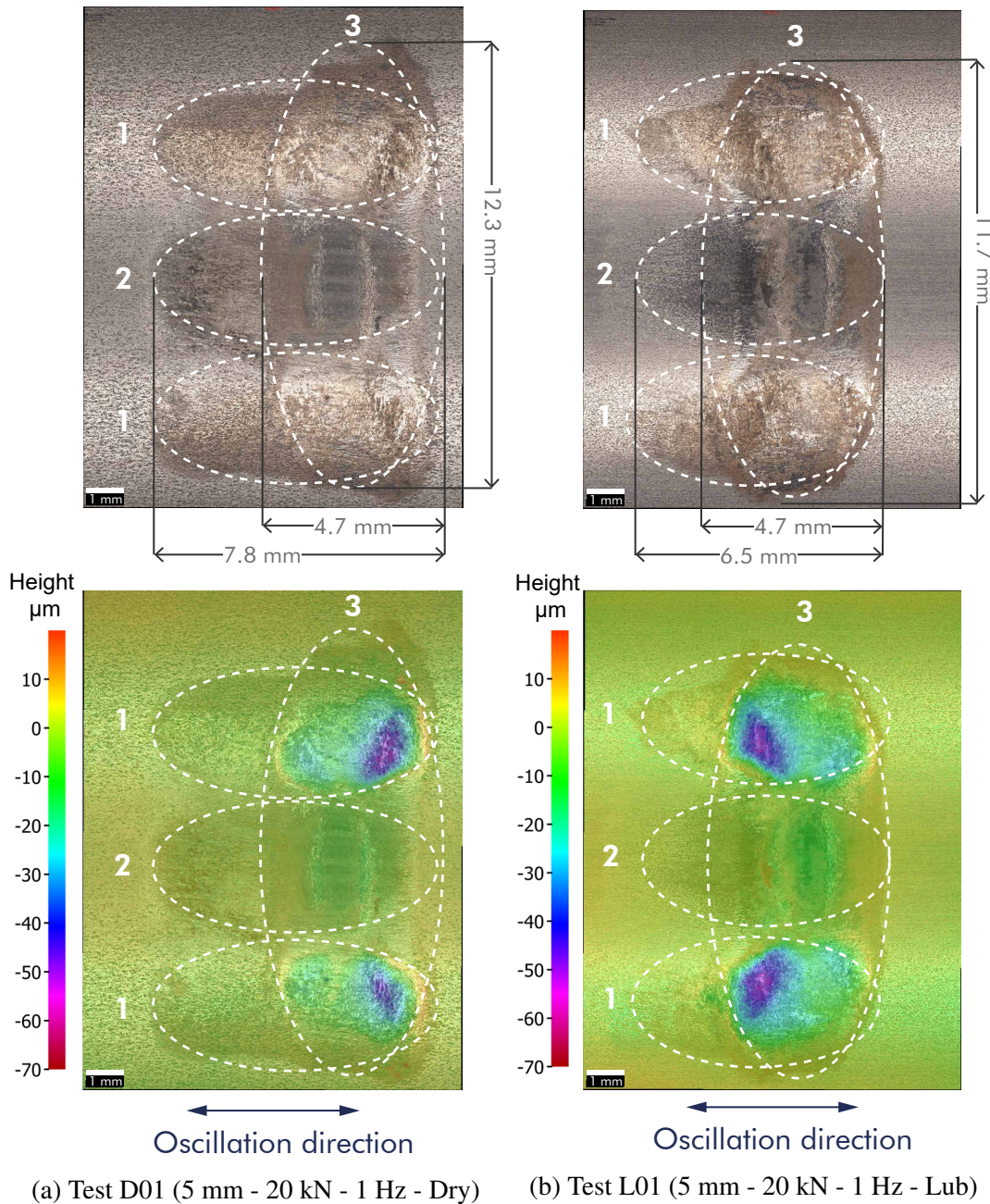


Figure 5.7: Surface measurements of tests D01 and L01 (texture and height colour maps).

elastic slip. Heathcote [84] studied microslip in closely conforming contacts of a hard ball on a grooved surface and determined that rolling without sliding is only possible along two lines of the contact area and slip was produced by the difference of surface velocities. Elastic slip results from the deformation of the two surfaces in contact to when loaded to establish the contact area. The elastic slip has been argued to be more relevant when the two bodies have dissimilar elastic properties [29]. Equations derived by Heathcote did not take into account the

elastic slip [94]. Johnson [99] considered both Heathcote and elastic slip to describe the sliding behaviour of a rolling ball on a raceway, as illustrated in Figure 5.8, and identified that sliding or microslip took place along all the contact area length, except at the narrow bands of pure rolling, and also that it was possible to have a locked region depending on the coefficient of friction.

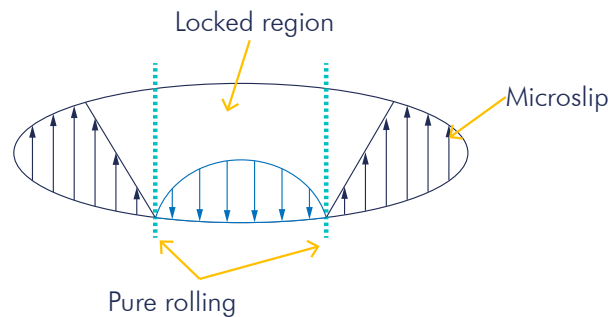


Figure 5.8: Locked and microslip regions.

The dimensions of the worn area of the test under dry condition D01 are approximately 5% larger than the grease lubricated worn area L01. Both worn areas were produced by the same ball in contact with top (dry) and bottom (lubricated) specimens during the same test. Therefore, this difference in the worn area dimensions can be attributed only to the lubricant. However, the maximum wear depth are almost the same for both tests ($60\ \mu\text{m}$).

To understand the effect of lubrication on the wear damage better, Figure 5.9 presents the wear scar profiles along the long axis of the worn area at the location of the maximum depth (A) and at the center of the wear scar (B). Both profiles show a w-shape. The main difference is that in the profile along the line A the wear is mostly accumulated at the end of elliptical contact area, while along the line B, located at the zero-crossing, smaller wear is observed at the centre. This difference suggests the presence of a locked region with no wear.

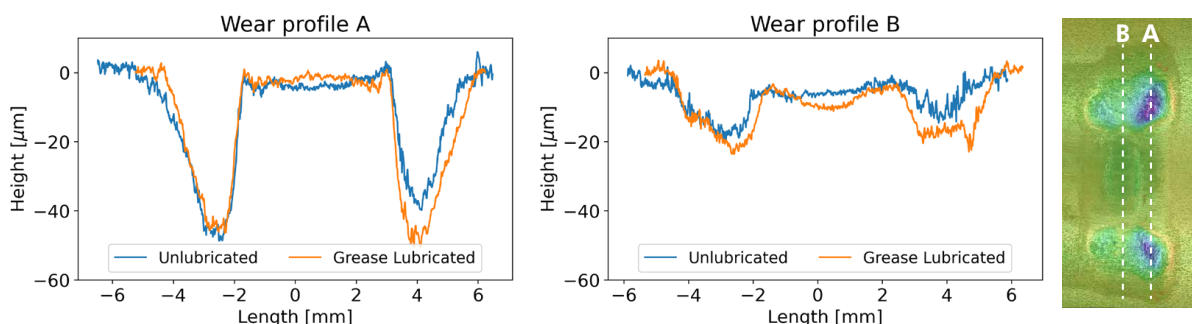


Figure 5.9: Wear profiles of tests D01 and L01 (5 mm - 20 kN - 1 Hz).

The results of the microstructure analysis are presented in Figure 5.10. Figure 5.10a depicts the microstructure of the annealed sample corresponding to a fine microstructure of cementite or iron carbide Fe_3C [98]. Figure 5.10b shows the microstructure of the heat-treated sample, consisting of tempered Martensite with small carbides [98]. Figure 5.10c shows the cross section of a tested sample just underneath a wear scar. The presence of a thin white layer just under the surface can be observed. This layer extends along the whole wear scar length and its average thickness is $6.4 \pm 1.7 \mu\text{m}$. This microstructural feature is attributed to the tribologically transformed structure [76].

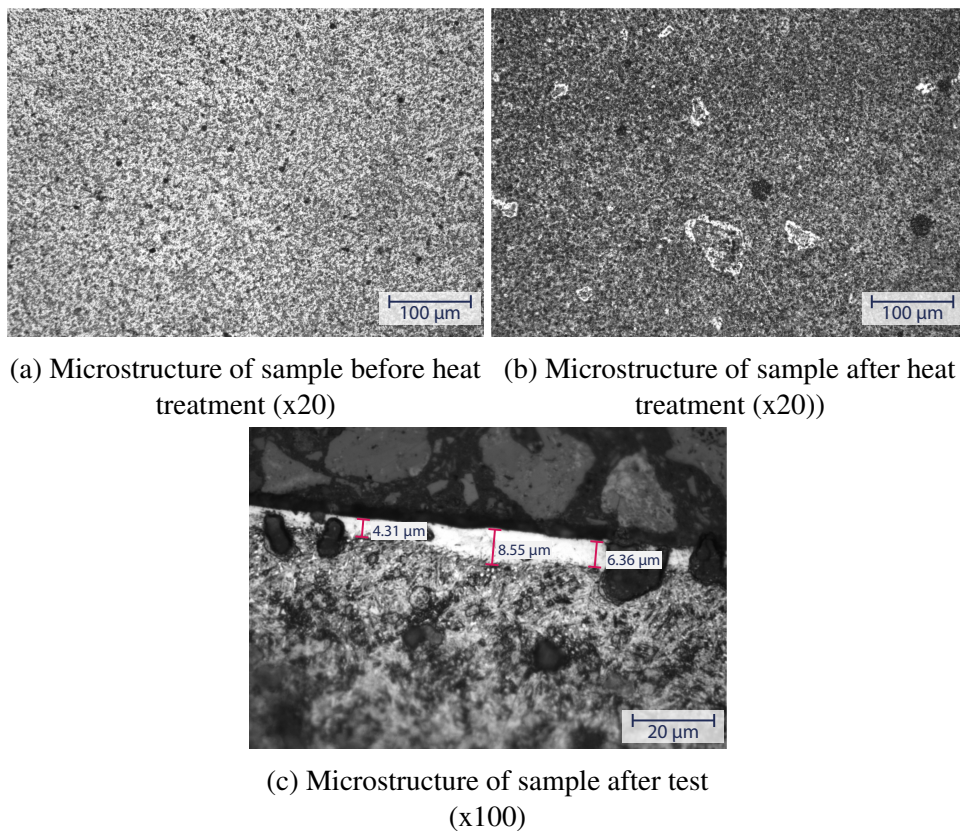


Figure 5.10: Microstructure analysis of AISI O1 steel samples under optical microscope.

5.4.2 Effect of Testing Conditions on Wear Damage

Wear scar surfaces of all tests were measured and analysed to study the effect of the oscillation amplitude, contact force, oscillation frequency, contact geometry and lubrication.

Figure 5.11 shows the maximum wear depth measured under different oscillation amplitudes. These results show a similar trend as the test on the UMT presented in the previous chapter. This is an increase of the wear depth from the smallest amplitude of 2 mm to the medium

amplitude of 5 mm. Then, from the medium to the largest amplitude of 8 mm, the wear depth remains almost constant. This confirms the existence of an upper threshold for the frictional energy density based on the sliding ratio that limits the maximum wear that a given point can accumulated per cycle if the other parameters remain unchanged [36]. These results also suggest that the transition between fretting and gross slip took place for an oscillation amplitude between 2 and 5 mm. This limit on the wear depth does not mean that the global wear damage remains constant when the oscillation amplitude limit is reached, as the extent of a wear scar produced by a larger amplitude is greater, but not deeper. In other words, larger oscillation amplitude affects only the wear volume. To illustrate this, Figure 5.12 shows a comparison for three unlubricated tests under three different oscillation amplitudes, 2 mm, 5 mm and 8 mm and the same contact force of 20 kN. Regarding the effect of lubrication, the same trend as that obtained from the tests on the UMT is also observed in these tests. The grease did not reduce the maximum wear, on the contrary, it slightly increased it. This effect was previously attributed to the grease being squeezed out of the contact in the early cycles and then only preventing the debris from being ejected, resulting in an increased and more severe wear damage.

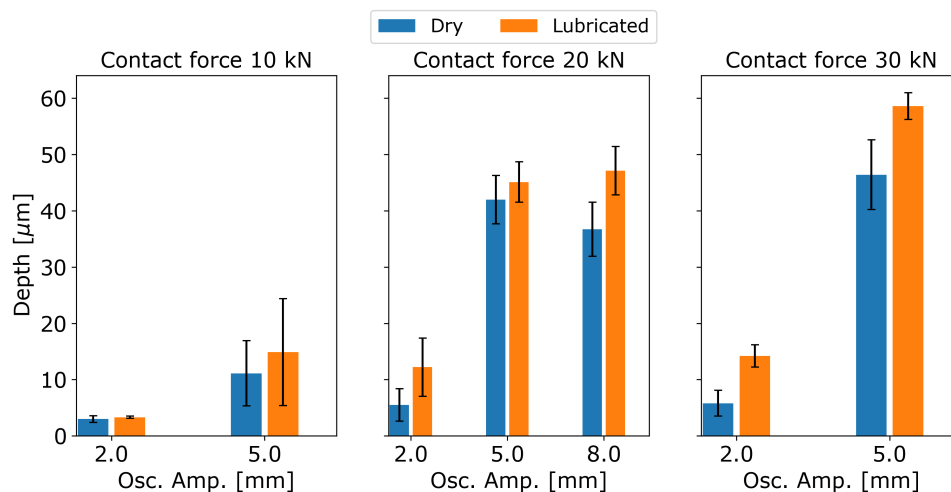


Figure 5.11: Maximum wear depth under different oscillation amplitudes.

Figure 5.13 shows the maximum wear depth under different contact forces. The wear depth increased with the contact force, but not linearly as observed in the small-scale tests conducted with the UMT. The results suggest that, under a higher load, the maximum wear could reach a maximum limit value. However, this behaviour could be also due to differences in the load distribution between the two balls during the test. To illustrate the effect of the contact force, Figure 5.14 shows a comparison between dry tests carried out under different contact forces and the same oscillation amplitude of 5 mm. The effect of the contact force on the wear depth

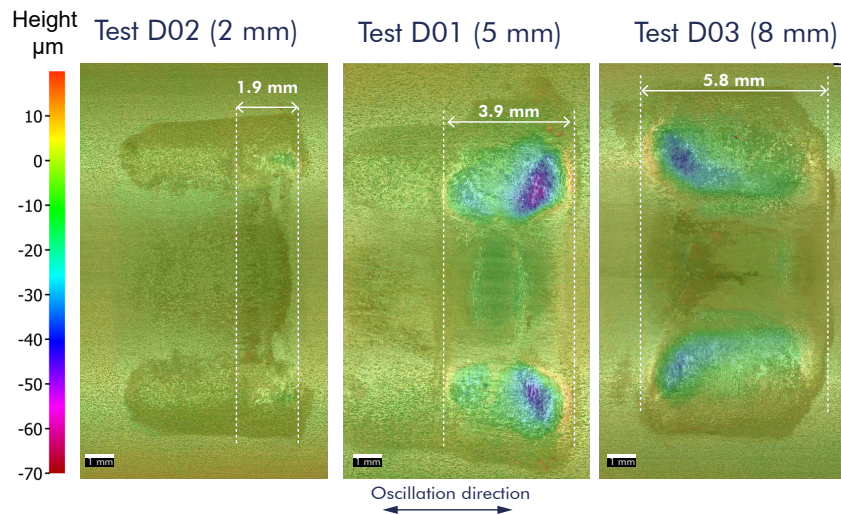


Figure 5.12: Comparison of wear maps of dry tests under different oscillation amplitudes.

can be seen from the comparison. Moreover, the reduction of the total sliding distance with the increase of the contact force (from 5.1 mm, to 3.9 mm and 3.5mm), which was discussed in the analysis of the fretting loops in the previous chapter, was also observed in these tests.

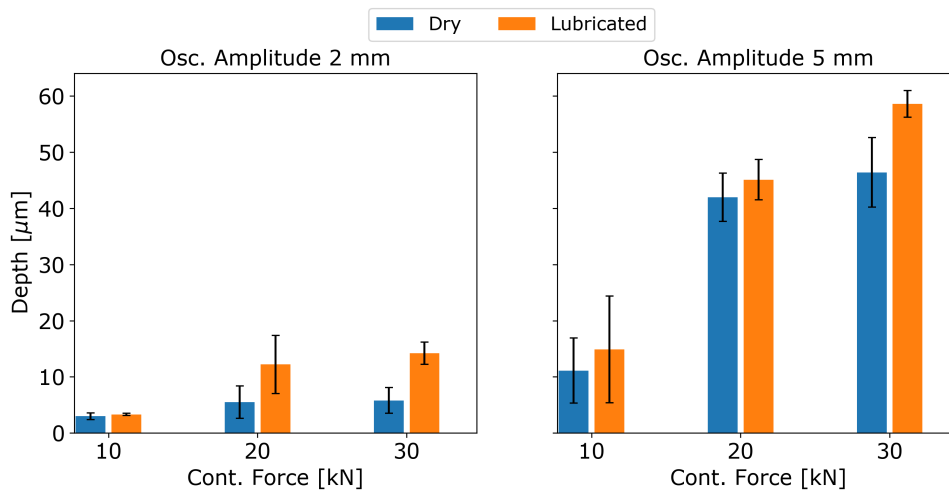


Figure 5.13: Maximum wear depth under different contact forces.

Figure 5.15 shows the maximum wear depth under different oscillation frequencies. No influence can be observed under the range of frequencies tested. Tests D12 and L12 conducted at 2 Hz were one of the cases where the greases lubricated test resulted in less wear damage. This may indicate that this particular grease performs better at higher speeds.

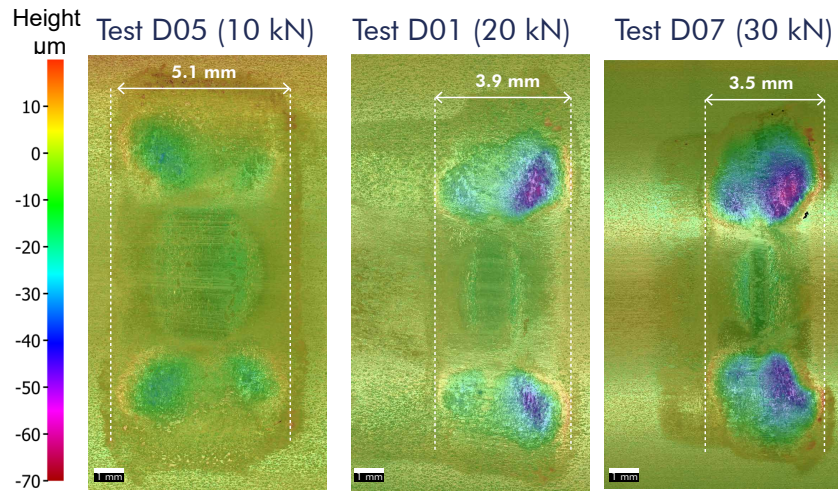


Figure 5.14: Comparison of wear maps of dry tests under different contact forces.

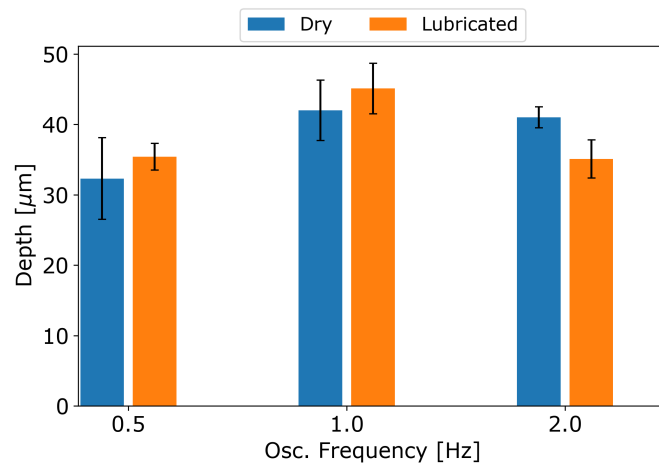


Figure 5.15: Maximum wear depth under different oscillation frequencies.

Figure 5.16 presents the wear depth versus two contact geometry parameters, the ball diameter and contact conformity. Results show that with a larger ball and the same conformity of 0.52 reduced the wear depth. A bigger ball and larger groove radius result in an increase in the contact area and a decrease in the contact pressure, which may explain the reduction of the wear depth. Increasing the conformity also reduced the wear depth. The explanation of this behaviour is less evident compared to the ball diameter. The conformity was increased by enlarging the groove radius and keeping the ball diameter unchanged. This results in higher contact pressure. However, the shape of the contact area changes, the major axis of the contact area becomes smaller, and the minor axis wider, which improves the distribution of the slip in

the contact area, as observed by Schwack et al. [43]. A comparison of wear maps of dry tests under different contact geometries is presented in Figure 5.17 where the increase of the worn area occurs with a bigger ball and the decrease of the worn area is seen with higher conformity, but with a reduced ovalised shape.

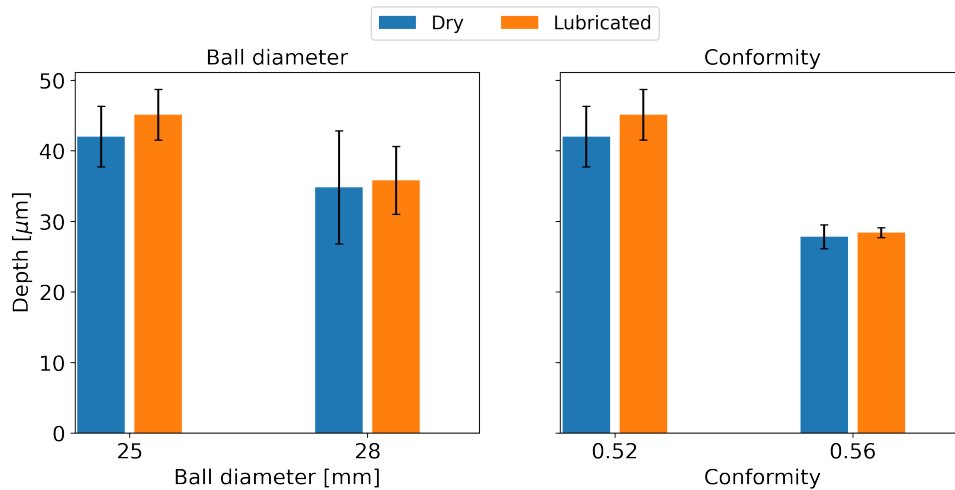


Figure 5.16: Maximum wear depth under different contact geometries.

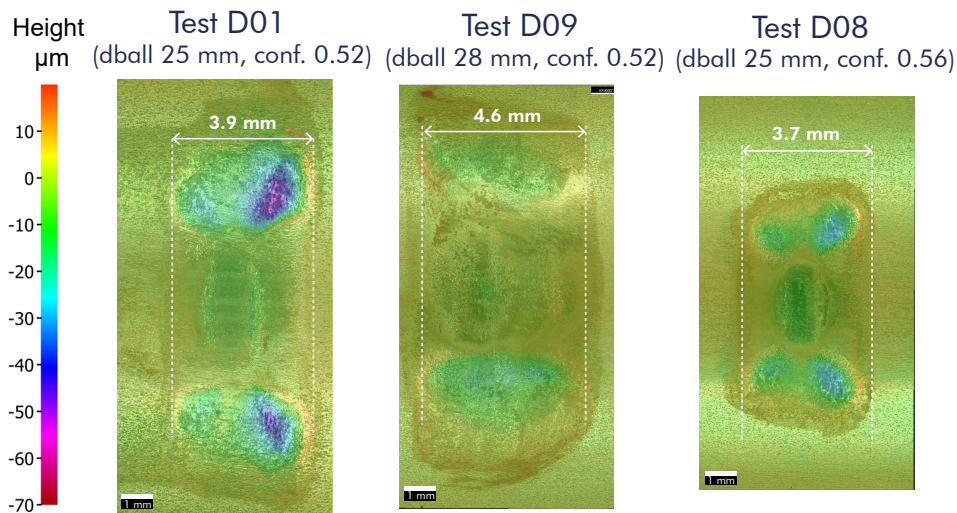


Figure 5.17: Comparison of wear maps of dry tests with different contact geometries.

The last test parameter analysed from these tests was the number of cycles. Figure 5.18 shows a plot of the wear depth at two different numbers of cycles 3000 and 10000. It can be observed that little damage was accumulated during the first cycles. The reason for the small amount of wear during the earlier cycles might be due to the formation of a TTS layer. In

a material that forms TTS, the frictional energy in early cycles is used to produce this layer, and no wear is accumulated. The graph of Figure 5.18 also shows an interesting observation regarding the effect of lubrication. It can be observed that at the first 3000 cycles, the wear depth in the grease lubricated test was not higher than the dry configuration. This might be because the grease had not been completely squeezed out of the contact. The positive effect of grease during the first cycles can be noticed in the comparison of the wear scars between the dry and lubricated conditions presented in Figure 5.19.

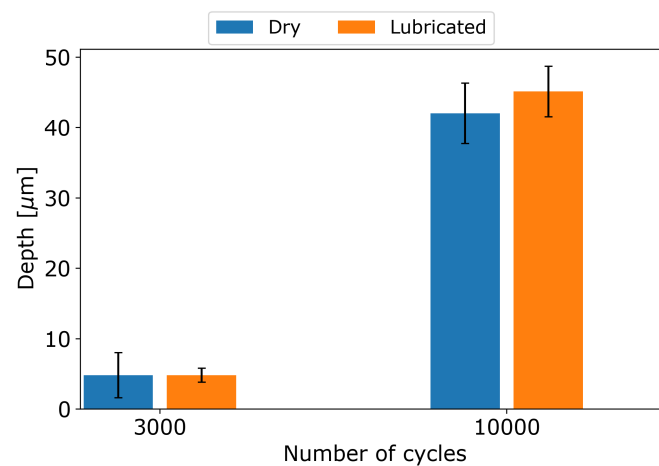


Figure 5.18: Maximum wear depth under different number of cycles.

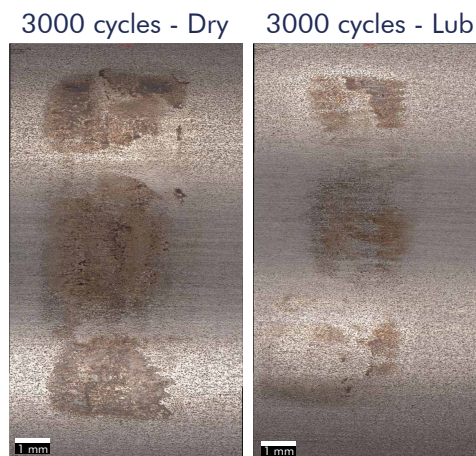


Figure 5.19: Comparison of wear maps of dry and lubricated tests at 3000 cycles.

5.4.3 Effect of Testing Conditions on Friction Indicator

A frictional indicator of the system was analysed by measuring the force at the lateral actuator where the oscillatory motion was applied. This force takes into consideration not only the frictional force between the balls and raceways, but also the inertial forces, which are small compared to the frictional forces, and the friction between the bottom sample holder and the PTFE. The coefficient of friction of PTFE on polished steel can vary between 0.02 and values higher than 1.0 depending on the tribological conditions [100, 101].

Figure 5.20 presents four representative plots of the time evolution of the frictional indicator. These plots show a similar behaviour of the frictional indicator. They start with an increase in the first 1000-2000 cycles and then reaches a stable value, except in test D03-L03.

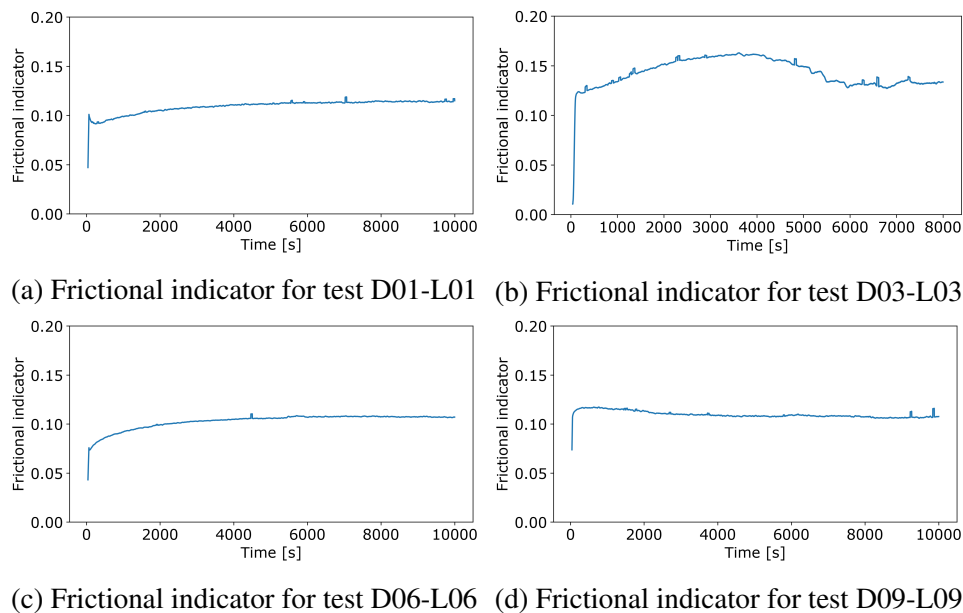


Figure 5.20: Plots of frictional indicator of four tests.

Considering the stable behaviour of the frictional indicator in the majority of the tests, the effect of the different testing parameters on this indicator was analysed by comparing the average value of the frictional indicator obtained for the different tests.

Figure 5.21a presents the frictional indicator under different oscillation amplitudes. A slightly increase trend can be observed from these results. However, these tests are under gross slip regime, where the coefficient of friction is independent of the oscillation amplitude. Therefore, the small increase of the frictional indicator with the oscillation amplitude did not come from the ball-raceway contacts, but likely from the PTFE plate-bottom holder contact.

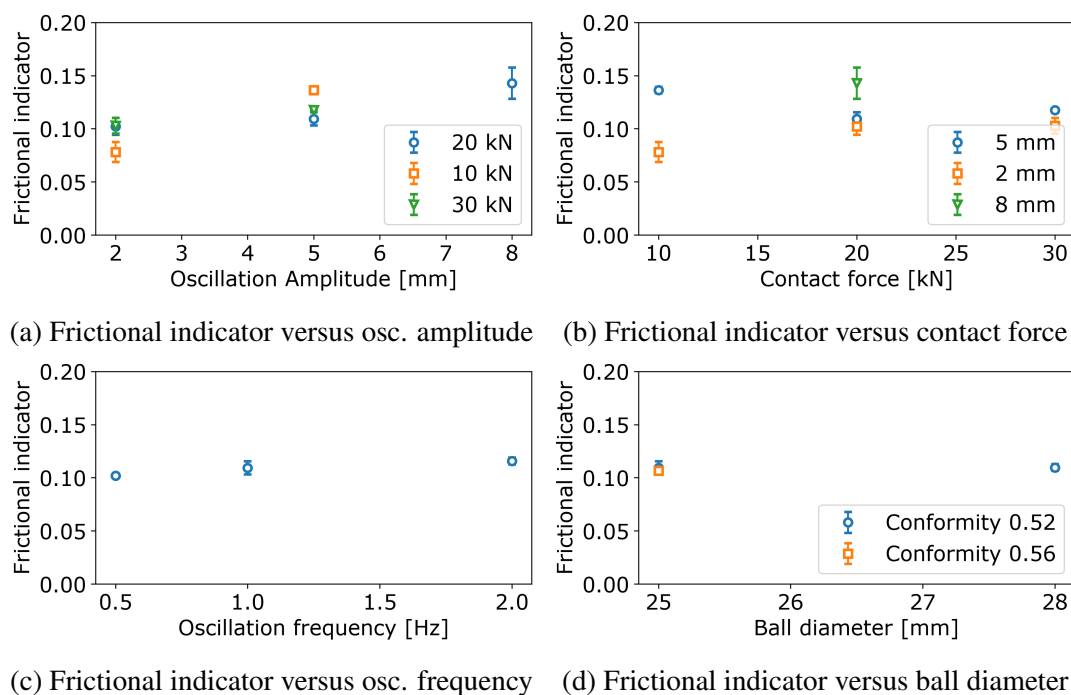


Figure 5.21: Average frictional indicator under different testing parameters.

Figures 5.21b, 5.21c and 5.21d presents the frictional indicator under different contact forces, oscillation frequencies, and contact geometries, respectively. All these plots show that these parameters has minimal effect on the frictional indicator.

5.5 Discussion

The design of a medium-scale fretting test rig and further experimental study aims to overcome the limitation found in typical experimental set-ups to understand the effect of main parameters on fretting under wind turbine pitch bearing operating conditions. The discussion of the results focuses on three main aspects. Firstly, comparing the damage characteristics of the medium-scale tests to the damages observed in the failed pitch bearing section presented in Chapter 3. Secondly, a comparison between the results obtained from the medium-scale and small-scale experimental set-ups to establish what findings are valid from the small-scale experimental study. Finally, establishing how the wear produced by small-amplitude oscillations could be reduced based on the experimental results presented in this chapter.

5.5.1 Analysis of Wear Scars

Wear scars produced by the medium-scale test rig using the bi-axial machined exhibited a w-shape, explained by the slip distribution in the contact area where most of the wear accumulates at the ends of the long axis of the elliptical contact area due to the Heathcote slip [84]. In contrast, the wear scars in the failed pitch bearing section exhibited u-shaped profiles. This difference was explained due to the more complex operating conditions in an actual pitch bearing compared to the constant contact force and oscillation amplitude considered in these tests. Variable load and oscillation amplitude might have generated a superposition of different sized w-shaped wear scars that in the end resulted in a u-shape, as illustrated in Figure 3.18 . Furthermore, contact pressure has a close association with wear scar profile shape. A low contact pressure is more likely to produce u-shaped wear scars, whereas a higher contact pressure can result in w-shaped wear scar [27]. The mean average contact pressure estimated for the failed pitch bearing section was 1.9 GPa as discussed in Chapter 2, while in these tests the contact pressure was higher than 2.2 GPa. Another difference between the actual bearing and the experiment is the absence of spinning of the ball produced by the non-zero contact angle and the curvature of the ball. This difference causes an asymmetric wear scar in the actual application.

High levels of oxidation were found in all tests under dry and grease lubricated conditions. However, the oxide particles and oxidized surfaces always had the same reddish appearance which is related to Hematite [8]. In the analysis of the failed pitch bearing section, both Hematite and Magnetite oxides were found on the surface. Many reasons could explain the lack of Magnetite in the tests. For example, the difference in the environment, humidity, temperature and salinity can be very different in wind farm sites, especially offshore. Grease and material could also affect the oxidation response of the surface. Lastly, it was possible that the tested condition did not correspond to the range that produces Magnetite as an oxidation product. Magnetite is associated with false Brinelling, and the wear scars in this wear mode suggest that the wear was produced mainly by elastic slip that takes place under variable load and extremely small oscillation amplitudes. These testing conditions were not considered in this study, as after preliminary tests on the UMT, it was found that the severity of the damage under these conditions was considerably lower than the damage produced by larger oscillations with sliding ratios larger than 1.0.

The results of the microstructure analysis revealed the formation of a tribologically transformed structure on the tested samples. No evidence was found underneath the wear scars in the pitch bearing section. Two possible reasons might explain this difference: the different materials between the samples and pitch bearing section or the number of cycles. The microstructure of the 42CrMo4 steel is pearlite inside austenite grains; however, it is tempered

martensite with iron carbides for O1 steel. It was mentioned that the microstructure has an influence on the tribological properties [98]. After a certain number of cycles the TTS is totally worn out and this is why this microstructure is not commonly found in applications where the worn component has been in service for long periods [27].

Regardless of the differences observed between the medium-scale tested samples with the pitch bearing section, the results obtained can be considered as a reference to the actual application. However, some precautions are necessary as there is much unknown information about the operating conditions of the studied pitch bearing, the test rig designed is capable of producing fretting wear damage under simplified pitch bearing operating conditions.

5.5.2 Comparison of Experimental Setups

Considerable results and analysis were carried out for both, small and medium scale experimental set-up tests, which makes it possible to evaluate whether the limitations of the small-scale test rig affect the key results such as the coefficient of friction or wear damage.

The measured coefficient of friction on the small-scale tests was on average 0.13, while in the medium-scale tests, it was 0.09. This means 15% of difference, considerably low taking into account the possible sources that could have led to larger differences. For example, sample size, contact geometry, holder or data acquisition. It was expected that removing the ball holder reduced the coefficient of friction, and it seems that the friction at the PTFE plate did not affect the measurements of the COF significantly. Moreover, the stable frictional behaviour under the gross sliding regime contributed to the good agreement between the two experimental set-ups. Therefore, it can be suggested that the small-scale tribometer is suitable for a preliminary assessment of the coefficient of friction.

In regard to the wear damage, the trend of the effect of the different testing parameters on the maximum wear depth was the same in both experimental set-ups. However, the wear scar characteristics of the damage generated by using these two test rigs were substantially different. The wear scar profiles are different, u-shape in the small-scale tests and w-shape in the medium-scale tests. The difference in the wear scar shape was produced by the different contact geometries. The w-shape in the medium-scale tests was produced by the Heathcote slip that occurs in highly conformal contacts, and in the small-scale set-up, this did not happen, as the surface of the samples was flat. Another difference in the wear damage was related to the oxidation. In the small-scale tests, very little oxidation was found only in a couple of tested samples, compared to the high levels of oxidation observed from by the samples of the medium-scale tests. This could be explained again by the difference in the contact geometry but also by the contact size between these two experimental set-ups.

Based on the discussion of the differences between the two different scale test rigs, it can be proposed that the small-scale test rig is useful to understand the impact of the different testing variables on the wear. The contribution of the medium-scale tests is its capability to create test conditions closer to the actual pitch bearing application. This helps developing the understating of the wear scar characteristics, as the produced is more realistic compared to the wear in pitch bearing. However, these results also suggest that testing under variable load and variable amplitude conditions would be required.

5.5.3 Mitigation of Wear Damage in Pitch Bearings

The results presented in this chapter allow a preliminary proposal of strategies to mitigate the wear damage produced by small-amplitude oscillations in pitch bearings. This proposal is important as the next chapter presents an FEA of a rolling ball under the same testing conditions of this experimental study, and it is necessary to understand which results should be analysed in the FE model to best complement the experimental results. The proposal is based on the effect of the different tested parameters on the wear damage development.

- **Oscillation amplitude:** Experimental tests presented in this chapter show that the oscillation amplitude is directly related to the upper limit of the wear damage defined by the maximum frictional energy density that a surface point can accumulate in one oscillation. This suggests that one possible approach to mitigating the wear would be to minimise the oscillating angle amplitude as much as possible or pitch the blade at amplitudes larger than the critical angle θ_{crit} defined by Harris et al. [3] where a second ball overlaps the stress area and the lubrication is argued to work better. In other words, the proposed strategy consists of minimizing the number of oscillations whose amplitudes are between the amplitude that corresponds to a sliding ratio equal to 1 and the Harris' critical angle.
- **Contact force:** Experimental tests show an intuitive result of the effect of the contact force on the wear damage. The wear depth increases with the contact force. Therefore, the strategy to reduce the wear damage from the contact force point of view is to reduce the load. Unfortunately, this cannot be achieved easily, as the loads acting on the pitch bearing depend on many external variables and operating conditions. However, the load distribution analysis presented in Chapter 2 shows that it is possible to improve the load distribution by modifying the flexibility of the hub, which in practical terms reduces the contact forces on the most loaded rolling elements.

- **Oscillation frequency and presence/absence of lubrication:** These two parameters did not show a significant effect on the wear damage. However, this work does not focus on analysing different greases and only one grease was used in the tests. A different grease could work better under pitch bearing operating conditions. The constant amplitude oscillations is probably one of the worse conditions for lubricated fretting wear, as it does not allow relubrication and lead to starvation [92]. A more in-depth analysis has to be done to identify the relevant grease properties that reduce wear under the most critical fretting wear condition, high loads and medium oscillation amplitude range. However, the detailed analysis of grease properties is not within the scope of this research project.
- **Contact geometry:** One of the main advantages of the medium-scale test rig is that allowed the understanding of contact geometry. This was possible as the ball kinematics is representative of the actual pitch bearing. These results show that either increasing the ball size or the conformity reduces the wear damage produced by small oscillations. Nevertheless, increasing the ball size could probably lead to a bearing with fewer rolling elements, and therefore an increase in the load on each ball. On the other hand, an increase in the conformity could result in a change in the bearing geometry and its stiffness, also increasing the maximum load in the rolling elements. Thus, even though modifications to the contact geometry have the potential to mitigate fretting wear, they must be analysed together with other factors to achieve an optimum design.

This preliminary proposal on how to mitigate the fretting wear are again discussed in the conclusions chapter after the FEA of the contact model that provides a better understanding of the slip and frictional energy density under pitch bearing operating conditions.

5.6 Conclusions

The experimental study presented in this chapter aimed to design a medium-scale test rig that overcame the limitations experienced when using a standard small-scale tribometer and investigate the effect of different test parameters on fretting wear damage under simplified pitch bearing operating conditions. The designed fretting test rig was able to effectively produce well-developed wear scars under the designed testing conditions. The results produced the expected features based on the analysis of the failed pitch bearing section which agreed with the results found in the literature under a reasonable testing time shorter than four hours.

The results of these tests confirmed that the scale and the ball kinematics are relevant to understand the development of wear damage under small-amplitude oscillations. They

play important roles in the access of oxygen to the fretted surface and in the slip distribution, respectively.

The main conclusions obtained from the analysis of the effect of the testing parameters are:

- The wear damage reaches a limit in terms of the wear depth that it can accumulate by the oscillation of one ball and it is a function mainly of the oscillation amplitude.
- Wear damage increases with the contact force/pressure.
- Oscillation frequency and lubrication did not significantly affect the wear damage in the tests. However, it was discussed that the testing conditions were not appropriate to evaluate lubrication, and using only one grease is not enough to conclude the effect of lubrication and oscillation frequency. More tests under different conditions and with different properties are required.
- Understanding the effect of contact geometry is one of the biggest contributions of this experimental study. Wear damage can be reduced by increasing the ball diameter or the conformity.

A preliminary proposal to mitigate fretting wear was outlined based on this experimental study.

Chapter 6

Finite Element Analysis of a Rolling Ball Contact

6.1 Introduction and Aims

The two experimental studies at different scales presented in the previous chapters provided key information to understand the effect of the different operating conditions in fretting wear under pitch bearing operating conditions. However, those experimental configurations did not make it possible to analyse what occurs in the contact area in regards to the slip or traction forces distribution. As discussed, the amount of wear in fretting contacts is directly related to the frictional energy density, defined as the product of the shear stress and the sliding distance [43], [36]. Therefore, analysing these magnitudes is essential to complement the results from the experimental studies.

This chapter presents a finite element analysis of a rolling ball contact. This FEA aims to study different contact parameters, such as the contact pressure, shear stresses, sliding distance, and frictional energy density under equivalent pitch bearing operating conditions to deepen the understanding of the effect of these conditions on the fretting wear. Moreover, a method to simulate wear based on the frictional energy density is developed and evaluated.

FEM is a powerful tool that allows the analysis of detailed contact results. A model validated with experimental results also provides additional results and further analysis. Moreover, a model capable of predicting wear damage and evaluate the effect of different testing conditions can be a valuable method to define the testing parameters in actual size tests.

6.2 Methods

The analysis of the rolling ball contact was carried out developing two FE models with different geometries.

The first model considered the contact geometry of the small-scale test rig and aimed to develop a method to simulate wear based on the frictional energy density. This model was developed in ABAQUS 2018 using the STANDARD module and static analysis. The simulation of the wear was implemented by coding in FORTRAN the equations to post-process the frictional energy density and define the material removal by using the UMESHMOTION user subroutine. This model was conducted under static analysis assumptions because it is a limitation of the UMESHMOTION user subroutine [102]. Another limitation of using the UMESHMOTION user subroutine is that it does not allow the use of multiple processors, which resulted in large running times of more than a week for each testing condition, even by using a high-performance computer. For this reason, only one set of testing conditions was assessed using this first model. This model aimed to validate the frictional energy density as an indicator of fretting wear and the use of the UMESHMOTION user-subroutine as a useful approach to efficiently simulate wear by comparing the modelling results with the testing results using the UMT tribometer.

The second model considered the contact geometry of the medium-scale test rig and aimed to analyse the frictional energy distribution in the contact area under different testing conditions. This model does not simulate the wear damage accumulation to achieve greater time-efficiency in running more models. Different to the first FE model, the analysis of the second FE model was performed by employing a dynamic model using the EXPLICIT solution method in ABAQUS. A detailed description of these two FE models is presented in the next section.

6.3 Description of the FE models

6.3.1 Small-Scale Contact FE Model

Geometry and Materials

A flat sample, one section of the ball, both modelled as solid bodies, and a simplified ball holder modelled as a beam were included in this model. Modelling the ball holder was necessary to account for its flexibility, as it affects the frictional behaviour and the measured fretting loop. Figure 6.1a presents an illustration of the model and the parts considered in it. Elastic material properties of steel were considered for the three components as presented in Table 6.1.

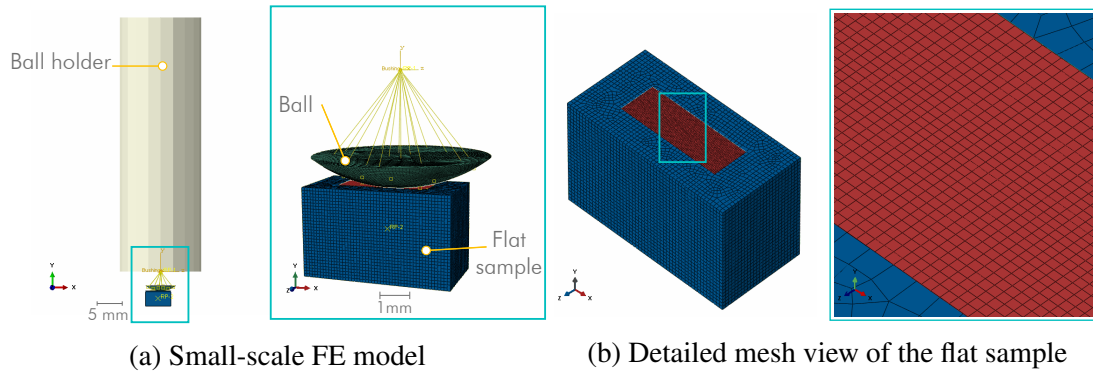


Figure 6.1: FE model of the small-scale contact configuration.

Table 6.1: Material properties for rolling ball contact FE model.

Young Modulus [GPa]	Poisson's ratio
200	0.3

Finite Element Mesh

The finite element mesh of this model was developed by using eight-node fully integrated brick elements (C3D8) for the solid bodies and three-node beam elements with full integration (B32) with the cross section properties representing the ball holder. For meshing purposes, the flat sample was sectioned into two different domains, as presented in Figure 6.1b. The domain in contact with the ball had a higher refinement as this was the region of interest. Figure 6.1a also shows the mesh of the whole model. To assess the quality of the mesh and the accuracy of the results provided by the model, a mesh convergence study was conducted by evaluating the contact pressure (CPRESS) and the sliding distance (CSLIP1) as indicators. Figure 6.2 presents the plot with the results of the mesh convergence study showing that the error of both magnitudes evaluated is below 10%. These results were achieved considering an element size of 0.03 mm in the contact region.

Interactions, Boundary Conditions and Loads

The interactions, boundary conditions and loads presented in Figure 6.3 below were defined when setting up the model and described as follows:

1. A reference point was created at the centre of the bottom face of the flat sample and linked to this surface by means of a coupling constraint where an oscillatory movement was defined with a sinusoidal function of range 1 mm and frequency 1 Hz.

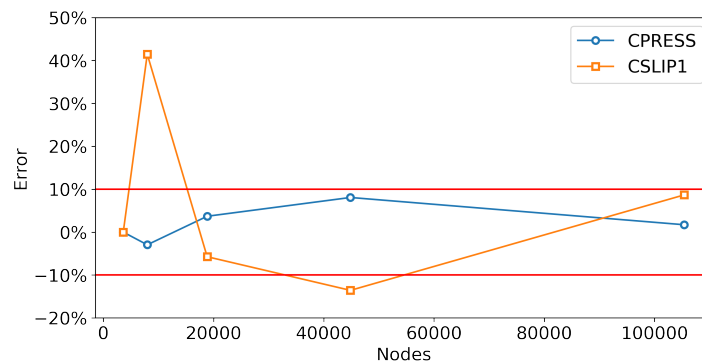


Figure 6.2: Mesh convergence results of small-scale contact configuration FE model.

2. A force of 100 N was applied at the top of the ball holder.
3. A contact interaction was defined between the ball and the flat sample surface with a coefficient of friction of 0.14 based on the experimental results. Master-slave approach in a surface to surface contact was used for this interaction. The surface of the flat sample was defined as slave and the ball as master surface. Coulomb's isotropic friction was defined as tangential behaviour and hard contact as the normal behaviour. The contact algorithm was set as Lagrange multipliers with the finite sliding formulation to improve the accuracy of the relative slip.
4. The section of the ball was linked to a reference point at the centre of the ball by means of a coupling constraint. This reference point was assembled to the beam element to represent the ball holder using a bushing constraint with a rotational stiffness in the main axis of rotation of the ball. The rotational stiffness was calibrated with the same stiffness as the experimental results to reproduce a fretting loop, which was achieved with a value of 1200 Nm/rad. This modelling approach allowed the sliding and rotation of the ball to be considered without modelling the contact of the ball holder.
5. The two meshing domains of the flat sample were assembled through a tie constraint. This boundary condition is used as an efficient method to connect two parts with different mesh refinements when the interface is far from the region of interest as this kind of constraint might impact the strain/stress distribution in nearby regions.

The load and the oscillatory movement were applied through different steps in the same way as that employed in the tests. Firstly, the load was applied onto the ball while the flat sample was fixed. In the subsequent steps, the fretting cycles were applied to the flat sample. During these steps, the load magnitude on the ball was maintained constant. Finally, the sample

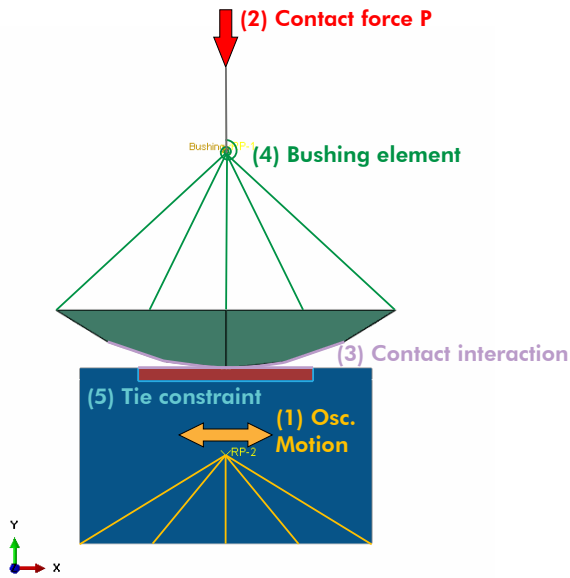


Figure 6.3: Boundary conditions, interactions and loads applied on the small-scale contact FE model.

was gradually unloaded and the ball moved away from the contact with the sample during the last step to remove the elastic effects from the wear results. An illustration showing the application of the load and displacement is presented in Figure 6.4.

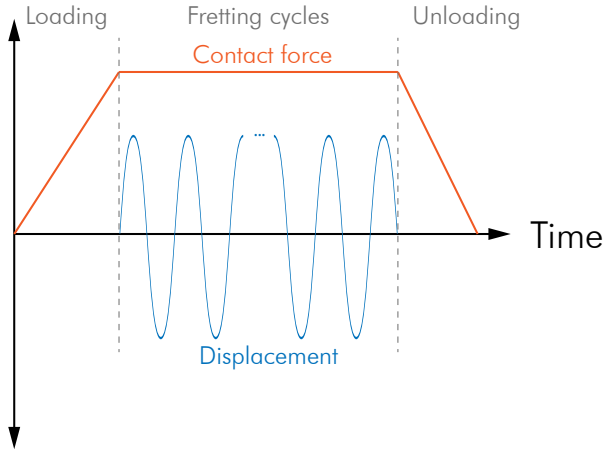


Figure 6.4: Loading and oscillations sequence in small-scale contact FE model.

Adaptive Mesh and UMESHMOTION

The user subroutine UMESHMOTION was used to define the motion of the nodes on the surface of the flat sample in contact with the ball section based on the frictional energy density, where an adaptive mesh constraint was applied during the oscillatory cycles. The wear equation implemented in this model is presented in Equation 6.1.

$$\Delta h_i = \alpha_h q_i(x) ds_i(x) \quad (6.1)$$

Where Δh_i is the incremental wear depth at the end of the i -th increment, α_h is the local wear rate coefficient, $q_i(x)$ is the shear stress and $ds_i(x)$ is the incremental slip. A local energy wear rate of $1118 \mu m^3/J$ under dry conditions derived from the tests conducted on the UMT was considered for the implementation of the user subroutine. In summary, this model calculate the wear on the flat sample nodes by calculating the slip rate and shear stress field and considering the the local wear coefficient measured in the small-scale tests.

The total number of cycles N was 1500 as the same in the UMT test. A jump cycle technique, firstly introduced by McColl et al. [65], was used to accelerate the wear simulations. In this method, widely used for wear simulation [103–106], a factor ΔN represents the number of cycles in which the contact variables used in the calculation of wear remain unchanged until processing the next ΔN cycles. For this model, a constant jump cycle factor of 100 was considered, which means that 15 oscillations cycles had to be calculated to obtain the wear accumulated by 1500 cycles. UMESHMOTION has been used in different applications to simulate wear; including 2D problems [107], suitable for example in roller bearings applications [18], 3D problems, such a polishing tool [108] or orthopaedic applications [22, 109]. All these applications have considered different wear equations, from Archard wear model to the previously mentioned frictional energy density. However, none of them has simulated wear using a 3D model considering rolling-sliding based on the frictional energy density, which is achieve in this study.

The code for the implementation of the UMESHMOTION user subroutine and the description of this method to simulate fretting wear are presented in Appendix D.

6.3.2 Medium-Scale Contact FE Model

Geometry and Material Properties

One ball and two grooved sample sections were considered in the medium-scale contact FE model. The possible instability issues, that required the use of two balls in the experimental tests, do not occur in the model; therefore, the simplification of using only one ball in the FE

model was possible. The assembly of these parts is presented in Figure 6.5. The material properties considered for the grooved samples and the ball were the steel elastic properties presented in Table 6.1.

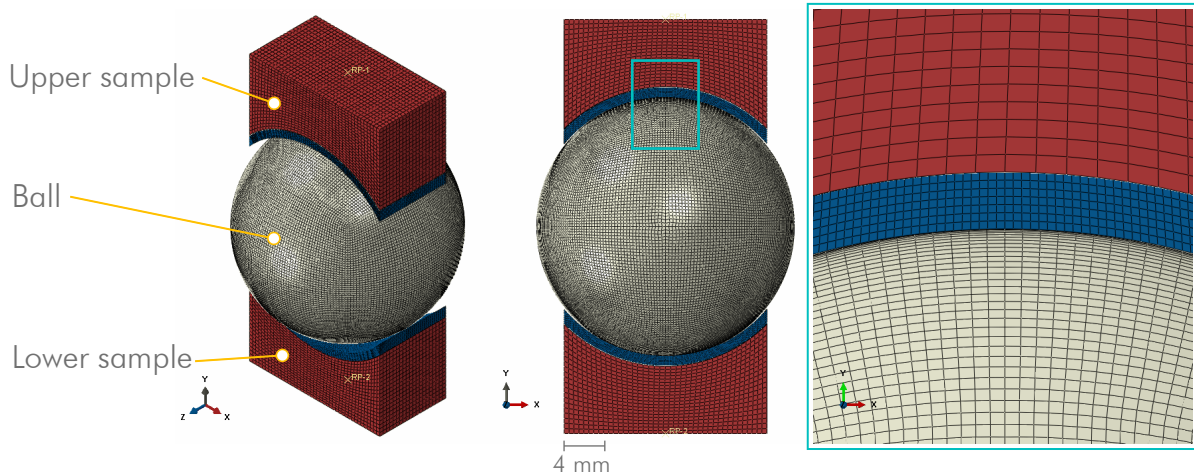


Figure 6.5: Medium-scale contact configuration FE model.

Finite Element Mesh

In this model, all the parts were modelled as solid bodies and meshed with eight-node fully integrated brick elements (C3D8). Similarly to the small-scale model, the grooved samples were split into two domains: a domain near the contact interface with the ball where a finer mesh was defined, and the rest of the sample was meshed with coarse elements. The FE mesh developed for this model is presented in Figure 6.5. In order to ensure the numerical quality of the results, a mesh convergence study was conducted by evaluating the contact pressure (CPRESS) and the slip magnitude (CSLIPEQ). Figure 6.6 presents the results of the mesh convergence showing that the error of both variables is below 5% with the refined models. These results were achieved by considering an element size of 0.15 mm in the contact region.

Interactions, Boundary Conditions and Loads

The interactions, boundary conditions and loads applied to this model are presented in Figure 6.7 and described below. Since the aim of this second model is to study the effect of the different testing conditions, different values of the oscillation amplitudes, contact forces, and contact geometries were considered. The different modelling conditions evaluated in this model are summarised in Table 6.2.

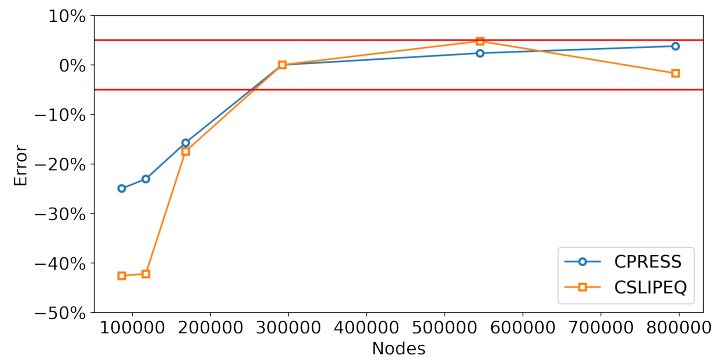


Figure 6.6: Mesh convergence results of medium-scale contact configuration FE model.

1. A reference point was created at the centre of the top face of the upper sample and linked to the surface where contact force was applied by means of a coupling constraint.
2. A reference point was created at the centre of the bottom face of the lower sample and linked to the surface where the oscillatory motion was applied by means of a coupling constraint.
3. A contact interaction was defined between the ball and each of the grooved samples with a coefficient of friction of 0.1 based on the experimental results. Master-slave approach in a surface to surface contact was used for this interaction. The surfaces of the grooved samples were defined as master and the ball's outer face as slave surface. Coulomb's isotropic friction was defined as tangential behaviour and hard contact as the normal behaviour. The contact algorithm was set as the penalty method. Since uncertainty existed on the measurement of the friction in the medium-scale tests, a sensitivity analysis on the coefficient of friction was performed as part of the results evaluated in this model.
4. The two meshing domains of each grooved sample were assembled through a tie constraint.

Different to the small-scale FE model where the aim was to simulate the wear damage accumulation, only one oscillation cycle was simulated in this medium-scale FE model. Figure 6.8 presents a scheme of the loading and displacement application.

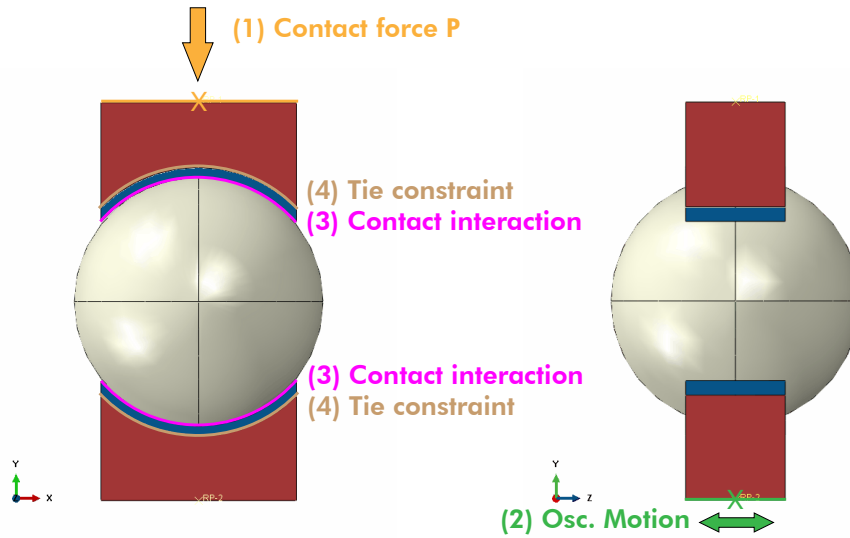


Figure 6.7: Boundary conditions, interactions and loads applied on the medium-scale contact FE mode.

Table 6.2: Different conditions evaluated in the medium-scale FE model.

Model	COF	Osc. Amp [mm]	Force [kN]	Freq. [Hz]	Ball diam. [mm]	Conformity
01	0.1	2	20	1	25	0.52
02	0.1	5	20	1	25	0.52
03	0.1	8	20	1	25	0.52
04	0.1	5	10	1	25	0.52
05	0.1	5	30	1	25	0.52
06	0.1	5	20	1	28	0.52
07	0.1	5	20	1	25	0.56

6.4 Results

6.4.1 Small-Scale Contact FE Model

Fretting Loops

The first verification of the model consisted of a comparison of the modelled fretting loops with the experimental data. For the comparison, an average cycle from the experimental test with an oscillation amplitude of 1 mm at 1 Hz, a contact force of 100 N under dry conditions was considered. Figure 6.9a shows both fretting loops. It can be observed that the shape of the fretting loop from the FE model is more idealised and encloses a slightly larger area, meaning that the energy accumulated in every cycle is larger than that in the tests. The accumulation of

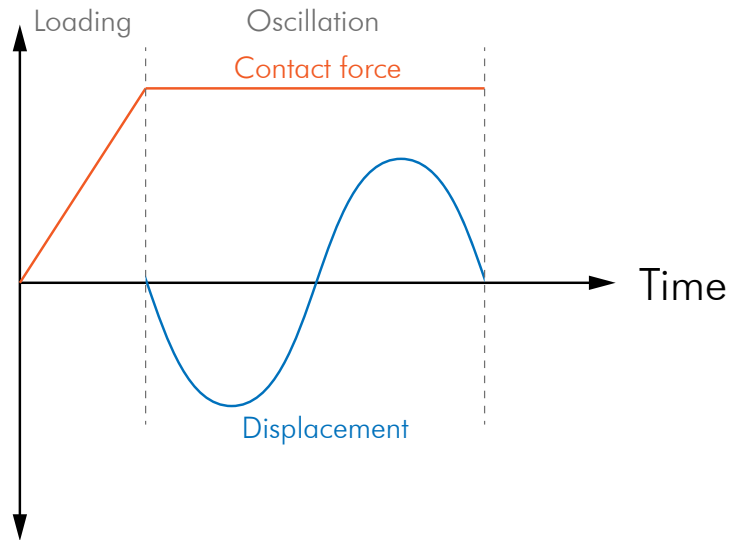


Figure 6.8: Loading and oscillation sequence in medium-scale contact FE model.

frictional energy over the total 1500 cycles from the model and the tests is plotted in Figure 6.9b. It can be observed the impact of the difference in the area of the fretting loops on the total frictional energy. The total frictional energy accumulated after 1500 cycles is 27.9 J in the test and 29.9 J in the FE model, meaning that the model overestimated the dissipated frictional energy by 7%. The effect of this difference is evaluated in the following section.

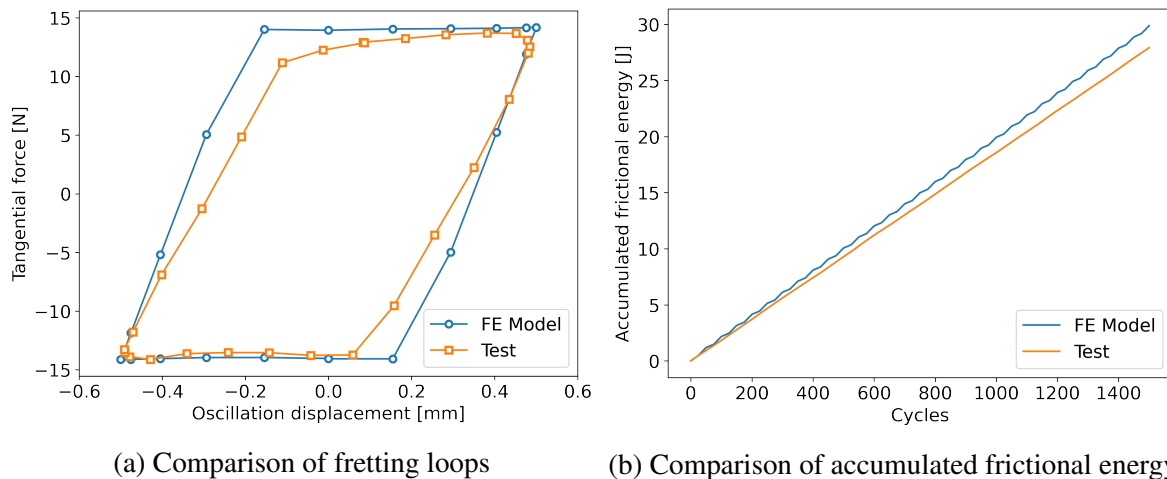


Figure 6.9: FE model verification by comparison of fretting loops and accumulated frictional energy.

Wear Depth

The worn surface obtained at the end of the simulation and the one measured from the tested specimen under the equivalent condition is presented in Figure 6.10. A comparison of the wear profiles is shown in Figure 6.11. Some clear differences can be observed from the comparison. Firstly, the wear profile along the oscillation direction is different; it is a w-shape in the model and a u-shape in the experiment. The different wear profiles resulted in the location of the maximum wear also being different; which was at both ends in the model, but located at the centre in the test. Regarding the magnitude of the maximum wear depth, the model overestimates it by 18%. This difference is larger than the difference that could be attributed to the larger fretting loop obtained in the FE model. Possible reasons for the larger difference in the wear depth between the model and the test are that the model assumes all the frictional energy is used for the material removal, while in reality, there are other processes taking place that can take a portion of the available frictional energy, such as plastic deformation, heat generation, and tribochemical reactions, which were not considered in the FE model.

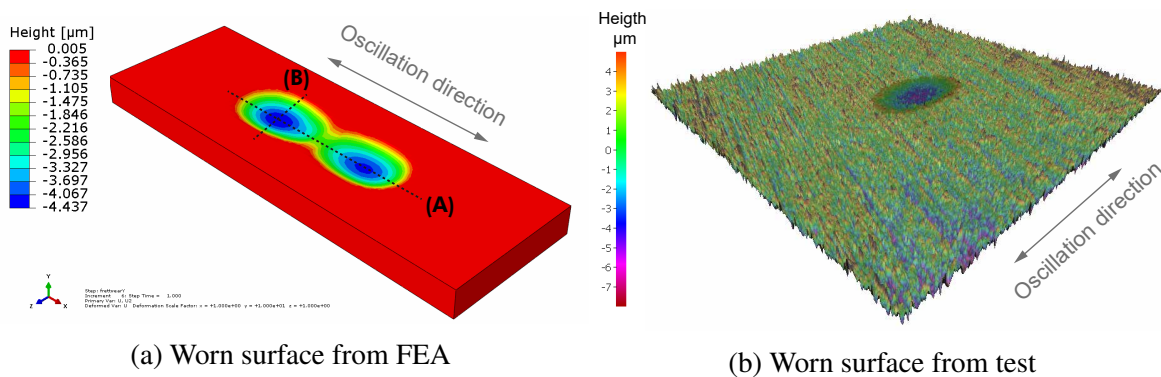


Figure 6.10: Comparison of worn surfaces under equivalent conditions.

Slip Distribution

The key results that define the wear damage accumulation are the slip or sliding distance and the shear stress. Figure 6.12 and 6.13 present the accumulated slip along both parallel and perpendicular directions to the oscillatory movement and the traction lines during the first oscillation cycle, respectively. The slip distribution explains why less wear damage is accumulated at the centre as there is little slip at this zone, even when the shear is constant along the oscillation cycle. The order of magnitude of the accumulated slip in the direction of oscillation is 1000 higher than that in the perpendicular direction. Although it is possible to calculate analytically the slip and shear stress fields [110], the value of doing this by using the FEM is that it is possible to account for the change in those field as the wear evolves.

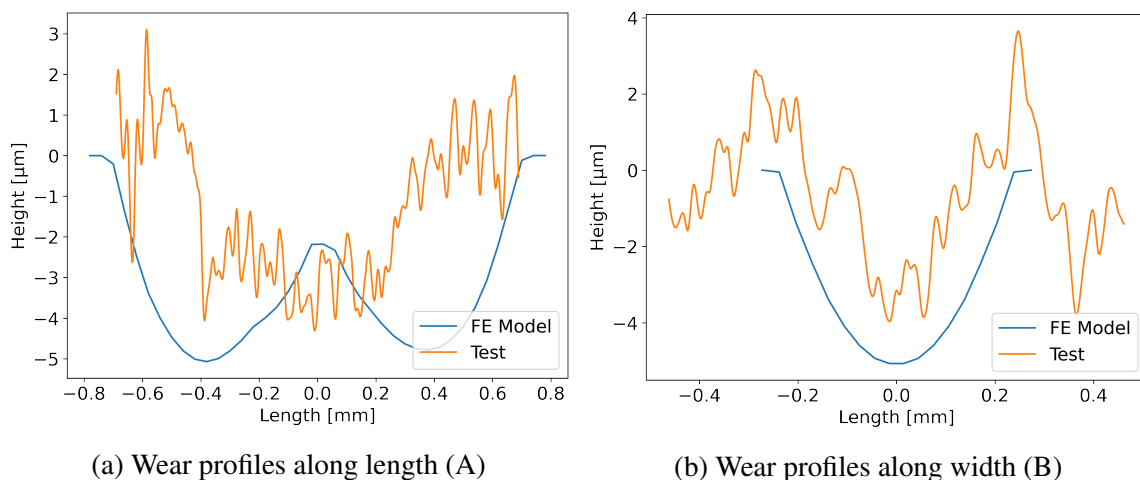


Figure 6.11: Comparison of wear profiles.

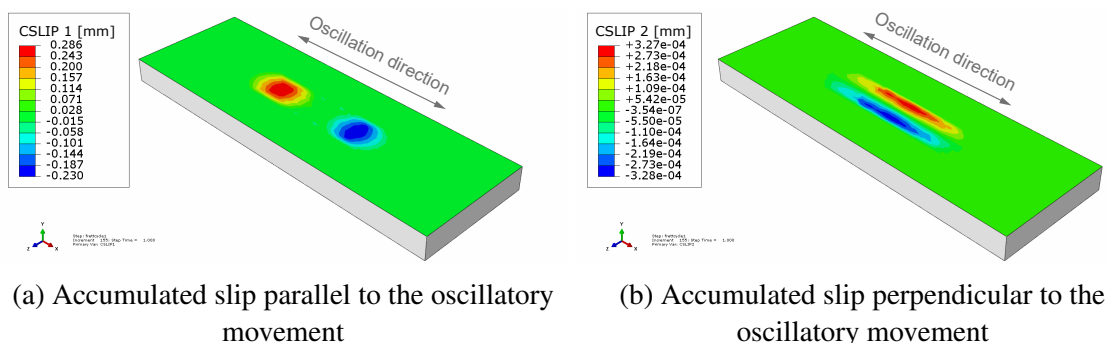


Figure 6.12: Accumulated slip during the first cycle.

The ball holder and the ball movement was uncertain in the small-scale tests on the UMT. Although it was proved that the movement of the ball was a combination of rolling and sliding, it was not possible to measure exactly how the ball was moving during the tests. The modelling strategy of using a bushing connector between the ball and the holder to simulate its rolling resistance might have led to different ball movements, which could explain the unexpected slip distribution. Figure 6.14 shows a plot with the rotation of the node associated with the bushing connector. This graph shows that the ball is not continuously rotating; it rotates at the beginning of the oscillation cycle, it stops when the ball passes through the centre and then continues the rotation. This might explain the unusual slip distribution. It can be also seen that the rotation amplitude only reached 2° . For a stroke of 1 mm and considering pure rotation the rotation should be 12° .

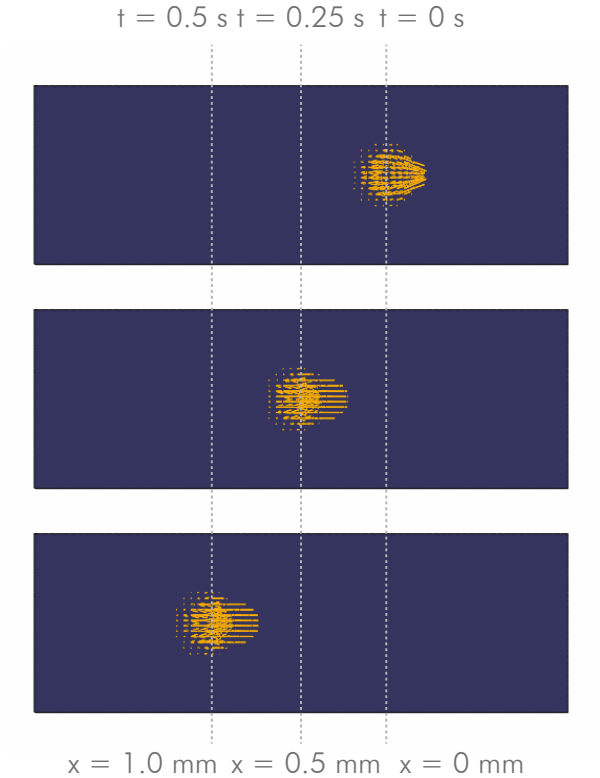


Figure 6.13: Traction lines during the first cycle.

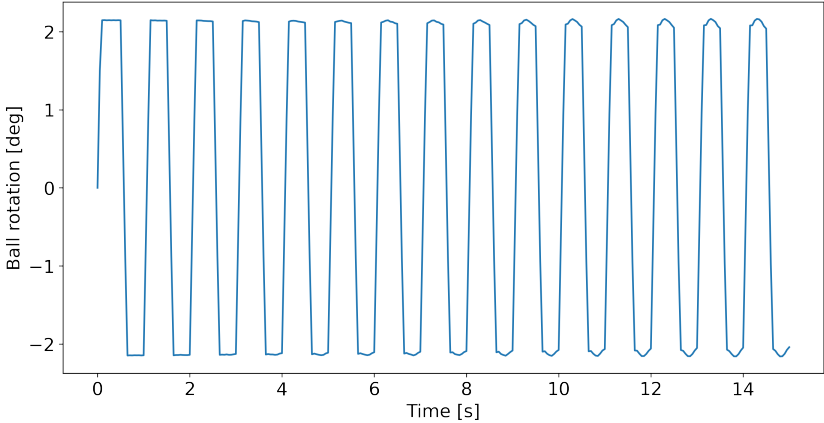


Figure 6.14: Ball rotation over the modelled cycles.

Effect of Wear Damage

Another useful results that can be obtained from this model is the evolution of the contact results with the wear damage accumulation. Figure 6.15 shows the change of the contact

pressure at the centre of the oscillation path (Pos. A) and at one of the ends (Pos. B) of the worn surface. Variations of the contact pressure over the cycles with a maximum difference of 22% can be observed, as well as significant change in the overall distribution. It may be expected a decrease in the contact pressure due to the wear because it increases the contact conformity. This would be true in a static contact, but in a rolling-sliding contact, the maximum change in the contact pressure is observed when the ball reaches the end of the worn surface and a change in the contact surface occurs.

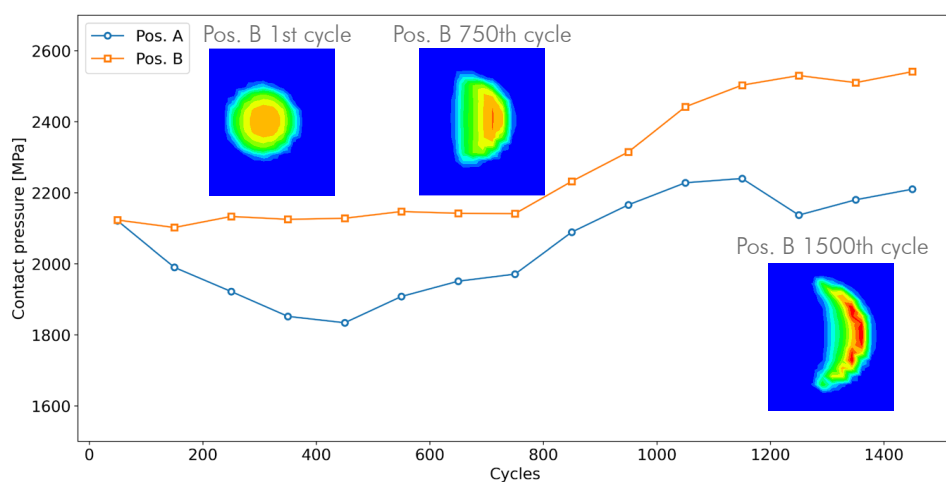


Figure 6.15: Contact pressure variation over cycles and wear damage accumulation.

6.4.2 Medium-Scale Contact FE Model

Frictional Energy Density Distribution

The first result post-processed from the medium-scale contact FE model was the frictional energy defined by Equation 6.1. This magnitude has been previously used in FEA to study false Brinelling and fretting corrosion in wind turbine pitch bearings [43, 111].

Figures 6.16, 6.17 and 6.18 show the modelling results of the frictional density distribution compared to the respective worn surface from the medium scale tests under different oscillation amplitudes, contact forces and contact geometries, respectively. The plots presented in Figure 6.19 summarise the maximum frictional energy density obtained in each model plotted together with the maximum wear depth measured from the tests.

The comparison of the modelled frictional energy density distribution with the measured wear maps shows a good degree of correlation in almost every case, except for the case with different conformity of the contact geometry. In general, both variables show a similar

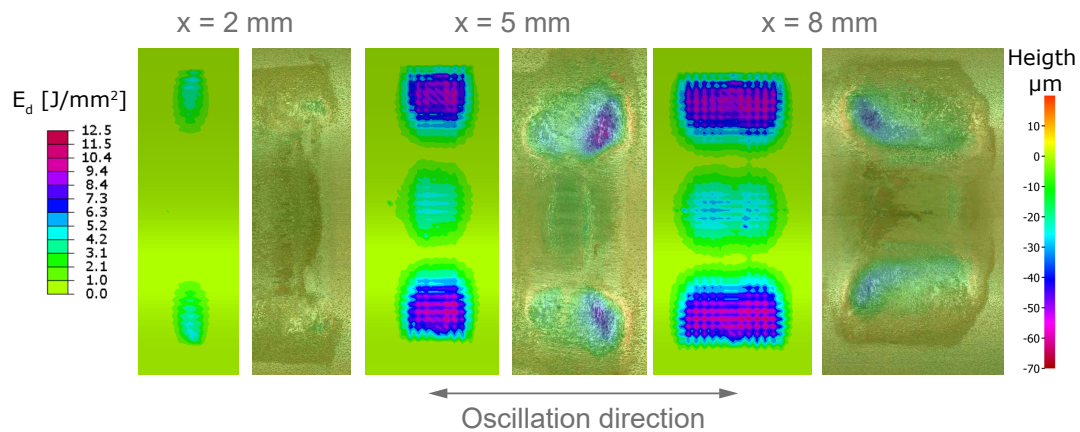


Figure 6.16: Frictional energy density (E_d) from FE model compared to measured worn surface (height) under different oscillation amplitudes.

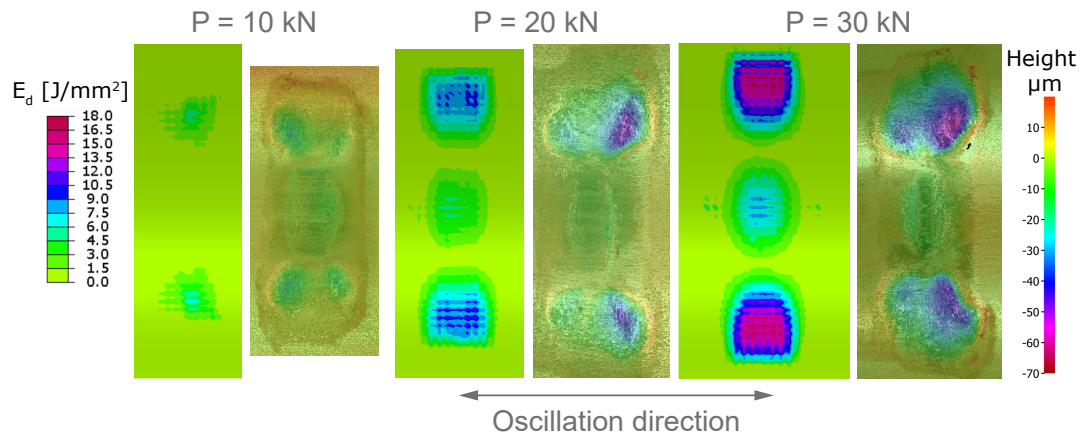


Figure 6.17: Frictional energy density (E_d) from FE model compared to measured worn surface (height) under different contact forces.

distribution where most of the energy density and wear depth are concentrated at the ends of the long axis of the contact area due to the differential slip or Heathcote slip that occurs in highly conformal contacts. One difference observed between the energy density distribution from the FE model and the wear maps from the experimental tests is that the energy density is uniformly distributed at the top and bottom of the worn surfaces, while the measured wear depth is normally higher on one of the sides. This difference may be explained due to the change in the contact results with the development of the wear scar over cycles, as previously shown in the results of the small-scale FE model. Regarding the case with different conformity, it was discussed in the previous chapter that higher conformity produces a higher contact pressure which would result in a higher energy density. However, Schwack [43] argued that higher

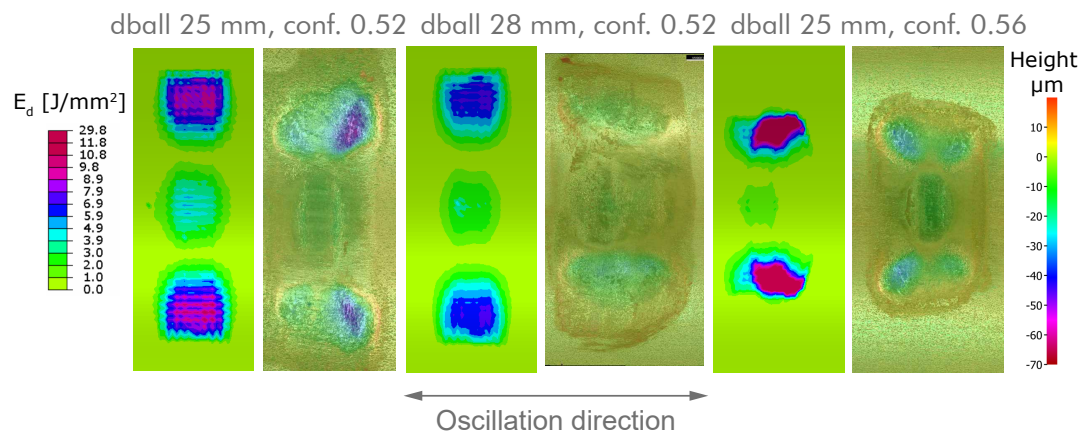


Figure 6.18: Frictional energy density (E_d) from FE model compared to measured worn surface (height) under different contact geometries.

conformity also produced a change in the slip distribution, resulting in a lower energy density. The fact that this was not observed in this model might be explained by the different geometry used in these two works.

The comparison of the maximum frictional energy density and wear depth presented in the plots of Figure 6.19 made it possible to analyse if the trend of the different testing parameters was similar to that observed from the experiments. This was confirmed for almost all the cases, except for the model with a different conformity.

Another analysis that allows the validation of the frictional energy density as an indicator of the occurrence of fretting wear was to post-process the evolution of this result along a path of the worn surface to obtain a profile and compare it to the wear profile measured from the tests. This comparison is presented in Figure 6.20 for the case with a oscillation amplitude of 5 mm and a contact force of 20 kN. The comparison shows a similar profile of the energy density and the wear depth, even considering that the energy results do not take into account the changes produced by the wear scar.

Slip and Shear Distribution

Similarly to the small-scale FE model, the slip and shear results were post-processed to understand the resulting frictional energy density. Figure 6.21 presents the incremental slip distribution and the traction lines at three points of the oscillation cycle: $x=2.5$, $x=0$ and $x=-2.5$. By comparing these results to the energy density distribution shown in Figure 6.16, it can be observed that the incremental slip has a more significant contribution to the energy density. Nevertheless, both results need to be analysed together.

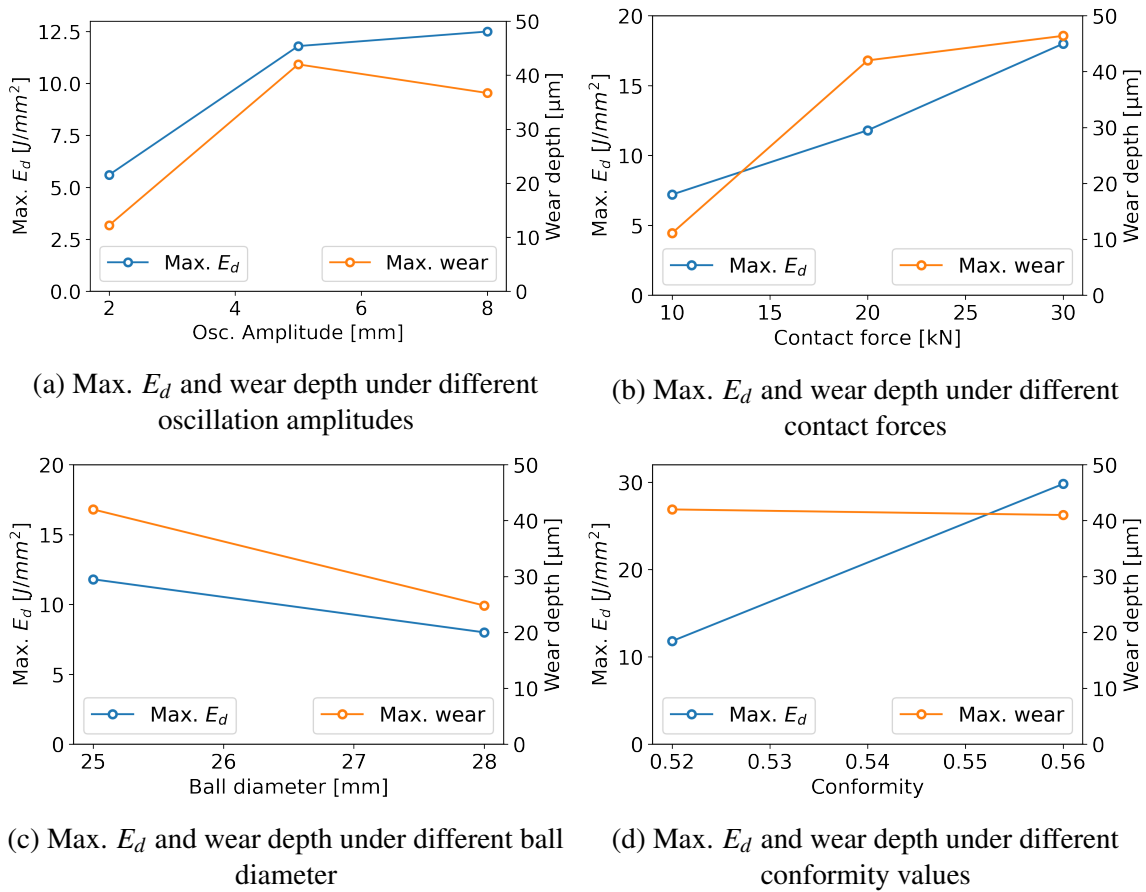


Figure 6.19: Summary of the maximum frictional energy density of all models and comparison with the maximum wear depth from experimental tests.

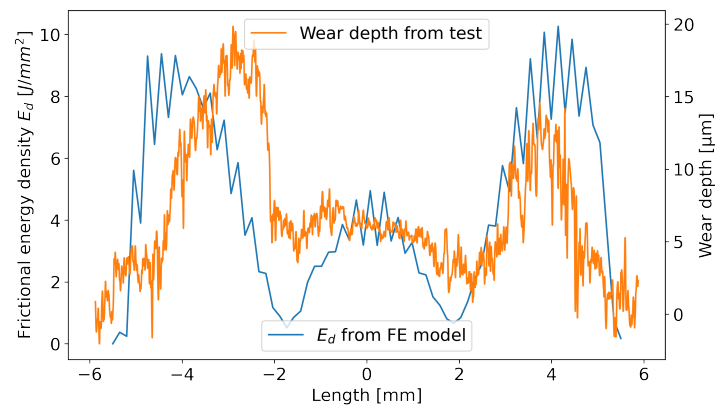


Figure 6.20: Frictional energy density (E_d) from FE model compared to measured worn surface (height) under an oscillation amplitude of 5 mm.

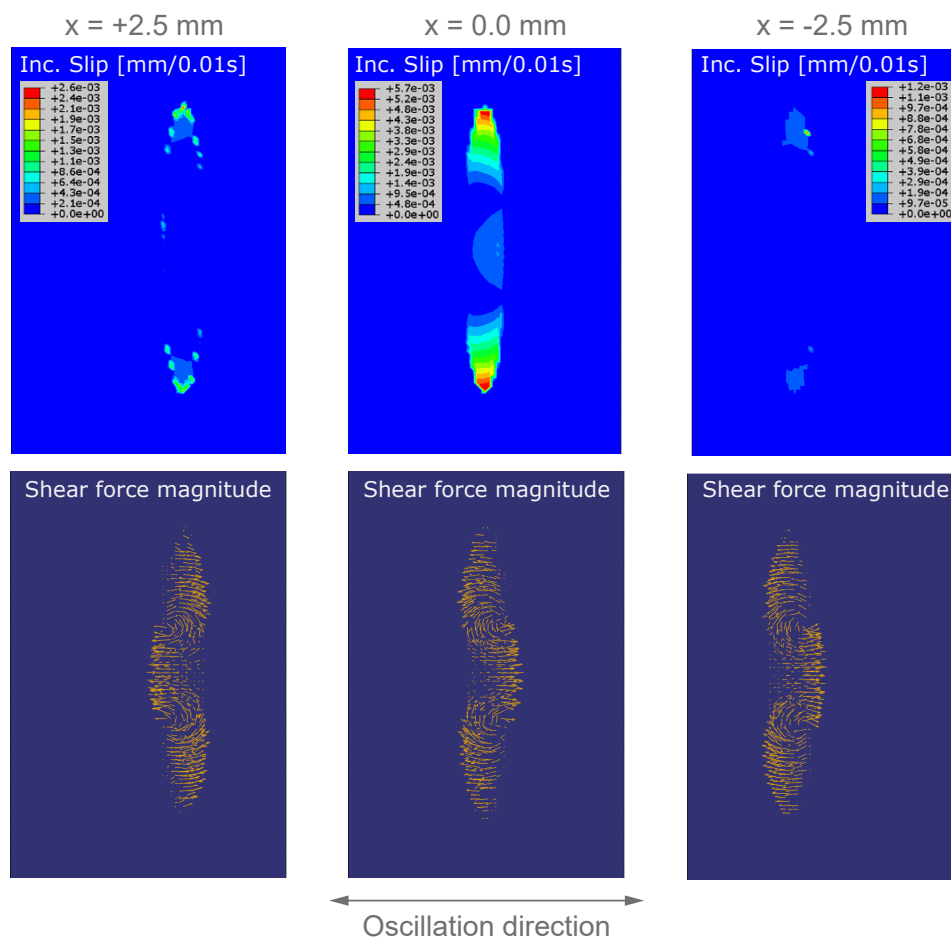


Figure 6.21: Incremental slip and traction lines at three points of the oscillation cycle.

6.4.3 Sensitivity Study on the Coefficient of Friction

All the models analysed in this section considered a coefficient of friction of 0.1. This value comes from the average frictional indicator measured in the medium-scale experimental tests. However, uncertainty existed in the measurement of the friction as it included not only the friction from the contact between the ball and the grooved samples but it also included inertial forces, and most significantly the friction between the bottom holder and the PTFE slider plate. To evaluate the impact of the uncertainty of the COF on the results, a sensitivity study was carried out considering three different values of COF: 0.1, 0.2 and 0.3. The graph presented in Figure 6.22 summarises the maximum frictional energy density and its distribution for the three COFs. It is observed that the maximum frictional energy density increased with the coefficient of friction. Moreover, the distribution of the frictional energy density also changed: with the increase of the COF, the frictional energy accumulated at the centre of the fretted area was

reduced and concentrated more at the two end areas. The ratio between the frictional energy density at the ends and at the centre obtained with a COF of 0.1 was similar to the ratio of the wear depth, as shown in Figure 6.20 showing the comparison between the profiles of the frictional energy density and measured wear depth along the long axis of the worn area.

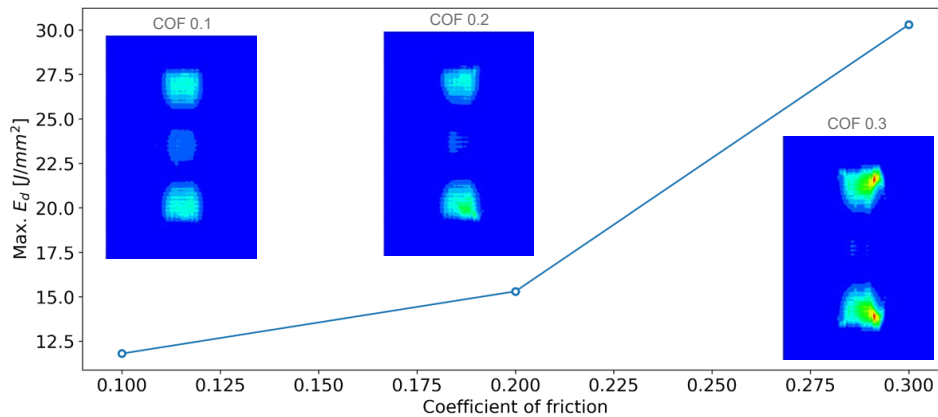


Figure 6.22: Maximum frictional energy density under different COFs.

6.5 Discussion

The finite element analysis of the rolling ball contact aimed to deepen the understanding of the testing parameters on the wear damage under pitch bearing operating conditions. The analysis presented in this section focuses on the contribution of the two models presented in this chapter and how the contact results can improve the analysis from the two experimental studies presented in Chapters 4 and 5.

The small-scale FE model based on the contact set-up employed in the UMT tribometer was used to implement a method to predict fretting wear. The model was not able to predict the wear scar shape when compared to the experimental results. The main difference was that in the FE modelling results the majority of the damage was accumulated at the ends of the oscillation path, while in the test, it occurred at the centre. Based on the slip result, it was possible to argue that this variation between the test and the FE model was not produced by the method developed to predict the wear damage based on the accumulation of frictional energy density, but it was associated with the complexity of modelling the interaction between the ball and the ball holder and the approach used to allow the rotation of the ball. Despite the deviation of the total frictional energy between the model and the test being lower than 10%, the slip distribution in the FE model caused a different frictional energy density distribution,

resulting in a different wear pattern. Regarding the maximum wear depth, it was found that the model overestimated it, by 18% for the conditions analysed. The fact that all the frictional energy is used in the wear process might be explained the higher wear depth predicted by the FE model. In the test, there is also a small part of the energy used in plastic deformation, heat generation and tribochemical transformation.

The medium-scale FE model based on the contact set-up employed in the bi-axial machine was used to study the effect of the testing conditions on the frictional energy density. The frictional energy density distribution showed a similar pattern compared to the wear maps from the tests. The differences can be explained because this model did not consider the effect of the wear depth accumulation and its impact on the variation of the contact variables, such as the contact pressure or the slip distribution. The comparison of the frictional energy density profile to the wear profile showed that this magnitude is appropriate to predict fretting wear. The comparison of the maximum values of the modelled frictional energy density and the measured wear depth under different testing conditions showed the same trend which confirms the effect of these parameters on the fretting wear.

The order of magnitude of the frictional energy density values may not be particularly intuitive. A simple verification with the available results is possible. The maximum frictional energy density in the model with an oscillation amplitude of 5 mm and a contact force of 20 kN was 11.8 J/mm^2 in one cycle. The local wear rate α_h under dry conditions in the small-scale tests was $1118 \mu\text{m}^3/\text{J}$ per cycle. Considering a total number of cycles equal to 10000, as in the tests, the maximum wear depth would be $131.9 \mu\text{m}$, 3.1 higher than the maximum wear depth measured in the tested sample under the same conditions. This estimated value is a reasonable estimation considering the following factors:

- (i) The material used in the medium-scale test had a different microstructure and was twice harder than the material used in the small-scale tests, where the wear rates were measured,
- (ii) the difference in size scale between the two experimental configurations,
- (iii) and the fact that the FE model does not take into account the effect of wear damage accumulation over cycles.

The simulation of the wear depth accumulation can be a valuable method for specific applications. However, the limitations of the UMESHMOTION user subroutine in ABAQUS makes it an inefficient method that requires long computing times, even for small models. The analysis based on the frictional energy density proved to be a reliable and efficient approach for designing and analysis of fretting wear under pitch bearing conditions. A similar strategy

is normally observed in fatigue analysis. In most cases, only a stress analysis is required to perform a fatigue life analysis, and only in specific applications, the crack growth is modelled.

The effect of lubrication may be a limitation of the potential of these models. The only method to account for the effect of lubrication is by modifying the coefficient of friction, and the local wear rate if the model includes the UMESHMOTION user subroutine to simulate wear. However, the effect of lubrication can be beyond reducing the coefficient of friction and can also alter the contact pressure. This limitation does not impact the results presented in this chapter, as the effect of the grease was not relevant in the tests. Nevertheless, there may be other greases that perform better under pitch bearing operating conditions or under more complex conditions, such as variable oscillation amplitude or load.

A preliminary proposal to mitigate wear due to small amplitude oscillations under pitch bearing conditions was presented in Chapter 5. After analysing the results of the finite element analysis, almost all the suggestions of the proposal can be maintained. The only discrepancy between the experimental tests and the FE model of the medium-scale configuration was the result when a different conformity was considered. In the experiment, increasing the conformity slightly reduced the wear, while the frictional energy density increased in the FE model. Increasing the conformity by increasing the groove radius decreases the contact pressure based on Hertzian equations of contact mechanics, increasing the frictional energy density and therefore the wear damage, which was observed in the experiment.

One last aspect to consider in this discussion is the purpose of the experimental tests and the models. They aim to understand the wear damage produced by small-amplitude oscillations in pitch bearings. Several simplifications were made during the design of the experimental tests and it is important to discuss the impact of these simplifications on the actual application. The main simplifications made in the medium-scale configuration consisted of the linearisation of the movement and the suppression of the contact angle. These simplifications resulted in a more simple kinematic of the ball, essentially suppressing the spin of the ball. In actual pitch bearing operation, the spin of the ball produces slip that varies from zero at the centre of the contact area to the maximum slip towards the ends. These maximum slips values have different directions at each end, and superpose to the Heathcote slip, increasing the total slip at the end where the spin and Heathcote slips have the same direction and decreasing the total slip at the end where they have opposite directions. The superposition results in an asymmetric wear depth distribution were analysed by Schwack et al. [43].

6.6 Conclusions

The two finite element analyses considering the contact geometry and testing conditions from the small-scale and medium-scale experimental configurations complemented the understanding gained from the experimental investigations. The main conclusions of the finite element analysis are summarised below:

- Although the implementation of the UMESHMOTION user subroutine failed to predict the worn shape in the small-scale configuration and overestimated the wear depth, this approach has applicability potential in particular cases when it is important to account for the evolution of the wear scar. For example, in a damage tolerance analysis. However, it is worth noticing that this method is extremely expensive in terms of computational resources.
- The pure analysis of the frictional energy density without wear simulation was found to be a computational efficient modelling approach to estimating the severity of the fretting wear from a design point of view of pitch bearing contact geometry.
- Most trends observed in the experimental tests were confirmed in the FEA of the medium-scale configuration. This allows the validation of the wear mitigation proposal outlined in the previous chapter. This proposal will be better elaborated in the final chapter.
- Finally it worth mentioning the main limitation of these models. They cannot account for the lubrication effects. It is only possible to consider the change in the coefficient of friction, but grease could also potentially change the slip field results.

Chapter 7

Conclusions and Future Work

This final chapter summarises the key findings of this study in regards to the main aims defined in Chapter 1.1 and outlines areas of future work based on the limitations identified from the different investigation areas presented along the various chapters and the state-of-art on pitch bearing wear.

7.1 Conclusions

This PhD study aimed to characterise the wear modes in pitch bearings produced by small-amplitude oscillations and investigate the effect of the main parameters involved. These aims were achieved by investigating a failed pitch bearing section, conducting experimental tests at two different scales, developing FE models of the load distribution of the pitch bearing rolling elements, as well as the FE contact models of the rolling ball on flat and grooved surfaces.

Wear damage characteristics under small-amplitude oscillations

Distinctive characteristics of the wear damage were found from the investigation of the failed pitch bearing section and the analysis of the tested samples. These characteristics are summarised as follows:

- The damage produced by small-amplitude oscillations under pitch bearing conditions consists of a combination of adhesive and abrasive wear with oxidation.
- The wear scar is defined by the elliptical shape of the contact area and the wear profile and severity are depended on the sliding regime. It can be a u-shape wear profile associated with gross slip regime or a w-shape wear profile associated with partial slip regime. The slip regime depends on the operating conditions.

- The wear depth distribution is normally concentrated at the ends of the wear scar area where the Heathcote slip and spin overlap.

The wear damage generated in the experimental tests exhibited similar characteristics in all the samples. A w-shaped profile and reddish oxide particles were found on the worn surface. In general the results and trends obtained in the experimental work are valid for the testing conditions considered in the experimental set-ups. These conditions intend to be representative of the operating conditions that produce fretting wear in pitch bearings and it is not intended to generalise the conclusions presented in this work to all fretting wear conditions. It is also important to note that false Brinelling takes place under smaller oscillation amplitudes than the ones considered in the experimental test of this thesis. The range of oscillation amplitudes and $x/2b$ values studied in this work were more focused on fretting wear as it was found to be more severe. Regarding the range of amplitudes and $x/2b$ values, it is worth commenting the difference in the definition of fretting between standard tangential fretting and pitch bearing application. In standard tangential fretting a clear transition between fretting and gross sliding exist at $x/2b$, whereas in pitch bearing, wear damage is usually referred as fretting under small amplitude oscillations but with values of $x/2b$ greater than 1. This could be either explained as the complex kinematics conditions in pitch bearing rolling elements contacts but also a misuse of the term fretting.

Effects of main parameters of Wear damage under small-amplitude oscillations

Regarding the effect of the operating conditions, it was found that the main parameters involved in fretting wear were the oscillation amplitude, contact force, oscillation frequency, contact geometry and lubrication. The effect of these parameters was investigated through the experimental studies and complemented by the finite element analysis of the rolling ball contact. The key findings and measures could be taken to reduce wear produced by small-amplitude oscillations in pitch bearing are summarised as follows:

- Oscillation amplitude: The wear damage increases with the oscillation amplitude until it reaches an upper limit where the frictional energy density becomes unchanged and the wear depth does not increase with this parameter. This limit corresponds to the gross slip transition limit. In an actual bearing, where several balls roll together, this upper threshold is only valid until the adjacent ball overlaps the same stressed area. If the oscillation amplitude is large enough then more than one ball rolls under the same area, it can be expected a fully developed lubricant film on the contact area, thus a reduction of the wear damage. Under these considerations, the range of oscillation amplitude to minimise the wear damage is when it is below the gross slip transition limit, $x/2b < 1.0$. However, this condition may lead to fretting fatigue depending on the operating conditions.

- **Contact force/pressure:** The effect of the contact force/pressure is directly proportional to the wear damage. The wear damage increases almost linearly with the contact force. Therefore, it is clear that reducing the contact force/pressure will reduce the wear damage. However, the contact force on each ball depends on the forces and moments acting on the pitch bearing that come from the blade. The loads acting on the blades are a constraint for the design of the pitch bearing and not a variable to modify. However, it is possible to improve the load distribution between the balls by modifying the stiffness of the bearing, which decreases the load at the balls with the maximum contact forces.
- **Oscillation frequency and presence of lubrication:** These two parameters did not show a significant effect on the wear damage based on the conducted experimental studies. Nevertheless, a different grease selection could probably be a measure to mitigate fretting wear in pitch bearings.
- **Contact geometry:** Experimental tests and the FE model showed that increasing the ball diameter can reduce the fretting wear damage. However, increasing the ball diameter would require to reduce the number of balls, having the opposite effect as it would increase the contact force. Therefore, finding the optimum ball diameter for a given pitch bearing design requires a comprehensive analysis that involves, among other things, the number of balls, conformity, bearing thickness, and load distribution.

7.2 Future Work

A preliminary proposal of recommendations to mitigate fretting wear in pitch bearings was discussed. The validation of the outcomes of this PhD project and the proposed recommendations requires further research considering the different limitations of the experimental tests compared to the actual operation of pitch bearings related to the operating conditions. This section presents suggestions for future work to carry on this research topic. These suggestions are divided into four areas: variable operating conditions, lubrication, damage tolerance, and large-scale tests.

- **Variable testing conditions:** Both experimental studies presented in this PhD project considered constant oscillation amplitude and contact force. Actual wind turbine pitch bearings work under highly variable operating conditions. Understanding the effect of variable operating conditions is essential to validate the results of this work. Particularly, the impact of the oscillating and loading sequence on the wear damage to answer the question of whether a linear law would apply to the wear damage accumulation. The

combined effect of variable oscillation amplitude and presence of lubricant is also suggested as future work as a high dependence is expected, mainly because how grease can penetrate the contact area is highly dependent on the oscillation amplitude.

- **Lubrication:** The properties of greases normally used in pitch bearing application vary significantly and there is no clear understanding of the contribution of these properties to the fretting wear resistance. A more in-depth study of the effect of different greases and their properties on fretting wear under pitch bearing operating conditions would be advantageous to understanding how to prevent the occurrence of this damage mode in pitch bearings. The relevant grease properties for this application to be considered as future work are base oil viscosity, anti-oxidation properties. The base oil viscosity determines how easily the grease oil can penetrate the contact area, while the anti-oxidation properties are relevant due to oxidation being a relevant mechanisms involve in fretting wear.
- **Damage tolerance:** No agreement exists on how much wear a pitch bearing raceway can accumulate before it fails to fulfil its main function, which is to accurately position the blade. Developing a method to define when the pitch bearing has accumulated a critical amount of wear damage could be potentially used as a condition monitoring system in wind turbine pitch controllers. This could be achieved by measuring the error between the oscillation amplitude given as input and the amplitude measured as the wear progresses during the tests.
- **Large-scale tests:** Conducting tests in large slewing bearings where all the simplifications from previous experimental tests are avoided to validate and prove all the knowledge and understanding developed under simplified conditions. Considering the actual size, the contact geometry, the interaction between balls, the effect of the cage, variable testing conditions, etc. is the only way of validation. To achieve this in a time and resource-efficient manner, the understanding acquired from the smaller scale tests, such as those achieved in this PhD study, is essential.

References

- [1] M. N. Kotzalas and G. L. Doll, "Tribological advancements for reliable wind turbine performance," *Philosophical Transactions of the Royal Society A: Mathematical, Physical and Engineering Sciences*, vol. 368, no. 1929, pp. 4829–4850, 2010.
- [2] A. Sevinc, M. Rosemeier, M. Bätge, R. Braun, F. Meng, M. Shan, D. Horte, C. Balzani, and A. Reuter, "IWES Wind Turbine IWT-7.5-164," no. June, p. 62, 2014.
- [3] T. Harris, J. H. Rumbarger, and C. P. Butterfield, "Wind Turbine Design Guideline DG03: Yaw and Pitch Rolling Bearing Life," *Nrel*, no. December, p. 63, 2009.
- [4] L. Houpert, "Bearing Life Calculation in Oscillatory Applications©," *Tribology Transactions*, vol. 42, pp. 136–143, jan 1999.
- [5] F. Schwack, M. Stammler, G. Poll, and A. Reuter, "Comparison of Life Calculations for Oscillating Bearings Considering Individual Pitch Control in Wind Turbines," *Journal of Physics: Conference Series*, vol. 753, no. 11, 2016.
- [6] M. Stammler, A. Reuter, and G. Poll, "Cycle counting of roller bearing oscillations – case study of wind turbine individual pitching system," *Renewable Energy Focus*, vol. 25, no. June, pp. 40–47, 2018.
- [7] E. A. Bossanyi, "Individual blade pitch control for load reduction," *Wind Energy*, vol. 6, no. 2, pp. 119–128, 2003.
- [8] D. Godfrey, "Fretting corrosion or false brinelling?," *Tribology & Lubrication Technology*, vol. 59, no. December, pp. 28–30, 2003.
- [9] A. Greco, S. Sheng, J. Keller, and A. Erdemir, "Material wear and fatigue in wind turbine Systems," *Wear*, vol. 302, no. 1-2, pp. 1583–1591, 2013.
- [10] T. A. Harris, *Essential Concepts of Bearing Technology, FIFTH EDITION*. Boca Raton: CRC Press, 5th edition ed., 2006.
- [11] International Organisation for Standardisation, "ISO 281: Rolling bearings — Dynamic load ratings and rating life," tech. rep., 2007.
- [12] International Organisation for Standardisation, "ISO Standard 76: "Rolling Bearings - Static Load Ratings"," tech. rep., 1989.
- [13] A. N. S. Institute, "ANSI/ABMA 9-1990: "Load Ratings and Fatigue Life for Ball Bearings"," tech. rep., 1990.

- [14] A. N. S. Institute, "ANSI/ABMA 11-1990: "Load Ratings and Fatigue Life for Roller Bearings"," tech. rep., 1999.
- [15] M. Stammli and A. Reuter, "Blade bearings : Damage mechanisms and test strategies," *2nd Conference for Wind Power Drives, WD 2015*, no. March, 2015.
- [16] I. O. for Standardization., *BS ISO 15243 : 2017 BSI Standards Publication Rolling bearings — Damage and failures — Terms , characteristics and causes*, 2017.
- [17] C. L. Lin, K. Fallahnezhad, O. Brinji, and P. A. Meehan, "Mitigation of False Brinelling in a Roller Bearing: A Case Study of Four Types of Greases," *Tribology Letters*, vol. 70, no. 1, pp. 1–18, 2022.
- [18] K. Fallahnezhad, S. Liu, O. Brinji, M. Marker, and P. A. Meehan, "Monitoring and modelling of false brinelling for railway bearings," *Wear*, vol. 424-425, pp. 151–164, 2019.
- [19] F. Massi, J. Rocchi, A. Culla, and Y. Berthier, "Coupling system dynamics and contact behaviour: Modelling bearings subjected to environmental induced vibrations and 'false brinelling' degradation," *Mechanical Systems and Signal Processing*, vol. 24, no. 4, 2010.
- [20] J. Silva and A. Cardoso, "Bearing failures diagnosis in three-phase induction motors by extended park's vector approach," in *31st Annual Conference of IEEE Industrial Electronics Society, 2005. IECON 2005.*, pp. 6 pp.–, 2005.
- [21] M. Zhang, R. Jiang, and H. Nie, "A numerical study on the friction and wear predictions of finger lock chuck in landing gear," *Proceedings of the Institution of Mechanical Engineers, Part G: Journal of Aerospace Engineering*, vol. 231, no. 1, pp. 109–123, 2017.
- [22] T. Bitter, I. Khan, T. Marriott, E. Lovelady, N. Verdonschot, and D. Janssen, "Finite element wear prediction using adaptive meshing at the modular taper interface of hip implants," *Journal of the Mechanical Behavior of Biomedical Materials*, vol. 77, pp. 616–623, 2018.
- [23] L. Zhao, X. He, B. Xing, X. Zhang, Q. Cheng, F. Gu, and A. Ball, "Fretting behavior of self-piercing riveted joints in titanium sheet materials," *Journal of Materials Processing Technology*, vol. 249, pp. 246–254, 2017.
- [24] F. Doyen, H. Zaïdi, J. Riviere, B. leclercq, and J. Rocchi, "Fretting contact study of stainless steel/graphite couples in a dry shaft/bearing contact with thrust," *Wear*, vol. 263, no. 1, pp. 508–517, 2007. 16th International Conference on Wear of Materials.
- [25] Z. R. Zhou and L. Vincent, "Lubrication in fretting - A review," *Wear*, vol. 225-229, no. PART II, pp. 962–967, 1999.
- [26] "Mineralogy: magnetite & hematite." <https://lifeinplanelight.wordpress.com/2011/02/28/mineralogy-magnetite-hematite-minerals-of-the-week-2/>. Accessed: 2022-03-18.

- [27] S. Fouvry, P. Arnaud, A. Mignot, and P. Neubauer, "Contact size, frequency and cyclic normal force effects on Ti-6Al-4V fretting wear processes: An approach combining friction power and contact oxygenation," *Tribology International*, vol. 113, pp. 460-473, sep 2017.
- [28] M. Godet, "The third-body approach: A mechanical view of wear," *Wear*, vol. 100, no. 1-3, pp. 437-452, 1984.
- [29] Y. Berthier, L. Vincent, and M. Godet, "Velocity accommodation in fretting," *Wear*, vol. 125, no. 1-2, pp. 25-38, 1988.
- [30] S. L. Sunde, F. Berto, and B. Haugen, "Predicting fretting fatigue in engineering design," *International Journal of Fatigue*, vol. 117, pp. 314-326, 2018.
- [31] S. R. Pearson and P. H. Shipway, "Is the wear coefficient dependent upon slip amplitude in fretting? Vingsbo and Söderberg revisited," *Wear*, vol. 330-331, pp. 93-102, 2015.
- [32] O. Vingsbo and S. Söderberg, "On fretting maps," *Wear*, vol. 126, no. 2, pp. 131-147, 1988.
- [33] R. D. Mindlin, "Compliance of Elastic Bodies in Contact," in *The Collected Papers of Raymond D. Mindlin Volume I*, vol. 16, pp. 197-206, 1989.
- [34] Z. R. Zhou and L. Vincent, "Mixed fretting regime," *Wear*, vol. 181-183, no. PART 2, pp. 531-536, 1995.
- [35] M. H. Zhu and Z. R. Zhou, "On the mechanisms of various fretting wear modes," *Tribology International*, vol. 44, no. 11, pp. 1378-1388, 2011.
- [36] S. Fouvry, T. Liskiewicz, P. Kapsa, S. Hannel, and E. Sauger, "An energy description of wear mechanisms and its applications to oscillating sliding contacts," *Wear*, vol. 255, pp. 287-298, aug 2003.
- [37] J. A. Collins, "Fretting-Fatigue Damage-Factor Determination," *Journal of Manufacturing Science and Engineering, Transactions of the ASME*, vol. 87, no. 3, pp. 298-302, 1965.
- [38] T. Maruyama and T. Saitoh, "Oil film behavior under minute vibrating conditions in EHL point contacts," *Tribology International*, vol. 43(8), p. 1279-1286, 2010.
- [39] F. Schwack, M. Stammer, G. Poll, and A. Reuter, "Comparison of Life Calculations for Oscillating Bearings Considering Individual Pitch Control in Wind Turbines," *Journal of Physics: Conference Series*, vol. 753, no. 11, 2016.
- [40] F. Schwack, N. Bader, J. Leckner, C. Demaille, and G. Poll, "A study of grease lubricants under wind turbine pitch bearing conditions," *Wear*, vol. 454-455, p. 203335, 2020.
- [41] G. Chen and J. Wen, "Load Performance of Large-Scale Rolling Bearings With Supporting Structure in Wind Turbines," *Journal of Tribology*, vol. 134, no. 4, p. 041105, 2012.

- [42] M. Olave, X. Sagartzazu, J. Damian, and A. Serna, "Design of four contact-point slewing bearing with a new load distribution procedure to account for structural stiffness," *Journal of Mechanical Design, Transactions of the ASME*, vol. 132, no. 2, pp. 0210061–02100610, 2010.
- [43] F. Schwack, F. Prigge, and G. Poll, "Finite element simulation and experimental analysis of false brinelling and fretting corrosion," *Tribology International*, vol. 126, pp. 352–362, 2018.
- [44] O. Brinji, K. Fallahnezhad, and P. Meehan, "Analytical model for predicting false brinelling in bearings," *Wear*, vol. 444–445, no. 0043–1648, p. 203135, 2020.
- [45] N. De Laurentis, A. Kadiric, P. Lugt, and P. Cann, "The influence of bearing grease composition on friction in rolling/sliding concentrated contacts," *Tribology International*, vol. 94, pp. 624–632, 2016.
- [46] L. Haviez, S. Fouvry, R. Toscano, and G. Yantio, "An energy-based approach to understand the effect of fretting displacement amplitude on grease-lubricated interface," *Wear*, vol. 338–339, pp. 422–429, 2015.
- [47] F. Schwack, M. Stammeler, A. Bartschat, F. Pape, and G. Poll, "Solutions to reduce wear in wind turbine blade bearings," in *Proceedings, Bearing World*, vol. 2, (Kaiserslautern, Germany), 2018.
- [48] T. Maruyama, T. Saitoh, and A. Yokouchi, "Differences in mechanisms for fretting wear reduction between oil and grease lubrication," *Tribology Transactions*, vol. 60, no. 3, pp. 497–505, 2017.
- [49] I. Llavori, A. Zabala, A. Aginagalde, W. Tato, J. J. Ayerdi, and X. Gómez, "Critical Analysis of Coefficient of Friction Derivation Methods for Fretting under Gross Slip Regime," *Tribology International*, vol. 143, 2020.
- [50] S. Fouvry, P. Duó, and P. Perruchaut, "A quantitative approach of Ti-6Al-4V fretting damage: Friction, wear and crack nucleation," *Wear*, vol. 257, no. 9–10, pp. 916–929, 2004.
- [51] D. M. Mulvihill, M. E. Kartal, A. V. Olver, D. Nowell, and D. A. Hills, "Investigation of non-Coulomb friction behaviour in reciprocating sliding," *Wear*, vol. 271, no. 5–6, pp. 802–816, 2011.
- [52] X. Jin, W. Sun, and P. H. Shipway, "Derivation of a wear scar geometry-independent coefficient of friction from fretting loops exhibiting non-Coulomb frictional behaviour," *Tribology International*, vol. 102, pp. 561–568, 2016.
- [53] J. Hintikka, A. Mäntylä, J. Vaara, T. Frondelius, and A. Lehtovaara, "Stable and unstable friction in fretting contacts," *Tribology International*, vol. 131, no. July 2018, pp. 73–82, 2019.
- [54] A. de Pannemaecker, S. Fouvry, J. Y. Buffiere, and M. Brochu, "Modelling the fretting fatigue crack growth: From short crack correction strategies to microstructural approaches," *International Journal of Fatigue*, vol. 117, no. April, pp. 75–89, 2018.

- [55] J. L. Mo, M. H. Zhu, J. F. Zheng, J. Luo, and Z. R. Zhou, "Study on rotational fretting wear of 7075 aluminum alloy," *Tribology International*, vol. 43, no. 5-6, pp. 912–917, 2010.
- [56] ASTM International, "ASTM D4170-16 Standard Test Method for Fretting Wear Protection by Lubricating Greases," tech. rep., 2017.
- [57] P. He, R. Hong, H. Wang, and C. Lu, "Pitch bearing/raceway fretting: Influence of contact angle," *Proceedings of the Institution of Mechanical Engineers, Part C: Journal of Mechanical Engineering Science*, vol. 233, no. 5, pp. 1734–1749, 2019.
- [58] K.-H. Zum Gahr, *Microstructure and wear of materials*, vol. 10. Elsevier, 1987.
- [59] H.-C. Meng, *Wear modeling: evaluation and categorization of wear models*. University of Michigan, 1994.
- [60] H. Meng and K. Ludema, "Wear models and predictive equations: their form and content," *Wear*, vol. 181, pp. 443–457, 1995.
- [61] S. Hsu, M. Shen, and A. Ruff, "Wear prediction for metals," *Tribology International*, vol. 30, no. 5, pp. 377–383, 1997.
- [62] P. J. Blau, "Fifty years of research on the wear of metals," *Tribology International*, vol. 30, no. 5, pp. 321–331, 1997.
- [63] A. Kapoor, "Wear by plastic ratchetting," *Wear*, vol. 212, no. 1, pp. 119–130, 1997.
- [64] V. Hegadekatte, S. Kurzenhäuser, N. Huber, and O. Kraft, "A predictive modeling scheme for wear in tribometers," *Tribology International*, vol. 41, pp. 1020–1031, nov 2008.
- [65] I. McColl, J. Ding, and S. Leen, "Finite element simulation and experimental validation of fretting wear," *Wear*, vol. 256, no. 11, pp. 1114–1127, 2004.
- [66] C. Mary and S. Fouvry, "Numerical prediction of fretting contact durability using energy wear approach: Optimisation of finite-element model," *Wear*, vol. 263, pp. 444–450, sep 2007.
- [67] J. F. Manwell, J. G. McGowan, and A. L. Rogers, *Wind Energy Explained*, ch. 4, pp. 157–203. John Wiley & Sons, Ltd, 2009.
- [68] DS/EN, "DS/EN 1090-2:2008 Execution of steel structures," tech. rep., 2008.
- [69] Det Norske Veritas (DNV), "Guideline for design of wind turbines," tech. rep., 2002.
- [70] P. Guay and A. Frikha, "Ball Bearing Stiffness: A New Approach Offering Analytical Expressions," *16th European Space Mechanisms and Tribology Symposium*, no. June, 2015.
- [71] A. Daidie, Z. Chaib, and A. Ghosn, "3D Simplified Finite Elements Analysis of Load and Contact Angle in a Slewing Ball Bearing," *ASME J. Mech. Des.*, vol. 130, no. 8, p. 0823011–0826018, 2008.

- [72] O. Menck, M. Stammeler, and F. Schleich, "Fatigue lifetime calculation of wind turbine blade bearings considering blade-dependent load distribution," *Wind Energy Science*, vol. 5, no. 4, pp. 1743–1754, 2020.
- [73] F. Schwack, M. Stammeler, and H. Flory, "Free Contact Angles in Pitch Bearings and their Impact on Contact and Stress Conditions," in *Wind Europe Conference Paper*, no. September, p. 2016, 2016.
- [74] "Inifitefocus-sl product information." <https://www.alicon.com/products/infinitefocus/>. Accessed: 2021-06-14.
- [75] Martin, "Alicona file format reader (al3d)," 2021.
- [76] E. Sauger, S. Fouvry, L. Ponsonnet, P. Kapsa, J. M. Martin, and L. Vincent, "Tribologically transformed structure in fretting," *Wear*, vol. 245, no. 1-2, pp. 39–52, 2000.
- [77] Buehler, *Buehler (R) SumMet (TM) A Guide to Materials Preparation and Analysis*, fourth edition ed., 2007.
- [78] D. Godfrey, "Iron oxides and rust (hydrated iron oxides) in tribology (c)," *Lubrication Engineering*, vol. 55, pp. 33–37, 1999.
- [79] "Extend wind turbine life with pitch bearing upgrades." https://www.kaydonbearings.com/white_papers_16.htm. Accessed: 2020-03-02.
- [80] R. Ferre, S. Fouvry, B. Berthel, R. Amargier, and J. A. Ruiz-Sabariago, "Prediction of the fretting fatigue crack nucleation endurance of a Ti-6V-4Al/ Ti-6V-4Al interface: Influence of plasticity and tensile/shear fatigue properties," in *Procedia Engineering*, vol. 66, pp. 803–812, 2013.
- [81] International Organisation for Standardisation, "ISO 4287: Geometrical Product Specifications (GPS) - Surface texture: Profile method - Terms, definitions and surface texture parameters," tech. rep., 1997.
- [82] International Organisation for Standardisation, "ISO 4288: Geometrical Product Specifications (GPS) — Surface texture: Profile method — Rules and procedures for the assessment of surface texture," tech. rep., 1997.
- [83] G. F. Vander Voort, "Revealing prior-austenite grain boundaries in heat-treated steels," *Industrial Heating*, vol. 78, pp. 48—52, 2010.
- [84] H. L. Heathcote, "The ball bearing: in the making, under test and on service," *Proceedings of the Institution of Automobile Engineers*, vol. 15, no. 1, pp. 569–702, 1920.
- [85] Castrol UK Limited, *Product Data LMX grease*, 2002.
- [86] P. J. Blau, *Friction science and technology from concepts to applications*, ch. 3, pp. 43–118. CRC Press, 2009.
- [87] P. Sandstrom, K. Sridharan, and J. Conrad, "A machine for fretting wear testing of plasma surface modified materials," *Wear*, vol. 166, no. 2, pp. 163–168, 1993.

- [88] J. F. Epperson, *An Introduction to Numerical Methods and Analysis, 2nd Edition*, ch. 5, pp. 249–332. Wiley, 2013.
- [89] R. D. Mindlin and H. Deresiewicz, “Elastic Spheres in Contact Under Varying Oblique Forces,” *Journal of Applied Mechanics*, vol. 20, pp. 327–344, 06 1953.
- [90] S. Fouvry, P. Kapsa, and L. Vincent, “Analysis of sliding behaviour for fretting loadings: determination of transition criteria,” *Wear*, vol. 185, no. 1, pp. 35–46, 1995.
- [91] M. Varenberg, I. Etsion, and G. Halperin, “Slip index: A new unified approach to fretting,” *Tribology Letters*, vol. 17, no. 3, pp. 569–573, 2004.
- [92] S. Wandel, N. Bader, F. Schwack, J. Glodowski, B. Lehnhardt, and G. Poll, “Starvation and relubrication mechanisms in grease lubricated oscillating bearings,” *Tribology International*, vol. 165, p. 107276, 2022.
- [93] P. Cann, F. Chevalier, and A. Lubrecht, “Track depletion and replenishment in a grease lubricated point contact: A quantitative analysis,” in *Elastohydrodynamics - '96 Fundamentals and Applications in Lubrication and Traction* (D. Dowson, C. Taylor, T. Childs, G. Dalmaz, Y. Berthier, L. Flamand, J.-M. Georges, and A. Lubrecht, eds.), vol. 32 of *Tribology Series*, pp. 405–413, Elsevier, 1997.
- [94] T. A. Harris, *Advanced Concepts of Bearing Technology: Rolling Bearing Analysis, Fifth Edition*. Boca Raton: CRC Press, 5th edition ed., 2006.
- [95] Moog, *Hardware Manual Moog Test Controller 2.0*, 2013.
- [96] “En19 datasheet.” <https://www.westyorkssteel.com/files/en19t.pdf>. Accessed: 2022-07-13.
- [97] “O1 datasheet.” <https://www.westyorkssteel.com/files/o1.pdf>. Accessed: 2022-07-13.
- [98] L. Bourithis, G. Papadimitriou, and J. Sideris, “Comparison of wear properties of tool steels aisi d2 and o1 with the same hardness,” *Tribology International*, vol. 39, no. 6, pp. 479–489, 2006.
- [99] K. Johnson, “A review of the theory of rolling contact stresses,” *Wear*, vol. 9, no. 1, pp. 4–19, 1966.
- [100] W. Wieleba, “The statistical correlation of the coefficient of friction and wear rate of ptfе composites with steel counterface roughness and hardness,” *Wear*, vol. 252, no. 9, pp. 719–729, 2002.
- [101] Z. Li, M. He, H. Dong, Z. Shu, and X. Wang, “Friction performance assessment of non-asbestos organic (nao) composite-to-steel interface and polytetrafluoroethylene (ptfe) composite-to-steel interface: Experimental evaluation and application in seismic resistant structures,” *Construction and Building Materials*, vol. 174, pp. 272–283, 2018.
- [102] D. Systèmes, *Abaqus 6.14 Documentation*.
- [103] J. Ding, S. Leen, and I. McColl, “The effect of slip regime on fretting wear-induced stress evolution,” *International Journal of Fatigue*, vol. 26, no. 5, pp. 521–531, 2004.

- [104] K. Elleuch and S. Fouvry, “Experimental and modelling aspects of abrasive wear of a a357 aluminium alloy under gross slip fretting conditions,” *Wear*, vol. 258, no. 1, pp. 40–49, 2005. Second International Conference on Erosive and Abrasive Wear.
- [105] T. Zhang, P. McHugh, and S. Leen, “Computational study on the effect of contact geometry on fretting behaviour,” *Wear*, vol. 271, no. 9, pp. 1462–1480, 2011. 18th International Conference on Wear of Materials.
- [106] L. Tang, S. Ding, Y. Xie, and Y. Huo, “A multilayer nodes update method in fem simulation of large depth fretting wear,” *Wear*, vol. 301, no. 1, pp. 483–490, 2013. *Wear of Materials 2013*.
- [107] T. Yue and M. Abdel Wahab, “Finite element analysis of fretting wear under variable coefficient of friction and different contact regimes,” *Tribology International*, vol. 107, no. December 2016, pp. 274–282, 2017.
- [108] A. P. S. Arunachalam and S. Idapalapati, “Material removal analysis for compliant polishing tool using adaptive meshing technique and archard wear model,” *Wear*, vol. 418-419, pp. 140–150, 2019.
- [109] M. Arjmandi, M. Ramezani, M. Giordano, and S. Schmid, “Finite element modelling of sliding wear in three-dimensional woven textiles,” *Tribology International*, vol. 115, pp. 452–460, 2017.
- [110] K. L. Johnson, “The Effect of a Tangential Contact Force Upon the Rolling Motion of an Elastic Sphere on a Plane,” *Journal of Applied Mechanics*, vol. 25, pp. 339–346, 06 2021.
- [111] F. Schwack, V. Schneider, S. Wandel, R. J. de la Presilla, G. Poll, and S. Glavatskih, “On the critical amplitude in oscillating rolling element bearings,” *Tribology International*, vol. 163, no. April, 2021.
- [112] J. Schijve, *Fatigue of Structures and Materials*. Kluwer Academic, 2001.

Appendix A

Python Functions for the Analysis of Fretting Loops

```
# Class definition and methods
#####
class FrettLoop:
    # General attributes
    def __init__(self,data,tini,tend,cof_max,cof_mean,z_amp):
        self.data = data
        self.tini = tini
        self.tend = tend
        self.period = tend-tini
        self.tavg = (tend+tini)/2.0
        self.freq = 1.0/self.period
        self.cof_max = cof_max
        self.cof_mean = cof_mean
        self.z_amp = z_amp
    # Methods
    def energy(self):
        # calculates the area enclosed within the fretting loop
        Ed = 0.0
        for i,point in enumerate(self.data):
            if i==0:
                inc_Ed = 0.5*(self.data[i+1,0]-point[0])*point[1]
                # print(inc_Ed)
                Ed+=inc_Ed
```

```
        elif i==len(self.data)-1:
            inc_Ed = 0.5*(self.data[0,0]-point[0])*point[1]
            # print(inc_Ed)
            Ed+=inc_Ed
        else:
            inc_Ed = (self.data[i+1,0]-point[0])*point[1]
            # print(inc_Ed)
            Ed+=inc_Ed
    if Ed <= 0:
        Ed = 0.0
    return Ed
def sliding(self):
    # calculates the area enclosed within the fretting loop
    d = []
    for i,point in enumerate(self.data):
        if i>=len(self.data)-1:
            if point[1]*self.data[0,1] <= 0:
                d.append((point[0]+self.data[0,0])/2)
            if len(d)>1:
                break
        elif point[1]*self.data[i+1,1] <= 0:
            d.append((point[0]+self.data[i+1,0])/2)
            if len(d)>1:
                break
    delta = abs(d[0]-d[1])
    return delta
def gicof(self,force):
    # calculates a geometrically independent COF
    gi_cof = 1.0
    # Calculate S (similar to the sliding function)
    slope = []
    error_pos = []
    error_neg = []
    q_star_pos = 0.0
    q_star_neg = 0.0
```

```

for i,point in enumerate(self.data):
    if i>=len(self.data)-1:
        if point[1]*self.data[0,1] <= 0:
            slope.append((self.data[1,1]-self.data[i,1])/
                (self.data[1,0]-self.data[i,0]))
        if len(slope)>1:
            break
    elif point[1]*self.data[i+1,1] <= 0:
        slope.append((self.data[i-2,1]-self.data[i,1])/
            (self.data[i-2,0]-self.data[i,0]))
        if len(slope)>1:
            break
s = (slope[0]+slope[1])/2
# For each data point (D_i,Q_i) calculates:
#   Q*_i = S*D_i
#   error_i = abs(Q_i-Q*_i)
#   if error_i < error_i-1 --> Q* = Q_i
#   GICOF=Q*/P
for i,point in enumerate(self.data):
    q_i = s*point[0]
    if point[1] >= 0:
        error_pos.append(abs(q_i-point[1]))
        if len(error_pos)<=1:
            continue
        if error_pos[-1]<=min(error_pos):
            q_star_pos = abs(point[1])
    else:
        error_neg.append(abs(q_i-point[1]))
        if len(error_neg)<=1:
            continue
        if error_neg[-1]<=min(error_neg):
            q_star_neg = abs(point[1])
    gi_cof = max(q_star_pos,q_star_neg)/(force)
    return gi_cof,s
def avgcof(self,force):
    avg_cof = 1.0

```

```

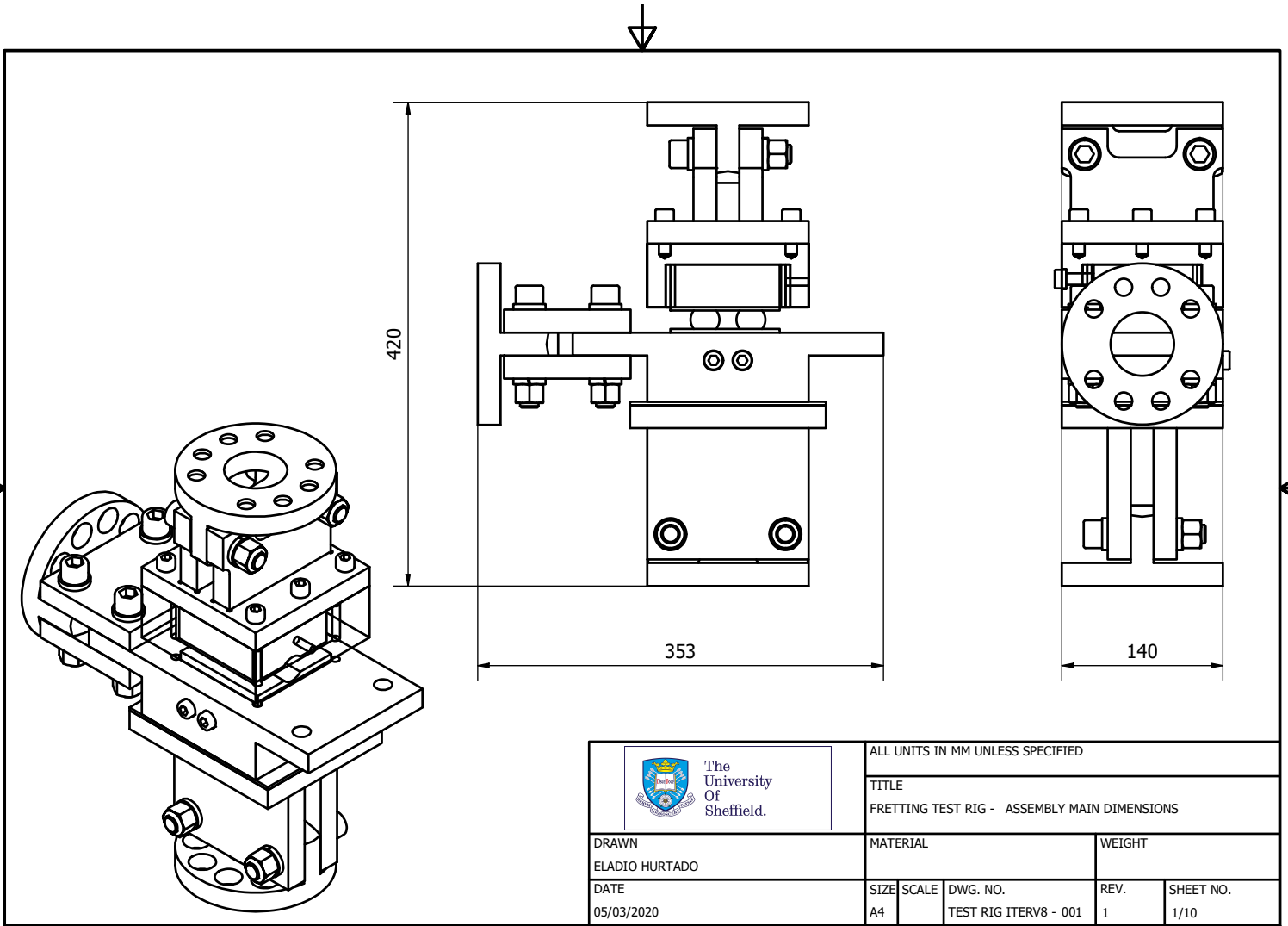
        # calculate upper and lower ten percent
        #print(self.data)
        q_max = abs(np.amax(self.data,axis=0)[1])
        q_min = abs(np.amin(self.data,axis=0)[1])
        return ((q_max+q_min)/(2*force))


# Definition of function for counting loop cycles
#####
def Loop_Count(sample,dT,T,tcycles):
# array contains the following columns:
time, disp,force,cof,dT,tcycles
    # center and clockwise loops
    mean_disp = sample.mean(0)[3]
    sample[:,3]=1*(sample[:,3]-mean_disp)
    mean_traction = sample.mean(0)[1]
    sample[:,1]=1*(sample[:,1]-mean_traction)
    ini = 0
    end = 0
    n = round(T/dT)
    cycles = []
    for i in range(tcycles):
        ini = 30+i*n
        end = 30+(i+1)*n+1
        loop = np.vstack((sample[ini:end,3],sample[ini:end,1])).T
        z_amp = np.amax(sample[ini:end],axis=0)[2]-
        np.amin(sample[ini:end],axis=0)[4]
        cycles.append(FrettLoop(loop,sample[ini,0],sample[end,0],
        np.amax(sample[ini:end],axis=0)[4],
        sample[ini:end].mean(0)[4],z_amp))
    return cycles

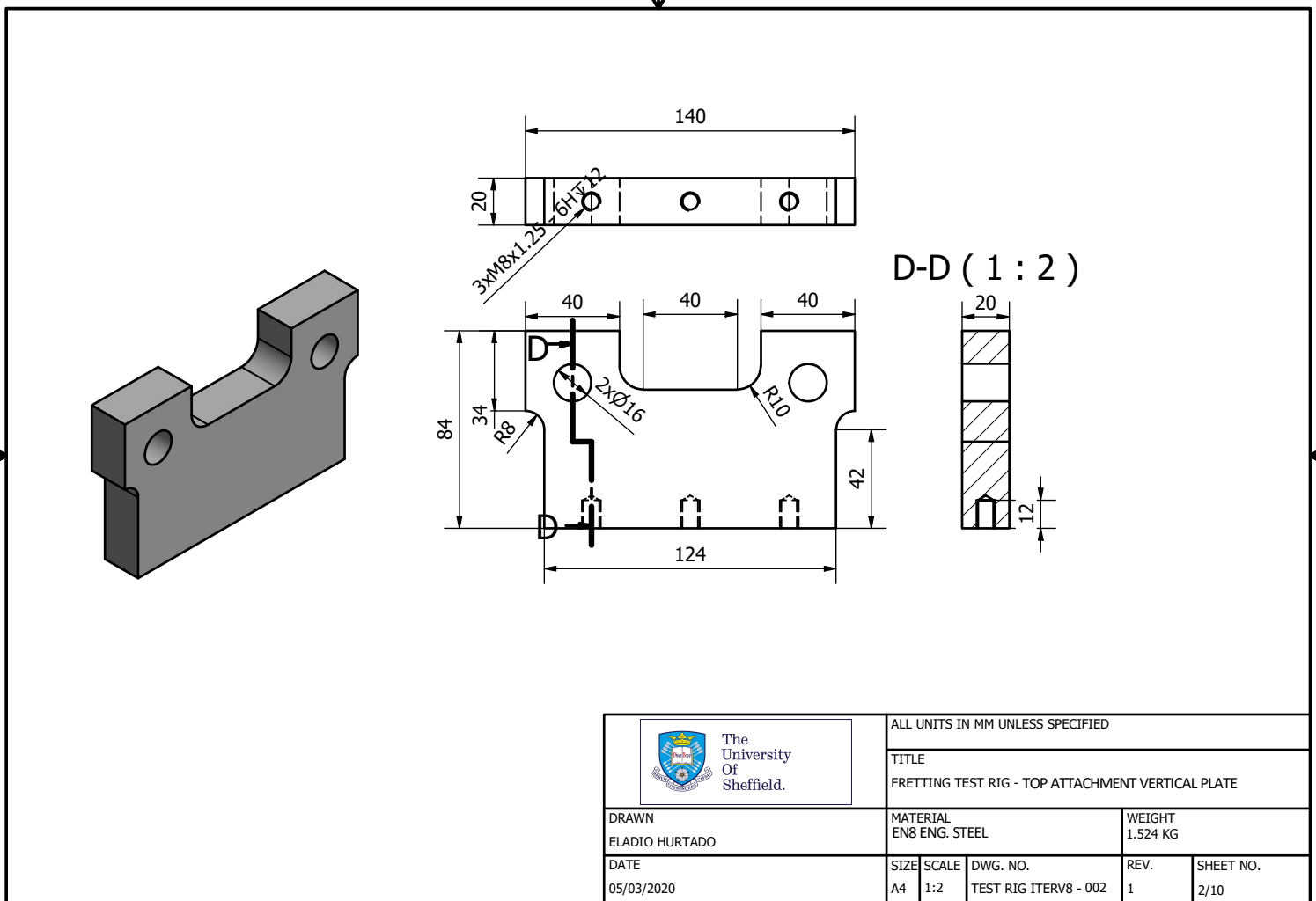
```


Appendix B

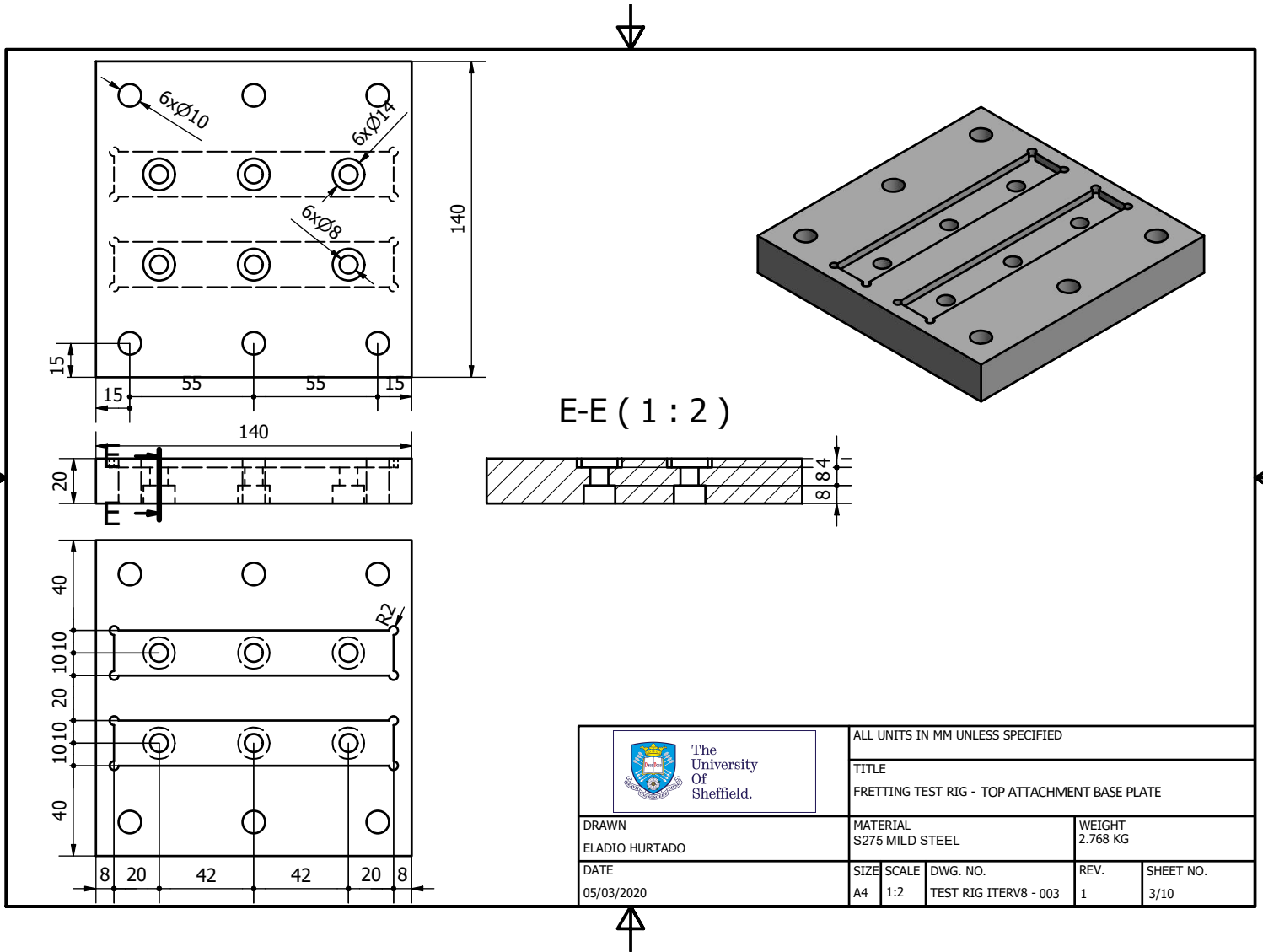
Medium-Scale Fretting Test-Rig Drawings

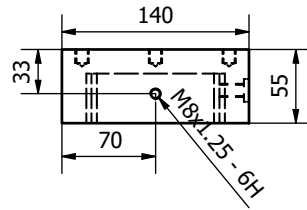
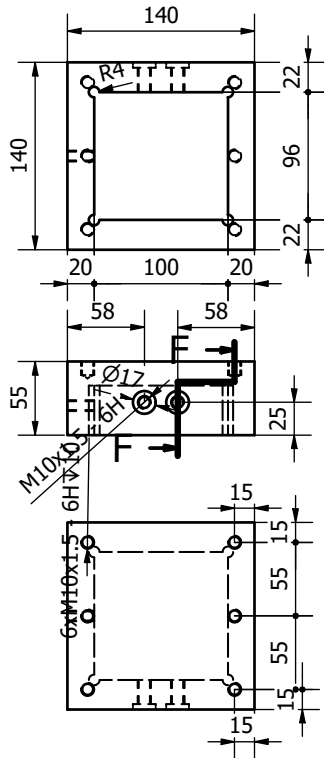
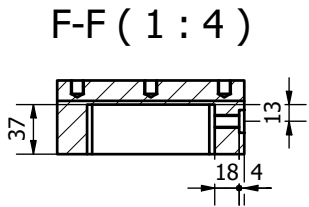
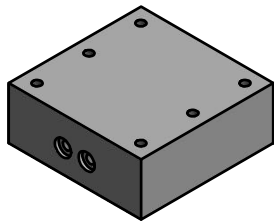



 The University Of Sheffield.		ALL UNITS IN MM UNLESS SPECIFIED				
		TITLE FRETTING TEST RIG - ASSEMBLY MAIN DIMENSIONS				
DRAWN ELADIO HURTADO		MATERIAL			WEIGHT	
DATE 05/03/2020		SIZE A4	SCALE	DWG. NO. TEST RIG ITERV8 - 001	REV. 1	SHEET NO. 1/10

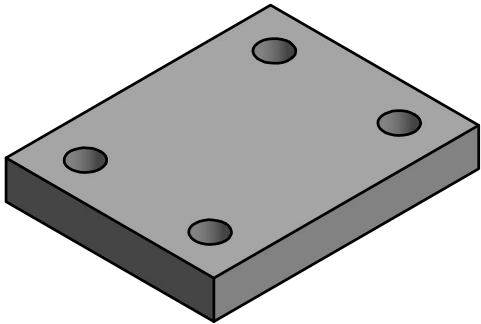
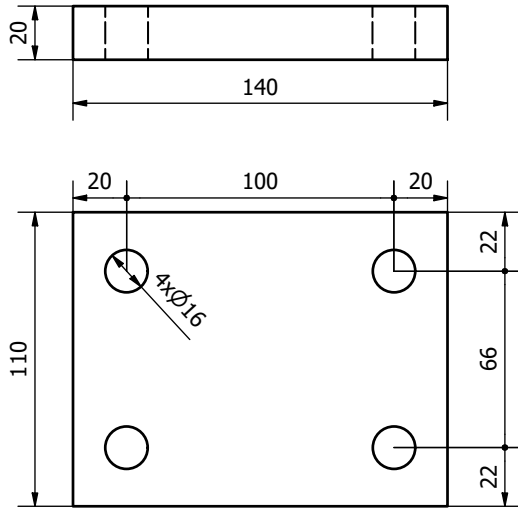



 The University Of Sheffield.		ALL UNITS IN MM UNLESS SPECIFIED				
		TITLE FRETTING TEST RIG - TOP ATTACHMENT VERTICAL PLATE				
DRAWN ELADIO HURTADO		MATERIAL EN8 ENG. STEEL		WEIGHT 1.524 KG		
DATE 05/03/2020		SIZE A4	SCALE 1:2	DWG. NO. TEST RIG ITERV8 - 002	REV. 1	SHEET NO. 2/10

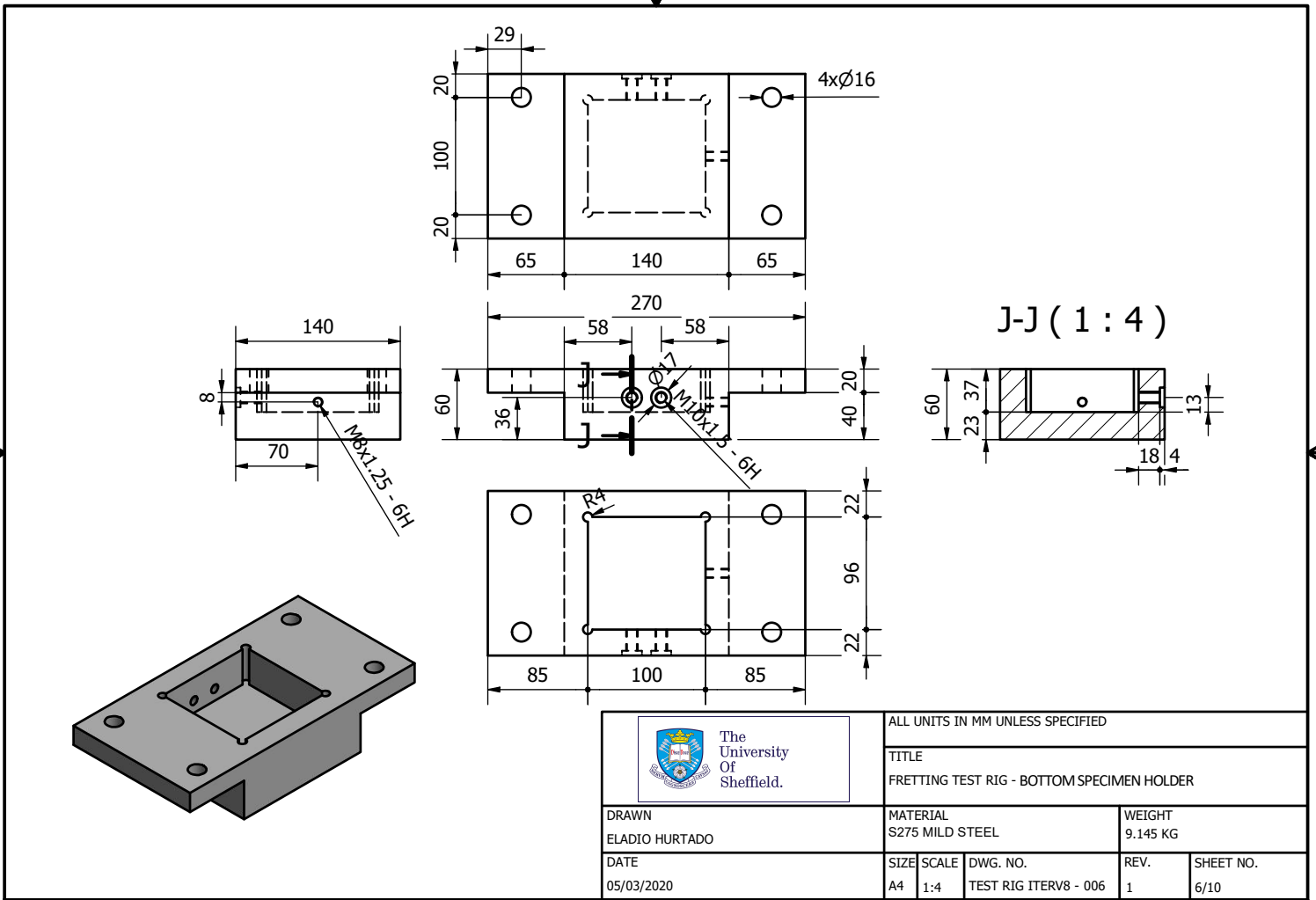





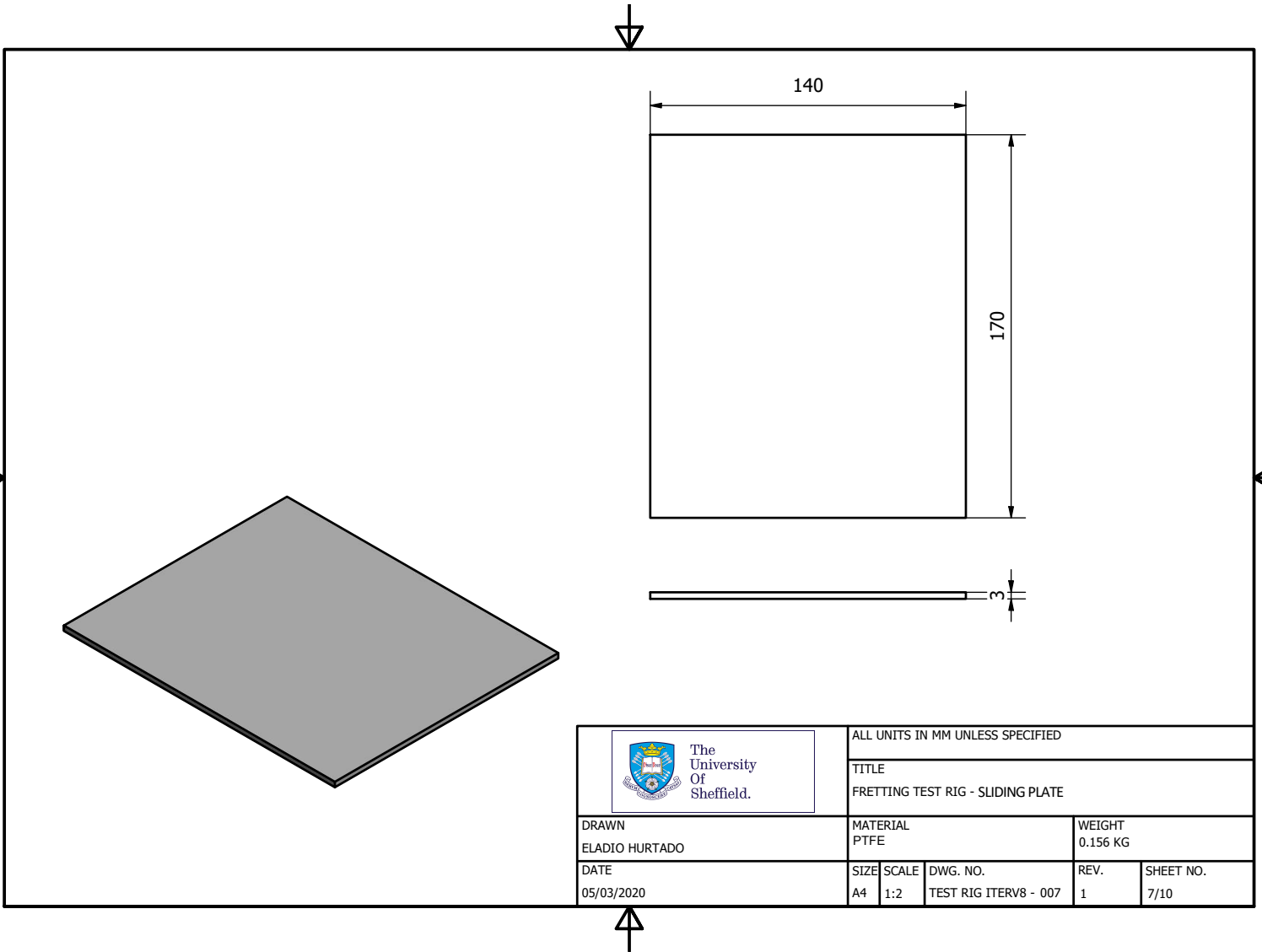
 The University Of Sheffield.		ALL UNITS IN MM UNLESS SPECIFIED			
		TITLE FRETTING TEST RIG - TOP SPECIMEN HOLDER			
DRAWN ELADIO HURTADO		MATERIAL S275 MILD STEEL		WEIGHT 5.589 KG	
DATE 05/03/2020		SIZE A4	SCALE 1:4	DWG. NO. TEST RIG ITERV8 - 004	SHEET NO. 4/10




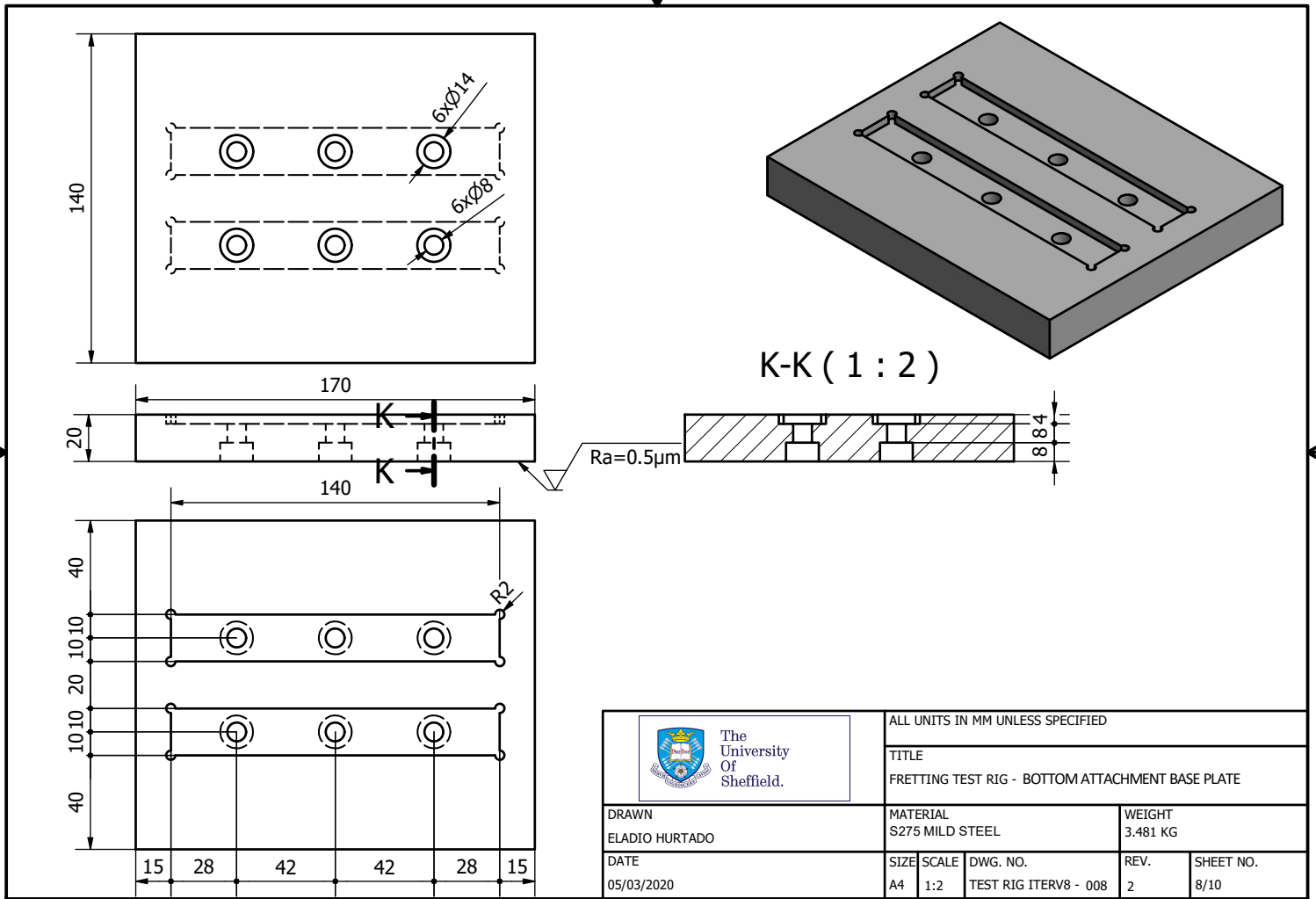
 The University Of Sheffield.		ALL UNITS IN MM UNLESS SPECIFIED				
		TITLE FRETTING TEST RIG - SIDE PLATE ATTACHMENT				
DRAWN ELADIO HURTADO		MATERIAL EN8 ENG. STEEL		WEIGHT 2.292 KG		
DATE 05/03/2020		SIZE A4	SCALE 002	DWG. NO. TEST RIG ITERV8 - 005	REV. 1	SHEET NO. 5/10

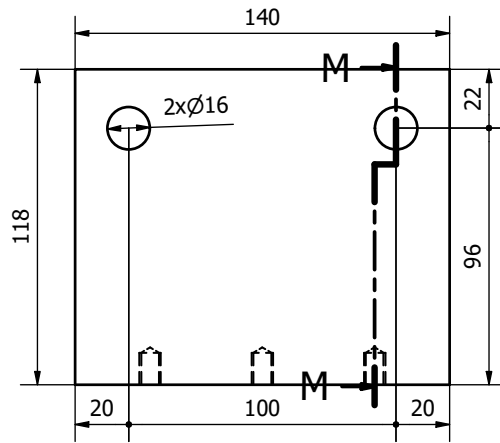
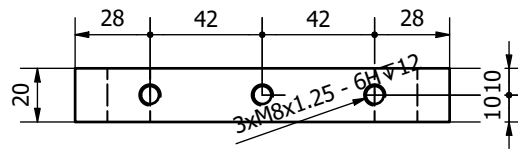
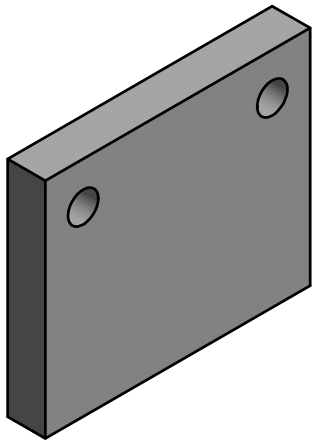


 The University Of Sheffield.					ALL UNITS IN MM UNLESS SPECIFIED				
					TITLE				
					FRETTING TEST RIG - BOTTOM SPECIMEN HOLDER				
DRAWN ELADIO HURTADO			MATERIAL S275 MILD STEEL		WEIGHT 9.145 KG				
DATE 05/03/2020			SIZE A4	SCALE 1:4	DWG. NO. TEST RIG ITERV8 - 006	REV. 1	SHEET NO. 6/10		

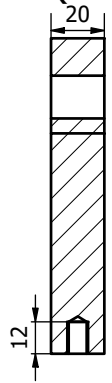



 The University Of Sheffield.		ALL UNITS IN MM UNLESS SPECIFIED				
		TITLE FRETTING TEST RIG - SLIDING PLATE				
DRAWN ELADIO HURTADO		MATERIAL PTFE		WEIGHT 0.156 KG		
DATE 05/03/2020		SIZE A4	SCALE 1:2	DWG. NO. TEST RIG ITERV8 - 007	REV. 1	SHEET NO. 7/10

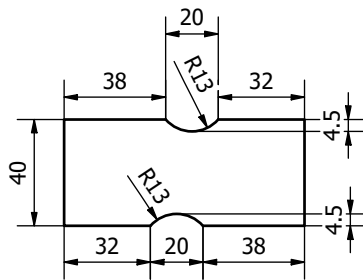
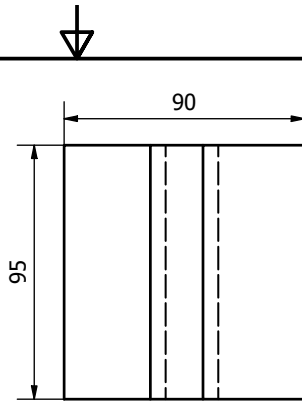
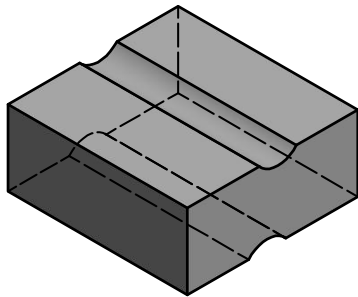





M-M (1 : 2)



 The University Of Sheffield.		ALL UNITS IN MM UNLESS SPECIFIED				
		TITLE FRETTING TEST RIG - BOTTOM ATTACHMENT VERTICAL PLATE				
DRAWN ELADIO HURTADO		MATERIAL EN8 ENG. STEEL		WEIGHT 2.520 KG		
DATE 05/03/2020		SIZE A4	SCALE 1:2	DWG. NO. TEST RIG ITERV8 - 009	REV. 1	SHEET NO. 9/10



 The University Of Sheffield.		ALL UNITS IN MM UNLESS SPECIFIED				
		TITLE FRETTING TEST RIG - SAMPLE (CONTACT ANGLE 0)				
DRAWN ELADIO HURTADO		MATERIAL ASTM 52100 BEARING STEEL		WEIGHT		
DATE 05/03/2020		SIZE A4	SCALE 1:2	DWG. NO. TEST RIG ITERV8 -010	REV. 1	SHEET NO. 10/10

Appendix C

Medium-Scale Fretting Test-Rig FEA

A finite element analysis of the medium-scale test rig was performed to assess its mechanical strength through a stress analysis.

C.1 Description of the FE Model

All the components of the test rig were considered for the analysis but some simplifications in the geometry were made. The geometry of all bolts was simplified by removing their threads. The top and bottom attachments, made of three plates assembled by bolted connections, were modelled as one single component. Figure C.1a shows the geometry considered for the FE model.

The model was fully meshed with hexahedral second order elements. Figure C.1b shows views of the meshed model.

The boundary conditions defined in the model are summarised below.

- Reference points were defined at the end of each actuator linked by means of MPC conditions
- All the bolted connections were modelled in detail. This means that frictional contacts were defined between all the surfaces in contact. A coefficient of friction equal to 0.3 was considered in all the interactions
- A frictional contact with a COF of 0.05 was defined between the sliding plate and the bottom holder, and between the sliding plate and the bottom attachment
- Tie interactions were defined between the bearing sections and their holders

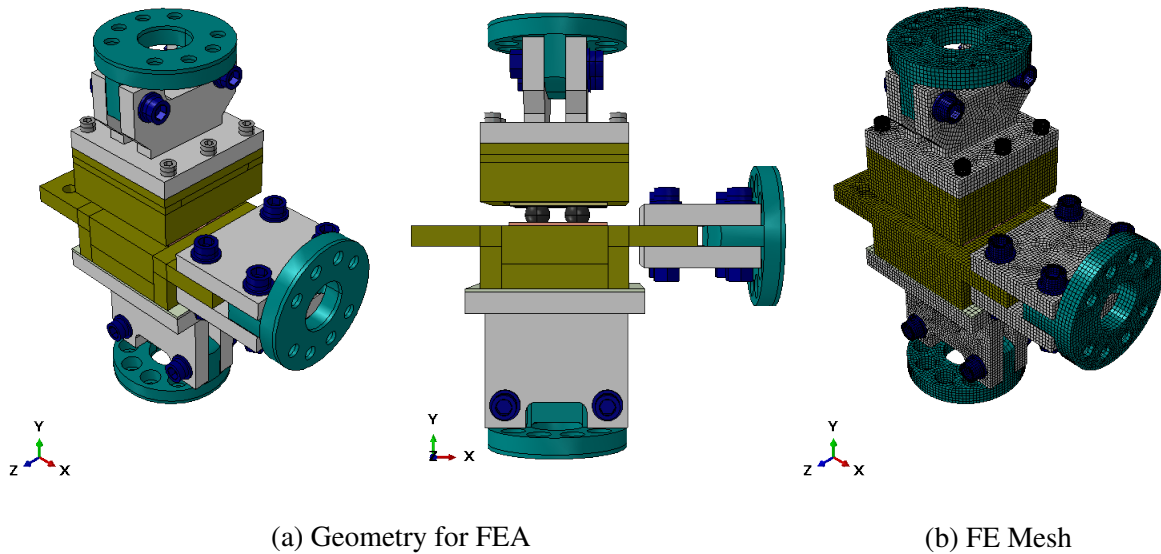


Figure C.1: Geometry and mesh for FEA of medium-scale test rig.

- The reference point located at the bottom actuator was fixed in all translation and rotation components
- The reference points located at the lateral actuators (left and right) were fixed in all translation and rotation components, but let free to move along the horizontal direction
- The reference point located at the top actuator was fixed in all translation and rotation components, but let free to move along the vertical direction

The mechanical strength of the test rig was assessed under design load conditions. These loading conditions consisted of the maximum normal load applied on the top actuator. The magnitude of this load was set to 100 kN. The tangential load due to frictional force was neglected in the analysis. However, three positions of the lateral attachments were considered to evaluate the stresses during the test rig operation. These cyclic stresses produced during the different positions in the oscillation cycle might result in fatigue failure. Figure C.2 presents the three positions considered for the analysis and the position where the load is applied.

C.2 Stress Analysis Results

Two failure criteria were considered for the mechanical strength analysis. The first criterion was yield failure. It was verified that the maximum von Mises stress on every component does not exceed the material yield stress. The second criterion was fatigue. It was verified that the

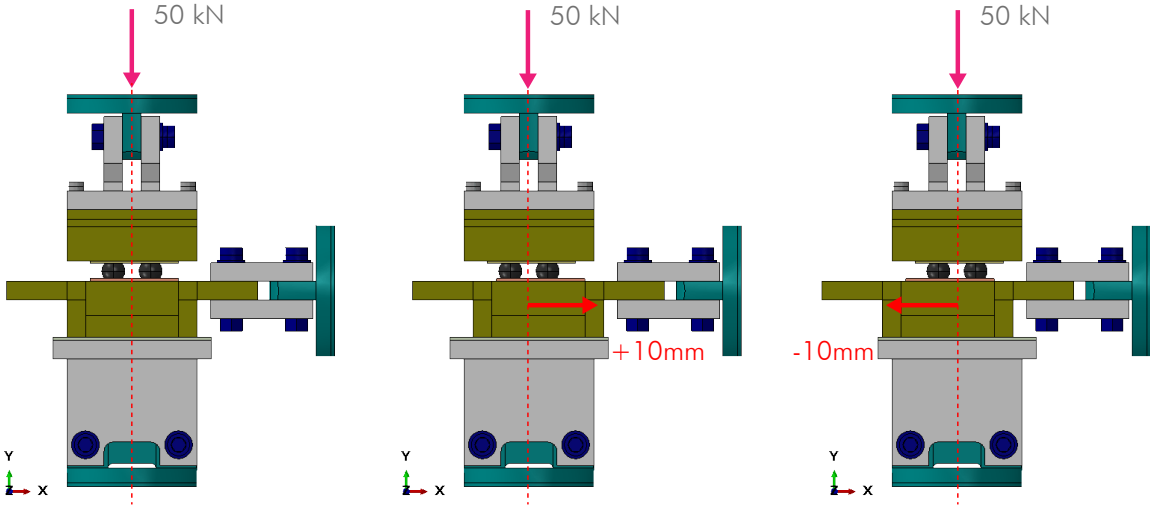


Figure C.2: Loads and positions considered for the FEA of the medium-scale test rig.

cyclic stresses on every component do not result in fatigue failure according to Goodman’s criterion [112] considering the principal stresses. The maximum principal stress distribution for all the components is presented in Figure C.3. Tables C.1 and C.2 summarise the results of the yield analysis and the fatigue analysis, respectively.

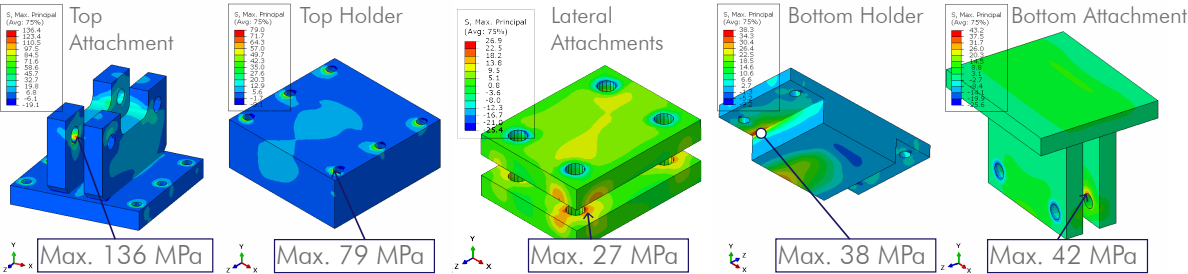


Figure C.3: Maximum principal stress distribution results [MPa].

Table C.1: Yield failure analysis results.

Part	von Mises Stress [MPa]			Max. Stress [MPa]	Yield Stress [MPa]	Safety Factor
	Pos. 0 mm	Pos. -10 mm	Pos. +10 mm			
Upper Attachment	443	448	450	450	450	1.0
Top Holder	68.2	74.8	69.3	74.8	275	3.7
Side Attachment	89.5	90.5	89.1	90.5	450	5.0
Bottom Holder	40	50.9	45.6	50.9	275	5.4
Lower Attachment	110	110	109	110	450	4.1

Table C.2: Fatigue analysis results.

Part	Principal Stress [MPa]			Alternating Stress [MPa]	Mean Stress [MPa]	Safety Factor
	Pos. 0 mm	Pos. -10 mm	Pos. +10 mm			
Upper Attachement	136	135	140	2.6	137	4.8
Top Holder	79.0	87.9	79.9	4.5	83.5	3.9
Side Attachement	26.9	26.8	29.0	1.1	27.9	22
Bottom Holder	38.0	44.1	31.5	6.3	37.8	6.6
Lower Attachement	43.2	43.3	24.7	9.3	34.0	11

Appendix D

Implementation of UMESHMOTION

D.1 Description of UMESHMOTION User Subroutine

UMESHMOTION is a user subroutine available in ABAQUS that can be used to define the motion of nodes in an adaptive mesh constraint. UMESHMOTION user subroutine can use utility routines GETVRN, GETNODETOELEMCONN, and GETVRMAVGATNODE to access results data at the nodes [102]. Fretting wear simulation requires the definition of two regions: i) a set of nodes of the contact surface and ii) a contact domain for the adaptive algorithm [107]. This user subroutine is called at the end of each increment and it works as follows:

1. Local wear depth calculation: The contact results are obtained at the end of every structural equilibrium iteration and the local incremental wear depth is calculated for each node based on Equation 6.1.
2. Adaptive meshing: Nodes of the contact domain are moved according to the adaptive meshing algorithm that consist of two steps: Sweeping and Advection. During the sweeping step the nodes are adjusted depending on the adjacent nodes. During the advection the result variables are mapped into the updated mesh.

D.2 UMESHMOTION Code for Fretting Wear

```
SUBROUTINE UMESHMOTION(UREF, ULOCAL, NODE, NNDOF, LNODETYPE, ALOCAL, NDIM,  
TIME, DTIME, &PNEWDT, KSTEP, KING, KMESHSWEEP, JMATYP, JGVBLOCK, LSMOOTH)
```

```
INCLUDE 'aba_param_dp.inc'

! UMESHMOTION standard variables

DIMENSION ULOCAL(NDIM),JELEMLIST(300000)
DIMENSION ALOCAL(NDIM,300000),TIME(2)
DIMENSION JMATYP(300000),JGVBLOCK(300000)

! generic variables

INTEGER::master,delta_n
REAL::CPRESS,CSHEARX,CSHEARY,CSLIPX,CSLIPY,COPEN,INCSLIPX,INCSLIPY,
dh,kappa,var_input

DIMENSION ARRAY(15)

common/wear/
&   isclock,isclock2,    ! counts slave nodes
&   isnodes(6000),      ! records slave nodes number
&   oldslipx(6000),     ! records slip from the last increment
&   oldslipy(6000),     ! records slip from the last increment
&   tempslipx(6000),    ! records current slip
&   tempslipy(6000),    ! records current slip
&   islave_ref(300000), ! slave nodes counter number
&   icounter            ! counts the number of times that
UMESHMOTION is consulted.

icounter = icounter + 1
LSMOOTH = 1
kappa = 1.118E-9 ! wear energy coefficient (mm/J/mm^2)
delta_n = 100    ! jumping cycle
master = 0       ! master = 1 -> master node, master = 0 -> slave node

! Getting information form abaqus subroutines
JTYP = 0 ! node number as input (JTYP = 1 means elements number as input)
NELEMS = 500 ! maximum allowable length of JELEMLIST
```

```
CALL GETNODETOELEMCONN(NODE,NELEMS,JELEMLIST,JELEMTYPE,JRCD,JGVBLOCK)
! retrieves elements connected to the node

JTYP = 0 ! defines how material point information is averaged (0 or 1)

CALL GETVRMAVGATNODE(NODE,JTYP,'CSTRESS',ARRAY,JRCD,JELEMLIST,NELEMS,
JMATYP,JGVBLOCK)
! contact stress

CPRESS = ARRAY(1)
CSHEARX = ARRAY(2)
CSHEARY = ARRAY(3)

JTYP = 0 ! defines how material point information is averaged (0 or 1)
CALL GETVRMAVGATNODE(NODE,JTYP,'CDISP',ARRAY,JRCD,JELEMLIST,
NELEMS,JMATYP,JGVBLOCK)
! contact isplacements

COPEN = ARRAY(1)
CSLIPX = ARRAY(2)
CSLIPY = ARRAY(3)

LTRN = 0
! global coordinate system (LTRN = 1 -> local coordinate system)

isclock2 = isclock2 + 1
IF(islave_ref(NODE)==0)THEN

    isclock=isclock+1
    isnodes(isclock)=NODE
    islave_ref(NODE)=isclock

END IF

tempslipx(islave_ref(NODE))=CSLIPX
```

```
tempslipy(islave_ref(NODE))=CSLIPY
INCSLIPX=CSLIPX-oldslipx(islave_ref(NODE))
INCSLIPY=CSLIPY-oldslipy(islave_ref(NODE))

IF(KMESHSWEEP>0) GO TO 10
! avoids compute the wear twice within the same increment

! wear computation and nodal position update

dh = kappa*(ABS(CSHEARX)*ABS(INCSLIPX)+
ABS(CSHEARY)*ABS(INCSLIPY))*delta_n

ULOCAL(3) = ULOCAL(3) - dh

10 CONTINUE

! resetting incremental slip for the next increment

isclock2 = 0

oldslipx(isclock)=tempslipx(isclock)
oldslipy(isclock)=tempslipy(isclock)

RETURN

END SUBROUTINE
```